

Feasibility studies of terrestrial laser scanning in Coastal Geomorphology, Agronomy, and Geoarchaeology

Inaugural-Dissertation
zur
Erlangung des Doktorgrades
der Mathematisch-Naturwissenschaftlichen Fakultät
der Universität zu Köln

vorgelegt von
Dirk Hoffmeister
aus Köln

Köln 2014

Berichtersteller:

Prof. Dr. G. Bareth

Prof. Dr. H. Brückner

Tag der mündlichen Prüfung:

6. Dezember 2013

Abstract

Terrestrial laser scanning (TLS) is a newer, active method of remote sensing for the automatic detection of 3D coordinate points. This method has been developed particularly during the last 20 years, in addition to airborne and mobile laser scanning methods. All these methods use laser light and additional angle measurements for the detection of distances and directions. Thus, several thousands to hundreds of thousands of polar coordinates per second can be measured directly by an automatic deflection of laser beams. For TLS measurements, the coordinates and orientation of the origin of the laser beam can be determined to register different scan positions in a common coordinate system. These measurements are usually conducted by Global Navigation Satellite Systems or total station surveying, but also identical points can be used and data driven methods are possible. Typically, accuracies and point densities of a few centimetres to a few millimetres are achieved depending on the method. The derived 3D point clouds contain millions of points, which can be evaluated in post-processing stages by symbolic or data-driven methods. Besides the creation of digital surface and terrain models, laser scanning is used in many areas for the determination of 3D objects, distances, dimensions, and volumes. In addition, changes can be determined by multi-temporal surveys.

The terrestrial laser scanner Riegl LMS Z-420i was used in this work in combination with the Differential Global Positioning System system Topcon Hiper Pro, based on Real Time Kinematic (RTK-DGPS). In addition to the direct position determination of the laser scanner, the position of a self-developed reflector on a ranging pole was measured by the RTK-DGPS system to accurately derive the orientation of each measured point cloud. Moreover, the scanner is equipped with an additional, mounted camera Nikon D200 to capture oriented pictures. These pictures allow colouring the point cloud in true colours and thus allow a better orientation. Furthermore, the pictures can be used for the extraction of detailed 3D information and for texturing the 3D objects. In one of the post-processing steps, the direct georeferencing by RTK-DGPS data was refined using the Multi Station Adjustment, which employs the Iterative Closest Point algorithm. According to the specific objectives, the point clouds were then filtered, clipped, and processed to establish 3D objects for further usage.

In this dissertation, the feasibility of the method has been analysed by investigating the applicability of the system, the accuracy, and the post-processing methods by means of case studies from the research areas of coastal geomorphology, agronomy, and geoarchaeology. In general, the measurement system has been proven to be robust and suitable for field surveys in all cases. The surveys themselves, including the selected georeferencing approach, were conducted quickly and reliably. With the refinement of the Multi Station Adjustment a relative accuracy of about 1 cm has been achieved. The absolute accuracy is about 1.5 m, limited by the RTK-DGPS system, which can be enhanced through advanced techniques. Specific post-processing steps have been conducted to solve the specific goals of each research area.

The method was applied for coastal geomorphological research in western Greece. This part of the study deals with 3D reconstructed volumes and corresponding masses of boulders, which have been dislocated by high energy events. The boulder masses and other parameters, such as the height and

distance to the current sea level, have been used in wave transport equations for the calculation of minimum wave heights and velocities of storm and tsunami scenarios and were compared to each other. A significant increase in accuracy of 30% on average compared with the conventional method of simply measuring the axes was detected.

For comparison, annual measurements at seven locations in western Greece were performed over three years (2009-2011) and changes in the sediment budget were successfully detected. The base points of the RTK-DGPS system were marked and used every year. Difficulties arose in areas with high surface roughness and slight changes in the annual position of the laser scanner led to an uneven point density and generated non-existing changes. For this reason, all results were additionally checked by pictures of the mounted camera and a direct point cloud comparison.

Similarly, agricultural plants were surveyed by a multi-temporal approach on a field over two years using the stated method. Plant heights and their variability within a field were successfully determined using Crop Surface Models, which represent the top canopy. The spatial variability of plant development was compared with topographic parameters as well as soil properties and significant correlations were found. Furthermore, the method was carried out with four different types of sugar-beet at a higher resolution, which was achieved by increasing the height of the measurement position. The differences between the crop varieties and their growth behaviour under drought stress were represented by the derived plant heights and a relation to biomass and the Leaf Area Index was successfully established.

With regard to geoarchaeological investigations in Jordan, Spain, and Egypt, the method was used in order to document respective sites and specific issues, such as proportions and volumes derived from the generated 3D models were solved. However, a full coverage of complexly structured sites, like caves or early settlements is partially prevented by the oversized scanner, slow measurement rates, and the necessary minimum measurement distance. The 3D data can be combined with other data for further research by the common georeference.

The selected method has been found suitable to create accurate 3D point clouds and corresponding 3D models that can be used in accordance with the respective research problem. The feasibility of the TLS method for various issues of the case studies was proven, but limitations of the used system have also been detected and are described in the respective chapters. Further methods or other, newer TLS systems may be better suited for specific cases.

Zusammenfassung

Terrestrisches Laser Scanning (TLS) ist eine neuere, aktive Methode der Fernerkundung zur automatischen Erfassung von 3D Koordinatenpunkten. Diese Methode hat sich in den letzten 20 Jahren zusätzlich zu flugzeuggestütztem und mobilem Laserscanning entwickelt. Alle Verfahren nutzen Laufzeiten von Laserlicht und zusätzliche Winkelmessungen zur Detektion von Distanzen und Richtungen. Es werden direkt mehrere tausend bis hunderttausende Polarkoordinaten pro Sekunde erfasst. Bei dem TLS Verfahren können die Koordinaten des Ursprungs des Laserstrahls bestimmt werden um verschiedene Scanpositionen in ein gemeinsames Koordinatensystem zu registrieren. Dazu werden Messungen von Globalen Navigations Satelliten Systemen oder tachymetrische Vermessungen durchgeführt, ebenso können aber auch gleiche Punkte oder Daten gestützte Verfahren genutzt werden. Üblicherweise werden je nach Verfahren Genauigkeiten und Punktdichten von wenigen Zentimetern bis zu einigen Millimetern erreicht. Daraus ergeben sich Punktwolken mit mehreren Millionen einzelner Punkte, die in der Nachverarbeitung über datengetriebene oder symbolische Verfahren ausgewertet werden können. Neben der Erstellung von Digitalen Oberflächen- und Geländemodellen, dient Laserscanning in vielen Bereichen zur Bestimmung von Oberflächen, Distanzen, Ausmaßen und Volumen. Darüber hinaus können durch multi-temporale Aufnahmen auch Veränderungen erfasst werden.

Der terrestrische Laserscanner, LMS Z-420i von Riegl wurde in dieser Arbeit in Kombination mit dem Differentiellen Globalen Positionierungs System Topcon Hiper Pro angewendet, welches das Verfahren Echtzeitkinematik (engl. Real Time Kinematic, RTK-DGPS) nutzt. Es wurde neben der direkten Positionsbestimmung des Laserscanners, zusätzlich die Position eines weiteren, selbst entwickelten Reflektors auf einem Fluchtstab mittels des RTK-DGPS Systems zur Orientierung der jeweiligen Punktwolke gemessen. Darüber hinaus ist der Scanner mit einer zusätzlich montierten Kamera Nikon D200, zur Erfassung von orientierten Fotos ausgestattet. Diese ermöglichen eine Einfärbung der Punktwolken in Echtfarben und erlauben damit eine bessere Orientierung. Weiterhin können die Fotos zur detaillierten Erstellung von 3D Informationen und zur Texturierung von 3D Objekten genutzt werden. In der Nachbearbeitung wurde die direkte Georeferenzierung durch die RTK-DGPS Daten mittels des Multi-Station-Adjustments, das den Iterative Closest Point-Algorithmus nutzt, verbessert. Entsprechend des jeweiligen Zieles, wurden die Punktwolken dann gefiltert und ausgeschnitten und in der Regel zur weiteren Verwendung in speziellen Programmen zu 3D Objekten verarbeitet.

In dieser Dissertation wurde die generelle Anwendbarkeit von TLS, dessen Genauigkeit, sowie entsprechende Auswerteverfahren anhand von Fallstudien aus den Bereichen der Küstengeomorphologie, der Agronomie und der Geoarchäologie untersucht. Generell hat sich das gewählte Messsystem in allen Fällen als robust und geeignet für Feldaufnahmen erwiesen. Die Aufnahme selbst, inklusive des gewählten Georeferenzierungsverfahrens, ist schnell und verlässlich durchführbar. Mit der entsprechenden Verbesserung der Registrierung ist eine relative Genauigkeit von ca. 1 cm erreicht worden. Die absolute Genauigkeit ist über das RTK-DGPS System auf ca. 1,5 m limitiert, welche sich über erweiterte Verfahren noch verbessern lässt.

Die Methode wurde für küstengeomorphologische Forschungen in Westgriechenland angewendet. Die Studie befasst sich einerseits mit rekonstruierten 3D Volumen- und entsprechenden Massenbestimmungen von dislozierten Blöcken, die durch starke Ereignisse verlagert wurden. Deren Massen und weitere Parameter, wie zum Beispiel die Höhe und Entfernung zum aktuellen Meeresstand, wurden in Wellentransportgleichungen zur Berechnung von Mindestwellenhöhen und -geschwindigkeiten für Sturm- und Tsunamiszenarien genutzt und miteinander verglichen. Es konnte eine deutliche Genauigkeitssteigerung von durchschnittlich 30% gegenüber dem herkömmlichen Verfahren der Achsenmessung festgestellt werden. Andererseits wurden zum Vergleich an sieben Standorten in Westgriechenland jährlich Messungen über drei Jahre durchgeführt und Veränderungen der Sedimentbilanz detektiert. Dabei wurden örtlich vermarkte Basispunkte für das RTK-DGPS System genutzt. Schwierigkeiten entstanden in Bereichen mit starker Zerklüftung und durch jährliche, leichte Veränderungen der Position des Laserscanners, die zu einer ungleichen Punktwolkendichte führten und nicht vorhandene Veränderungen erzeugten. Aus diesem Grund wurden alle Resultate mittels Fotos der montierten Kamera und einem direkten Punktwolkenvergleich überprüft.

In gleicher Weise wurden Agrarpflanzen auf einem Feld multitemporal über zwei Jahre mit der genannten Methodik erfasst und Pflanzenhöhen und deren Variabilität innerhalb eines Feldes mit Hilfe von Crop Surface Models erfolgreich bestimmt, welche die Pflanzenoberflächen repräsentieren. Deren Variabilität wurde mit topographischen Parametern sowie Bodenwerten verglichen und es konnten signifikante Zusammenhänge gefunden werden. Weiterhin wurde die Methode mit vier verschiedenen Zuckerrübensorten in einer höheren Auflösung, die durch eine erhöhte Messposition erreicht wurde, durchgeführt. Die Unterschiede zwischen den einzelnen Sorten und ihr Verhalten bei Trockenstreß können durch die Erfassung der Pflanzenhöhe dargestellt werden. Ein Zusammenhang zwischen den Pflanzenhöhen, Biomasse und dem Blattflächenindex wurde erfolgreich hergestellt.

Im Rahmen von geoarchäologischen Untersuchungen in Jordanien, Spanien und Ägypten wurde die Methode weiterhin genutzt um die jeweiligen Standorte zu dokumentieren und spezifische Fragestellungen durch beispielsweise Größenverhältnisse und Volumina aus den erstellten 3D-Modellen zu beantworten. Als Nachteil der Methode erwies sich, dass der Scanner teilweise zu groß, zu langsam und der nötige Mindestmessabstand zu groß ist um in der anvisierten Zeit stark strukturierte Standorte, wie z.B. Höhlen oder frühe Siedlungen vollständig zu erfassen. Die 3D Daten können durch die Georeferenzierung mit anderen Daten für weitere Untersuchungen und Berechnungen kombiniert werden.

Das gewählte Verfahren hat sich als geeignet erwiesen um genaue 3D Koordinaten Punktwolken und entsprechenden 3D Modelle zu erstellen. Diese konnten für die jeweilige Fragestellung entsprechend genutzt werden. Die Arbeit stellt damit die Anwendbarkeit der Methode für verschiedenste Fragestellungen in den einzelnen Themenbereichen heraus, zeigt aber auch die Grenzen des hier genutzten Systems auf. Andere Verfahren oder andere, neuere TLS Systeme sind für spezifische Fragestellungen eventuell besser geeignet.

Acknowledgements

The dissertation was conducted at the Institute of Geography, University of Cologne. I like to thank all the people, who helped me throughout all the years in any way to successfully complete this work. In particular, I give many thanks to:

- Prof. Dr. Georg Bareth, who gave me the opportunity to work in the very different, interesting projects and for his support throughout the years.
- Prof. Dr. Helmut Brückner for the co-examination of my thesis.
- Prof. Dr. Bülent Tezkan and Dr. Andreas Bolten as members of the disputation committee.
- Prof. Dr. Andreas Vött, Konstantin Ntageretzis and the whole “remote” working group at the University of Mainz for patience and support.
- All my colleagues of the working group for GIS & Remote Sensing.
- The colleagues, who were proofreading the manuscript and gave very valuable comments, namely Constanze Curdt, Dr. Karin Kindermann, Dr. Andreas Bolten, Dr. Max Engel, Christoph Hütt and PD Dr. Martin Kehl.
- Jun.-Prof. Dr. Bernhard Höfle, University of Heidelberg, and Dr. Andreas Pastoors, Neanderthal Museum, Mettmann, who helped me with specific measurements and analyses.
- The excellent work of Mrs. Kirstin Jacobson.
- The German Research Foundation (DFG) and the Federal Ministry of Education and Research (BMBF) for funding all the involved research projects.
- The Chinese colleagues, who introduced me into a very different region, culture, and cuisine.
- Everyone at the different hard- and software corporations for fast responding to awkward questions and giving me support in every situation.
- All people who helped me during the field surveys in Egypt, Germany, Greece, Jordan, and Spain.
- My friends, who successfully supported me and were able to distract me.
- My parents and my whole family for continuous support.
- Last but not least, my girlfriend for her excellent and caring support, for giving me motivation, and for a lot of patience.

Danke, Ευχαριστώ, Gracias, Thank you, 谢谢, شكرا

Table of Contents

Abstract	I
Zusammenfassung	III
Acknowledgements	V
Table of Contents	VI
List of Figures	IX
List of Tables	XII
List of Abbreviations	XIII
1 Introduction and background	1
1.1 Introduction.....	1
1.2 Study aims	2
1.3 Study outline	2
2 Methods of 3D-data acquisition	4
2.1 Supporting and challenging methods for 3D acquisition	5
2.1.1 Geodesy and surveying	5
2.1.2 Satellite geodesy	6
2.1.3 Photogrammetry.....	10
2.1.4 Radar	11
2.2 Laser scanning: basic principles.....	14
2.2.1 Laser light	16
2.2.2 Measurement methods	17
2.2.3 Beam deflection	22
2.2.4 Propagation of laser light in the atmosphere	24
2.2.5 Beam reflection and detection	27
2.2.6 Systematic errors	31
2.3 Laser scanning campaigns	32
2.4 Post-processing of laser scanning data	34
2.4.1 Data preparation and visualization	34

2.4.2	Registration.....	36
2.4.3	Processing of point clouds	38
2.5	Applications of laser scanning	39
3	The general method	42
3.1	The laser scanner: Riegl LMS-Z420i.....	42
3.2	The RTK-DGPS system: Topcon HiPer Pro	45
3.3	Direct georeferencing.....	47
3.4	Fieldwork	48
3.5	Post-processing	50
3.5.1	Preparation	51
3.5.2	General registration	51
3.5.3	Adjustment.....	52
3.5.4	Feature extraction.....	54
4	Case study 1: Coastal geomorphology.....	58
4.1	Introduction.....	58
4.2	Research sites	61
4.3	Specific method	64
4.3.1	Estimation of boulder masses	64
4.3.2	Wave transport equations	65
4.3.3	Annual monitoring of coastal sites.....	68
4.4	General results	68
4.4.1	3D model-based measurements of dislocated boulders	68
4.4.2	Annual changes of coastal sites in western Greece	78
4.4.3	Comparison with buoy data	81
4.5	Discussion	83
5	Case study 2: Agronomy	87
5.1	Introduction.....	87
5.2	Main procedure	88
5.3	In-field variability of crop height in two consecutive years	89
5.3.1	Specific methods and data	90
5.3.2	Results.....	93
5.4	Detection of crop varieties	100
5.4.1	Specific methods and data	100
5.4.2	Results.....	101

5.5	Discussion	105
6	Case study 3: Geoarchaeology	109
6.1	Introduction.....	109
6.2	Neolithic sites in Jordan	111
6.2.1	Geoarchaeological background.....	111
6.2.2	Survey description and results	112
6.3	The Ardales cave (Cueva de Ardales) in Spain.....	114
6.3.1	Geoarchaeological background.....	114
6.3.2	Survey description.....	115
6.3.3	Results	117
6.4	The Sodmein Cave, Egypt	120
6.4.1	Geoarchaeological background.....	120
6.4.2	Survey description.....	120
6.4.3	Results.....	121
6.5	Discussion	124
7	Discussion and perspectives	127
7.1	General issues.....	127
7.2	Accuracy of the chosen method.....	128
7.3	Case studies	129
7.4	Perspectives.....	132
	References	134
	Appendix.....	153
	Erklärung.....	156

List of Figures

Figure 2-1: Remote sensing methods	4
Figure 2-2: Preselected single measurements	5
Figure 2-3: Accuracies of different global positioning methods	10
Figure 2-4: Principle of side-looking radar	12
Figure 2-5: Raster measurement approach of a terrestrial laser scanner	15
Figure 2-6: Simplified diagram of laser amplification.	16
Figure 2-7: Common measurement principles of laser scanning.....	17
Figure 2-8: Principle and layout of a triangulation based measurement.....	18
Figure 2-9: Principle of phase-shift detection by continuous wave measurements.....	20
Figure 2-10: Principle of time-of-flight measurements.....	21
Figure 2-11: Common reflection principles of laser scanners.....	23
Figure 2-12: Intensity profile of a laser beam	25
Figure 2-13: Dimensions of a Gaussian beam	26
Figure 2-14: Resolution of the laser scanning method	27
Figure 2-15: Reflection effects on different surfaces.....	27
Figure 2-16: Comparison of full-waveform recording and discrete echo determination	29
Figure 2-17: Gray-scale 2D intensity image	30
Figure 2-18: Geometric model of a laser scanning device	31
Figure 2-19: Issues for laser scanning campaigns.	32
Figure 2-20: Examples of MLS (1) and ALS (2) systems.	33
Figure 2-21: 2D images with different colourizations.....	35
Figure 2-22: Possible direct georeferencing approach	36
Figure 2-23: Principle of indirect registration	37
Figure 2-24: Schematic description of different elevation models.....	39
Figure 3-1: Typical TLS set-up with various additional equipment.	42
Figure 3-2: Estimated spacing between footprints.....	44
Figure 3-3: Selfmade cylindrical reflector	47
Figure 3-4: Different transport principles of the laser scanning device.....	49
Figure 3-5: Software window for the scan configuration (A) and intensity image (B).....	50
Figure 3-6: The extent of a scan project and the Areas of Interest (AOI)	54
Figure 4-1: Wave propagation, coastal zones and parameters	59
Figure 4-2: Forces acting on a boulder.....	60
Figure 4-3: Map of research sites in Greece.	62

Figure 4-4: Boulder GER-ST 5 at Cape Gerogombos, Cefalonia Island, lying upside down	63
Figure 4-5: The base station of the RTK-DGPS system.....	64
Figure 4-6: Perspective view of the imbrication train.....	68
Figure 4-7: Maps of Cape Skalas (Peloponnese) and Cape Gerogombos (Cefalonia Island) based on topographical information and elevation contours created by TLS surveys.	72
Figure 4-8: Graphs for tsunami and storm cases for all sites in western Greece.....	73
Figure 4-9: Dislocated boulders encountered at the study site at Aghia Pelaghia (Cefalonia Island).	77
Figure 4-10: Annual sediment budget for the years 2009/2010 and 2010/2011 at Kaminia Beach, Lefkada Island	79
Figure 4-11: Annual sediment budget for the years 2009/2010 and 2010/2011 near Cape Katakolo, western Peloponnese.	80
Figure 4-12: Annual sedimentary budget for the years 2009/2010 and 2010/2011 at Aghia Pelagia, Cefalonia Island	81
Figure 4-13: Maximum wave heights registered by a buoy offshore Pylos	82
Figure 4-14: Maximum wave heights registered by a buoy offshore Zakynthos.....	82
Figure 4-15: Irregularly shaped boulders from Cape Skalas, Peloponnese.....	84
Figure 4-16: Relations between calculated results of wave transport equations.....	84
Figure 5-1: Derivation of Crop Height (CH) and Crop Growth (CG).....	89
Figure 5-2: Orthophotos of the observed field	90
Figure 5-3: Overview of the different, incorporated parameters for correlation analysis	92
Figure 5-4: Perspective view of a 3D point cloud.....	93
Figure 5-5: Maps of Crop Height (CH), Crop Growth (CG) and the DTM for the year 2008.....	94
Figure 5-6: Panoramic picture from one scan position from 24 July 2008.	94
Figure 5-7: Regression of the measured and derived plant heights of 2008.	95
Figure 5-8: Comparison of the manual measured crop heights and dry leaf biomass	96
Figure 5-9: Maps of Crop Height (CH), Crop Growth (CG) and the DTM for the year 2009.....	97
Figure 5-10: The platform with the mounted scanner located ~4 m above ground.....	100
Figure 5-11: Comparison of derived and manually measured crop heights	101
Figure 5-12: Crop Height (CH) for the three surveying dates.....	102
Figure 5-13: Panoramic image from the scan position ZR4	103
Figure 5-14: Comparison of derived plant height and dry leaf biomass	103
Figure 5-15: Comparison of dry leaf biomass and LAI to derived plant height.....	104
Figure 5-16: Point density per square metre for selected dates of 2008 and 2009	105
Figure 5-17: Intensity correction of the data	106
Figure 5-18: The manual measurement problem	107
Figure 5-19: Map from 1953	107
Figure 6-1: Research areas of the CRC 806	109
Figure 6-2: Overview map of the Zarqa River valley in NE-Amman	112
Figure 6-3: Perspective views of the Zarqa river valley and the archaeological site of 'Ain Ghaizal.	113

Figure 6-4: Overview map of the archaeological site of ‘Ain Jamman, Jordan.	114
Figure 6-5: Scan position in the cave of Ardales.	116
Figure 6-6: Map of the Ardales cave.	117
Figure 6-7: Perspective views of the 3D model of the Ardales cave.	118
Figure 6-8: 3D model and panoramic picture of the mounted camera from the inside debris cone	119
Figure 6-9: Part of the 3D cave model	119
Figure 6-10: Overview map of the Sodmein cave location	121
Figure 6-11: Perspective view of the 3D model of the Sodmein Cave.	122
Figure 6-12: Overview map of the Sodmein cave	123
Figure 6-13: 3D model of the Sima de las Palomas de Teba.	125
Figure A-1: Annual sediment budget for the years 2009/2010 and 2010/2011 at Cape Gerogombos A, Cefalonia Island	153
Figure A-2: Annual sediment budget for the years 2009/2010 and 2010/2011 at Cape Gerogombos B, Cefalonia Island	154
Figure A-3: Annual sediment budget for the years 2009/2010 and 2010/2011 at Cape Schinou, Cefalonia Island	154
Figure A-4: Annual sediment budget for the years 2009/2010 and 2010/2011 at Gialous Skala, Lefkada Island	155

List of Tables

Table 2-1: Main error sources and according range errors for GNSS signals (SEEBER, 2003).....	9
Table 2-2: Classes of lasers and their potential hazard.....	17
Table 2-3: Overview of several triangulation (Tri.) and structured light (SL) based scanners	19
Table 2-4: Examples for terrestrial continuous wave scanner systems	21
Table 2-5: Examples for terrestrial time-of-flight scanner systems	22
Table 2-6: Typical reflectivity of different material for 900 nm wavelength (WEHR & LOHR, 1999).	28
Table 3-1: Properties of the laser scanner	43
Table 3-2: Properties of the Nikon D200.....	43
Table 3-3: Technical specification: Topcon HiPer Pro.	45
Table 3-4: Absolute error of GNSS measurements regarding the carrier phase.....	46
Table 3-5: Error of GNSS measurements with the own RTK correction.....	46
Table 3-6: Error of GNSS measurements with external RTK correction.....	46
Table 3-7: Error of the different registration modes compared to the local network.....	52
Table 3-8: Accuracy of the overall registration prior to the adjustment	53
Table 3-9: Typical steps and parameters used for MSA.....	53
Table 3-10: Registration results after the MSA.....	54
Table 4-1: Overview of volume, density and mass data of dislocated boulders by conventional and 3D model based approaches.....	70
Table 4-2: Results of different wave transport equations of tsunami and storm scenarios for the area of Cape Skalas, Peloponnese	75
Table 4-3: Results of different wave transport equations of tsunami and storm scenarios for the area of Katakolo, Peloponnese.	76
Table 4-4: Results of different wave transport equation of tsunami and storm scenarios for the area of Ag. Pelagia, Cefalonia Island.....	77
Table 4-5: Results of different wave transport equation of tsunami and storm scenarios for the area of Cape Gerogombos and Schinou, Peloponnese.....	78
Table 5-1: Parameters incorporated for analysis of the detected variability of crop height.....	91
Table 5-2: Results of the comparison between the derived DTM and the DGM1L of the surveying agency.	95
Table 5-3: Comparison of mean calculated and manually measured crop heights	95
Table 5-4: Derived correlation coefficients (r) and adjusted R ² values.....	99
Table 5-5: Height values derived by CSMs and manual measurements.	101
Table 5-6: Correlation coefficients (r) of mean plot heights to fresh leaf biomass, dry leaf biomass, and LAI.....	104
Table 7-1: Major advantages and disadvantages of the proposed method.	131

List of Abbreviations

ALS	Airborne Laser Scanning	IMU	Inertial Measurement Unit
AMH	Anatomically Modern Humans	INS	Inertial Navigation System
AOI	Area of Interest	InSar	Interferometric Radar
APD	Avalanche Photodiode Detector	JBBS	Joint-Bounded Boulder Scenario
a.p.s.l.	above present sea level	LAAS	Local Area Augmentation System
AS	Anti-Spoofing	LAI	Leaf Area Index
C/A	Coarse Access	LASER	Light Amplification by Stimulated Emission of Radiation
CAD	Computer Aided Design	LIDAR	Light Detection and Ranging
CEP	Circular Error Probable	MEMS	Micro-Electro-Mechanical Systems
CG	Crop Growth	MLS	Mobile Laser Scanning
CH	Crop Height	MPIa	Multiple Pulse in Air
CHM	Canopy Height Model	MSA	Multi Station Adjustment
CMCS	Camera Coordinate System	NAVSTAR-GPS	Navigation Satellite Timing and Ranging-Global Positioning System
CRC806	Collaborative Research Centre 806	nDSM	Normalized DSM
CRC/TR32	Transregional Collaborative Research Centre 32	NURBS	Non-Uniform Rational B-Splines
CSM	Crop Surface Models	PA	Precision Agriculture
CW	Continuous Wave	PCRS	Project Coordinate System
DGPS	Differential Global Positioning System	PDGPS	Precise DGPS
DOP	Dilution of Precision	PN	Pseudo-Noise
DSM	Digital Surface Model	PPNB	Pre-Pottery Neolithic B
DTM	Digital Terrain Model	PPP	Precise Point Positioning
d.t.s.	distance to sea	RADAR	Radio Detection and Ranging
EC	Electromagnetic Conductivity	RANSAC	Random Sample Consensus
EDM	Electronic Distance Measurements	RCC	Rapid Climate Change
EMI	Electromagnetic Induction	RIM	Range Imaging Camera
ESRI	Environmental Systems Research Institute, Inc.	RTCM	Radio Technical Commission for Maritime
FM	Frequency Modulation	RTK	Real Time Kinematic
GBS	Ground-Based System	SA	Selective Availability
GDOP	Geometrical Dilution of Precision	SBAS	Satellite-Based System
GIS	Geographical Information System	SNR	Signal-to-Noise-Ratio
GLCS	Global Coordinate System	SOCS	Scanner Own Coordinate System
GLONASS	Global'naya Nawigazionnaya Sputnikowaya Sistema (russian)	SOP	Sensor Orientation and Position
GNSS	Global Navigation Satellite Systems	SRTM	Shuttle Radar Topography Mission
GPS	Global Positioning System	SVA	Soil-Vegetation-Atmosphere
HDOP	Horizontal Dilution of Precision	TDOP	Time Dilution of Precision
HRDEM	High-Resolution Digital Elevation Model	TIN	Triangulated Irregular Network
ICP	Iterative Closest Point	TLS	Terrestrial Laser Scanning
IDW	Inverse Distance Weighting	TOF	Time-of-Flight
		UAV	Unmanned Aerial Vehicle
		UERE	User Equivalent Range Error
		VR	Virtual Reality
		WAAS	Wide Area Augmentation System
		YRL	Yarmoukian Rubble Layer

1 Introduction and background

1.1 Introduction

The theoretical idea of *Einstein* and the experimental development of a laser in 1960 (MAIMAN, 1960) was a major discovery of the 20th century (TOWNES, 2003). Nowadays, laser pointers, laser printers, CD and BlueRay players, as well as bar code readers in supermarkets and shops are important in everyday live (CAMPBELL & WYNNE, 2011). All applications use the advantages of the highly intense, monochromatic, directional, coherent, amplified light, called laser.

Laser scanning and profiling incorporates laser technology to determine distances to remote objects (BERALDIN et al., 2010). In addition, automatic deflection and the according angle measurements allow a direct, active, contactless, and accurate measurement of dense 3D point clouds to derive information. Within the last 20 years airborne laser scanning (ALS) has become a standard surveying method and a wide range of instruments, algorithms and associated software has emerged for a huge amount of applications (PETRIE & TOTH, 2009a). Digital elevation models are mainly generated nowadays from ALS measurements, particularly by the surveying agencies (PETZOLD et al., 1999), but the method is also important for the environmental sciences (HERITAGE & LARGE, 2009). The precise and active measurements in combination with the rapid coverage are for example often used to estimate forest inventories and to derive 3D city models for planning and visualization purposes. Terrestrial laser scanning (TLS) and mobile laser scanning (MLS) or also called mobile mapping are important further methods, whereas the ground-based acquisition of 3D point clouds delivers data from this specific perspective. MLS enables a fast coverage of larger areas from any mobile vehicle, such as cars, quads and boats. In cities, it allows filling the gap of facade detection, which are not reachable by ALS and assists the documentation of road inventories and clearance measurements (KUTTERER, 2010). TLS is a reliable method particularly in the area of geomorphology, for the documentation of cultural heritage, industrial sites, and in forensics (VOSSELMAN & MAAS, 2010).

However, laser scanning is just one remote sensing method and the results of other methods are comprehensive (CAMPBELL & WYNNE, 2011). A complementary usage of several remote sensing methods is recommended (BALSAVIAS, 1999b). For instance, photogrammetric, dense image-matching allows establishing accurate point clouds (WESTOBY et al., 2012) and radar interferometry procedures are able to deliver high-resolution digital elevation models (KRIEGER et al., 2007). Single 3D points can be accurately measured with current GNSS or surveying solutions (KAHMEN, 2006). Additionally, several algorithms in laser scanning have been altered from radar equations and position estimations of laser scanning devices are conducted by GNSS or total station measurements. In contrast to these other methods, laser scanning surveys achieving the point clouds are easily conductible, but dealing with the large point clouds in post-processing stages requires a bigger effort. Thus, a huge amount of research is conducted on calibration and algorithms to automatically derive 2D and 3D objects (VOSSELMAN & KLEIN, 2010).

1.2 Study aims

This contribution will give an overview and detailed examples about possible applications of terrestrial laser scanning and analyse its feasibility for specific research areas, which are coastal geomorphology, agronomy, and geoarchaeology. For this purpose, the Riegl LMS-Z420i laser scanner was used, mostly in combination with a Topcon HiPer Pro, a Global Differential Positioning System, involving Real Time Kinematic (RTK-DGPS), for direct measurements of the laser scanner position. In addition, one self-developed reflector on a ranging pole was measured by the RTK-DGPS system for the accurate estimation of the scan position orientation. This georeferencing approach is enhanced by the Multi Station Adjustment (MSA), which applies the Iterative Closest Point (ICP) algorithm. The laser scanner was additionally equipped with a digital camera Nikon D200 that delivered digital pictures, which can be used to obtain further details, as the internal and external orientation is known. Furthermore, it is possible to use the information of the pictures to colour the resulting point clouds, as well as to map the pictures on established 3D objects.

Besides the determination of the overall error of the selected approach, this particular method is used

- (i) to accurately reconstruct 3D models of dislocated boulders for an enhanced volume and mass determination and the incorporation of these masses and further parameters in wave transport equations,
- (ii) to monitor in contrast annual changes of the sediment budget at several coastal sites,
- (iii) to determine the plant heights of agricultural crops and detect their height variability within one field,
- (iv) to observe different cultivars of sugar-beet and the plants' development during a growing period,
- (v) to document geoarchaeological sites by reconstructing 3D models that can be used for further measurements, visualisations, and enhanced analyses.

In conclusion, this thesis contributes to the specific research areas by presenting the potential and feasibility of this new survey method for geoscientific research. Overall, accurate results have been achieved in all of the observed research areas, but all applications reveal some challenges.

1.3 Study outline

For a proper description of laser scanning as an active remote sensing method, a general overview of other remote sensing methods capable of deriving 3D information is presented in chapter 2. Mainly, a detailed description of the development and the recent laser scanning methods, remarks on laser scanning surveys, as well as on common applications of laser scanning is given.

The specific method applied in this contribution is shown in chapter 3. The laser scanning device, the Riegl LMS Z-420i is described in detail. It was used in combination with the Topcon HiPer Pro RTK-DGPS for registration purposes. A special method, using self-made larger reflectors on ranging poles was evolved, which is introduced and described in this chapter. The set-up and the general work flow is also presented in detail, followed by the most common post-processing stages.

Examples of different applications of TLS are shown in chapter 4-6. The focus of the first case study (chapter 4) is the support for coastal geomorphological research within the framework of an interdisciplinary project on palaeo-tsunami impacts along the coasts of the eastern Ionian Sea in western Greece. For this purpose, boulders that had been dislocated by high-energy events, were measured and reconstructed. The accurate 3D volume in combination with density probes was integrated into wave transport equations, which allow an estimation of minimum wave heights and velocities necessary to move these boulders. To distinguish between annual changes and high-energy events, an annual monitoring approach of seven selected sites in Greece was additionally applied for three years.

In chapter 5, the selected approach is used in the area of agronomy. Multi-temporal surveys were conducted to estimate plant height distribution of a single field in the years of 2008 and 2009 within the Transregional Collaborative Research Centre 32 "Patterns in Soil-Vegetation-Atmosphere" (CRC/TR32, 2013). The approach was further applied to another experiment of the CROP.SENSE.net project (CROP.SENSE.net, 2013), which is an interdisciplinary research network examining sensor technology for crop breeding and management. Differences between sugar-beet cultivars in 2010 were detected. In this approach, a platform with a lifted position was used. For both cases, Crop Surface Models (CSM) were established that allow visualising and calculating plant growth behaviour.

In the third case study (chapter 6), TLS has been applied to geoarchaeological research sites within the framework of the Collaborative Research Centre 806 (CRC806) "Our Way to Europe – Culture-Environment Interaction and Human Mobility in the Late Quaternary" (CRC806, 2013) in Jordan, Egypt and Spain. Beside the rougher circumstances during the surveys, the generation of 3D models, profiles and plans was successful and shows a major enhancement for the research in this area, as well as a reliable documentation of the sites.

The exemplary applications of chapters 4 to 6 are summarized in a general discussion (chapter 7) of the applied method. Finally, future perspectives of the technology and an outlook are presented.

2 Methods of 3D-data acquisition

LIDAR (light detection and ranging) is the broad term of every method that involves the measurement of distances by laser light (LILLESAND et al., 2008). It is an active remote sensing technique, which is familiar to RADAR (radio wave detection and ranging) remote sensing, concerning an active transmission and reception of the backscattered signal. Both can be interpreted for range detection and for the characteristics of the backscattered signal (CAMPBELL & WYNNE, 2011). Familiar and alternative methods to achieve dense 3D descriptions of surfaces are the processing of passively measured stereo imagery and radar remote sensing (JENSEN, 2007). Methods for the detection of single 3D points are Global Navigation Satellite Systems (GNSS) or tachymetric measurements (KAHMEN, 2006). These methods, their possible accuracy, and the detectable object sizes are depicted in Figure 2-1, sorted in terms of accuracy and possible object size.

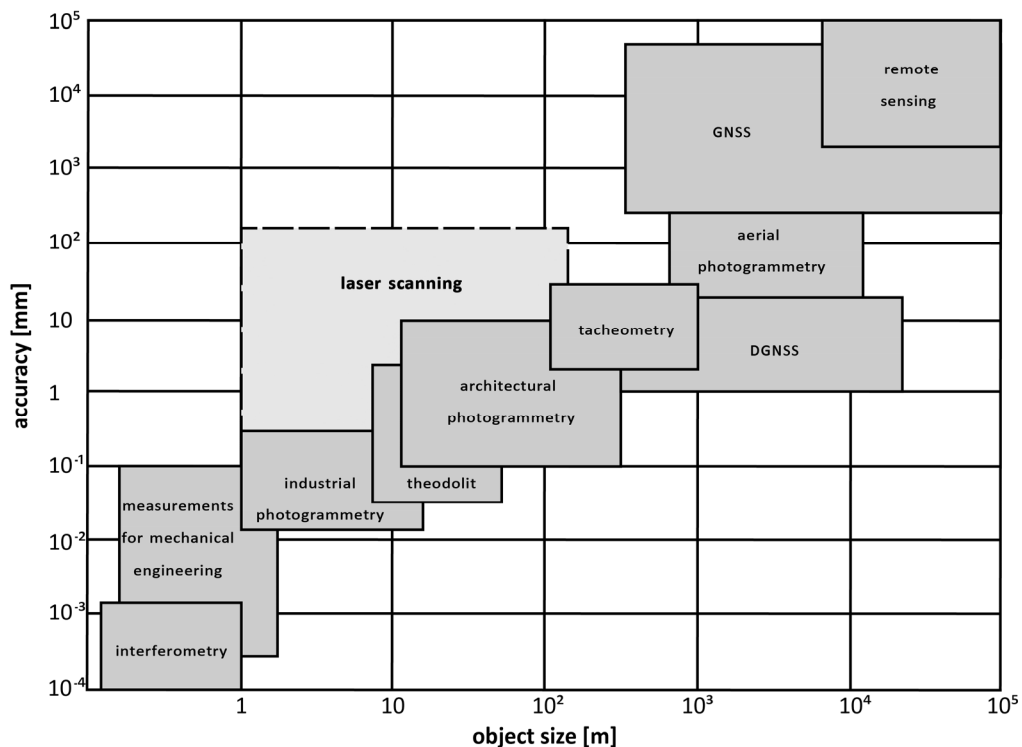


Figure 2-1: Remote sensing methods and their principal accuracy and detectable object sizes, modified after LUHMANN (2003).

The first section of this chapter describes the other methods for 3D measurements in comparison to laser scanning. Thus, in section 2.1, surveying by theodolites and tachymeters, GNSS measurements, as well as photogrammetry, and radar remote sensing are presented. This is followed by a description of the development of laser scanning, basic principles and components (2.2). Major tasks of laser scanning surveying (2.3), common post-processing steps (2.4), and different types of applications are presented (2.5).

2.1 Supporting and challenging methods for 3D acquisition

2.1.1 Geodesy and surveying

The main duty of geodesy and surveying is the accurate measurement of the Earth's surface and objects by using specific instruments and methods, which allow reliable results (ANDERSON & MIKHAIL, 1998; KAHMEN, 2006). The reliability of every measurement is resolved by statistical analyses of the measurements and the instruments in terms of precision and accuracy, mainly based on the adjustment theory (NIEMEIER, 2002). Geodesy can be further subdivided in global, regional and local surveying, each with specific methods and results, as well as the determination of transformations between these scales (TORGE, 2002). For instance, globally derived geodetic reference systems are used in regional surveying and local surveys are connected to these reference systems. Global and regional measurements that allow establishing models of the earth and precise reference systems, considering the Earth's gravity field are known as geodesy (ger.: "höhere Geodäsie"). It particularly enables the establishment of accurate height reference systems (geoid), which are also important for the estimation of satellite orbits. Regional and local measurements are termed surveying (ger.: "niedere Geodäsie"). These measurements refer mostly to plane reference areas when conducted for small topographic units, cadastre measurements and the inventory of buildings or other facilities (TORGE, 2002).

Surveying generally relies on the accurate measurements of angles and distances for the determination of spatial positions. Simple distance measurements can be conducted by tapes or chains and more recently by Electronic Distance Measurements (EDM) (KAHMEN, 2006). In addition, measurements can be conducted in a vertical direction, known as levelling. Angles in horizontal and vertical directions are measured to a high degree of precision by theodolites, which were used since the 19th century. In such a case, baselines of known distance were used to achieve the determination of the desired point by triangulation. With the new EDM method, a combination of distances (slant range) and angle measurements is the basis for analog tachymeters and electronic tachymeters (total stations). An overestimation of points with the latter instruments by automatically combined measurements of angles and distances is possible and a statistical solution is derived by trilateration (KAHMEN, 2006).

Total stations allow fast and precise surveying of 3D points in the order of millimetres (ANDERSON & MIKHAIL, 1998). Starting with a known (existing surveying mark) or a new base point, 3D coordinates can be derived by using the instrument and a prism for each new point. A georeference is enabled by the incorporation of known surveying points, which might need for the connection a huge amount of additional measurements. Furthermore, the measurements rely on the line of sight. Typical approaches for the measurement of base points and the establishment of new points are for instance arc-, inter-, and resection, as well as polar point determination and traversing (KAHMEN, 2006).

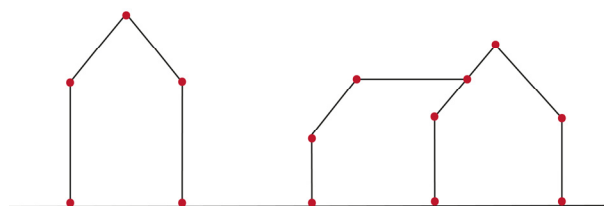


Figure 2-2: Preselected single measurements (red dots) of an object by total station surveying.

Nowadays, total stations that measure electronically are widely used (WITTE & SCHMIDT, 2000). These instruments are capable to determine points without prisms (“reflectorless”). Thus, a contactless, fast, and very accurate survey of objects by single 3D point measurements is possible. Most of the devices show an accuracy of millimetres for a range of up to 5 km. However, only single preselected points can be measured, as shown in Figure 2-2. This method is often used in combination with terrestrial laser scanning for the registration of different scan positions and calibration purposes of these instruments (RÜTHER et al., 2012).

Another method of geodesy is inertial navigation, which indicates position and velocity of a moving object in real time (JEKELI, 2001; KAHMEN, 2006). This method is important for ALS and MLS approaches for a high precise determination of the position and orientation. *Newton’s* law of motion is applied, which gives the relation between the acceleration, force and mass. This allows the measurement of acceleration by force changes. Additional time integration gives speed and position changes. Inertial Navigation Systems (INS) consists of Inertial Measurement Units (IMUs) that measure the translational and rotational motion. The latter movement is commonly known as roll, pitch and yaw. Two types of IMUs exist, which are motion sensors (accelerometers) and rotation sensors (gyroscopes) (JEKELI, 2001). Depending on the application, usually three IMUs of each type are implemented perpendicularly in an INS for the accurate estimation of the orientation and velocity of the instrument’s coordinate system. Gyroscopes with various accuracies are based on mechanical or optical principles. Newer Micro-Electro-Mechanical Systems (MEMS) allow a wide-spread integration of inertial measurements in manifold devices, such as automobiles or smartphones. Accelerometers mostly rely on a proof mass on a spring, which moves by a certain, measurable amount when a force is applied. The data of these singular devices is recorded and computed in the INS with frequencies up to 100 Mhz. However, the gyroscopes are affected by a drift error that accumulates with time. Further error sources are gravitational and rotational influences of the Earth. Thus, an INS is mostly connected to GNSS signals (see chapter 2.1.2) and allows a very accurate position determination, where the INS data is used for interpolation between single GNSS measurements. This integration is mostly computed by *Kalman* filtering, which statistically computes the optimal trajectory (JEKELI, 2001; LICHTI & SKALLOUD, 2010).

2.1.2 Satellite geodesy

Satellite geodesy as a part of geodesy, regards measurements “to, from, or between artificial, mostly near-Earth, satellites” (TORGE, 2002: 1). In addition to the determination of the Earth’s gravity field and geodynamical phenomena like crustal deformation and crustal plate movements (BOGUSZ et al., 2012), satellite geodesy uses Global Navigation Satellite Systems (GNSS) for precise determinations of 3D positions and navigation purposes through received satellite signals. This method can be combined with laser scanning for the position determination of laser scanning devices, as well as for INS trajectory estimation (LICHTI & SKALLOUD, 2010). The available GNSS can be distinguished by the respective space, control and user segments (HOFMANN-WELLENHOF et al., 2008). Detailed information about the available systems and the method itself are presented in SEEBER (2003), HOFMANN-WELLENHOF et al. (2008), MANSFELD (2010) and BAUER (2003). The derived accuracies of the measurements can be enhanced by corrections of the retrieved signals and differential methods.

Satellites of GNSS are broadcasting a direct signal that contains orbital data (ephemerides) and a precise time, which is given by an atomic clock on each satellite (HOFMANN-WELLENHOF et al., 2008). The orbital data gives the position of the satellite. Both values are transmitted in a data message that is superimposed as a code on the carrier phase. The receiver compares the broadcasted time encoded in the transmission with the time of reception. The transmission speed is the group velocity, which enables to obtain the range to the specific satellite by the difference of the received time signals of the satellite and the receiver. With a constellation of three satellites, their ranges, and the broadcasted orbital information, a 3D position can be measured, when the clock of the receiver is set congruent to the system time. However, the receivers contain only an inexpensive crystal clock, which has an offset with regard to the system time of the GNSS. Thus, every range, which is derived, is a pseudo-range and a fourth signal is necessary, which resolves the time offset or clock bias independently. This method allows a continual fix to be generated in real time using an adapted version of trilateration (MANSFELD, 2010).

A description of the two available GNSS, namely NAVSTAR-GPS and GLONASS, is depicted below. The regionally available Chinese system BeiDou will be developed into a full GNSS called Compass (MONTENBRUCK et al., 2012). Further regionally available systems are for example the Indian Regional Navigation Satellite System and the Japanese Quasi-Zenit-Satellite System. Galileo, the European GNSS system is in the In-Orbit Validation (IOV) phase and will be a further worldwide GNSS, fully operational around 2020 (HOFMANN-WELLENHOF et al., 2008; SCHÜLER et al., 2009). The system will be compatible to NAVSTAR-GPS by broadcasting data on five frequencies a more accurate signal, as well as redundancies for Safety of Life (SoL) services for rescue purposes can be ensured. The latter issue is also addressed by updates of all other GNSS.

The most important and widely used system is the Navigation Satellite Timing and Ranging – Global Positioning System (short: NAVSTAR-GPS or only GPS) (MANSFELD, 2010). The system has been developed, operated and maintained by the US military since 1973. The control segment consists of six base stations around the world with the main station being located at Colorado Springs, CO (USA). This distribution defines the reference system, which is the World Geodetic System 1984 (WGS 1984).

Nowadays, the space segment consists of 24 operational and several spare satellites in circular orbits about 20,200 km above the Earth (HOFMANN-WELLENHOF et al., 2008). Like every system, it is continuously updated and enhanced. Signals are broadcasted on several frequencies (L_1 to L_5) and some s-band frequencies. The most important ones are L_1 and L_2 , whereby L_1 carries the C/A Code and P code. The C/A-code (coarse access) is a coarse, open code, whereas the P-code is more precise, but is encrypted by a secret W-code to the Y-code. This method avoids the transmission of a faked signal of an enemy and is called “anti-spoofing” (AS). The precise service is restricted to US armed forces, federal agencies and some allies. Both services have nearly the same accuracy (SEEBER, 2003), but the accuracy of the precise services for military is enhanced by the dual frequency availability of the Y-code on the L_2 signal, which reduces errors of the ionospheric refraction. In addition, the signal is more robust, faster and has a higher availability (HOFMANN-WELLENHOF et al., 2008).

A very important characteristic of this system was the fact that a method called Selective Availability (SA) had been incorporated into the system. SA was used to reduce the accuracy of the C/A signal, by dithering the frequencies of the satellite clocks and manipulating the transferred ephemerides. The SA

was activated in 1990 and deactivated on May 2nd, 2000. The accuracy has improved for horizontal positioning from more than 100 m to about 8 m, and has enabled a worldwide use of the system for surveying and navigation purposes. The SA method has been one important reason for the development of the independent other GNSS, such as Galileo (HOFMANN-WELLENHOF et al., 2008).

However, a more secure and enhanced civilian use of the system, as well as a new distinction with regard to military services has begun with the start of the first IIR-M satellite in September 2005. This will add a second civilian code on the L_2 frequency (L_2C), a L_5 frequency, which will be four times more powerful as well as a new military M-code on both frequencies, being finalized about 2015. This enhancement will general improve measurements under difficult conditions, leading to a reduced position error of about 3 m (SEEBER, 2003; HOFMANN-WELLENHOF et al., 2008).

The second world-wide available and fully functional system is GLONASS (russian: Global'naya Nawigazionnaya Sputnikowaya Sistema), which has been developed since the mid 1970s by the former Union of Soviet Socialist Republic (BAUER, 2003). Nowadays, the system is operated and maintained by the Russian military. The control segment consists of 14 stations across the GUS states, with the main station at Moscow, Russia.

The space segment was fully operational with 24 satellites in 1996. Due to the lack of funding and limited satellite life times, the number of satellites decreased to six satellites in 2001. Today (mid-2013) 24 satellites, which were launched between 2007 and 2012, are operational (FDA, 2013). The signals' frequencies are within the range of the NAVSTAR-GPS. In contrast, each satellite is sending signals on its own frequency. Similarly, a coarse code on the G_1 signal is given, and the precise, encrypted P-code is modulated on both frequencies, G_1 and G_2 . Having started in 2003, enhanced satellites (type GLONASS-M), which set-up a C/A code on G_2 are currently still being launched. Further enhancements are given by GLONASS-K satellites, which will establish a third C/A- and P-code on G_3 (MANSFELD, 2010). Generally, the same accuracy as by NAVSTAR-GPS is achievable.

GNSS receivers that are capable to receive both signal types show a better signal availability, in particular for areas affected by shadowing effects (EL-MOWAFY, 2002). In addition, GLONASS is available at higher latitudes. Accuracy is not enhanced, but particularly with regard to the SA function of the NAVSTAR-GPS, a better reliability is given (MANSFELD, 2010). The typical accuracy is denoted as ~ 8 m. However, due to the latest updates of the systems and Galileo, the accuracy will be enhanced to 3-5 m, mainly derived by the integration of further code signals on different carrier phases that reduce signal propagation errors (HOFMANN-WELLENHOF, 2013).

The stated accuracies of the measurements with both GNSS show the same errors, which need to be corrected, when a higher accuracy is needed (MANSFELD, 2010). The errors that are inherent to the method are satellite errors, signal errors and receiver errors (Table 2-1). These errors can be summarized in an accuracy value, called DOP (Dilution of Precision) that is generated by the standard deviation of the pseudo-range measurement (or the User Equivalent Range Error, UERE) and the standard deviation of positioning, taken from the geometric configuration of the satellites. The DOP can be further assigned to a specific accuracy, e.g. the horizontal positioning (HDOP) or time determination (TDOP) error. The combined accuracy is given by the GDOP (Geometrical Dilution of Precision). Typically GNSS-receivers show another accuracy value in meters, mostly the 50% CEP (Circular Error Probable)

that shows the radius containing the position of 50% of several measurements (HOFMANN-WELLENHOF et al., 2008).

Table 2-1: Main error sources and according range errors for GNSS signals (SEEBER, 2003).

Error source	RMS range error
Satellite	
-orbit	1-2 m
-clock	1-2 m
Signal propagation	
-ionosphere (2 frequencies)	cm-dm
-ionosphere (model, best)	1-2 m
-ionosphere (model, average)	5-10 m
-ionosphere (model, worst)	10-50 m
-troposphere (model)	dm
-multipath	1-2 m
Receiver	
-observation noise	0.2-1 m
-hardware delays	dm-m
-antenna phase center	mm-cm

For an enhanced accuracy of single GNSS measurements, three different methods exist, which are the incorporation of phase measurements of the carrier signal, Precise Point Positioning (PPP) and utilization of pseudolite signals (MANSFELD, 2010). Phase measurements in addition to the stated observations of the modulated signals on the carrier signal usually allow an accuracy of several decimetres. These receivers are more expensive in comparison to simple receivers (SEEBER, 2003). Another method to enhance the measuring result is called PPP, which uses precise corrections of the measured ephemerides and system times (ZUMBERGE et al., 1997). These corrections can also be delivered in real time and can lead to centimetre accuracy (CAI & GAO, 2012; HUISMAN et al., 2012). A third possibility to improve the accuracy of a position is the use of pseudolites. These transmitters are sending similar signals as the satellites, but avoid signal propagation errors. This method is important for aviation and allows indoor positioning (MANSFELD, 2010).

In addition to the mentioned methods, further accuracy enhancements can be achieved with differential solutions (differential GPS, DPGS or DGNS), as depicted in Figure 2-3 (MANSFELD, 2010). This method involves using two or more stations to minimize satellite- and signal propagation errors. Correction vectors are calculated by comparing signals from different receivers to enhance the measurements. The accuracy is about 1 m. Usually, correction data is submitted in the standard of the Radio Technical Commission for Maritime services (RTCM), but proprietary formats are also used. The augmentation systems can be divided in ground-based systems (GBAS) and satellite-based systems (SBAS) and accordingly in local (LAAS) and wide area augmentation systems (WAAS). SBAS uses a network of ground monitoring stations to generate corrections that are distributed by geostationary satellites. These are for example the European EGNOS and American WAAS, as well as the private OmniStar system (WITTE & WILSON, 2005; PFLUGMACHER et al., 2009). Local GBAS are used for example for aviation and marine applications (MANSFELD, 2010) and can be set up by one or several additional receivers.

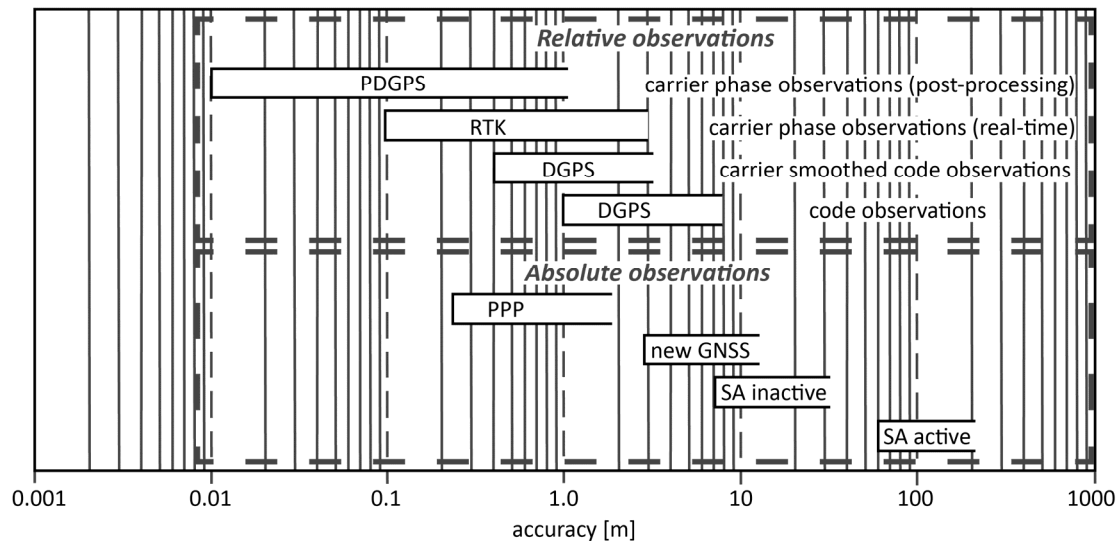


Figure 2-3: Accuracies of different global positioning methods applying absolute or relative observations. Modified after SEEBER (2003).

For surveying purposes the carrier phases of the transmitted signals are also considered to enhance the measurements (HOFMANN-WELLENHOF et al., 2008). This method is called precise DGPS (PDGPS), when the measurement is stationary and the data is post-processed. PDGPS accuracies can reach up to millimetre accuracy and are available by post-processing of the measurements with computational services. Real time solutions are called Real Time Kinematic (RTK) measurements. Generally, an accuracy of 1-2 cm is possible (EL-MOWAFY, 2000; MEKIK & ARSLANOGLU, 2009). RTK solutions can be derived by establishing separate reference stations or by a connection to service providers. The providers deliver services in different qualities and with different connection types (e.g. GSM-dial up lines or GPRS data streams). In Germany, for instance, the positioning service SAPOS of the surveying agencies and the service of the AXIO-NET GmbH are available service providers (MANSFELD, 2010; AXIO-NET GmbH, 2013). Both providers share about 250 of reference stations. Similar services exist in other countries, such as Greece or the United Kingdom (GIANNIOU, 2008; APONTE et al., 2009). In addition, local transformation services are available (MANSFELD, 2010). Overall, GNSS measurements allow the determination of single 3D points in various accuracies and are combined with most of the other methods to achieve a georeference.

2.1.3 Photogrammetry

Photogrammetry is an extensive method of obtaining position and shape of objects from pictures, which were photochemical, analog products in the past, but are mostly digital nowadays (KRAUS, 2004; ALBERTZ, 2007). The first approach of using pictures for measurements was conducted by *Laussedat* (France, 1859), as well as *Meydenbauer* (Germany). The method is available for terrestrial, airborne and space-borne applications and numerous results can be achieved particularly in combination with interpretation and classification methods. For instance, digital elevation models and 3D (city-) models, oblique images, orthoimages, as well as thematic and topographic data for maps and analysis in Geographic Information Systems (GIS) are very common. Further information can be derived, when multi- or hyperspectral sensors that cover several reflective areas of the electromagnetic spectrum

from the illuminated earth or object surface are applied. Overall, the method is a passive remote sensing technique (ALBERTZ, 2007).

In general, photogrammetry relies on the central perspective as the mathematical model (LUHMANN, 2003). Shape and position of an object are estimated by the reconstruction of a beam of rays that are defined each by the object point, the projective center, and the image point. For this purpose, the internal and external orientation of the camera is essential. The internal orientation is given by the manufacturer or can be derived by calibration. For the derivation of the external orientation, several methods are available. Images can be oriented by (ground) control points or combined by identical points. Nowadays, digital cameras in combination with precise GNSS and an INS measurements (section 2.1.1) are used for aerial and space-borne cases, which minimize the need of ground control points (ALBERTZ, 2007). The bundle adjustment is used to automatically derive or enhance the external orientation of a set of images. A 3D measurement is possible, when at least two known homologous rays from two or more different images are available. Finally, every point of the image gives a 3D coordinate. This particular method is called stereophotogrammetry (also: stereoscopy) (KRAUS, 2004).

In the past, stereoscopic analysis was conducted on analogue images by optical or mechanical projection with stereo comparators (KRAUS, 2004). After a 2D analysis of the image, an elevation analysis followed, where contour lines and single point measurements were accomplished. This approach was replaced by digital analysis (KAHMEN, 2006). The method is used particularly for the establishment of 3D city models since the 1990s with an accuracy less than one metre (WEIDNER & FÖRSTNER, 1995; GÜLCH, 2005). In general, the method is applicable for the determination of all 3D objects. The accuracy of close range photogrammetry as a terrestrial application is of millimetres (KRAUS, 2004). Stereoscopic images and terrain data can be used to generate orthophotos by differential rectification. Orthophotos are images without tilting or relief displacement. Shadowed areas or gaps are filled by information of other overlapping images. The latter products are called true-orthophotos (MAYR, 2002; GÜLCH, 2005).

As an alternative carrier for photogrammetric surveying, Unmanned Aerial Vehicles (UAVs) play an increasingly important role (EISENBEISS & SAUERBIER, 2011). Apart from military use, civilian applications for documentation and monitoring purposes have risen. The fast, low-cost surveying offers a major advantage. Recent developments in algorithms (HIRSCHMÜLLER, 2008; HAALA & ROTHERMEL, 2012; HARWIN & LUCIEER, 2012), cameras (KIM et al., 2013) and autonomous flight modes (EISENBEISS & SAUERBIER, 2011) support this development. The implementation of newer computer vision methods, like structure from motion and dense stereo imaging in low-cost or open source software and even by online tools allows an easier generation of 3D products (REMONDINO, 2011; PLETS et al., 2012; WESTOBY et al., 2012; DE REU et al., 2013; LERMA et al., 2013). However, such 3D information acquisition is dependent on illumination and is acquired indirectly, and for accurate results, accurately measured ground control points are mandatory.

2.1.4 Radar

In contrast to photogrammetry, RADAR (radio wave detection and ranging) is an active remote sensing method, as it is not passively detecting parts of the emitted electromagnetic spectrum. The active signals are able to penetrate through clouds, water vapor and smoke and are applicable day and night. It

incorporates microwaves with a wavelength of 1 to 100 cm (LILLESAND et al., 2008; CAMPBELL & WYNNE, 2011).

Generally, a small narrow beam is transmitted and a wave front propagates by time in the order of microseconds. Objects and surfaces at certain distances reflect parts of the signal (LILLESAND et al., 2008). The received signals are amplified and stored, whereas the strength of the received signal is depending on the reflectivity of the object. Ranges between the sensor and the objects (slant range) can be derived by measuring the time difference of sending and receiving the pulsed signal. Various systems are available, which emit a continuous wave, measure velocities (continuous wave radar) or are used to measure distances and heights as well as for navigation purposes (frequency modulated CW radar) (LILLESAND et al., 2008).

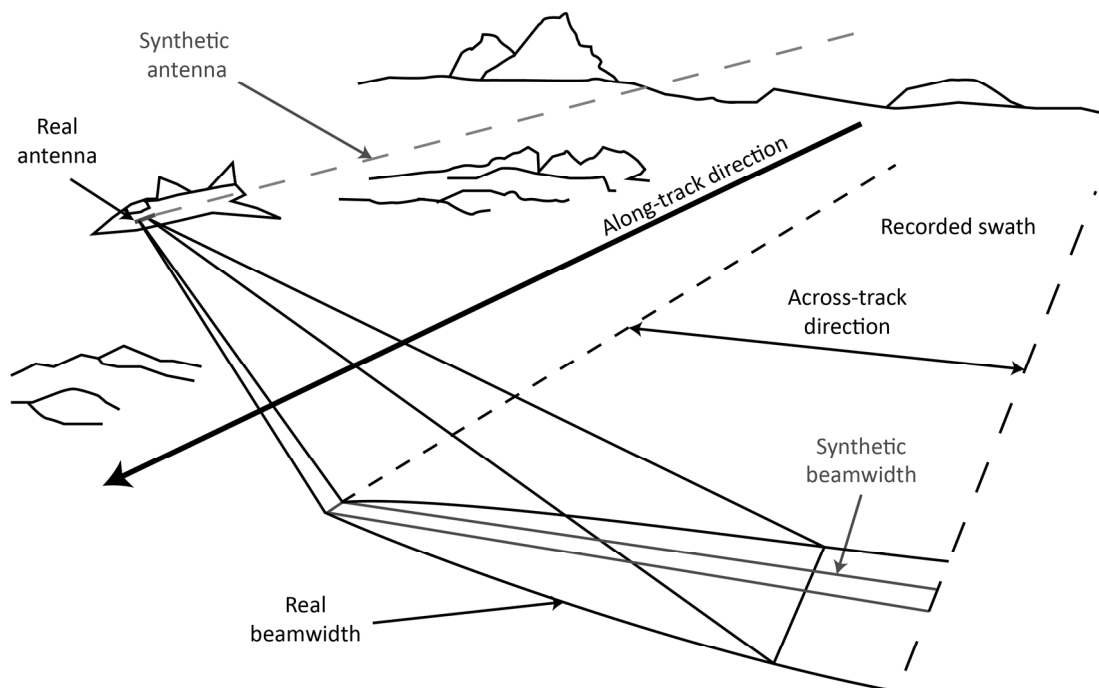


Figure 2-4: Principle of side-looking radar showing the across-track ground resolution for real and synthetic apertures, modified after LILLESAND et al. (2008).

The radar sensors, which generally in use for imaging purposes, are pulsed, side-looking radar sensors (LEWIS & HENDERSON, 1998). These are mounted on one side of aircrafts or satellites and form an image stripe perpendicular to the ground track of the carrier. The movement leads to image lines along one side (as depicted in Figure 2-4).

The minimum determination difference between objects in the range direction, which is assigned as the range resolution or slant-range resolution, is only depending on the incorporated pulse length of the beam (LEWIS & HENDERSON, 1998). Objects that are closer to each other than half of the pulse length are not distinguishable by the radar beam. This detection capability is independent of the flight height and depression angle. For real aperture systems, the achieved ground resolution or cell size in contrast depends on the depression angle of the emitting antenna perpendicular to the flight direction and on

the beam width angle, which is caused by beam widening with increasing distance. This angular beam width is given by the selected wavelength and the antenna length, which is a logistical constraint (LILLESAND et al., 2008). Such real aperture systems can only achieve useful accuracies at low altitudes.

For better accuracies and in particular for space-borne applications, systems with synthetic apertures are applied (LEWIS & HENDERSON, 1998). These systems use a repeated exposure of objects that are evaluated in complex recording systems. The repeated exposure shows a different ground resolution, as it is only depending on half of the antenna length. Thus, in contrast to real apertures systems, the spatial resolution is not dependent on ranges or flying altitudes and these systems are therefore applied to aircrafts and satellite systems for radar imaging. The first satellite that carried such a radar sensor was Seasat 1 (1978) and several systems followed, like ERS-1 and -2, ALOS, as well as Radarsat-1 and -2 (ALBERTZ, 2007).

Just like in the case of photogrammetry, depicted in chapter 2.1.3, images resulting from radar only retrieve 2D information. Likewise, 3D information can be added by using stereoscopic methods. Two images with a certain overlap can be used for a radargrammetric approach. In contrast, phase shifts between two receiving antennas (single-pass) or between two overpasses (repeat-pass) are compared for Interferometric Radar (InSar) (GOLDSTEIN et al., 1988; MASSONNET & FEIGL, 1998). For both cases, the accurate determination of the baseline between both antennas is important. Highly accurate DEMs can be derived in addition to the general imagery. Regarding the active signal distribution, this is an important method for areas with high cloud coverage or humidity. As an example for a single-pass system, a space shuttle was equipped with two antennas for the Shuttle Radar Topography Mission (SRTM), which started in February 2000 (ALBERTZ, 2007). The global DEM is given in a 30 m resolution and can be used in particular in combination with other remote sensing satellite data (BUBENZER & BOLTEN, 2008). In addition, the satellites ERS-1 and ERS-2 were able to fly in a tandem approach, but also the repeated-pass mode was employed. A similar approach is used by the TerraSAR-X and TanDEM-X satellite, which will be able to derive a global digital elevation model in a high resolution and accuracy of several meters (KRIEGER et al., 2007). Multi-temporal approaches allow the detection of changes. For instance, this method allows the observation of the Greenland ice shield fluctuations (RIGNOT & KANAGARATNAM, 2006).

The representation of surfaces in radar imagery is dependent on characteristics of the system and the recorded surface, which are for instance roughness, topography and electrical properties of the material. The sensor geometry and the recorded topography cause different effects, which need to be taken into consideration for radar imagery, such as foreshortening, lay-over, shadowing, speckle, distortion, displacement and parallax (LILLESAND et al., 2008). However, the method is able to derive high-resolution DEMs in a sub-metre accuracy by airborne surveys, which is usable for 3D city models and further research (LILLESAND et al., 2008). In addition, terrestrial solutions are available, which also allow detecting displacements on a millimeter scale in multi-temporal approaches (NICO et al., 2004; NOFERINI et al., 2006; LUZI et al., 2009). The properties of the reflected signals, the backscatter, can be used to derive further information. Radar polarimetry concerns the electrical field conditions of the emitted and received signals. The transmitted beam and the receiver of the backscatter signal can be set to a horizontal or vertical polarization. This allows four different polarization combinations important for

interpretation purposes. For example, soil moisture estimations are possible, when surface roughness is accurately determined, which can be conducted by laser scanning (KOYAMA, 2010; KOYAMA et al., 2010).

Generally, this active method is able to derive 3D information. However, the derivation of ranges or heights is not direct, as also shown for the photogrammetric approach. Several error sources occur, which affect the accuracy and precision of this specific information.

2.2 Laser scanning: basic principles

Laser scanning specifically means the embedded automatic deflection of laser beams, which are actively emitted and the backscattered signal is captured by a sensor to achieve an extensive 3D description of a surface by point clouds (WEHR & LOHR, 1999). Laser scanners are applied on airborne vehicles (airborne laser scanning, ALS), on ground (terrestrial laser scanning, TLS) or on mobile vehicles (mobile mapping or mobile laser scanning, MLS). In contrast to ALS and MLS, TLS measurements need a second redirection of the laser beam to achieve a point cloud, since these instruments are not moving.

The theoretical principle of laser was introduced by *Einstein* in 1916 and the idea lead to several experiments with micro-wave amplifiers called masers in the 1950s (SIEGMAN, 1986; PETRIE & TOTH, 2009a), until finally the first functional laser was constructed on 15th of May, 1960 by *Maiman* at Hughes Research Laboratories, Malibu, CA, USA (MAIMAN, 1960; SMITH, 1984; TOWNES, 2003). This invention rapidly initiated research for applications, with one of the earliest mentioned laser altimeters being presented by MILLER (1965) and SHEPERD (1965). Several bathymetric applications with laser altimeters, or also called profilers, followed that not contain an automatic reflection (HICKMAN & HOGG, 1969; HOGE & SWIFT, 1979, 1980; HOGE et al., 1980). The method was also applied to forest and bare earth detection (ARP & GRIESBACH, 1982; KRABILL et al., 1984; NELSON et al., 1984; MACLEAN & KRABILL, 1986), and accuracy as well as backscatter values were investigated (SCHREIER et al., 1984; SCHREIER et al., 1985). Further pioneer research was conducted on forest applications and surface topography in the late 1980s to 1990s, still relying on laser profilers (NELSON et al., 1988; NELSON et al., 1997).

After the completion of NAVSTAR-GPS, an absolute position could be determined by GNSS measurements (cf. section 2.1.2) (BUFTON et al., 1991; RITCHIE, 1995; NILSSON, 1996; RITCHIE et al., 1996). For instance, multi-temporal observations of the Arctic topography and changes of the ice shield were conducted (KRABILL et al., 1999; KRABILL et al., 2000a). In particular, the development of the supporting technologies, e.g. advances in computing, the incorporation of scanning mechanisms by mirrors and the introduction of direct georeferencing by IMUs in the 1980s to mid-1990s (SHAN & TOTH, 2009; CAMPBELL & WYNNE, 2011), led to an enhanced absolute accuracy and better coverage (VAUGHN et al., 1996; NAESSET, 1997). The ALTM 1020 scanner by Optech was the first commercially available airborne laser scanning system in 1993 (PETRIE & TOTH, 2009b).

These developments were also used in space for early range measurements in the Apollo mission 15-17, followed by the Shuttle Laser Altimeter (SLA) on the Space Shuttle Endeavour in 1996 for measurements with global coverage (GARVIN et al., 1998). The Geoscience Laser Altimeter System (GLAS) incorporated on the Ice, Cloud and land Elevation Satellite (ICESat) was used successfully for research on changes of

the polar ice shield, general topographic profiling, and canopy height determination, from 2002 to 2010 (ZWALLY, 2002; LEFSKY et al., 2005; SCHUTZ et al., 2005; DUONG et al., 2008; WANG et al., 2011).

Meanwhile, terrestrial applications were driven by the military for aiming and tracking purposes (PETRIE & TOTH, 2009c). The technique was constantly enhanced, it replaced classic instruments and hence enabled the rise of electronic tachymetric surveying (SCHERER & LERMA, 2009). Finally, the first terrestrial laser scanners and mobile applications emerged in the late 1990s. With regard to the history of ALS, a small lag of development is recognizable that is maybe related to the greater costs compared to traditional surveying instruments (PETRIE & TOTH, 2009c). One of the first commercial terrestrial laser scanners was provided by Callidus, Germany in 1996 (PETRIE & TOTH, 2009c).

In general, all laser scanning systems deliver polar 3D coordinates for each measured point. In contrast to single measurements being produced, for example by tachymetric surveying (Figure 2-2), scanning mechanisms record a huge amount of single measurements: the point clouds (Figure 2-5).

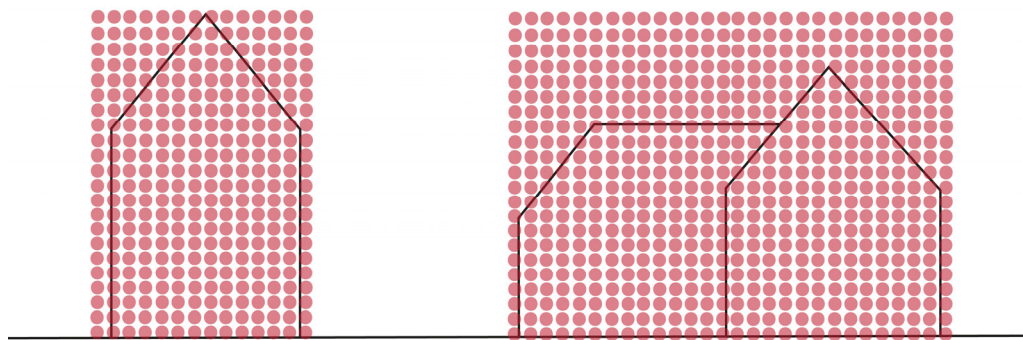


Figure 2-5: Raster measurement approach of a terrestrial laser scanner. Red dots indicate single 3D point measurements.

These unstructured huge point clouds need, as opposed to single measurements, other post-processing steps. They are comparable to methods of photogrammetry or radar procedures, in particular concerning the derivation of DEMs (BALTAVIAS, 1999b). However, to achieve such point clouds, several effects and systematic influences need to be considered first.

Thus, in the succeeding subchapters the basic principles of laser light are explained (2.2.1), followed by the major measurement principles (2.2.2) and possibilities of automatic beam deflection (2.2.3). Propagation characteristics of laser beams (2.2.4), as well as reflection and detection (2.2.5) effects are described, leading to an overview of possible error sources (2.2.6). The quite complex laser scanning surveys (2.3) and common post-processing steps (2.4) are also presented. The chapter ends with a section describing applications of laser scanning (2.5), which are not considered in the detailed parts of this contribution.

2.2.1 Laser light

As described in JOECKEL et al. (2008), SIEGMAN (1986) and PETRIE & TOTH (2009a), a laser consists of three components, namely an external energy source, an active material and an optical feedback system. As a basic explanation, the electron of an atom on the energy level E_0 can be stimulated with energy of an external energy source to a higher level E_1 (SIEGMAN, 1986). When the atom drops back very shortly after the stimulation, a photon will spontaneously be emitted. This is associated with a radiation of a certain frequency f , obtained by $E_1 - E_0 = h \cdot f$ (after *Planck*), where h is a natural constant. In contrast, *Einstein* introduced the theoretical possibility of a direct, stimulated emission of a photon. For this purpose the majority of the electrons need to be in the excited state, called a population inversion that is enabled by a continuous pumping of energy by the external energy source (Figure 2-6). External photons from any light source that pass through this active laser medium are amplified by the generation of an additional photon with the same frequency. Additional mirrors facilitate a cascading effect. The amplified output light beam is released continuously or as single laser pulses by an optical system (BERALDIN et al., 2010).

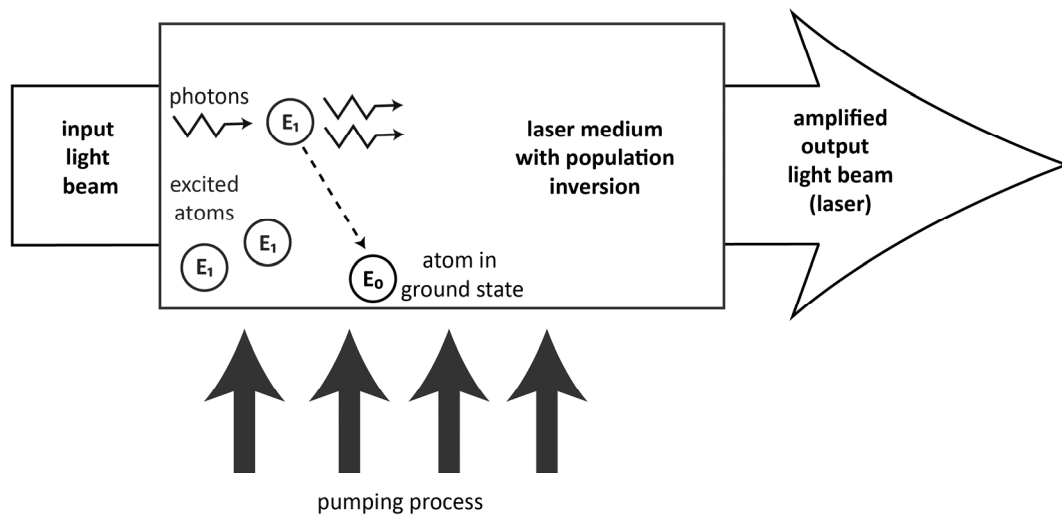


Figure 2-6: Simplified diagram of laser amplification. The input radiation is coherently reproduced by stimulated emission, modified after SIEGMAN (1986).

Overall, this process results in highly intense, monochromatic, directional, coherent amplified light, called laser (Light Amplification by Stimulated Emission of Radiation) (BERALDIN et al., 2010). The active materials can be crystals or gases, such as rubies, CO_2 , helium-neon, and argon. Two types of laser are commonly considered for range detection, which are solid-state and semiconductor lasers. Solid-state lasers (usually type: Nd:YAG, Neo-dymium: Yttrium Aluminum Garnet) are mainly in use for the later described time-of-flight method (WEHR & LOHR, 1999), whereas semiconductor lasers are mostly used for the continuous wave method (PETRIE & TOTH, 2009a).

The wavelength of the laser light depends on the active material, normally in the area of short infrared light (830-1350 nm). Frequency doubling methods, which halve the wavelength, allow wavelengths in the visible light spectrum (~ 530 nm), which is important for bathymetric measurements, due to their

ability to penetrate water (e.g. IRISH & LILLYCROP, 1999; KLEMAS, 2011; DONEUS et al., 2013). All lasers are classified according to their emitted energy and their wavelength. There are seven classes with regard to safety. Particular protection advice has been assigned to each of these classes, as denoted in Table 2-2 (2007; PETRIE & TOTH, 2009a).

Table 2-2: Classes of lasers and their potential hazard.

Class	Description
1	All lasers that not permit any radiation for humans, except maintenance.
1M	Lasers that belong to class 1, but are potentially hazardous when additional optical devices are used.
2	All lasers in the visible wavelength ranges (400-700 nm) that not permit any radiation for humans, except maintenance. The human aversion of bright light, e.g. the blink reflex of the eye will avoid radiation.
2M	Similar to class 1M, but for lasers of class 2.
3R	Direct beam viewing is slightly hazardous.
3B	In contrast to class 3R direct beam viewing is hazardous.
4	Lasers and the diffuse reflections cause hazardous emissions for the skin and are a fire hazard. Mostly, ALS scanners use this class.

2.2.2 Measurement methods

Laser scanning devices, in particular terrestrial laser scanners, are mostly distinguished by the method of distance measurement that represents major specific characteristics. Further possibilities to distinguish TLS systems are for example the maximum range or the maximum visible area. After BERARDIN et al. (2010), existing principles for single point measurements are triangulation and the measurement of light transit time (Figure 2-7). Methods of transit time measurements can be further subdivided into the different methods using phase-shifts in continuous waves and the direct time-of-flight (TOF) method of pulsed lasers. These different measurement methods are briefly described in this section. Interferometric systems are not covered here, as this method relies on very precise installations and is focusing on sub-millimetric change detection (BLAIS, 2004; BERARDIN et al., 2010).

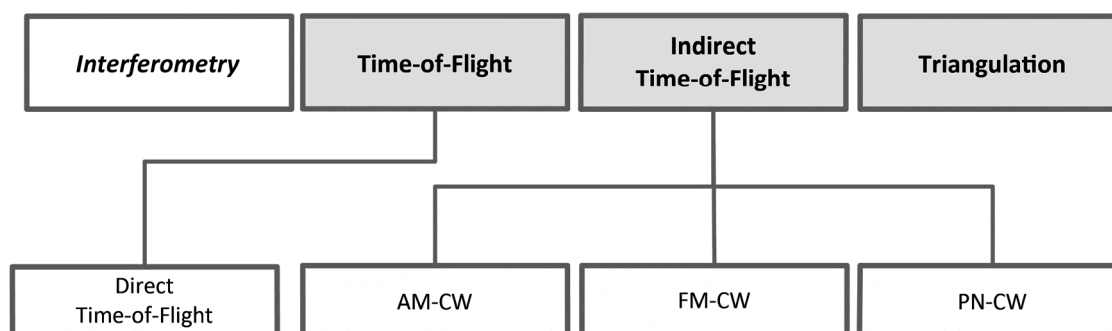


Figure 2-7: Common measurement principles of laser scanning.

In contrast to the laser scanning principle that involves the automatic deflection of single point measurements, range imaging cameras (RIM) work differently (LANGE & SEITZ, 2001; BERARDIN et al., 2010; LICHTI et al., 2012). These devices incorporate equal principles (triangulation, direct TOF, indirect TOF),

but directly record an entire scene in 3D and detect the reflected signal by image sensors, like CCD or CMOS (REMONDINO, 2011). The range measurements are conducted for each pixel and a direct, complete 3D or depth image of a certain view is captured. Devices, which use time-of-flight measurements, can be also called flash lidar. The devices are limited in maximum range and resolution, but are a real-time solution (BERALDIN et al., 2010). One well-known sensor is the wide-spread Kinect system by Microsoft (HENRY et al., 2012). The small size of the instruments allows their installation on UAVs, as they do not require moving parts (ZHOU et al., 2012).

Triangulation

Devices incorporating the triangulation method show a high resolution and accuracy, which is used particularly for close-range measurements in industrial applications, reverse engineering and medical research (JOECKEL et al., 2008). A beam is projected onto an object and partially reflected to the position-sensitive receiver, usually a CCD-sensor. In many triangulation devices, the relation between the emitting device and the CCD-sensor is in a *Scheimpflug* condition, which is a specific angle to keep the reflection point in focus (BERALDIN et al., 2010). The distance to an object is calculated by using the information about the distance between the emitting and detecting sensor b , the projective angle α , and the base angle β (Figure 2-8). Differences to this base angle are detected by displacement on the CCD-sensor and result in the shifted receiving angle $\Delta\beta$ (JOECKEL et al., 2008).

Thus, the ranges can be calculated by:

$$r = \frac{b}{\tan \beta} \text{ and } r' = \frac{b}{\tan \beta + \tan \Delta\beta} \quad (\text{eq. 2.1})$$

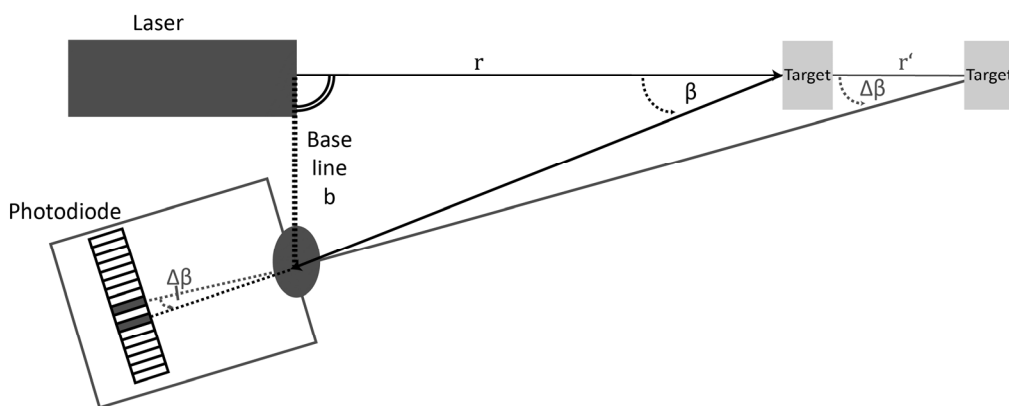


Figure 2-8: Principle and layout of a triangulation based measurement, according to JOECKEL et al. (2008).

The length of the CCD-Sensor is restricting the maximum range for measurements. Additionally, the Signal-to-Noise-Ratio (SNR) diminishes the maximum range (BERALDIN et al., 2010). All components can be arranged to build a scanning device. The basic configuration of the triangulation method is also incorporated for slit measurements and pattern projection (BLAIS, 2004). Light patterns or sequences of patterns are projected onto the surface of the measuring object and recorded by a camera, which is similarly set. These devices detect the displacements of the patterns for the exact geometric reconstruction of an object. Generally, small objects are measured on automatic turning tables.

Additionally, measurement arms or optically tracked hand devices exist (BLAIS, 2004). Exemplarily systems are listed in Table 2-3.

Table 2-3: Overview of several triangulation (Tri.) and structured light (SL) based scanners, compiled after BLAIS (2004), PETRIE & TOTH (2009c), REMONDINO (2011), and own research.

Company	Name	Range [m]	Points/sec.	Accuracy	Meas. Principle	Homepage
3D digital corp	Optix 400M 3D Scanner	<0.65			Tri.	www.3ddigitalcorp.com
3d3 Solutions	HDI Blitz			120 μm	Tri.	www.3d3solutions.com
3d3 Solutions	HDI Advance			45 μm	Tri.	www.3d3solutions.com
Aicon3D	smartSCAN ^{3D} -HE				SL	www.aicon3d.de
Arius3D	A3DColor Scanners				Tri.	www.arius3d.com
Callidus	CT900		4,000	70 μm	Tri.	ww.callidus.de
Creaform3D	EXAscanner		25,000	40 μm	Tri.	www.creaform3d.com
Gom	ATOS III Triple Scan	<2			SL	www.gom.com
Konica	Minolta Range7	<0.8		40 μm	Tri.	www.konicaminolta.eu
Kreon	Solano SL-100	<0.1	40,000	30 μm	Tri.	www.kreon3d.com
Laser Design	Surveyor Auto Gage 3D			0.03 mm	Tri.	www.laserdesign.com
Laser Design	Surveyor Space Arm				Tri.	www.laserdesign.com
Neptec	OPAL-360				Tri.	www.neptectechnologies.com
Neptec	OPAL-120				Tri.	www.neptectechnologies.com
Nextec	WIZprobe		50	6 μm	Tri.	www.nextec-wiz.com
Nextengine	3D Scanner HD		50,000		Tri.	www.nextengine.com
Nikon	LC15Dx		70,000		Tri.	www.nikonmetrology.com
Perceptron	ScanWorks V5	<6m	458,400	60 μm	Tri.	www.perceptron.com
Polhemus	PolhemusFastSCAN	<0.75		130 μm	Tri.	www.polhemus.com
Roland	LPX-60RE			0.1 mm	Tri.	www.rolanddg.com
Scantech	OneCam 3D Scanner	<0.2		0.1 mm	Tri.	www.scantech.com
Shapegrabber	Ai810		100,000		Tri.	www.shapegrabber.com
Steinbichler	PROBEscanner		64,000	40 μm	Tri.	www.steinbichler.de
Steinbichler	T-Track	<3.5	240		Tri.	www.steinbichler.de
Taicaan	Xyris 2000 TL Profiler				Tri.	www.taicaan.com
Vialux	zSnapper 4M			40 μm	SL	www.vialux.de
Vitronic	VitusLC				Tri.	www.vitronic.de
Wolf&Beck	OTM3				Tri.	www.wolfbeck.com
Wolf&Beck	OTP6				Tri.	www.wolfbeck.com

Phase comparison of continuous wave lasers

Following PETRIE & TOTH (2009a), the phase comparison method is used with continuous wave (CW) lasers. This method is most commonly used by short-range laser scanners. A modulated sinusoidal wave is emitted and the pattern of the emitted and received signal is compared, as depicted in Figure 2-9. The wavelength is related to the frequency by the assumed velocity of light ($\lambda_m = c/f_m$). The following equation (BALSAVIAS, 1999a) determines the range r , incorporating the phase difference, measured by the phase shift angle $\Delta\varphi$, according to the wavelength λ_m :

$$r = \frac{\Delta\varphi}{4\pi} \lambda_m \quad (\text{eq. 2.2})$$

The maximum range r_{max} of a system, which employs a CW measurement, is given by the following equation (BALSAVIAS, 1999a):

$$r_{max} = \frac{\lambda_{max}}{2} \quad (\text{eq. 2.3})$$

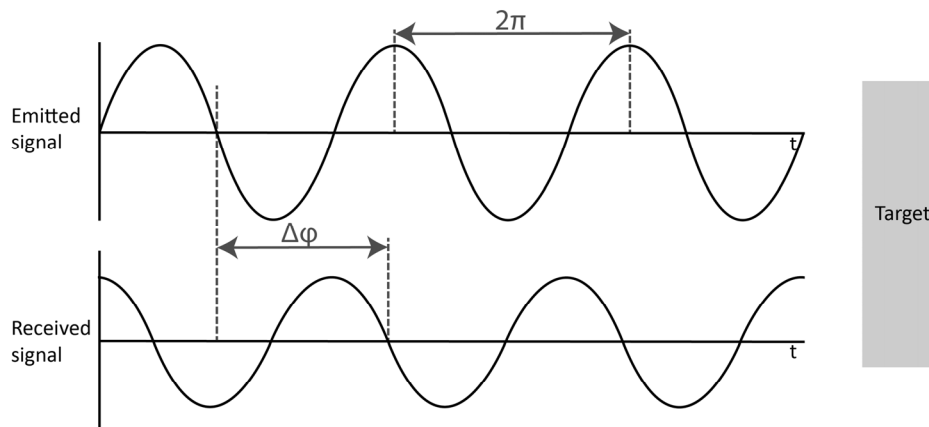


Figure 2-9: Principle of phase-shift detection by continuous wave measurements, modified after BERALDIN et al. (2010).

An exemplary frequency of 10 MHz leads to a maximum, unambiguous range or ambiguity interval of ~ 15 m. The range uncertainty or accuracy of a CW system is given by (WEHR & LOHR, 1999):

$$\Delta r_{-AM} \approx \frac{1}{4\pi} \frac{\lambda_m}{\sqrt{SNR}} \quad (\text{eq. 2.4})$$

Using eq. 2.4, and assuming a SNR of 1000 and a frequency of 100 MHz results in an accuracy of 0.24 mm.

However, the peaks of the wave of the retrieved signal cannot be related to the peaks of the original signal (BERALDIN et al., 2010). Correspondingly, the oddment of the wave is used to determine the phase-shift, but not every peak of the wave can be counted, which is called the ambiguity resolution problem (JOECKEL et al., 2008). Several methods exist to solve this problem by incorporation of several frequencies by Amplitude Modulation (AM), Frequency Modulation (FM) or Pseudo-Noise (PN) sequences (BERALDIN et al., 2010). Multi-frequency systems or AM systems are the most common. They work with frequencies of 10 to 600 kHz and operate with a maximum range of about 200 m (PETRIE & TOTH, 2009a). These systems automatically change the wavelength vary rapidly and solve a set of variations of eq. 2.2 to estimate the distance. The ambiguity interval (eq. 2.3), here about 15 m, is given by the longest incorporated wavelength, whereas the shortest incorporated wavelength resolves the minimum accuracy. The second possibility is to use a FM, where the signal is commonly linearly modulated as a triangular or sawtooth wave (chirp) mode, whereas the PN-method uses algorithms to modulate the signal. This specific pattern allows to determine the round trip time directly (BERALDIN et al., 2010). Both methods are also incorporated in radar measurements (section 2.1.4) and the latter method is the basic method for GNSS measurements by the code signal (section 2.1.2). Several of such continuous wave systems exist, which are exemplarily depicted in Table 2-4. They are all capable to achieve high data rates (up to 1 million pts./s) at a high accuracy, but with a maximum range of < 200 m.

Table 2-4: Examples for terrestrial continuous wave scanner systems, compiled after BLAIS (2004), PETRIE & TOTH (2009c), REMONDINO (2011), and own research.

Company	Name	Range [m]	Points/sec.	Accuracy [mm/m]	Meas. Principle	Homepage
FARO	LS880	0.6-76	120,000	2.6 / 10	CW	www.faro.com
FARO	Photon120	0.6-120	976,000		CW	www.faro.com
FARO	Focus3D	120	976,000	2	CW	www.faro.com
Leica	HDS8810	2.5-2,000	8,800	8 / 200	CW	www.leica-geosystems.de
Leica	HDS8400	2.5-700	8,800	20	CW	www.leica-geosystems.de
Surphaser	25HSX IR_X	0.4-30	216,000-1,200,000	0.1 / 3	CW	www.surphaser.com
Surphaser	100HSX IR_100HS	1-50	216,000-1,200,000	0.16/ 10	CW	www.surphaser.com
Trimble	TX5	0.6-120	122,000-976,000		CW	www.trimble.com
Trimble	FX3D		216,000	0.6 / 11	CW	www.trimble.com
Z+F	Imager 5006h	0.4-79	1,016,000		CW	www.zf-laser.com
Z+F	Imager 5010	0.3-187	1,016,000		CW	www.zf-laser.com
Z+F	Imager 5010-C	0.3-187	1,016,000		CW	www.zf-laser.com
Z+F	IMAGER 5006EX	0.4-79	508,000		CW	www.zf-laser.com

Time-of-flight principle

Time-of-Flight (TOF) measurements use very short, intense laser beams, which are reflected by an object and partly received back (PETRIE & TOTH, 2009a), as shown in Figure 2-10. This principle is used for measurements from airborne and space-borne platforms and it is also suitable for terrestrial applications with a longer maximum range of kilometres, but a slightly worse accuracy.

Emitting and receiving of each single laser beam is triggered, and the time interval τ is precisely measured by high-speed counters generated by an oscillator. As the laser light wave travels with a constant, known velocity combined with the measurement of the time intervals, the estimation of range r (BALTSAVIAS, 1999a), where $\Delta\tau$ is the measured time difference and c the assumed light velocity, is possible by using the equation:

$$r = c \frac{\Delta\tau}{2} \quad (\text{eq. 2.5})$$

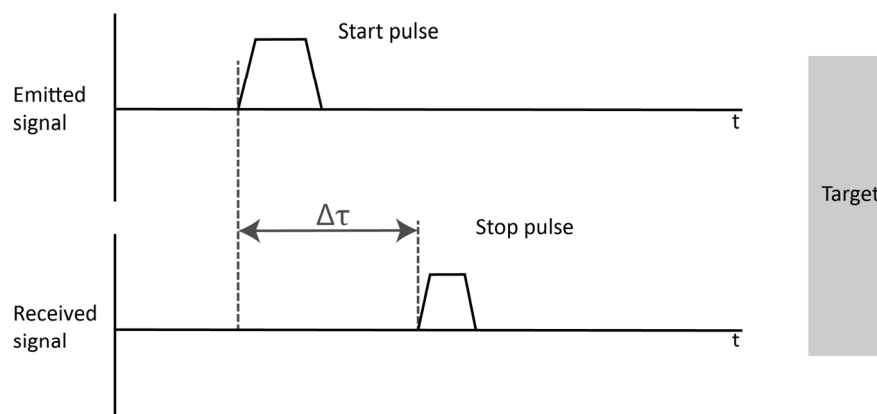


Figure 2-10: Principle of time-of-flight measurements, modified after BERARDIN et al. (2010).

Thus, in 5 ns the range of 1.5 m is reached. Reverting this equation and using a typical survey height of an ALS system or a range of a TLS system of 1,000 m leads to a round trip time of the laser light of about 0.0067 ms (BERARDIN et al., 2010).

The uncertainty of a range is theoretically derived using:

$$\Delta_{r-\rho} \approx \frac{c}{2} \frac{\tau}{\sqrt{SNR}} \quad (\text{eq. 2.6})$$

Assuming a SNR of 100 and a τ of 1 ns gives an uncertainty of about 15 mm. In contrast to the CW method, TOF allows longer ranges for equal power outputs and no ambiguity problem evolves. However, the accuracy is lower, due to the single measurement of an object and the resolution of the time measuring unit. Mostly all ALS systems are using the TOF principle. Additionally, newer ALS systems are capable to release several echoes simultaneously, called Multiple Pulse in Air (MPiA) technology (RIEGER & ULLRICH, 2012). Examples of different terrestrial TOF scanners are shown in Table 2-5. Some of them are equipped with an integrated camera, others have additionally mounted cameras, such as scanners from Riegl. The newer scanners from Riegl (VZ-series) are capable to record the full-waveform, which is explained later.

Table 2-5: Examples for terrestrial time-of-flight scanner systems, compiled after BLAIS (2004), PETRIE & TOTH (2009c), REMONDINO (2011), and own research.

Company	Name	Range [m]	Max. points/s	Accuracy [mm/m]	Meas. principle	Homepage
Callidus	CP3200	<32		5	TOF	www.callidus.de
Callidus	CPW 8000	<80	50,000	2 / 30	CW/TOF	www.callidus.de
Deltasphere	DS3000	0.5-15	15,000	7 / 9	TOF	www.deltasphere.com
Leica	Scanstation2	<300	50,000	4 / 50	TOF	www.leica-geosystems.de
Leica	ScanstationC10	0.1-300	50,000	4 / 50	TOF	www.leica-geosystems.de
Leica	Cyrax 2500	1.5-100		6 / 50	TOF	www.leica-geosystems.de
Leica	HDS3000	<300	4,000	6 / 50	TOF	www.leica-geosystems.de
Maptek	I-Site 8810	2.5-2,000		8	TOF	www.maptek.com
Maptek	I-Site 8840	2.5-1,000		8	TOF	www.maptek.com
Maptek	I-Site 8820	1-200		8	TOF	www.maptek.com
MDL	LaserAce	<700	250	5	TOF	www.mdlaustralia.com
Neptec	OPAL-120				TOF	www.neptectechnologies.com
Neptec	OPAL-360				TOF	www.neptectechnologies.com
Optech	ILRIS HD	3-1,250		7 / 100	TOF	www.optech.ca
Optech	ILRIS-HD-ER	3-1,800		7 / 100	TOF	www.optech.ca
Optech	ILRIS-LR	3-3,000		7 / 100	TOF	www.optech.ca
Optech	ILRIS-3D	3-1,500	2,500	7 / 100	TOF	www.optech.ca
Riegl	VZ-400	1.5-350	122,000	5	TOF	www.riegl.com
Riegl	VZ-1000	2.5-1,400	29,000-122,000	8	TOF	www.riegl.com
Riegl	VZ-4000	5-4,000	23,000-222,000	15	TOF	www.riegl.com
Riegl	VZ-6000	5-6,000	23,000-222,000	15	TOF	www.riegl.com
Topcon	GLS-1500	1-330	30,000	4 / 150	TOF	www.topconpositioning.com
Trimble	GX-3D	<350	5,000	7 / 100	TOF	www.trimble.com
Trimble	CX	<80	54,000	1.2 / 30	CW/TOF	www.trimble.com
Trimble	Mensi GS100	2-100	5,000	6	TOF	www.trimble.com
Velodyne	HDL-64E	<120	1,333	20	TOF	www.velodynelidar.com

2.2.3 Beam deflection

As stated before, laser scanning involves the automatic deflection of single laser beams in two different directions to capture an area or a 3D image. For ALS and MLS, the first deflection is conducted by

mirrors, which can be of several types. In addition, one fiber-glass system exists. The second direction is given by the motion of the carrier system.

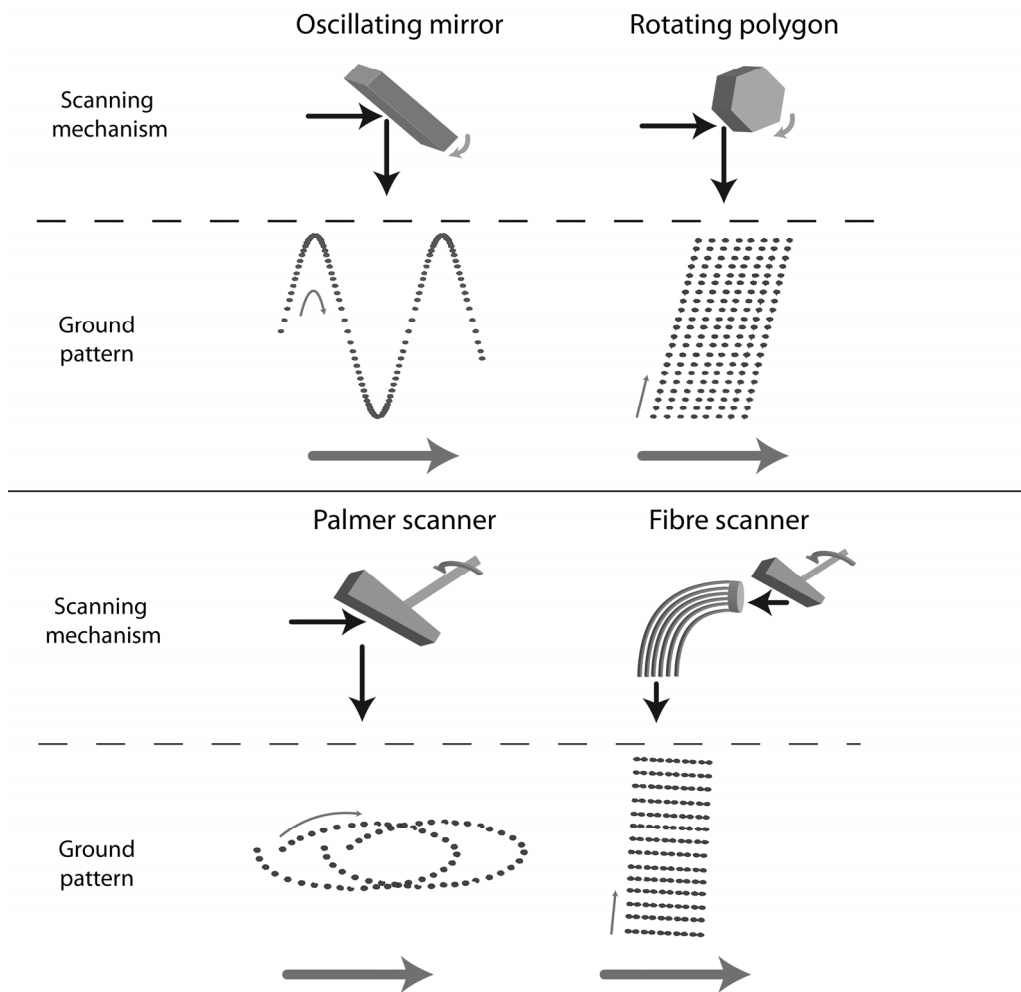


Figure 2-11: Common reflection principles of laser scanners applied on airplanes, modified after BERALDIN et al. (2010) and PETRIE & TOTH (2009b).

Generally, most systems use an oscillating mirror, where a mirror deflects the laser beams across a swath by swivelling (BERALDIN et al., 2010). Considering the moving direction for ALS and MLS applications a zigzag pattern is achieved on the ground (Figure 2-11, top left). In addition, this pattern is modulated, as point spaces are bigger in the mid area of the swath. Rotating polygonal mirrors allow capturing a more uniform spread of points on the ground (Figure 2-11, top right). The mirror surface of Palmer Scanners is not orthogonal to the rotation axis, which results in an elliptical scan pattern for ALS and MLS applications (Figure 2-11, bottom left). For a fiber scanner, single laser beams are consecutively distributed in neighbouring glass fibers by a mirror (Figure 2-11, bottom right). Further information and equations to derive point spacing are given in BALSAVIAS (1999a) and WEHR & LOHR (1999).

In contrast to the prior mentioned second direction that is conducted by the movement of the carrier, TLS devices incorporate a second movement of the head of the system, which allows several accurate profile measurements around the vertical axis of the scanner.

2.2.4 Propagation of laser light in the atmosphere

In section 2.2.2 it is assumed that laser light is emitted with light velocity in a vacuum and the laser light itself is lying in one frequency, which is apparently not the case in real world applications (BERALDIN et al., 2010). Additionally, laser light is not perfectly collimated and shows widening effects that need to be taken into consideration, as well as every laser scanning device using certain angular steps between each laser beam that shape the final resolution.

Unlike conditions in a vacuum, the propagation of laser light is influenced by atmospheric conditions, like temperature, pressure and humidity. In addition, the laser beam consists of a thin group of frequencies and thus is not perfectly monochromatic. For an accurate determination of the group velocity c_{Gr} , which is necessary to estimate ranges, the velocity of light c_0 needs to be altered by an atmospheric index n_{Gr} (JOECKEL et al., 2008):

$$c_{Gr} = \frac{c_0}{n_{Gr}} \quad (\text{eq. 2.5})$$

This atmospheric index is set in relation to standard atmospheric conditions and includes the gaseous composition (CO₂: 0.03%), the amount of water vapour pressure (0), the temperature (0°C), the pressure (1013.25 hPA) and the frequency of the signal. It is derived by a *Cauchy* sequence (JOECKEL et al., 2008):

$$n_{Gr} = \left(A + 3 \frac{B}{\lambda_{eff}^2} + 5 \frac{C}{\lambda_{eff}^4} \right) \times 10^{-6} \quad (\text{eq. 2.6})$$

where A, B and C are constants derived in the laboratory and λ_{eff} is the effective wavelength. Several versions for the constants are available. The atmospheric index needs to be adjusted to contemporary atmospheric conditions n_L during the measurements:

$$n_L = n_{Gr} \left(\frac{273.15 p}{1013.25 T} - \frac{11.27}{T \cdot e} \right) \times 10^{-6} \quad (\text{eq. 2.7})$$

where T is the temperature, p is the pressure and e is the partial pressure of the water vapor. This is particularly important for geodetic measurements and surveying. The error lies within millimetres for a distance of a kilometre (JOECKEL et al., 2008). For instance, a temperature change of 50°C results in a change correction of 50 ppm, which is an error of 5 mm for a range of 100 m. Hence, in extreme conditions and depending on the general accuracy of the laser scanners, it is necessary to apply the appropriate corrections by accurately measuring the atmospheric conditions.

Divergence of a laser beam

In addition to the previously described constraint of atmospheric effects on range determination, a single laser beam is also not perfectly collimated (BERALDIN et al., 2010). The propagation of a single laser beam as an optical, infrared wave can be described by a *Gaussian* beam (KOGELNIK & LI, 1966; SIEGMAN, 1986; FISCHER et al., 2008). The transversal profile of the beam is a *Gauss* curve, where the maximum of intensity is at the center of the beam and intensity decreases at each side, forming a bell-shaped curve. The diameter of a beam is thus defined as the *Gaussian* diameter, which is the radius of the beam at the

$1/e^2$ intensity, as depicted in Figure 2-12. Thus, this beam diameter describes a width, where 86.5% of the whole intensity is represented.

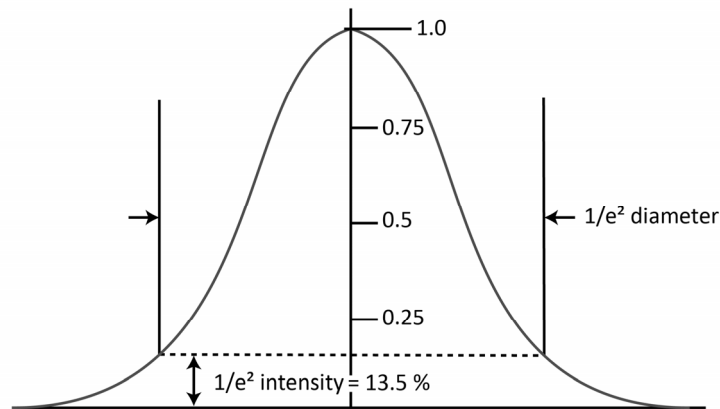


Figure 2-12: Intensity profile of a laser beam as a Gauss curve, modified after FISCHER et al. (2008).

For a *Gaussian* beam, as depicted in Figure 2-13, which propagates in free space and is focused by a lens, the beam radius $w(z)$ in the near field at a distance z is given by (FISCHER et al., 2008; BERARDIN et al., 2010):

$$w(z) = w_0 \left[1 + \left(\frac{\lambda(z-z_0)}{n \pi w_0^2} \right)^2 \right]^{1/2} \quad (\text{eq. 2.8})$$

where w_0 is the minimum radius at the beam waist, λ is the wavelength of the laser beam and n the refractive index. In addition, the beam faces the *Guoy* effect, which is a small phase-shift that affects every optical beam travelling through a focal region (SIEGMAN, 1986).

A further parameter to accurately describe a *Gaussian* beam is the range of the focus field b . b is determined as the range between the *Rayleigh* range z_0 in each direction from the beam's waist, where the beam is most intense:

$$\pm z_0 = w_0 \sqrt{2} \quad (\text{eq. 2.9})$$

The range between both points is the confocal parameter or depth of focus b , which is defined as:

$$b = \frac{2\pi n}{\lambda} w_0^2 \quad (\text{eq. 2.10})$$

Beyond the depth of focus, in the far-field, the divergence of the laser beam θ is given:

$$\theta = \frac{2\lambda}{\pi n w_0} \quad (\text{eq. 2.11})$$

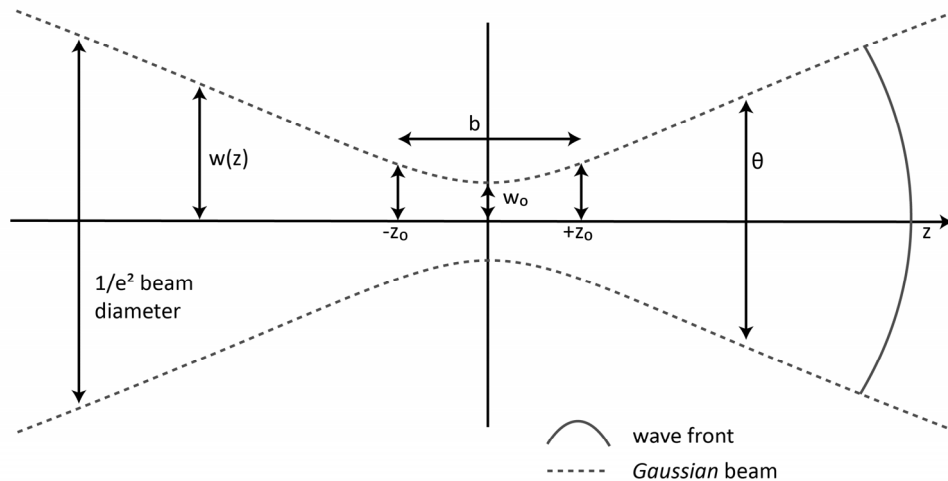


Figure 2-13: Dimensions of a Gaussian beam, modified after FISCHER et al. (2008).

This far field divergence or total angular spread is the beam divergence angle (BERALDIN et al., 2010). The divergence angle θ is given in milliradians (mrad), which is numerically equal to the corresponding length of an arc. For example, 0.25 mrad describes a laser beam that diverges with a diameter of 25 mm at a 100 m range. The following simple equation can be used to estimate the beam diameter d (in m) according to the range r (in m) by:

$$d = \frac{r\theta}{1000} \quad (\text{eq. 2.12})$$

This latter equation is used mostly for estimations of spot diameters in laser scanning, relying on the beam divergence given by the manufacturers. This is still the postulated size of the $1/e^2$ intensity irradiance contour (86.5 % of the whole intensity) and not the full beam divergence.

Theoretical resolution

The previously presented spot diameter of a single laser beam in a certain distance is one part of the theoretical resolution of a point cloud. The theoretical resolution in a distance perpendicular to the sensor further depends on the sample step width between each emitted laser pulse (Figure 2-14). In addition, the precision of each single laser measurement has to be taken into consideration.

Under- or over sampling occurs, when the chosen step width is smaller or larger than the beam diameter at a particular distance (BUCKLEY et al., 2008). For ALS and MLS systems this is an issue for the direction perpendicular to the moving direction. For 3D coverage, sampling rate and moving speed are crucial. For TLS measurements the step width of the moving head can result in this over- or under sampling.

The resolution can be verified by a test propagated by BOEHLER et al. (2003), who used a modified Siemens-Star for image accuracy, as a 3D resolution test for terrestrial laser scanning. However, this theoretical resolution at a given distance is of course not suitable for real surveying, where objects are in various distances, have a surface structure and are tilted in some direction. As a result, irregular spot patterns arise in an unstructured point cloud.

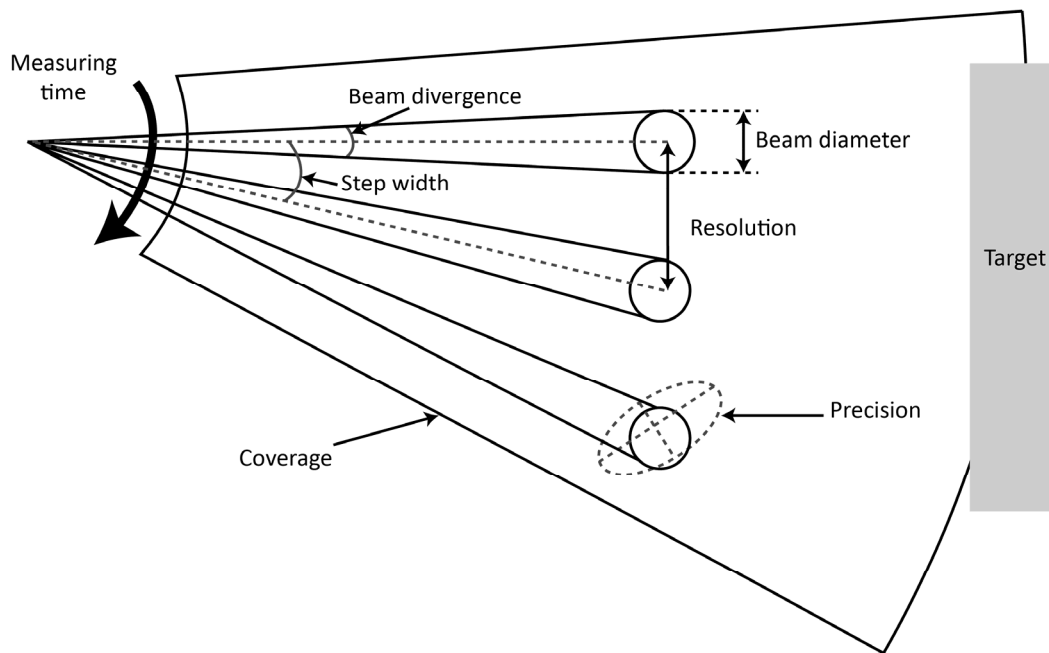


Figure 2-14: Resolution of the laser scanning method considering of step width, beam divergence and precision dependent on range, modified after KERN (2003).

2.2.5 Beam reflection and detection

The emitted beam is reflected by distant objects, which involves various reflection effects and a weaker reflected signal is detected and recorded according to specific system probabilities (PETRIE & TOTH, 2009a). The strength of target reflection depends on several factors, like the surface roughness in relation to the wavelength and the incident angle (LILLESAND et al., 2008). Reflection geometry ranges between the ideal specular reflection and the ideal diffuse reflection (*Lambertian*) (Figure 2-15). Most surfaces are diffusive reflectors, which leads to a perpendicular reflection to the incident angle. However, specular reflection can also occur, like on calm water, glass or icy surfaces under certain angles, which leads to gaps and noise (PETRIE & TOTH, 2009a).

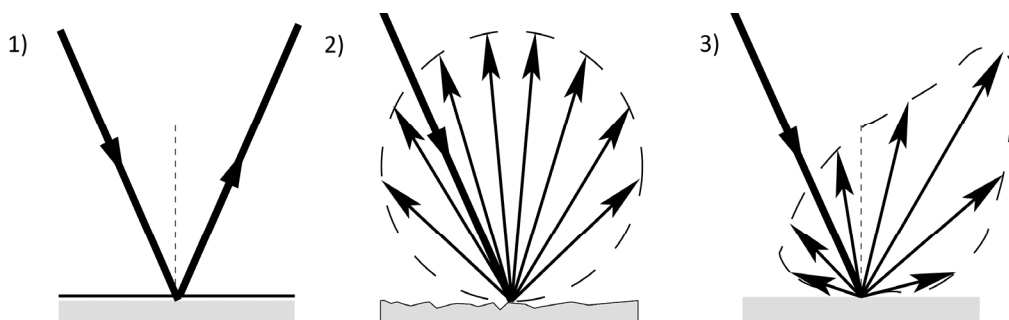


Figure 2-15: Reflection effects on different surfaces. Ideal specular (1), ideal diffusive (2) and mixed reflection (3), modified after KERN (2003).

The reflective characteristics of the target vary with the wavelength of the incoming laser beam (WEHR & LOHR, 1999). Reflectivity values of various objects for a typical wavelength of laser scanners are shown in Table 2-6. Most natural targets, like soils or trees show a reflectivity below 50%.

Table 2-6: Typical reflectivity of different material for 900 nm wavelength (WEHR & LOHR, 1999).

Material	Reflectivity [%]
Dimension lumber	94
Snow	80-90
White masonry	85
Limestone, clay	>75
Deciduous forest	~60
Coniferous forest	~30
Carbonate sand (dry)	57
Carbonate sand (wet)	41
Beach sands, bare areas in dessert	50
Rough wood pallet (clean)	25
Concrete, smooth	24
Asphalt with pebbles	17
Lava	8
Black neoprene (synthetic rubber)	5

Concerning the beam divergence described in chapter 2.2.4, edge effects may occur that are a consequence of objects smaller than the theoretical footprint at a specific position (HEBERT & KROTKOV, 1992; ADAMS & PROBERT, 1996; LAMBROU & PANTAZIS, 2010). Thus, a mean range is calculated, which is considerably different to the exact range of the edge. Systems, which are capable to record several echoes or the full-waveform of a reflected beam are able to distinguish between several nearby objects. Without that property they would only be able to distinguish between surfaces that are separated by more than half of the pulse length. Otherwise, the mentioned effect, known as mixed-pixels, occurs. This effect can be minimized by incorporating specific model approaches (TANG et al., 2009).

Targets

For registration purposes artificial targets are used particularly for TLS. Depending on the type of laser scanner these targets can vary. For example spheres, cylinders, paddles, paper targets and flat retroreflectors can be employed (LICHTI, 2010; LICHTI & SKALLOUD, 2010; BECERIK-GERBER et al., 2011). Some of these are adhesive or magnetic, paper targets are printable, and spheres, and cylinders can be installed on tripods or similar equipment. The targets are usually oversampled to estimate the centre of the specific type of target. In addition, the targets show a strong contrast or are painted or covered with a highly reflective material. The estimated coordinate of the targets can be measured by a second device (e.g. by tachymetry or DGPS) and the measured coordinates can be used to compute translations and rotations. Two effects are related to highly reflective targets, which are walk and blooming. The walk effect is defined as a trail of points before or behind a target, resulting from the energy received, exceeding the range of the detector. The blooming effect occurs surrounding a target, where the reflection of the target itself overburdens the surrounding material. Thus, the targets appear to be bigger (LICHTI & SKALLOUD, 2010).

Detection and recorded echoes

For all sensors, the detection of the reflected laser beam in laser scanners is most commonly facilitated by Avalanche Photodiode Detectors (APD) (WEHR, 2009). The signal is usually very weak and is thus amplified prior to recording. After WEHR (2009) and BERARDIN et al. (2010), three detection methods for peaks exist:

- General peak detection: one trigger pulse is set at the maximum received peak, which can get problematic, when several peaks of equal value appear.
- Threshold or leading edge detection: the trigger is set at the first and often the last rising edge of the echo, which is determined by the manufacturer.
- Constant fraction detection: the trigger is activated when a preset amplitude fraction is met.

In general, recent laser scanners are able to record several discrete echoes of the reflected laser beam, usually the first and last pulse (BALSAVIAS, 1999a). A single laser beam is able to penetrate through vegetation. Thus, several reflection peaks can be detected (Figure 2-16). However, these can only be determined, when the distance between both objects is at least half of the pulse's length. For example, a typical pulse width of 1 ns separates minimum distances of 0.075 m (BERARDIN et al., 2010).

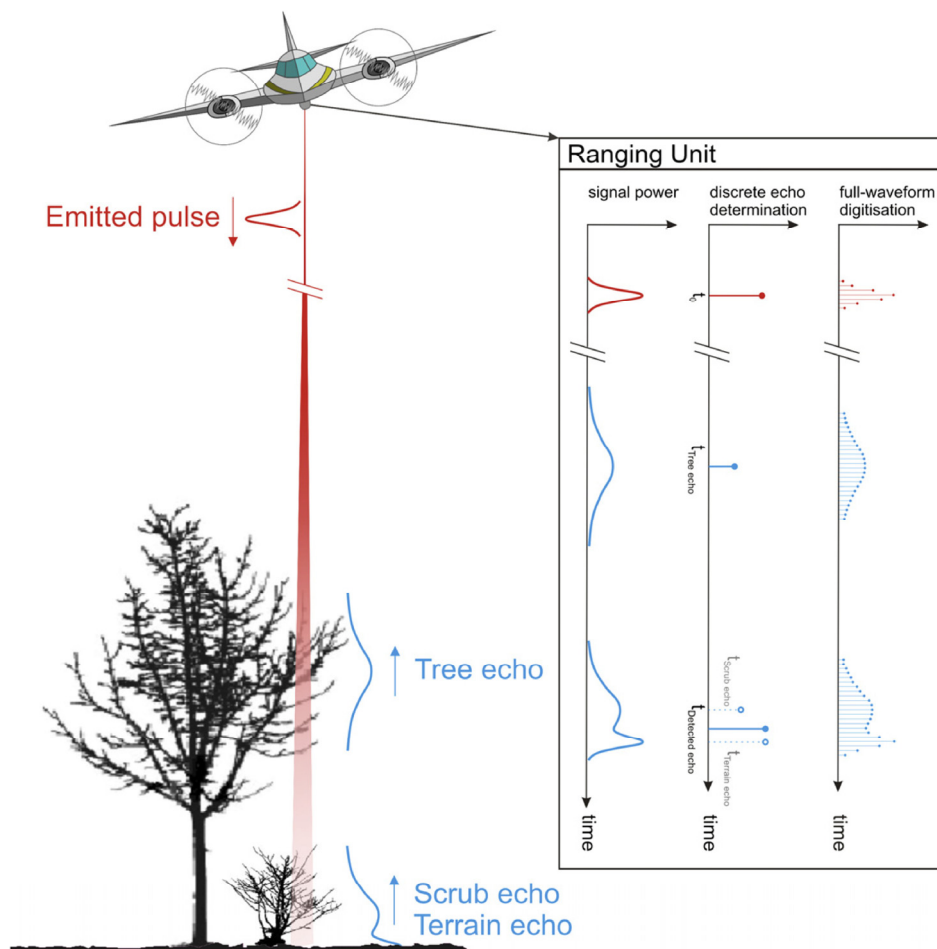


Figure 2-16: Comparison of full-waveform recording and discrete echo determination (DONEUS et al., 2008).

Full-waveform

More recent TOF-devices are able to record the full-waveform of each laser beam (Figure 2-16). The time-varying power of the entire reflected signal is recorded until a surface is reached, which cannot be penetrated (MALLET & BRETAR, 2009). This new function has an enormous advantage for vegetation detection (KOETZ et al., 2006; DUONG et al., 2008; HYYPPÄ et al., 2008) and for the removal of vegetation for instance for DEM extraction and archaeological prospection in forested areas (DONEUS et al., 2008). Usually, the signal is decomposed into *Gaussian* functions and their echo width, amplitude and the overall number of returns is usable for segmentation purposes (WAGNER et al., 2006). ALEXANDER et al. (2010) use a backscatter coefficient, estimated by echo amplitude, echo width and object range and show promising results for land cover classification of urban areas.

Intensity

Most sensors are capable to record the strength of the deflected signal, which is a value of the reflectance of the target and is recorded as amplitude or also called as the intensity value (BERALDIN et al., 2010). Intensity images show the relative reflectivity at a specific wavelength of the laser (monochromatic image). However, this intensity value is influenced by range, instrumental and atmospheric effects, the target backscatter and emission, as well as the measurement geometry (KAASALAINEN et al., 2011). Thus, it needs radiometric corrections (HÖFLE & PFEIFER, 2007; HÖFLE, 2014) or an in-situ radiometric calibration with reference panels (KAASALAINEN et al., 2009; WUJANZ, 2009; EITEL et al., 2011). Intensity is useful for the classification of objects, e.g. for outcrop modeling (BURTON et al., 2011), land use detection (ANTONARAKIS et al., 2008; MESAS-CARRASCOSA et al., 2012; YAN et al., 2012) and particularly for automatic segmentation purposes (WUJANZ, 2009).

As an example, one of the earliest tests with the laser scanner used in this contribution is depicted in Figure 2-17, showing a gray scaled 2D image of the recorded data. Objects that are within the minimum range are coloured in blue (1), as these are not recorded. The high contrast of the different surfaces is visible at several areas (2, 3) and noise is detectable (4). Specular reflection, as denoted before, occurs at a perpendicular, metallic surface (5).



Figure 2-17: Gray-scale 2D intensity image, depicting the contrast (2,3), noise (4) and specular reflection (5). Blue colors (1) assign areas not recorded. Recording date: 22/11/2007.

2.2.6 Systematic errors

Error sources in laser scanning can be divided into systematic, external, and registration errors. Systematic errors exist as a consequence of imperfections in manufacturing and assembly of the complex systems. Atmospheric effects (section 2.2.4) and backscattering effects (section 2.2.5) are summarized as external errors. In the following, systematic errors are described.

Systematic error sources are based on the range measurement itself, errors in the horizontal and vertical direction and polygonal mirror errors (LICHTI et al., 2005; GLENNIE & LICHTI, 2011; LICHTI et al., 2011). All errors are detectable by comparing laser scanner readings to tachymetric surveying observations of calibration fields. The comparison of these measurements allows the establishment of (statistical) models for correction. Thus, calibration deals with all the systematic error sources of laser scanning systems and uses models to improve measurement quality.

As shown in Figure 2-18, several axes are incorporated in laser scanning devices, which are not perfectly aligned. The vertical axis, the horizontal or trunnion axis, and the collimation axis, which is the axis of the emitted laser beam, are shifted slightly off the orthogonal in random directions. In addition, the reflection mirrors have imperfections, as well as the range measuring unit (the amplifiers, oscillators, etc.) (LICHTI & SKALOU, 2010).

As stated before, models exist that consider all probable errors. For instance, an additive constant, a scale error, a vertical offset, as well as internal optical errors and electrical interferences have to be considered for range errors. The relative offset of the laser axis to the trunnion axis for a CW-scanner (e.g. Faro 880) shows an 8 mm inaccuracy depending on the vertical angle (LICHTI, 2007). Similar errors exist for the horizontal and vertical directions of the measurements; in particular the wobble of the axes is incorporated in calibration equations. For several laser scanners similar error models were derived, mostly enhancing the same amount of inaccuracy (SCHNEIDER, 2009; RESHETYUK, 2010; GONZALEZ-AGUILERA et al., 2011b; GARCÍA-SAN-MIGUEL & LERMA, 2013).

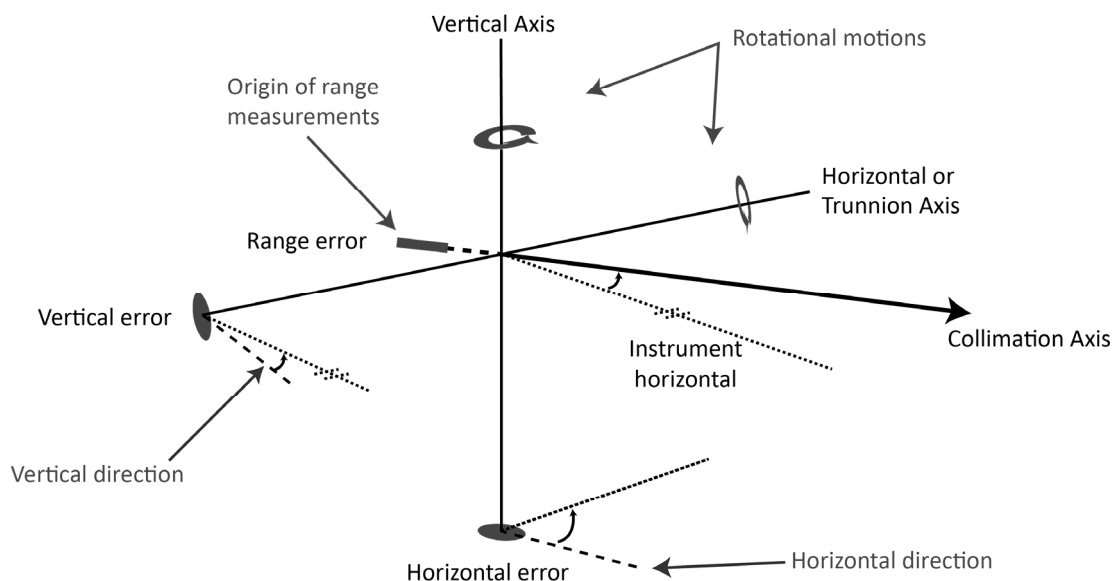


Figure 2-18: Geometric model of a laser scanning device and possible errors assigned by dark grey areas.

2.3 Laser scanning campaigns

Laser scanning campaigns involve several steps before promising results are achieved (CHARLTON et al., 2009). Starting with the formation of the overall objective, logistical issues, detailed planning particularly regarding scan positions, safety, weather, and further issues have to be considered. Several elements need to be considered in order to define an exact objective. Besides the point density, accuracy, and the size of an area or object, also the measurement output and processing result, such as 3D models or 2D maps have to be taken into account. Logistical tasks concerning general field survey issues also have to be part of the survey planning, such as transport, permissions, customs, batteries and electrical power supply, and file backups. In all circumstances, the safety of the surveying personal is important (CHARLTON et al., 2009).

Therefore, thorough inspection of the survey area is a very important step (BUCKLEY et al., 2008; RÜTHER et al., 2012). The optimal, possible scan positions should be selected with regard to the complete coverage and the minimum amount of scan positions, as well as a certain overlap. The scanning device needs installed securely, considering wind, precipitation and vibration. Furthermore, obstacles need to be taken into account, as well as resolution, accuracy and ranges. In addition, registration and georeferencing tasks need to be kept in mind. The method chosen for merging or georeferencing is critical for the choice of reflecting targets as well as geodetic determination of these targets, when necessary. The targets need to be placed in such a way that enough of them (> 3) are visible in at least two overlapping point clouds. In addition, fixing those targets is not always allowed (CHARLTON et al., 2009).

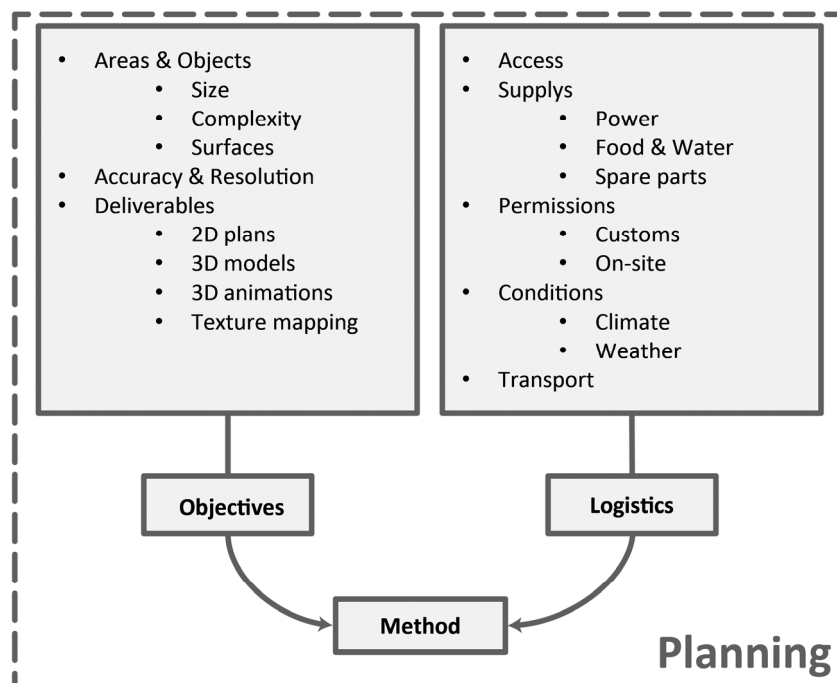


Figure 2-19: Issues for laser scanning campaigns.



Figure 2-20: Examples of MLS (1) and ALS (2) systems. MLS picture from 2009, showing the complexity of these systems that uses here two laser scanning and camera devices (Picture: C. Curdt). Newer systems are much smaller. ALS picture shows the MetAir Dimona, which was successfully applied in a campaign in the year 2008 (Picture by Jörg Hacker ARA/MetAir).

Further issues need to be solved for ALS and MLS surveys. Particularly, safety and permissions play an important role in the planning process (BERALDIN et al., 2010; KUTTERER, 2010). Besides the aircraft or helicopter or any vehicle, necessary additional components are the GNSS antenna and receiver, the IMUs, complementary digital cameras, an operation laptop, a flight management system or navigation system and a controlling and recording unit. The latter is synchronising and controlling the whole system, as well as recording all data, which requires up to 20 GB hard disk space per hour. Additionally, DGPS calculations are necessary to enhance the recorded GNSS data, which is possibly supplied by a further GNSS ground station or according correction services (BERALDIN et al., 2010). Further cameras are mostly mounted as a control and for visualization purposes. As an example, an ALS and MLS system are shown in Figure 2-20.

2.4 Post-processing of laser scanning data

All the steps that are necessary to process the raw data and generate results are summarized in this chapter on post-processing. The results are manifold, ranging from simple range and distance measurements, 2D plans and maps, to sophisticated 3D animations. Basically, post-processing can be subdivided into stages of data preparation (section 2.4.1), registration (section 2.4.2) and processing (section 2.4.3), leading to accurate point clouds that are used in various applications (section 2.5). In contrast to the acquisition process, the post-processing is more time-consuming and is heavily dependent on the project goals and the experience of the operator (CHARLTON et al., 2009). In the following, the individual stages involved in post-processing will be described in detail.

2.4.1 Data preparation and visualization

First of all, the data collected during the laser scanning survey has to be renamed, stored, copied and archived (CHARLTON et al., 2009; GRAHAM, 2009). This step also involves various additional data, like DGPS or tachymetric measurements, protocols of the surveys or captured digital images. All these data need to be prepared for post-processing. For example, coordinates for georeferencing purposes need to be transformed or adjusted and digital images might need colour balancing or contrast enhancements. Afterwards, points can be assigned with according RGB values or derived 3D surfaces can be texturized by these images (JOECKEL et al., 2008).

Basic visualizations of all or some of the points are already possible in different colours, for example true colours derived by additional RGB capturing, intensity values, heights or ranges (Figure 2-21). The points are handled as primitives by standard graphic APIs such as DirectX or OpenGL and allow further characteristics for each primitive, like size and colour (VOSSELMAN & KLEIN, 2010). Important for a fast visualization are pre-processed point normals and the z-buffer algorithm for the computation of occlusions (VOSSELMAN & KLEIN, 2010). Basic measurements, like distances between points can already be fulfilled in the unstructured point clouds of single scan positions.

Besides proprietary formats of the different vendors, laser scanning data is typically handled by ASCII data sets using the TXT file extension or alternatively in the LAS data standard (ASPRS, 2009; GRAHAM, 2009). Furthermore, the ASTM E57 format is currently being developed and can handle more extensive

metadata (HUBER, 2011). Derived 3D objects are usually interchanged in OBJ- or STL-format or accordingly in CAD-formats, like DWG or DXF.

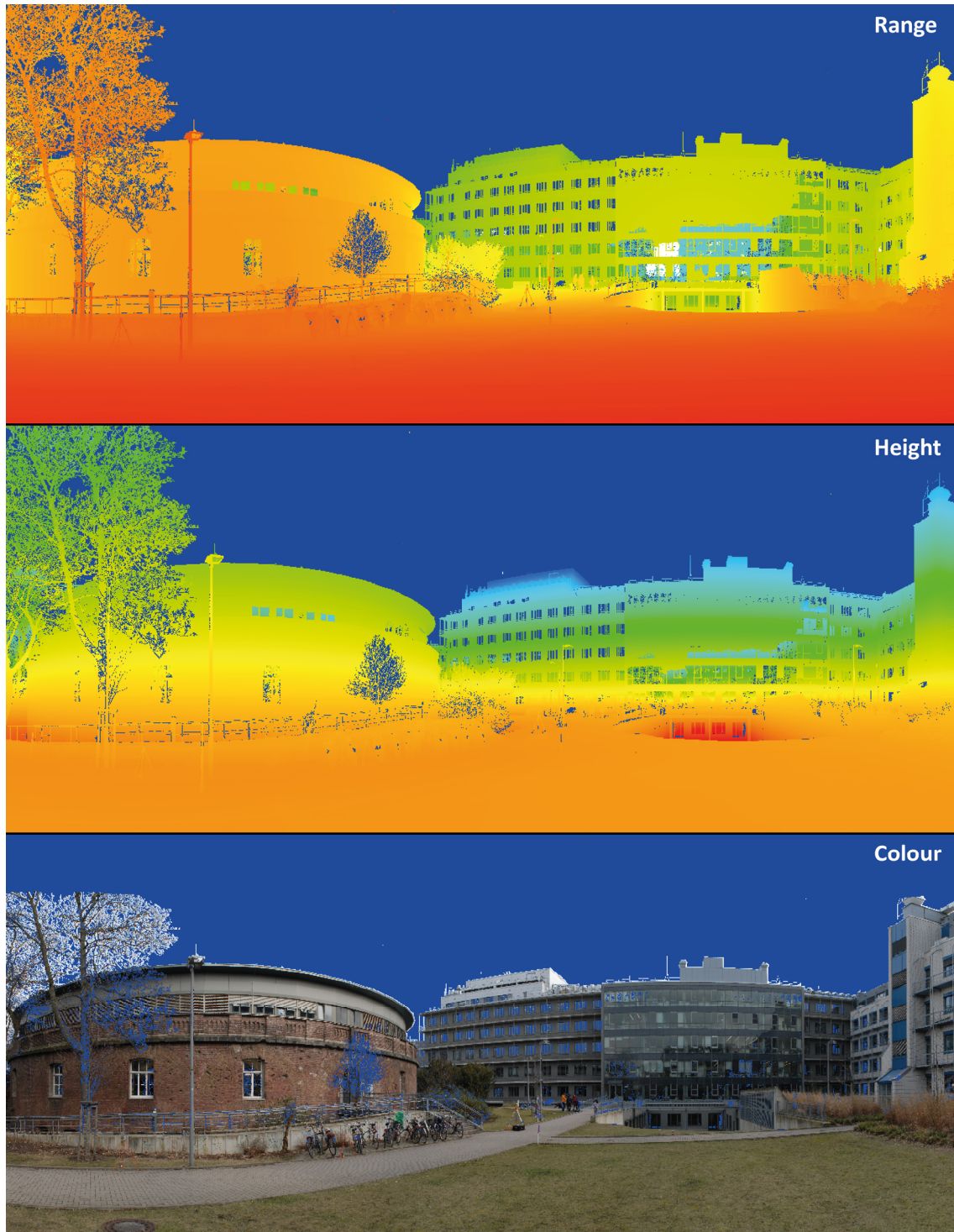


Figure 2-21: 2D images with different colourizations (relative range, relative height and RGB true colour) of points. Range and height are calculated according to the position of the laser scanner, from near/low in red to far/high in blue. The blue colour also depicts areas that are not recorded, due to noise, extent or specular reflection effects.

2.4.2 Registration

For further processing, the most important step is the registration process to achieve a consistent point cloud measured by different scan positions. Registration comprises the transformation of the acquired data from one coordinate system into another, e.g. several scan positions can be transformed into a single, consistent system and additionally into a geodetic system. Point clouds from a single scan are usually in a right-handed Cartesian coordinate system, where the laser beam output point is the origin (LICHTI, 2010; LICHTI & SKALLOUD, 2010). One translation and rotation is necessary for each scan position and a second transformation is needed, when the data has to be integrated into a geodetic system. The transformation parameters are usually estimated by a spatial similarity transformation or 3D-Helmert transformation. For this purpose, seven parameters are necessary, three of which are for translation with regard to the origin, three for the rotation around the coordinate axes and one for scale. The parameters are derived differently, but mostly by similar points of two different systems. The whole registration process is an important step, which needs to be recognized in the planning, surveying and post-processing. The overall accuracy of the whole project is the result of these steps (RÜTHER et al., 2012).

Generally, the registration is concerned with the estimation of parameters for the related transformation of the whole point cloud (LICHTI & SKALLOUD, 2010). For ALS and MLS approaches, INS data and GNSS positions are incorporated to obtain the orientation of right-handed frames (2D lines). All relations between the sensor, the INS, the GNSS antenna (section 2.1.1) and the carrier system need to be described accurately to solve the different translations. Every of these items can lead to errors for the final derivation of a 3D coordinate (PETRIE & TOTH, 2009b; WEHR, 2009).

For TLS point cloud registration, several direct and indirect registration opportunities exist, depending on the equipment, accuracy requirements and task (DOS SANTOS et al., 2013). Direct registration means that the position and orientation of the scanner is directly determined (Figure 2-22). This is possible by setting up a scanner like a total station in a levelled position above a known survey point. Modern scanning devices can be equipped with inclination sensors for an easier set up (SILVIA & OLSEN, 2012).

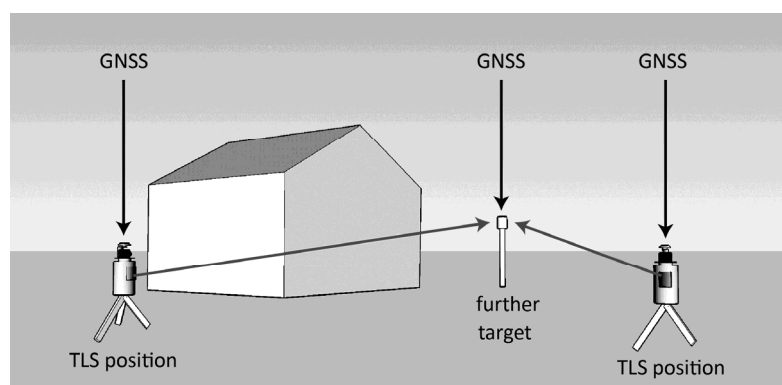


Figure 2-22: Possible direct georeferencing approach by GNSS position determination of the TLS and one further object for orientation.

As a further approach, the position and orientation of the laser scanner can be directly measured by DGPS and tachymetric surveying, whereas a target or a DGPS receiver is being mounted in relation to the laser scanning device. The orientation of the point cloud can be estimated by measuring one further target in a high oversampled resolution (MÅRTENSSON et al., 2012) or at least by a direction reading from a compass (RÜTHER et al., 2012). As a more sophisticated approach, two DGPS receivers and their circular measurement that is achieved by the scanner's movement can be used to estimate the central position (MOHAMED & WILKINSON, 2009; VENNEGEERTS et al., 2009).

Indirect registration can be conducted with overlapping point clouds and according algorithms that derive a best-fit approximation of the registration parameters (LICHTI & SKALLOUD, 2010). Usually, similar, manually selected points of two adjacent scan positions are used to retrieve a first rough registration that is enhanced by certain algorithms. As a more accurate approach, targets are applied for registration (cf. section 2.2.5), as depicted in Figure 2-23. At least four similar targets (or tie points) derived from two or more scan positions are required for a cloud to cloud registration. These targets are fine-scanned, with the highest resolution and the coordinates are measured with a high accuracy. The targets can be planar targets, which may be of a highly reflective surface, or geometric primitives, mostly spheres. All are designed to determine the centre with great precision. These targets can be measured additionally by a totalstation or DGPS solutions for an accurate translation to national grids (ENTWISTLE et al., 2009).

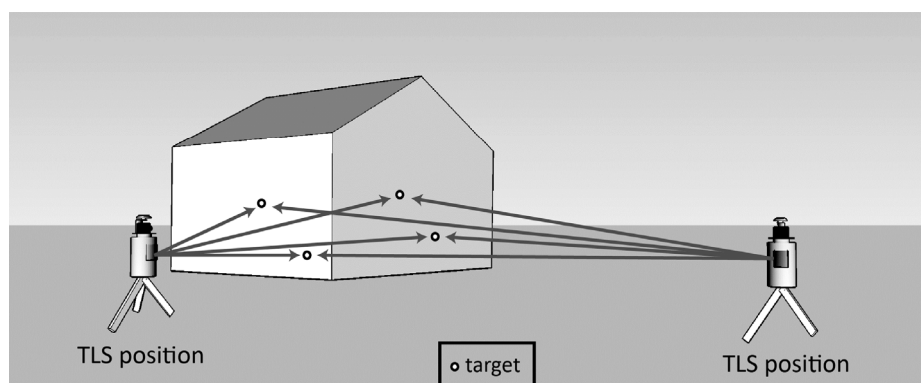


Figure 2-23: Principle of indirect registration, where several identical targets are recorded from each scan position. For georeferencing these targets need according coordinates.

These first and partially rough estimations of point cloud registration can be enhanced by algorithms that are capable of merging point clouds. These approaches can be divided into iterative closest point methods and feature-based registrations (GRANT et al., 2012). The ICP-algorithm (Iterative Closest Point) is the most popular algorithm, based on the work of BESL & MCKAY (1992). The registration of approximately registered point clouds is enhanced by iteratively searching the closest points of similar regions until the Euclidean distance is within a threshold, whereas a transformation is conducted in every step (KRAUS, 2004). At the same time, a further algorithm was developed, where a surface is used as the master fitting area (CHEN & MEDIONI, 1992). This approach is generally faster. Further approaches based on these methods are for example, the incorporation of objects (BAE & LICHTI, 2008; BAE, 2009), Triangulated Irregular Network (TIN) least square matching (MAAS, 2000), as well as least square surface and curve matching (GRUEN & AKCA, 2005).

2.4.3 Processing of point clouds

The primary goal of laser scanning is the generation of models that represent features of the Earth. Generally, two options for establishing 2D or 3D models out of the point clouds exist that involve either an iconic or a symbolic processing (BRENNER, 2008). Iconic processing, as a data driven approach, is the direct use of 3D points. In contrast, the symbolic interpretation is a model driven approach, using the data for reconstruction of primitives that fit partially into the point cloud. The symbolic reconstruction can be conducted manually, normally in Computer Aided Design (CAD) software but automatic algorithms are also available (LINDENBERGH, 2010). For all purposes, cleaning of the point clouds is one important step, as it is mostly conducted manually. In particular, for TLS point clouds only some of the existing filters are actually helpful (RÜTHER et al., 2012). For this step, the Area of Interest (AOI) needs to be regarded. Likewise, a calibration or correction of the derived intensity information is necessary (HÖFLE & PFEIFER, 2007; HÖFLE, 2014).

A typical iconic processing result is a 2.5D representation, where additional information is assigned to each 2D coordinate cell of a raster (VOSSelman & Klein, 2010). This 2.5D representation is of importance due to the available amount of image processing methods, but is associated with data loss, in particular regarding multiple surfaces of complex objects derived from MLS or TLS (VOSSelman & Klein, 2010). The 2.5D representation is derived by binning, interpolation or the setting up of TIN surfaces. Binning simply uses the mean, median, lowest or any other simplification rule of point values in a certain previously set cell size. Interpolation methods are able to statistically derive surfaces and are able to fill gaps, whereas the interpolation varies from simple (e.g. Inverse Distance Weighting, IDW) to sophisticated geo-statistical analysis, like kriging (BRUNSDON, 2009). Triangulation produces TINs from the unstructured point clouds for a meshed, closed surface. The most popular possibility is the *Delaunay* triangulation, which relies on the assumption that no further point lies within the circumference of any derived triangle (VOSSelman & Klein, 2010). However, a 2D data structure is assumed for this method. Thus, every triangulation process of this type considers a plane, usually the XY-plane (VOSSelman & Klein, 2010). A further triangulation method, which establishes water-tight surfaces of 3D objects is the Poisson surface reconstruction (KAZHDAN et al., 2006). Those operations all result in polygonal meshes, which are a popular representation of 3D objects (CAMPBELL & FLYNN, 2001). The vertices or edges of all triangles are stored. Objects that are smoothed surface approximations can be called free-form objects, which are compact descriptions of complex objects. These objects can be stored as Non-Uniform Rational B-Splines (NURBS), which are an industrial norm for surfaces, as they are mathematically defined and compressed. Usually, NURBS are applied in modelling approaches of automotive parts, but any other surface can also be modelled (FOLEY et al., 1999; HARING et al., 2003).

Irregular objects and objects with uncommon characteristics need manual processing. This is supported by numerous functions in specific programs. In preparation mainly for automatic or semi-automatic visualization, registration, segmentation, and modelling purposes, an unstructured point cloud has to be structured (VOSSelman & Klein, 2010). For this purpose and enhanced, faster representations of point clouds, octree or k-D tree algorithms are used (ELSEBERG et al., 2013).

Hence, an automatic segmentation of point clouds, which is the sorting of points according to a specific criterion, such as spatial coherence, is possible. The segmentation enables to extract information, and can be used to automate or support, modelling, registration and filtering (VOSSelman & Klein, 2010). In

all these approaches, noise, point density and associated thresholds are of major importance. All methods are interchangeable and show constant enhancements. For instance, the important *Hough* transformation enables the detection of 2D lines and has been extended to 3D lines, planes and cylinder detection. Basically all points are transformed in a parameter space (or *Hough* space), depending on the angle and distance to a predefined origin. The most common angle and distance of all points is found and all points fitting to these parameters are set as a line (BRENNER, 2008). Furthermore, the well-known Random Sample Consensus algorithm (RANSAC) uses the paradigm of minimum points to define a geometry (FISCHLER & BOLLES, 1981). The algorithm randomly chooses minimal subsets and considers the model derived from each subset that has the greatest number of inlying points as the final result. The surface growing method is an extended version of the 2D region growing approach from image processing, which groups points that are homogenous. The process starts with seeding randomly points that are initially estimated to be similar by the previous mentioned methods of *Hough* transformation or RANSAC. In a second step, points are tested to fit to the initially found surfaces and the surface is extended (VOSSelman & KLEIN, 2010).

2.5 Applications of laser scanning

Common applications of laser scanning that use the previously stated methods and algorithms are presented in this section. As stated earlier, ALS is nowadays a standard method for the acquisition of topography, in particular for surveying and mapping agencies (PETZOLD et al., 1999). For this purpose, point clouds are filtered and processed to derive Digital Elevation Models (DEM) or Digital Terrain Models (DTM) that represent the bare-earth and accordingly Digital Surface Models (DSM), which represent the top surface including vegetation and buildings (PFEIFER & MANDLBURGER, 2009). As depicted in Figure 2-24, the difference between both models (DSM, DTM) is a normalized DSM (nDSM), which is sometimes called Canopy Height Model (CHM) in forestry applications (HYYPÄ et al., 2009). In the case of data derived from a dense point cloud, particularly from TLS, a High-Resolution Digital Elevation Model (HRDEM) with a resolution of less than 20 cm is established (NGUYEN et al., 2011). All models represent important input data for further processing, combination with other data, and visualization purposes of Geographical Information Systems (GIS) (BILL, 1999).

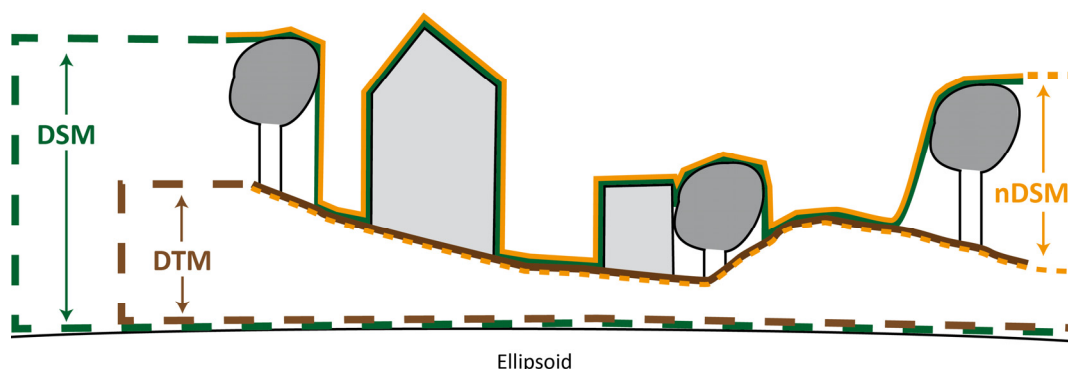


Figure 2-24: Schematic description of different elevation models. A nDSM is also called CHM in forestry applications, modified after STEINLE (2005).

For the purpose of distinguishing between terrain and off-terrain points and finally to derive DTMs and DSMs, several filters are available (KRAUS & PFEIFER, 1998; SITHOLE & VOSSelman, 2004). Besides simple binning filters, morphological filters, progressive densification, surface-based filters and segment-based filters also exist. All of them employed statistical analyses on the points. The filter algorithms showed different results in complex areas with high buildings or challenging topography in a comparison by SITHOLE & VOSSelman (2004). The exploitation of intensity values and the recording of the full-waveform might solve the problem to distinguish between the points. Additionally, other sensor data like multispectral satellite images are used for this purpose (PFEIFER & MANDLBURGER, 2009). Structure line derivation for the accurate representation of break lines in DEMs is also considered by filter algorithms (BRIESE, 2010).

The derived data can be used for automatic building extraction from all sensors, which is achieved by the previously mentioned general segmentation approaches and additional algorithms (BRENNER, 2010). In addition, these algorithms are distinguishable in model and data driven approaches. Several issues and constraints need to be considered in this area, for instance the difference between trees and roofs (FORLANI et al., 2006; LAFARGE et al., 2008). Again, the full-waveform sensors deliver promising new information for that purpose (HÖFLE et al., 2012). Furthermore, automatic facade reconstruction algorithms from MLS and TLS data have already been presented in several publications (BECKER & HAALA, 2008; PU & VOSSelman, 2009; ZHU et al., 2011; MARTÍNEZ et al., 2012; AIJAZI et al., 2013; YANG & DONG, 2013).

Monitoring of man-made structures (CHMELINA et al., 2012; CHOW et al., 2012; HAN et al., 2013) and the accurate modelling of industrial sites, which lack actual plans, are a further field of application (LINDENBERGH, 2010; GONZALEZ-AGUILERA et al., 2012). Automatic algorithms exist, which are capable to model an entire industrial scene (RABBANI et al., 2007).

Besides the previously mentioned derivation of DEMs, city models, and inventory of industrial sites, several further important applications exist that are presented in the following. Forestry is one major research area that deals with ALS and TLS data. Conventional intensive fieldwork is conducted to count trees, measure the height of trees, and the diameter at breast height to estimate timber volume (MAAS, 2010). This kind of fieldwork is expensive and inaccurate and demands for automatic remote sensing approaches. Beside the market value of timber, the accurate estimation of stand-wise or tree-wise parameters is important for the global carbon cycle, habitat determination and for the protection against natural hazards, like rock fall, slides, avalanches and fire risk assessment (LEFSKY et al., 2002; MORSDORF et al., 2004; LEFSKY et al., 2005; HYYPPÄ et al., 2008; NAESSET, 2009; KAARTINEN et al., 2012). Stand-wise estimations usually incorporate geostatistics on CHMs. Tree-wise methods use sophisticated algorithms on dense point clouds to derive the position of each single tree and its associated attributes. In addition, full-waveform data delivers promising results (REITBERGER et al., 2009). Terrestrial applications actually allow denser point clouds with a different perspective for a detailed geometric description and reconstruction of single trees (HENNING & RADTKE, 2006; HOSOI & OMASA, 2006; CLAWGES et al., 2007; BELAND et al., 2011; CÔTÉ et al., 2012).

A further research area that deals with extensive, inaccurate fieldwork and inaccuracies is fluvial geomorphology. The derivation of surface grain size is important for the estimation of channel bed roughness and sediment transport estimation (HERITAGE & HETHERINGTON, 2007; HERITAGE & MILAN, 2009;

HOHENTHAL et al., 2011; BAEWERT et al., 2013). In addition, multi-temporal approaches allow to document changes in the fluvial environment (RESOP & HESSION, 2010).

Multi-temporal approaches by TLS are also an important method for the determination of landslides (TEZA et al., 2007; TEZA et al., 2008; AVIAN et al., 2009), rockfalls (RABATEL et al., 2008; ABELLÁN et al., 2010; ABELLÁN et al., 2011; NGUYEN et al., 2011) and glacier change (KELLER et al., 2007). In addition, ARMESTO et al. (2009) investigated the stability of a large granite boulder in order to estimate the hazard of mass movement. Furthermore, digital outcrop modelling allows the visualization and easy measurement of thickness and orientation of sedimentological units (BUCKLEY et al., 2008; MCCAFFREY et al., 2008). Complementary hyperspectral imaging enables automatic classification of these units (KURZ et al., 2011). A combination of high resolution topography achieved by TLS measurements and subsurface data enables new insights into geomorphologic processes of dolines (SIART et al., 2013). WIATR et al. (2013) introduce TLS measurements for a paleostress analysis of a fault scarp.

Overall, very different applications exist that deal with the accuracy of laser scanning and therefore with large amounts of data. Thus, a huge amount of research is conducted in the stated processes of structuring, segmentation, and automation to ease workflows. However, the broad spectrum of the application of laser scanning as remote sensing method is obvious. Further, very important application examples that are missing here are presented in the respective case studies of coastal geomorphology (chapter 4), agronomy (chapter 5) and geoarchaeology (chapter 6).

3 The general method

In this chapter, the specific method used in this contribution is described in detail. The description of the main components, the laser scanner (3.1) and the RTK-DGPS system (3.2), is followed by an explanation of the combined method of direct georeferencing (3.3). The usual field work regarding this particular method is described in section 0. Resulting general post-processing steps are depicted in section 3.5.

3.1 The laser scanner: Riegl LMS-Z420i

The laser scanner LMS-Z420i from Riegl, Austria was used in this contribution. It applies the time-of-flight principle (Riegl LMS GmbH, 2013a). The main characteristics are shown in Table 3-1. The device, shown in Figure 3-1, is delivered with a bigger, removable base frame, the tilt mount, which is capable to tilt the whole device from -90° to $+90^{\circ}$ in 5° -steps. The main scanner consists of a solid part, onto which a single handle bar can be attached, when the tilting mount is not used. The moveable head contains the polygonal mirror to deflect the laser beam. An optional digital camera is mountable on the scanning device, as well as a DGPS receiver. The laser scanner is controlled by a laptop and powered by a larger battery. The laser scanner uses a rotating polygonal mirror, which allows measurement rates of up to 11,000 pts./sec. In addition, the head of the laser scanner is moving around the horizontal axis in defined intervals after a single scan line is finished. For fine scanning of targets for registration or other purposes, the mirror swivels instead of rotating.



Figure 3-1: Typical TLS set-up with various additional equipment.

Table 3-1: Properties of the laser scanner (RiegL LMS GmbH, 2013a).

Distance measurements	
Range for natural targets, $\rho \geq 80\%$	up to 1000 m
Range for natural targets, $\rho \geq 10\%$	up to 350m
Minimum range	2m
Accuracy	10mm
Repeatability	8mm (single shot), 4mm (averaged)
Measurement rate	24,000 Hz resulting in: up to 11,000 pts/sec. at low scanning rate (osz. mirror) up to 8,000 pts/sec. at high scanning rate (rotating mirror)
Eye safety class	Class 1
Laser wavelength	1550 nm
Laser output	8mW
Laser pulse duration	1 ns
Laser beam divergence	0.25 mrad 3 mrad (with beam-widening)
Direction measurements	
Vertical	
Scanning range	0° to 80° by rotating/oscillation mirror
Angle step width	0.004° to 0.2°
Angular resolution	0.002°
Horizontal	
Scanning range	0° to 360° by rotation optical head
Angle step width	0.004° to 0.75°
Angular resolution	0.0025°
Further Information	
Main dimensions	210 mm (diameter) x 463 mm (height)
Weight	16 kg
Inclination sensors	Range ± 5 deg, accuracy ± 0.05 deg
Protection class	IP64, dust and splash-water proof

For all studies of this contribution, a Nikon D200 camera (Table 3-2) was used in combination with a Nikon AF Nikkor 20 mm f/2.8D lens on top of the laser scanner. Additionally, a Nikon AF Nikkor 50 mm f/1.8D lens can be used for far field measurements. As the camera is detachable, the mounting needs to be readjusted every time the camera is assembled. Therefore, targets need to be fine-scanned by the scanner and detected in the pictures of the camera. Furthermore, the laser scanner is equipped with inclination sensors, an optional piece of equipment that detects the inclination of 0.05° at a maximum tilt of 5° (RiegL LMS GmbH, 2013b). Thus, a levelled position is not necessary and vibrations are adjusted.

Table 3-2: Properties of the Nikon D200 (RiegL LMS GmbH, 2013a).

Dimensions	147 x 113 x 74 mm
Resolution	3872 x 2592 Pixel (10,2 Mio. Pixel)
Sensor	Nikon DX format, CCD
Shutter speed	30 up to 1/8000 sec.
ISO-range	100 up to 1600
Connection	USB 2.0
Weight	830g
Storage	Compact-Flash

The laser scanning device, as well as the data exchange is controlled via a laptop, which is connected by a network connection. In addition, camera control and data exchange is facilitated by a USB connection. The whole control of the device is enabled with the software RiSCAN PRO from Riegl (Riegl LMS GmbH, 2008). However, developing one's own software by using the internal, documented interface is possible. Angles, intensity and RGB-value are assigned to each point, with the latter being added in a post-processing step.

In combination with the step width between each laser beam, the resolution of a scanning pattern, assuming a vertical plane at a certain distance, is given (section 2.2.4). To avoid an over- or undersampling, the specific beam width for a certain distance needs to be known. In this case, beam widening is 0.25 mrad, which corresponds to 0.145° and a beam diameter is 25 mm in 100 m distance. An oversampling only occurs, when the step width in each direction is smaller than the angle of the beam. The theoretical minimum step width is stated by the manufacturer as 0.004° in both the vertical and the horizontal direction (Table 3-2). However, bigger point spacing between each point should be avoided or at least be considered for certain research questions. Typical resolutions used in this contribution are shown in Figure 3-2, denoted with the overall estimated time for a full scan (360° horizontally, 80° vertically). These values are assumed for a vertical plane at a certain distance. The step width is similar for both directions.

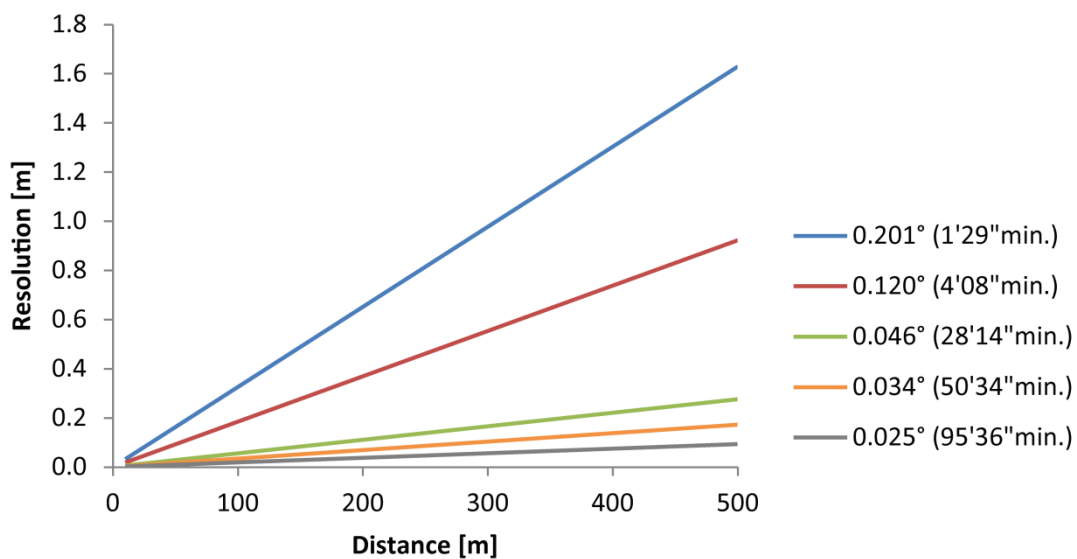


Figure 3-2: Estimated spacing between footprints regarding different step width and distance for a vertical plane in the given distance.

For this type of scanner in comparison to others, a medium noise level in the range direction and an average edge detection quality is reported (BOEHLER et al., 2003). PFEIFER et al. (2008) examine the intensity values of this type of scanner by a radiometric calibration approach (section 2.2.4) with reference targets of known reflectivity in different distances. A decrease and increase of intensity with a minimum at 15 m was found. A bi-cubic model can correct the gathered intensity data to fit to the reflection values of the chosen targets, depending on range and the specific laser scanner wavelength.

3.2 The RTK-DGPS system: Topcon HiPer Pro

The Topcon HiPer Pro (Topcon, Japan) RTK-DGPS system consists of two receivers, which are both capable to retrieve GPS and GLONASS satellite signals (Table 3-3). From the two GNSS both codes and each carrier phase is retrieved and considered for precise position measurements. As the system is analyzing the carrier phase signals and the corresponding corrections are being exchanged by a radio signal in real time, it is a RTK system (section 2.1.2). Likewise, it is also a precise DGPS, when a static measurement and according post-processing is conducted. Both receivers are operated with a PDA by Bluetooth that enables the handling of the measurement process using the software TOPSurf. Additionally, basic measurements can be conducted by an interface on each receiver, called MINTER. Some data are only stored internally, such as carrier phase signals and further other data for post-processing purposes. One receiver can be connected to a correctional service by a GSM-/GPRS- modem (type: Wavecom GSM/GPRS Modem with tri-band antenna). Usually the Axio-Net PED service is used here (AXIO-NET GmbH, 2013).

Table 3-3: Technical specification: Topcon HiPer Pro.

Description	40 channel integrated receiver antenna with interface (MINTER)
Tracking channels	GPS L1+L2 (C/A- Code & carrier phase) GLONASS L1+L2 (P-Code & carrier phase)
Accuracy, static mode	H: 3mm + 0.5ppm V: 5mm + 0.5ppm
Accuracy, RTK mode	H: 10mm + 1ppm V: 15mm + 1ppm
RTK update rate	10Hz
Radio communication (Power output)	Internal UHF (Selectable frequency range) 1.0W/0.25W (selectable)
PDA	FC-200 WinCE PDA (520Mhz)
PDA Communication	Bluetooth 1.1
Weight	1650 g
Internal Storage	128 MB

In order to test the accuracy of the chosen set-up, an error analysis was conducted. For this purpose, the RTK-DGPS was tested with three available survey points of the surveying agency. The base station of the RTK-DGPS is normally set-up on an unknown point. Thus, the overall accuracy of the system was confirmed first. The base station was levelled three times above a known survey point (here: 2109) of the country wide reference system. The data was recorded in ETRS89/UTM 32N. A mean value of 300 single measurements for each individual set up was compared to the coordinate of the survey point. The results are depicted in Table 3-4. As expected, the overall horizontal accuracy is within a decimetre range, the vertical accuracy within meters.

Table 3-4: Absolute error of GNSS measurements regarding the carrier phase.

Measurement	ΔX [m]	ΔY [m]	ΔZ [m]
1	0.213	0.429	1.958
2	0.848	0.296	1.645
3	0.668	0.119	0.749
\bar{x}	0.576	0.281	1.451
$\bar{x} (\Delta X, \Delta Y)$	0.429		

Afterwards, the assignment of the true coordinates of the survey point was carried out in the software for the base station, which was leveled above the survey point. Thus, the relative accuracy of the RTK mode of the system was controlled with the rover by measuring two other survey points (here: 2102 and 9404), lying in a distance of ~ 200 m and $\sim 1,100$ m in two directions to the base point. The mean position of twenty measurements was compared to the coordinates of these survey points. The results are presented in Table 3-5. The relative accuracy with the own RTK correction from the base station lies within the expected range of a centimetre in each direction. The accuracy seems to be dependent on the distance, as the values are worse for the more distant point 9404, but this distance is hardly used in this contribution.

Table 3-5: Error of GNSS measurements with the own RTK correction.

Survey point	ΔX [m]	ΔY [m]	ΔZ [m]
2102	0.006	0.009	0.008
9404	0.012	0.027	0.015
\bar{x}	0.009	0.018	0.011
$\bar{x} (\Delta X, \Delta Y)$	0.014		

According to the previous method, an additionally accuracy test of the external RTK correction by the Axio-Net PED service with the described modem was also conducted. The results of this test are depicted in Table 3-6 and show slightly inferior values of about 2 cm in every direction. However, these results are within the expected range offered by the correction service. In general, more accurate results might be achieved with a longer measurement time.

Table 3-6: Error of GNSS measurements with external RTK correction.

Survey point	ΔX [m]	ΔY [m]	ΔZ [m]
2102	0.055	0.009	0.015
2109	0.034	0.006	0.018
9404	0.023	0.018	0.031
\bar{x}	0.037	0.011	0.021
$\bar{x} (\Delta X, \Delta Y)$	0.024		

Overall, these errors of the chosen GNSS bias the overall accuracy of the combined RTK-DGPS and TLS approach. The world-wide absolute accuracy without any surveying points or correctional service that is mostly used in this contribution is within 0.5 m horizontally and about 1.5 m vertically. The relative positioning, with the own RTK solution is about 1 cm in every direction, which is suitable for a good, initial estimation of the point cloud orientation.

3.3 Direct georeferencing

The registration or combination of several scan positions is a major issue in TLS. In addition, assuming that a dataset with a georeference is needed, a translation of the whole project coordinate system is recommended. In this case, regarding the possibilities shown in chapter 2, a direct georeference approach is usually chosen that allows the determination of the position and orientation of point clouds. For this purpose, the position of the laser scanner as well as one further object needs to be measured. The position of the laser scanner is directly measured by the RTK-DGPS receiver, which was mounted on the GNSS-handle on top of the laser scanner. All dimensions between the GNSS receiver and the output beam are known from dimensional drawings of the manufacturer. As shown before, the laser scanner is capable of inclination measurement and accurate levelling is not needed.

A further reference point was required for the orientation of the point cloud. In order to estimate the orientation of the point cloud very rapidly and by the same RTK-DGPS system, as well as to avoid the use of too many targets, a modified reference method was applied. Larger cylindrical, low-cost reflectors were developed, which can be fixed to the top of standard ranging poles (Figure 3-3). The ground point of these ranging poles is easily measurable by the RTK-DGPS. Subsequently, the ranging pole with the reflector is perpendicularly set-up on the same point. The height of the reflector was measured from the ground to the middle of the reflector and is added to the ground point measurement.



Figure 3-3: Selfmade cylindrical reflector on ranging pole (1), detail image (2), and small reflector on flower pot.

For an easy detection by the laser scanner, a “diamond grade” highly reflective foil covers the reflector to achieve an accurate automatic detection by the laser scanner (3M GmbH, 2013). The reflecting foil has a height of 10.5 cm and a diameter of 7.6 cm. By choosing normed products, a lot of similar reflectors can be produced. The chosen method avoids having to use an indirect registration with the manufactured small targets. These need to be glued on walls or other hard materials and are therefore only single-use targets. However, depending on the research site, the latter small reflectors are used for indirect referencing, when a GNSS signal is not available. In addition, several small reflectors are glued on small flower pots (Figure 3-3). These reusable reflectors can be used to readjust the orientation of the camera (section 3.1) and for referencing purposes without glueing.

3.4 Fieldwork

The most important part for a successful survey is the planning stage (section 2.3). This includes all travelling issues such as customs control, on-site permits and in particular the main aim of the survey has to be clarified by consultation with all involved parties. Prior site investigation with maps and pictures is important. However, as for any type of fieldwork, variations may occur. The whole equipment is quite extensive and therefore its acquisition as well as the maintenance are critical issues. Transport to remote sites is a further issue, as depicted in Figure 3-4.

First task on the survey site is a thorough inspection. Sometimes this is assisted by prior consultation of maps and pictures. As shown before, TLS is dependent on the line-of-sight. Thus, determination of the scan positions is always important, but may take longer and the scan positions can hardly be estimated in the planning phase (RÜTHER et al., 2012). As BUCKLEY et al. (2008) state for geologic outcrop modelling, opposing scan positions in an elevated position yield the best results. However, this recommendation focuses on outcrops, which are mostly vertical walls and an elevated position is required. Scan positions for horizontal investigation areas are strongly dependent on the topography and surface roughness. More complex areas, like caves, buildings or archaeological sites need more time for inspection.

As shown in chapter 3.3, a direct georeferencing approach was used for most of the measurements in this study. Thus, the position of the RTK-DGPS base station and the ranging poles also had to be taken into account. The RTK-DGPS base station shows a range of about 2 km. Every pole is detectable for at least 300 m by the TLS. However, the base station and all poles should not cause shadows.

All surveys started with the set-up of the base station of the RTK-DGPS. For this and all other steps in the survey procedure a protocol was developed. With the rover of the RTK-DGPS all ranging poles were measured first, and then the rover was fixed on the TLS to determine the coordinates of each scan position. As introduced, small reflectors mostly on flower pots were used for indirect registration purposes, when no GNSS signal was available.



Figure 3-4: Different transport principles of the laser scanning device. Bottom left: Sodmein cave, Egypt (Picture: H. Decker). All others: Surveys in Greece (Pictures: C. Curdt).

Every time the digital camera is newly fixed on the laser scanner, the mounting changes. Thus, an improvement and control of the mounting is required. For this purpose, six small circular reflectors on the small flower pots (Figure 3-3), were arranged around the TLS. Different heights and distances as well as a distribution in every direction is recommended. According to the manufacturer, these small reflectors are scanned and photographed mostly black, with small aperture and flash light. This ensures an easier automatic extraction of the reflectors in the pictures. To achieve a very good recalibration these reflectors are fine-scanned, which means that they are automatically measured in a very high resolution by the scanner.

After these steps the TLS is ready for use. At every scan position, the following steps were fulfilled in the nominated order:

- Measuring of the scan position by the RTK-DGPS
- An overview scan or panorama scan is started to achieve a first impression, as well as the opportunity to detect the larger reflectors (Figure 3-5, A). These first measurements need 1 to 4 minutes for a full 360° horizontal scan with a coarser resolution of ~2.1 cm to 3.5 cm in a 10 m distance.
- Reflectors were fine-scanned after automatic detection or manual selection (Figure 3-5, B). Areas with reflectors, which were not detectable, due to minor resolution needed a further measurement. This was typically conducted in a higher resolution with the beam-widening function, which widens the laser beam to achieve an oversampled, full coverage of a certain area.
- The aperture and exposure time of the digital camera were checked and adjusted to the current situation
- The main scan was started with a higher resolution, typically with a step width of 0.046°, which equals to 8 mm in a 10 m distance and takes about 15 minutes for a 180° horizontal scan.
- Check of the measurements and the picture quality and illumination.

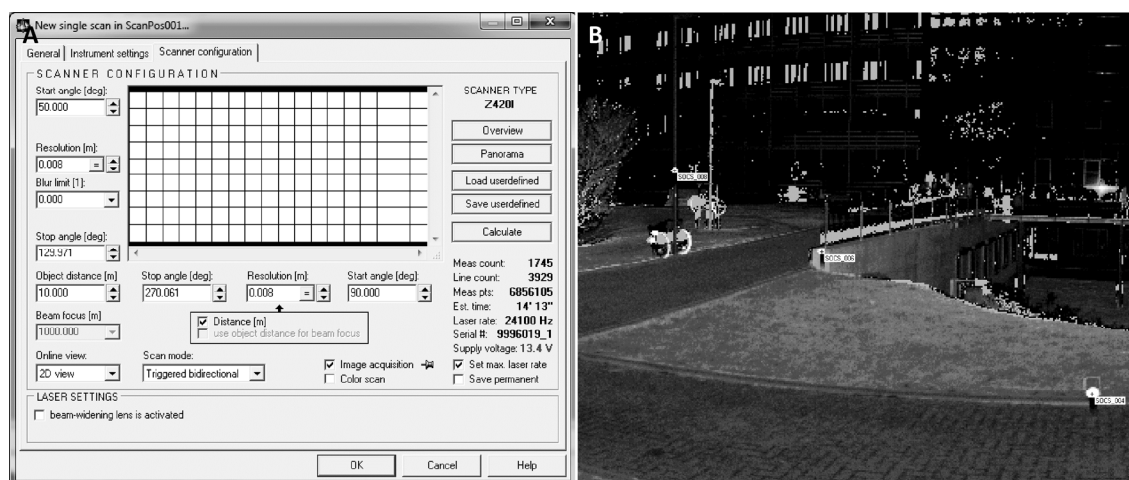


Figure 3-5: Software window for the scan configuration (A) and intensity image (B) with denoted highly reflective targets.

3.5 Post-processing

As already stated in section 0, several processing steps are necessary to prepare the collected data depending on the research question. Several of the mentioned steps are interchangeable to a certain degree, but mostly the subsequently presented order has been applied. The specific procedures were adjusted to the available software, whereas other software would enable other workflows or processing steps.

3.5.1 Preparation

The first step is to establish a backup of the measured data. This includes copying of the whole scan project and the RTK-DGPS data, as well as the digital recording of the values of the protocol. The scan project, as used in this contribution, consists of all data files being stored in a folder structure provided by the software RiSCAN PRO. The overall mean project file size is ~500 MB, with several projects reaching >1 GB of raw data.

In a second step, the scan project data was thoroughly examined. In particular, problems, errors and gaps of the acquired data were checked. Renaming of scan positions in the project file system as well as early deleting of unusable files was conducted. The Camera Coordinate System (CMCS) of the camera has to be adjusted every time, after remounting of the camera has taken place. The CMCS is responsible for the accurate colourisation of the points. The RGB-information of the points is obtained from the images taken by the camera. The automatic adjustment of the camera orientation can be started, when image centre points and according reflector centres are available. Likewise, centre points can be manually assigned within the images. Then, in the third step of preparation, the point clouds can be coloured and the coloured point clouds can be used, as well as other visualization modes (colours by range or height) to manually extract the Area of Interest (AOI) or any object and to remove noise.

3.5.2 General registration

Every point cloud of every scan position needs a registration or georeference depending on the overall project. In RiSCAN PRO (Riegl LMS GmbH, 2008) this step is available through several different options. Every scan position and its associated point clouds are stored in a local coordinate system, which is called the Scanner Own Coordinate System (SOCS).

By translations of a four by four matrix, all single systems can be translated to each other. Here, this coordinate system is called Project Coordinate System (PCRS). In addition, this can be transformed to a Global Coordinate System (GLCS). Each matrix M_{SOP} (Sensor Orientation and Position, SOP) consists of nine parameters for rotation (r) and translation (t):

$$M_{SOP} = \begin{pmatrix} r_{11} & r_{12} & r_{13} & t_1 \\ r_{21} & r_{22} & r_{23} & t_2 \\ r_{31} & r_{32} & r_{33} & t_3 \\ 0 & 0 & 0 & 1 \end{pmatrix} \quad (\text{eq. 3.1})$$

The following methods are possible for the registration:

- For direct georeferencing, as proposed in this contribution, the position of the scanner can be derived by the backsighting function. This method can be conducted in several ways, for instance DGPS and compass measurements can be integrated. In addition, inclination sensor measurements can be involved. In this study, the coordinates of a second object, a reflector as the according fine-scanned object were incorporated.
- Indirect georeferencing or registration can be conducted by automatically assigning corresponding points of different scan positions or finding corresponding point of previous imported control points.

- A manual, coarse registration is possible by marking similar points in different scan positions or by using a turning, tilting and moving function to set the position of the point cloud.
- Scan positions with a tilted mounting can be assigned to the according up-ward position by an additional function.

For the research in this contribution, the backsighting function was generally employed and in the case of no available GNSS signal indirect registration was applied. The accuracy of the direct georeferencing method was analysed in a small survey with two scan positions and two large reflectors on ranging poles, which were measured by the RTK-DGPS for the backsighting registration. Thus, four different registration possibilities for the two TLS scan positions were available. The results of these registrations were compared to 18 small, flat reflectors (diameter: 5.5 cm) that were measured by tachymetric surveying with a Trimble M3 5" total station* in a local reference system. The 18 small reflectors, which are the control points of the network, were measured by TLS from each scan position. For the transformation between the two systems, six metal screws were located around the surveying area to allow easy measurements for both instruments. These six points are used for the independent transformation of the 18 reflectors, which was conducted by a 3D-Helmert transformation in the Java Graticule 3D software (derletztekick, 2013).

Table 3-7: Error of the different registration modes compared to the local network

Registration method	ΔX [m]	ΔY [m]	ΔZ [m]
SP1 - STA1	0.025	0.024	0.018
SP1 - STA2	0.010	0.007	0.018
SP2 - STA1	0.029	0.024	0.021
SP2 - STA2	0.019	0.020	0.020
\bar{x} - STA1	0.027	0.024	0.019
\bar{x} ($\Delta X, \Delta Y$)	0.025		
\bar{x} - STA2	0.015	0.013	0.019
\bar{x} ($\Delta X, \Delta Y$)	0.014		

As expected, the overall error of about 2 cm is nearly within the range of the incorporated RTK solution error. The accuracy seems to depend on the selected larger cylindrical reflector. In this case, the incorporation of reflector STA2 leads to slightly better results, as depicted in Table 3-7. The horizontal accuracy is 1.5 cm, the vertical accuracy is 2.3 cm.

3.5.3 Adjustment

Depending on the previously selected method, the registration may need an additional adjustment or enhancement. The accuracy test revealed that in this case the error depends both on the relative RTK error and on the chosen reflector. This pattern is shown by the overall accuracy of the registration prior to the adjustment, as shown in Table 3-8.

* Measurements by Dr. A. Pastoors, Neanderthal Museum, Mettmann, Germany.

Table 3-8: Accuracy of the overall registration prior to the adjustment

Registration method	ΔX [m]	ΔY [m]	ΔZ [m]
\bar{x} - STA 1	0.051	0.046	0.026
\bar{x} ($\Delta X, \Delta Y$)	0.048		0.026
\bar{x} - STA 2	0.020	0.024	0.032
\bar{x} ($\Delta X, \Delta Y$)	0.022		0.032

As stated in section 2.4.2, the ICP-algorithm is capable to find a solution for the alignment of associated point clouds. In RiSCAN Pro this method is implemented as Multi Station Adjustment (MSA). As mentioned previously, the orientation and position of each considered scan position is iteratively modified to find the best-fit solution (RiegI LMS GmbH, 2008). For this purpose, the data was reduced with the plane surface filter to representative planes, which can be manually or automatically derived by different criteria, such as maximum distance. Subsequently, the planes were used by the modified ICP-algorithm. Every scan position and its orientation is fixable and according data can be selected. It is recommended to fix the accurately measured positions of the scanner and to adjust only the orientation. In addition, the previously used reflectors on ranging poles were not considered, as these were only for the approximate estimation of the point cloud's orientation.

All steps of the MSA were conducted according to the recommendations of the manufacturer and a specific scheme was evolved that is usually applied. These steps are listed in Table 3-9. A manual iterative process is conducted and in each step the results, their distribution and the quantity of the incorporated triangles is checked, which might lead to slightly different steps. The initial search radius was decreased first, with the error range being reduced thereafter. Finally, a standard deviation of generally less than 1 cm was reached for the polydata concerned.

Table 3-9: Typical steps and parameters used for MSA.

Step	Search radius [m]	Min. chance of error 1 [m]	Min. change of error 2 [m]	Outlier threshold
1	5	2	1	2
2	3	2	1	2
3	2	2	1	2
4	1	2	1	2
5	1	1	0.5	2
6	1	0.5	0.1	2
7	1	0.1	0.05	2
8	1	0.1	0.05	1
9	1	0.01	0.005	1
10	1	0.008	0.003	1
11	0.5	0.008	0.003	1
12	0.25	0.008	0.003	1
13	0.1	0.008	0.003	1

This MSA approach results in an overall consistent point cloud of every scan position that shows only a minor error. For the accuracy test, the results derived by comparison of the coordinates of the small reflectors measured by the total station and the final coordinates from the post-MSA point cloud are

listed in Table 3-10 for both pre-MSA registrations. The comparison reveals almost similar results for both initial registrations with a horizontal error of 17 mm and a vertical error of 12 mm.

Table 3-10: Registration results after the MSA.

Registration method	ΔX [m]	ΔY [m]	ΔZ [m]
\bar{x} - STA 1	0.008	0.026	0.012
\bar{x} ($\Delta X, \Delta Y$)	0.017		0.012
\bar{x} - STA2	0.009	0.026	0.012
\bar{x} ($\Delta X, \Delta Y$)	0.017		0.012

3.5.4 Feature extraction

With the step of adjusting the registration, all data from all scan positions are available in an overall consistent project system (PCRS or GLCS). Then, as the first step of this processing stage, data of the Area of Interest (AOI) is selected from the detailed and coloured scan data and a new data object is created for each scan position. Additionally, noise is removed manually or by filter functions from each of these new data objects. Finally, a cleaned, coloured point cloud can be combined and used for further analysis. Several of these analyses were conducted in RiSCAN PRO, whereas iconic reconstruction was undertaken in Geomagic Studio and symbolic reconstruction was executed in AutoCAD in combination with PointCloud Pro. In general, the derived data sets were further analysed, visualised and compared to other datasets in ESRI's ArcMap.

RiSCAN PRO

Most of the data preparation was conducted in RiSCAN PRO. The first task in all projects was to extract the AOI, which typically made up only a very small part in terms of the extent received by the laser scanner. This is depicted in Figure 3-6, where the AOI is marked by a black rectangle and all other points are disregarded.

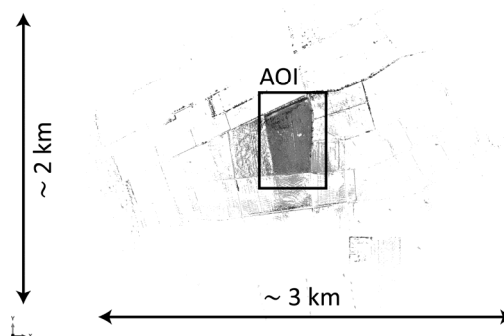


Figure 3-6: The extent of a scan project and the Areas of Interest (AOI), assigned by the black rectangle, showing the huge recorded ranges of the TLS device.

The extraction of points of the AOI was mostly conducted by manually masking points that belong to the AOI and establishing a new object containing only these points. This step was undertaken for point clouds of each scan position. In addition, a further important step was to delete noise and obstacles,

which was again partly done by manual selection. The latter step can also be fulfilled by the automatic selection tool that automatically selects points of the whole point cloud by type, such as specific ranges, angles or amplitudes. A combination of filters is possible as well as additive selection.

The following automatic filters are available for structuring and thinning of the point clouds (RiegI LMS GmbH, 2008), but particularly for HRDEMS:

Range and amplitude gate: According to the settings in the automatic selection tool, point clouds can be filtered by range or amplitude values.

Point filter: The point filter enables a simple reduction of the point cloud by selecting every n-th point.

Octree filter: This filter establishes an octree structure, where minimum values for the division can be set.

Create organized point cloud: This filter also uses an octree algorithm, but with different criteria.

2.5D raster: The filter uses binning to a certain reference plane, a 2D plane, to reduce the point density. The binning procedure can be set to retrieve the minimum, average or maximum value for the cell. Additionally, the true minimum, maximum and average can be used and the according point will be considered for each cell, instead of establishing a centre point with an assigned value as in the first case. With this filter tool, data can be triangulated automatically.

Terrain filter: The terrain filter is based on the 2.5D raster filter. The tool automatically and iteratively establishes 2.5D grids and compares the result to the original point cloud. Points outside a certain threshold are deleted. This procedure is a simple binning filter as depicted in section 2.5. The procedure can be manually conducted by using the 2.5D raster filter and the comparison tools.

Several of the previously mentioned filters can be combined in one step, as well as several or just single point clouds can be looked at. Finally the cleaned, consistent point cloud of the AOI of each scan position is derived, which can then be combined and used for further analysis. One possibility is to triangulate the data in RiSCAN PRO (RiegI LMS GmbH, 2008). For this purpose, several tools exist:

Plane Triangulation: In this mode, the triangulation is computed from the 2D coordinates of the mapped points to the computer screen (cf. section 2.4.3). The maximum angle and edge length can be defined.

Polar triangulation: The polar triangulation works similarly to the plane triangulation, but is independent from the viewpoint.

Volume Triangulation: The volumes of objects, represented by point clouds or in the form of triangulated meshes are calculated by three different modes. Depending on the calculation mode, it is also possible to calculate the surface area of an object. The volume is calculated between the plane and the surface, which is created from the selected area and the minimum, maximum or a bilinear, averaged value can be used. Additionally, the volume between two surfaces can be calculated and a "cut" volume and a "fill" volume are created according to a specified threshold value. All operations can be limited by a polyline.

Smooth & Decimation: This function modifies the surface structure of the triangulated object by optimising the point data (smoothing) and reducing the amount of triangles (decimating) with several adjustment options.

Further tools used on the triangulated objects are:

Image Mapping: This function textures 3D objects with the information of the images taken by the camera. Texture resolution, scale and overlap factor can be chosen.

Sections: The creation of cross-sections of objects is important. Several adjustments, such as the considered planes and extents, are possible to achieve the suitable sections

Extract outer surface: The function allows the extraction of the outer, watertight surface of any triangulated mesh.

Iconic processing in Geomagic Studio

As previously depicted, RiSCAN Pro uses a 2.5D triangulation (polar triangulation) that depends on the viewing angle. For better triangulation results, particularly for smaller objects, the volume based triangulation of Geomagic Studio was applied. This software is mainly intended for reverse engineering and is capable to derive highly accurate surfaces and CAD models from 3D scan data (Geomagic Inc., 2013). For this purpose, imported point clouds were examined, reduced and were smoothed in the point phase before triangulation. The triangulated model can again be optimised, cleaned and repaired with particular functions. For instance, the Mesh Doctor is applied on meshes, which automatically improves the model by editing spikes, intersections, small components and so on. In further steps, exact surfaces of objects for precise reproduction can be established as NURBS or parametric surfaces that reflect the indented design are generated (Geomagic Inc., 2013). Finally, the data can be exported to various formats and models can be accurately stored in 3D-PDFs for an easy distribution. In this contribution, the point clouds are usually hardly smoothed and triangulated polygon objects are exported after gap filling and repairing.

Symbolic reconstruction in AutoCAD Civil 3D with PointCloud Pro

Similar to the previously mentioned software, PointCloud Pro from Kubit GmbH (Kubit GmbH, 2013) was used, which is an add-on for the CAD-software Civil 3D 2013 from Autodesk Inc. (Autodesk Inc., 2013), for the derivation of small-scale objects as well as 2D maps and cross sections. The software is now termed PointSense. The general workflow was facilitated by an automated object capture and fitting functions for primitives, as well as a sophisticated slicing management. In addition, the software enables usage of the oriented images of the mounted camera, to establish highly detailed sketches of the objects. For this purpose, point clouds and images can be imported directly from the RiSCAN PRO project data files by an interface.

Maps and geostatistical analysis

All data can be imported and exported amongst all used programs. For visualisation purposes and additional analysis functions, most data were imported to ArcMap, now ArcGIS for Desktop (ESRI Inc., 2013) from the Environmental Systems Research Institute, Inc. (ESRI). In particular for the derivation of DEMs, the interpolation functions, like Inverse Distance Weighting (IDW) or Kriging

functions were used. The data can be combined with further data, for example from geological maps, satellite imagery, orthophotos, RTK-DGPS measurements, other DEMs, and tachymetric measurements. Thus, accurate maps can be established according to the different research goals. Further statistical analysis were conducted in R-statistical software (R-software, 2013).

4 Case study 1: Coastal geomorphology*

4.1 Introduction

Coastal areas are under permanent change and are also the result of past processes (WOODROFFE, 2002; KELLETAT, 2013). These processes are for example sediment transport, accumulation and erosion by normal and extreme waves (storms or tsunamis). Tidal processes are an additional cause of change for some regions. Fluvial, aeolian, biological and anthropogenic influences also have to be considered as sources for coastal change and development. In general, knowledge of coastal processes is important for a better understanding of possible changes in the future, since about 23% of the World's population lives within a 100 km distance of coasts (NICHOLLS et al., 2007). The devastating recent tsunami events like the Indian Ocean Tsunami 2004 (PARIS et al., 2009) and the Japanese Tōhoku Tsunami 2011 (TAPPIN et al., 2012) demonstrated profoundly the high vulnerability of coastal areas.

In general, it is possible to estimate the stated effects by coastal monitoring. This can be conducted through several methods (DORNBUSCH, 2010; GENS, 2010) with regard to changes in the sedimentary budget and coastline configuration. Furthermore, timescales and the dimensions of affected areas can be estimated. Ground-based methods with a high spatial and temporal resolution range from transects achieved by tape measurements, a surveyor's optical level, a total station or DGPS measurements (STONE et al., 2004; BAPTISTA et al., 2008) to video imaging (ALEXANDER & HOLMAN, 2004; ARMAROLI & CIAVOLA, 2011). Airborne or space-borne imagery (DEL RÍO et al., 2013) as well as ALS observations provide data in a lower temporal and spatial resolution. They are more useful for larger areas (KRABILL et al., 2000b; SALLENGER et al., 2003; MILLER et al., 2008) and thorough observations of annual coastal changes can be carried out (RICHTER et al., 2013). TLS can be applied to monitor the erosion of coastal cliffs (LIM et al., 2005; ROSSER et al., 2005; LIM et al., 2011), the performance of beach nourishments (PIETRO et al., 2008), and small-scale sand movements (LINDENBERGH et al., 2011). A combination of such methods allows long-term monitoring (HARLEY et al., 2011). Boulders and pebbles at coastal sites can also be observed by using photography in combination with DGPS measurements (CRUSLOCK et al., 2010; FICHAUT & SUANEZ, 2011; KNIGHT & BURNINGHAM, 2011), additional colouring (STEPHENSON & NAYLOR, 2011) or RFID-based tracing methods (BERTONI et al., 2012; MILLER & WARRICK, 2012).

In addition to these monitoring approaches, the historic and pre-historic development of coasts is of importance. Palaeo-events can be detected as specific storm and tsunami deposits in the geological record that can be derived by vibracoring or trenching (DAWSON, 1994; NOTT, 2004; DAWSON & STEWART, 2007; KORTEKAAS & DAWSON, 2007; VÖTT et al., 2010). However, a contentious debate concerning the interpretation of such deposits has ensued and a wide range of proxies is usually drawn on nowadays to identify palaeo-events. Additional evidence can also be obtained from historical and archaeological findings (GOFF et al., 2012). As an example, past high-energy impacts have been detected on Bonaire,

* The chapter is an extended version of two articles: HOFFMEISTER et al. (2013a); HOFFMEISTER et al. (2013b).

Netherlands Antilles (ENGEL et al., 2012), Greece (MAY et al., 2012a) and Thailand (BRILL et al., 2011), as well as for numerous other regions (SCHEFFERS & KELLETAT, 2003).

Tsunamis occur as a result of a sudden vertical movement of a large column of water, which can be triggered for instance by seismic events, eruptive volcanism, landslides, asteroid impact, explosions and meteorological phenomena (BRYANT, 2008). In contrast to normal sea waves, tsunamis show a much greater wave length of up to hundreds of kilometres or wave periods between each crest lasting hours (Figure 4-1) in combination with relatively small wave heights in open water. In addition, those waves show a high wave propagation of up to 250 m/s in the open sea (BRYANT, 2008). Reaching the shoreline, tsunamis reduce speed, shoaling increases wave height and a longer lasting inland inundation follows. All waves induce strong pressure at first contact, but tsunamis establish a turbulent flow for several minutes (ENGEL & MAY, 2012) that is confirmed by eye witnesses and videos of the last devastating events. Depending on the coast type, the affected area can be larger than hundreds of square kilometres (GOTO et al., 2012). Modelling approaches exist to estimate wave heights and inundation limits of tsunami waves (WEISS et al., 2006; TSELENTIS et al., 2010; RÖBKE et al., 2013).

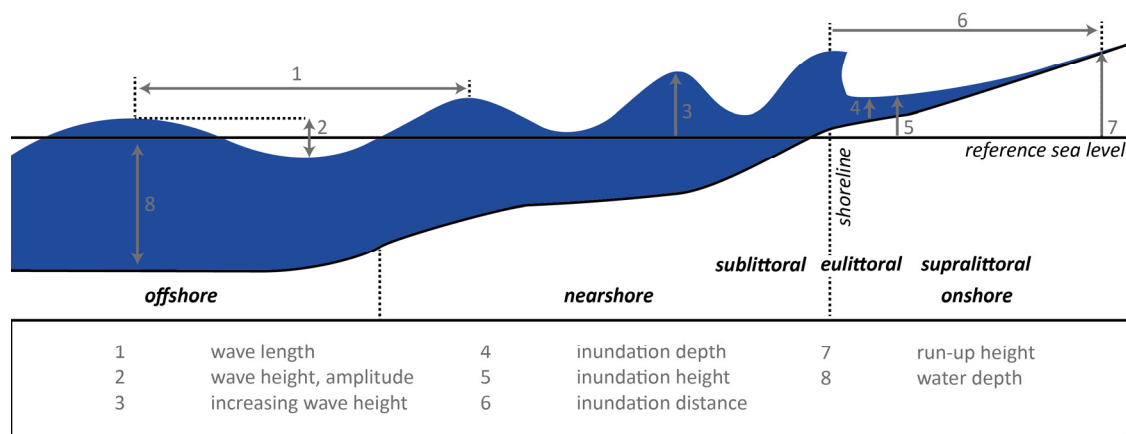


Figure 4-1: Wave propagation, coastal zones and parameters considered in this part, modified after BRILL (2012) and KELLETAT (2013).

As a further result of high-energy impacts, large boulders are dislocated inland from the littoral zone, which can be identified by upside down rock pools, adhering remains of marine fauna, algal rims and notches, sometimes forming imbrication trains (e.g. SCHEFFERS et al., 2008). Other processes, which might have caused the dislocation of boulders in coastal environments, such as gravity induced movements, higher relative sea levels in the past, exhumation of bedrock and glacial processes need to be ruled out before tsunamis are established as a causal factor (TERRY et al., 2013). However, such dislocated boulders have been reported from many other coasts of the world (SCHEFFERS & KELLETAT, 2003). They are again subject of a controversial debate, whether their origin is related to tsunamis or to powerful storms, which has important implications for coastal hazard assessment (NOTT, 2003a; SPISKE et al., 2008; GOTO et al., 2010a; PARIS et al., 2011). These boulders can be further used to approximate the age of the according events by mortality age dating of adherent marine organisms, such as corals, mussels and molluscs (TERRY et al., 2013).

Several hydrodynamic wave transport equations have been developed in order to achieve approximations of minimum wave heights and wave velocities of extreme events that are necessary to move boulders (NOTT, 2003a; BENNER et al., 2010; LORANG, 2011; NANDASENA et al., 2011; ENGEL & MAY, 2012). Imamura et al. (2008) introduced a more sophisticated modelling approach achieved by experiments in a water channel with cubic and rectangular shaped boulder models. Rolling and saltation were determined to be the major transport mechanisms. This modeling approach was recently proven by NANDASENA & TANAKA (2013). All wave transport equations basically estimate the forces, which might act on a boulder hit by a wave (Figure 4-2). As introduced by NOTT (2003b), who presents the most commonly used equations (TERRY et al., 2013), three different pre-transport settings are usually considered. These are a subaerial, submerged or joint-bounded setting.

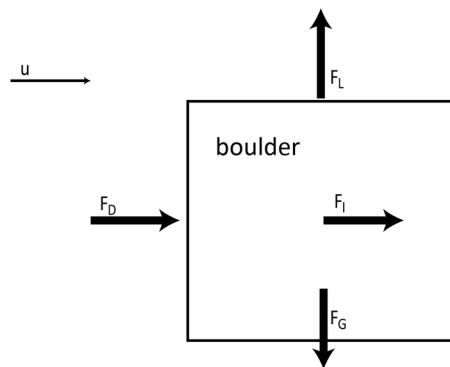


Figure 4-2: Forces acting on a boulder, which have to be taken into account in hydrodynamic wave transport equations: u (velocity of current), F_D (force of drag), F_L (force of lift), F_G (force of gravity), and F_I (inertia force), modified after BENNER et al. (2010).

In order to distinguish between storm and tsunami waves, NOTT (2003b) also introduced two different equations for each pre-transport setting, one for the estimation of minimum tsunami wave heights and one for minimum storm wave heights, necessary to move one and the same boulder. However, he refers to the tsunami bore velocity analysis of FUKUI et al. (1963), which is mostly depending on an empirically derived friction factor. NOTT (2003b) chose a friction factor of $\eta = 0.875$ to reach a wave type parameter $\delta = 4$ for tsunami waves and $\delta = 1$ for storm waves. This “crude assumption” (BARBANO et al., 2010: 148) results in different transport capabilities of storm and tsunami waves, where a storm wave has to be four times higher than a tsunami wave to develop the same energy to dislocate one and the same boulder. This simple relation has unfortunately not been proven to be correct recently, but was still used by several authors (MASTRONUZZI et al., 2007; BARBANO et al., 2010; LORANG, 2011; ENGEL & MAY, 2012). As stated before, the energy evolved by tsunami waves is particularly depending on wave length (BENNER et al., 2010). Thus, future approaches will rather have to focus on the differences in energetic capacities between storm and tsunami waves, concerning wave length, inundation time and water depth.

For the determination of geomorphometric parameters of dislocated boulders, measurements of the three main axes are commonly taken by tape during field surveys (GOTO et al., 2010b; PARIS et al., 2010; SWITZER & BURSTON, 2010; SHAH-HOSSEINI et al., 2011). The measurements of the axes are, however, carried out differently. PIGNATELLI et al. (2009) for example, use the a- and b-axis as major and medium

axis, whereas others define the axes by their orientation to the coastline (NOORMETS et al., 2004; BENNER et al., 2010; ETIENNE et al., 2011). The importance of the axis orientation was recently proven by NANDASENA & TANAKA (2013).

Some wave transport equations rely on the “mass” of a boulder as a direct input parameter (NOORMETS et al., 2004; BENNER et al., 2010; ETIENNE et al., 2011; ENGEL & MAY, 2012), which is a function of volume and density. Thus, some authors take into consideration an approximation of the shape for each boulder to achieve better mass estimations based on the measurement of boulder’s axes (PARIS et al., 2010; PARIS et al., 2011). SPISKE et al. (2008) actually weighed smaller boulders and compared their data to measurements of a laser profiler and the simplified method of multiplying the axes. Further considerable inaccuracies concerning the determination of the mass of each boulder occur from rough approximations of rock density values. The calculation of reliable results to be used in wave transport equations requires more accurate input parameters. However, even through utilising particular remote sensing techniques such as TLS or measurements with DGPS, several assumptions are still involved by these wave transport equations and all results should be used with caution.

In order to achieve 3D models of dislocated boulders and further parameters of their environment, TLS is used in this contribution in combination with accurate density measurements for the taken rock samples, carried out in the laboratory. Recent studies have shown that the quality of boulder parameters is strongly increased by more accurate measurements of the boulder mass. The latter can be conducted for instance by DGPS measurements and certain photogrammetric analyses (ENGEL & MAY, 2012), stereophotogrammetric approaches (TERRY et al., 2013) or TLS measurements (MASTRONUZZI & PIGNATELLI, 2012; SCICCHITANO et al., 2012; HOFFMANN et al., 2013). In this contribution, annual changes of the sediment budget of seven selected sites, which differ in their coastal configuration, were additionally determined by TLS surveys during 2009 to 2011.

4.2 Research sites

The TLS field campaigns were carried out every year in the late summer of 2008-2011. Selected coastal sites in western Greece were surveyed within the framework of an interdisciplinary project on palaeo-tsunami impacts along the coasts of the eastern Ionian Sea (VÖTT et al., 2010). In particular, western Greece is directly exposed to the Hellenic trench, which is a major tectonic zone in the eastern Mediterranean (PAPAZACHOS & KIRATZI, 1996; CLEMENT et al., 2000; LAIGLE et al., 2002; MAKROPOULOS et al., 2012). Thus, the region is characterized by a high seismic and tsunami hazard risk (PAPAZACHOS & DIMITRIU, 1991). In fact, numerous historical accounts (SOLOVIEV et al., 2000) as well as detailed sedimentary studies indicate repeated tsunami landfall in western Greece (SCHEFFERS et al., 2008; VÖTT et al., 2008; 2009; 2010; 2011; MAY et al., 2012a). In addition, these coastal areas experience gradual and seasonal changes. Thus, winter storms in this region may have also considerable impact on the coastal configuration, as reported for the Italian coasts of the Ionian Sea (MASTRONUZZI & SANSÒ, 2004; BARBANO et al., 2010).

For several sites of the Mediterranean area, wave transport equations set up by NOTT (2003b) are widely used and partly refined in several studies. For example, SCICCHITANO et al. (2007) obtained minimum tsunami wave heights of 2-3 m for the Maddalena Peninsula, SE Sicily. For the Algerian coast, larger

boulders are reported by MAOUCHE et al. (2009) and minimum tsunami wave heights of about 2 m were calculated. Boulders encountered in southern Apulia, Italy, are described by MASTRONUZZI & SANSÒ (2004), who determined required tsunami wave heights of 1.5 m. Revised equations of NOTT (2003b) were applied by BARBANO et al. (2010) for Sicily and PIGNATELLI et al. (2009) for southern Italy, yielding minimum tsunami wave heights of around 1 m and storm wave heights of approximately 10 m.



Figure 4-3: Map of research sites in Greece. Annual changes of the sedimentary budget were determined for seven coastal sites (white dots) and two additional sites were considered for boulder measurements (red dots). The inside box shows a detailed view of the southwestern part of Cefalonia Island. The locations of the two Poseidon buoys are marked by white crosses, modified after HOFFMEISTER et al. (2013b). Imagery: Modis (2009), Landsat ETM+ (2003). Country data: ArcWorld Supplement.

Altogether, seven coastal sites were repeatedly surveyed, which differ in location, coastal configuration and coast type. For a comparison of the determined annual changes, data of two buoys of the Poseidon network (HCMR, 2013) were taken into account (Figure 4-3). In addition, two sites, namely Cape Skalas, Peloponnese and one part of Cape Gerogombos, Cefalonia Island, were surveyed only once.

The sites of Gialous Skala and Kaminia Beach are characterized by narrow beaches in front of steep inactive cliffs on the windward, northwestern part of Lefkada Island. The local bedrock is made out of Pantokrator limestone, a neritic, gravelly, massive and bright limestone of Triassic age (IGME, 1963). The coastal section at Kaminia Beach, which was surveyed by TLS, is only ~170 m long and the beach is

composed of loose cobbles and small boulders of up to 50 cm in diameter. Adjacent to the beach section, recent notch formation takes place. The beach section studied at Gialous Skala is approximately 500 m long and consists also of sand, pebbles, and small boulders. Similar to the constellation at Kaminia Beach, this beach is also flanked by a rocky coast. Towards the south, steep slopes, covered by debris, descend directly into the sea.

The study sites near Cape Gerogombos and Cape Schinou are situated on the Paliki Peninsula, Cefalonia Island and represent rocky coastal areas exposed to strong wind and wave dynamics. The two capes are separated by a small embayment, where beachrock-type tsunamites were described by VÖTT et al. (2010). At Cape Gerogombos, big dislocated boulders occur up to several meters above present sea level on a ramp-like structure and a cliff-top platform made of Eocene to Oligocene limestone (IGME, 1985). Some of the boulders lie scattered around, others are imbricated and turned upside down. The (supra)littoral origin of the boulders is documented by rock pools formed by marine organisms. At Cape Schinou, larger dislocated boulders are lying on a coastal ramp of Pliocene sediments (IGME, 1985).



Figure 4-4: Boulder GER-ST 5 at Cape Gerogombos, Cefalonia Island, lying upside down. An inactive overturned rock pool is indicated, modified after HOFFMEISTER et al. (2013a). Photo: K. Ntageretzis, 2008.

Cape Aghia Pelagia is situated in the south of Cefalonia Island, about 8 km south of Argostoli. The site is characterized by Pliocene bedrock (IGME, 1985), forming a cliff-top platform ~4 m above present sea level (a.p.s.l.) in the south-eastern and a ramp-type topography in the south-western part. Both areas are covered by abundant dislocated boulders up to 30 m inland.

Cape Katakolo is located about 12 km west of Pyrgos, at the northern part of the Kyparissian Gulf at the western Peloponnese. The Katakolo promontory consists mainly of limestone (IGMR, 1980). Towards the southwest, it is directly exposed to the open Ionian Sea and characterized by a narrow rocky coastline gradually descending to the present shore with numerous dislocated boulders lying up to 30 m inland (Figure 4-4). In addition, trim lines, where the vegetation is almost completely missing, extend more than 40 m inland and document strong wave activity. For this particular area, RÖBKE et al. (2013) conducted numerical simulations of different tsunami scenarios, which have been proven by sedimentary evidence.

The site of Cape Skalas in southern Lakonia, Peloponnese, is a flat lying coastal section in the leeward position of Elaphonissos Island with outstanding imbrication trains of dislocated boulders (SCHEFFERS et al., 2008). Besides the mentioned boulders, the rocky coast also consists of Upper Pliocene to Lower

Pleistocene calcarenites, comprising marine to lacustrine facies and clastic as well as biogenic sediments (IGME, 2002). Geoarchaeological on-site findings testify that the relative sea level has never been higher during the Holocene than it is at present (SCHEFFERS et al., 2008). It is generally assumed for all areas that the distance between the present location of the boulders and the shoreline at the moment of boulder displacement was at least as long as today or even longer (KRAFT et al., 1977; ENGEL et al., 2009; BRÜCKNER et al., 2010).

4.3 Specific method

For the surveys in Greece, the direct georeferencing method introduced in section 3.3 was applied. Therefore, the position of the RTK-DGPS base station at each site was measured 500 times, which takes about 20 minutes, to achieve a reasonable mean position. All positions are recorded in the WGS 1984, UTM 34N. In each study area, the base station of the RTK-DGPS was set up at exactly the same position every year, which was marked by a metal screw on bedrock outcrops (Figure 4-5). In addition, two secure points were marked that were used to verify the accuracy of the position. The average resolution for a detailed scan was around 0.8 cm at a distance of 10 m. Between two and six different scan positions were chosen for each site depending on the size of the study area and the geomorphological setting. Nearly the same scan positions were used every year to obtain comparable datasets.



Figure 4-5: The base station of the RTK-DGPS system was set up at the same position every year marked by a metal screw (see detail photo). The photo shows a field of scattered blocks at the site Cape Gerogombos A, Cefalonia Island, modified after HOFFMEISTER et al. (2013b).

4.3.1 Estimation of boulder masses

For the accurate reconstruction of boulder volumes, the different scan positions at each site were directly georeferenced and merged. Afterwards, the registration was enhanced by the MSA approach, as

described in section 3.5. Noise and outliers of the final point cloud for each site were removed manually. The parameters for the wave transport equations, such as the distance to the shoreline, elevation above sea level and the mean length of the boulder axes were measured manually for each boulder based on the geo-referenced dataset. While some authors classify the axes by size (PIGNATELLI et al., 2009; PARIS et al., 2010), for this study the a-axis was measured as parallel to the coast line, the b-axis as perpendicular to the coast line and the c-axis as height of the boulder, which is common practice in other studies (NOORMETS et al., 2004; BENNER et al., 2010; ETIENNE et al., 2011).

For optimal reconstruction and gap-filling of the 3D model, the software Geomagic Studio was used (Geomagic Inc., 2013). Therefore, a new object was created, exported, processed and finally re-imported for each boulder by manually masking points. Digital photographs were used to visually control the reconstruction process. Subsequently, the shape of each 3D boulder model was extracted together with shapes of other boulders, which were detected in the coloured point clouds. For the creation of a DTM, points were imported to ArcMap and the DTM was generated by Inverse Distance Weighting (IDW) an exact and fast interpolation method (BRUNSDON, 2009). Contour lines were extracted from the DTMs according to the manually measured sea level to interpolate the data and extract contour lines for the elevation above sea level. Hereafter, the creation of maps for the visualisation of relevant data was enabled.

To estimate the energy needed to move a boulder inland from the littoral zone, the mass of the boulder is required, which is the product of its density and volume. Density measurements were obtained by applying the principle of *Archimedes*, using hand-sized samples that had been taken from dislocated boulders in the study areas (NTAGERETZIS, 2009). In the laboratory, each rock sample was dried and weighed. Then it was soaked with water, weighed again, and put into an overflow tank. The displaced water flowed into a measuring cup, positioned on a precision scale. The ratio between the mass of the displaced water and the water density at laboratory temperature (20 °C) yields the volume of the displaced water. The water volume in turn is consistent with the volume of the rock sample. In order to achieve a better reproducibility, waterlogged rock samples were used for the measurements and the volume of pore water was subtracted using the dry and waterlogged masses weighed before. Finally, the density of each rock sample was determined using the equation:

$$\rho_b = \frac{m_b}{V_b} \quad (\text{eq. 4.1})$$

4.3.2 Wave transport equations

Most publications aiming to reconstruct minimum heights of waves necessary to move boulders, utilise the wave transport equations developed by NOTT (2003b). However, these equations have been revised by several authors (PIGNATELLI et al., 2009; BENNER et al., 2010; NANDASENA et al., 2011). All equations require the lengths of the axes of a selected dislocated boulder as parameters. In contrast, several wave transport equations were chosen here that use the mass of a boulder as a direct input parameter (NOORMETS et al., 2004; BENNER et al., 2010; ETIENNE et al., 2011; ENGEL & MAY, 2012). Generally, the equations can be classified by the pre-transport scenario, with the first three contributions considering a submerged scenario (NOORMETS et al., 2004; BENNER et al., 2010; ETIENNE et al., 2011) and the latter one assumes a joint-bounded scenario (ENGEL & MAY, 2012). In the submerged scenario the boulder is lying

loosely on the water bottom, whereas in the joint-bounded scenario the boulder is quarried from a seaward edge. For these equations the mass of a boulder is considered as being $m_b = V_b(\rho_b - \rho_w)$.

The approach by BENNER et al. (2010), calculating the momentum and friction forces, is represented by eq. 4.2 and eq. 4.6. Generally, the theorem of the conservation of energy is considered. These equations were inverted to estimate wave height H_t and velocity v_t , dependent on the mass of the boulders, the horizontal and vertical displacement, as well as the wave period and the water depth. The wave height H_t actually means the inundation height at a specific point along the coastline, which is required to initiate boulder movement. The inverted equations after BENNER et al. (2010) are :

$$H_{t/s} = \sqrt{\frac{E_{kin}}{0.125 \rho_w a g L}} \quad \text{for wave height} \quad (\text{eq. 4.2})$$

$$E_{kin} = E_f + E_h = [\mu m_b g X_{transport}] + [m_b g H_{uplift}] \quad (\text{eq. 4.3})$$

$$L = L_0 \left[\tanh\left(\frac{2\pi d}{L_0}\right)^4 \right]^{\frac{2}{3}} \quad (\text{eq. 4.4})$$

$$L_0 = \frac{gT^2}{2\pi} \quad (\text{eq. 4.5})$$

$$v_{t/s} = \sqrt[3]{\frac{E_{kin}}{0.5 \rho_w q a c T}} \quad \text{for wave velocity} \quad (\text{eq. 4.6})$$

Generally, the assumed kinematic energy (E_{kin}) necessary to move and uplift a boulder is evaluated against the probable energy of the wave. This kinematic energy is the sum of the necessary friction energy (E_f), which estimates the transport in a horizontal direction ($X_{transport}$) by recognizing the mass of a boulder (m_b), the Earth's gravity (g), and a friction coefficient ($\mu = 0.65$) according to BENNER et al. (2010), and the energy of height (E_h) or uplift, which is similarly built by the implementation of the height a.p.s.l. (H_{uplift}). In the case of eq. 4.2, the wave height is derived as the relation of E_{kin} and the wave energy, assumed by the wave length (L) per metre, water density ρ_w , the Earth's gravity g , acting on a boulder with a certain width (axis length a). The wave length (L) is mathematically derived by the estimation of the wave length in open water (L_0) as a function of the wave period (T) at a certain water depth ($d = 1$ m). The wave period of eq. 4.4 allows the estimation of wave heights and wave velocities for storm and tsunami scenarios. The wave period of storms is several seconds, whereas tsunami waves could last for several minutes or hours. Thus, 20 sec. are used here for the storm scenario and 300 sec. are estimated for the tsunami case (WOODROFFE, 2002). This is of additional importance in the case of eq. 4.5, where the wave velocity is inferred from the proportion between E_{kin} and the wave energy acting on the front face of the boulder (product of the length of axes a and c). The latter area is reduced as being not rectangular by the factor q that is set to 0.73 (ENGEL & MAY, 2012).

The results for the wave velocity, calculated for all boulders using the eq. 4.6, were compared to the data resulting from the equations of NOORMETS et al. (2004), ETIENNE et al. (2011) and ENGEL & MAY (2012). The equation by NOORMETS et al. (2004) reflects also the scenario of a submerged boulder. The coefficient of drag (C_d) is generally set to 1.95 (NOORMETS et al., 2004; ETIENNE et al., 2011; ENGEL & MAY, 2012). The minimum velocity v_t for sliding is calculated by:

$$v_t = \sqrt{\frac{2\mu m_b g}{C_d q a c \rho_w}} \quad (\text{eq. 4.7})$$

ETIENNE et al. (2011) developed an equation to calculate the minimum velocity for overturning:

$$v_t = \sqrt{\frac{b m_b g}{0.5 C_d q a c^2 \rho_w}} \quad (\text{eq. 4.8})$$

The equations presented by ENGEL & MAY (2012) include adjustments based on several existing approaches. The presumed pre-transport scenario is a joint-bounded boulder scenario (JBBS), which assumes an initial quarrying out of cliff edges and a subsequent sliding scenario.

$$H_{t/s} = \frac{m_b (\cos \theta + \mu \sin \theta)}{2 \rho_w C_L q a b} \quad (\text{eq. 4.9})$$

As stated before, rolling or saltation are the most frequent transportation modes in the turbulent flow conditions of a tsunami wave. Thus, for that scenario, a different equation is given by ENGEL & MAY (2012) and BARBANO et al. (2010) that results in minimum values, where movement of this type ends:

$$H_{t/s} = \frac{0.5 \mu m_b}{C_D q a c \rho_w} \quad (\text{eq. 4.10})$$

In particular, the latter values are compared to wave decay curves derived from the equation of BARBANO et al. (2010) and ENGEL & MAY (2012):

$$H_i = \left(\sqrt{H_w - E} - \frac{5 X_i}{T \sqrt{g}} \right)^2 \quad (\text{eq. 4.11})$$

where H_i is the height at a certain distance X_i , reduced by the difference of the estimated wave height H_w and the mean elevation (E). The wave height H_w is in this case delivered by the maximum tsunami wave height from eq. 4.9 for each site and the according storm wave height, which is four times higher than the tsunami wave height. Several authors add scenarios that fit to the specific region or have been observed by eye-witnesses (BARBANO et al., 2010; ENGEL & MAY, 2012). In this study, a tsunami scenario with an inundation height of 4 m is added, which matches to the result of the numerical simulations in the Gulf of Kyparissia, Peloponnese by RÖBKE et al. (2013). For the storm case, a stronger storm scenario ($H_i=13.6$ m) is evolved according to BARBANO et al. (2010). The mean of the twenty maximum values of the maximum wave height (12.3 m) and associated wave periods (13 s) between 2008 and 2011 of buoy data (buoys: Zakythos and Pylos) from the Poseidon network (HCMR, 2013) is taken into account, which reflects the whole survey period. This averaging diminishes overestimations, due to buoy malfunctions. Higher storm wave heights are possible.

All these presented equations incorporate the mass, which was achieved by the combination of the 3D model-based volume and density measurement for each studied boulder. 3D model-based calculations of mass were subsequently compared to results derived from conventional approaches using the length of boulder axes and approximated density values.

4.3.3 Annual monitoring of coastal sites

For the annual measurements, the base point of the RTK-DGPS base station was marked by a metal screw and the point was measured 500 times to achieve a mean position. All measurements in relation to this base point were within the stated accuracy of ~ 1 cm (section 3.2). Additionally, in each year similar scan positions were chosen. Noise and outliers were removed manually or by semi-automatic functions. An HRDEM with a resolution of 10 cm was established for each year and each area by interpolation of the reduced point clouds. The triangulation was conducted by the plane triangulation function (section 3.5.4) with small maximum edge lengths to avoid a triangulation of areas with no points. Finally, the HRDEMs of every site and the individual years were compared to each other by building the difference of two consecutive years. For a generalized visualisation, the gridded values of elevation change were imported in ArcMap and interpolated. Changes smaller than 10 cm were neglected. The derived raster values can be used to estimate the volumetric change by multiplication of the derived height change with the cell size area. The results were controlled by photos from the digital camera and by using the CloudCompare software (GIRARDEAU-MONTAUT, 2013) to avoid misinterpretation.

4.4 General results

During the field campaigns of the years 2008 to 2011, TLS and RTK-DGPS measurements were carried out and resulted in 3D models of the dislocated boulders, as well as additional parameters for wave transport equations. As an example, the imbrication train of the boulders ELA-B28 to ELA-B31 from Cape Skalas, Peloponnese is presented in Figure 4-6. In addition, annual changes of the sediment budget of selected coastal sites on the Ionian Islands and the western Peloponnese were detected by the comparison of TLS-based HRDEMs.

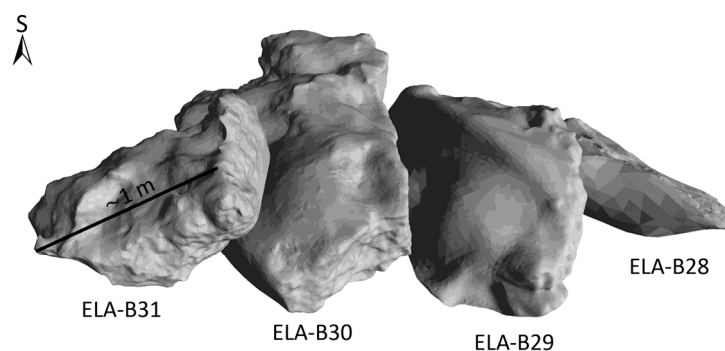


Figure 4-6: Perspective view of the imbrication train of the triangulated boulders ELA-B28 to ELA-B31 at Cape Skalas, Peloponnese. Modified after HOFFMEISTER et al. (2013a).

4.4.1 3D model-based measurements of dislocated boulders

All parameters from the 3D models of the dislocated boulders, as well as mass calculations based on rock density analyses (3D mass), are listed in Table 4-1. The table also shows the volume calculated by multiplying the different axes (calc.) based on a cubic scenario and the estimated masses calculated with

estimated density values (est.). For the boulders in the area of Cape Skalas, a density of 2.1 g/cm^3 was used (SCHEFFERS et al., 2008); for the limestone in the area of Cape Gerogombos a density of 2.3 g/cm^3 is suggested, as well as 2.5 g/cm^3 for the areas of Katakolo and Ag. Pelagia. For the latter areas, no density measurements were conducted. The distance to the sea (d.t.s.) is measured from the centre of the boulder to the nearest point of the present shoreline. The same procedure was used for the determination of the elevation a.p.s.l.

Generally, most values of the 3D model-based masses in Table 4-1 are considerably smaller than masses calculated with the measurement of boulder axes. Obviously, the difference is bigger for bigger boulders. The 3D model-based mass data are site dependent generally by 12-44 % smaller than calculations using the volumes based on axes calculations and estimated densities, with the greatest difference having been calculated for boulder ELA-B29, which exhibits only 43% of the estimated mass. Several exceptional boulders, depending on their irregular shape, show nearly similar or bigger values (>90%) for the achieved 3D mass, in contrast to their estimated mass. These are for example ELA-B31, ELA-B32, KAT-5, PEL-10, SCI-5, SCI-7, SCI-18 and SCI-23. The boulders of Cape Skalas, southern Peloponnese, are located more closely to the present sea-level as well as being situated at the lowest height above present sea-level, in comparison to all other observed areas. The highest position above present sea level is noted for the boulders from the area of Ag. Pelagia, which are located on a cliff-top platform. The biggest boulder (SCI-4) is found at Cape Schinou, Cefalonia Island, with a mass of 25.4 t.

Table 4-1: Overview of volume, density and mass data of dislocated boulders by conventional and 3D model based approaches. Note: a.p.s.l. = above present sea level, d.t.s. = distance to sea, est. = estimated parameters, calc. = calculated by multiplying the axes, 3D = achieved by 3D analysis

boulder -Id	a.p.s.l. [m]	d.t.s. [m]	a-, b-, c-axis [m]			calc. vol. [m ³]	est. density [g/cm ³]	est. Mass [t]	meas. density [g/cm ³]	3D volume [m ³]	3D mass [t]	ratio meas. to est. density [%]	ratio 3D to est. mass [%]
Area of Cape Skalas, Peloponnese													
ELA-B28	0.5	10.9	1.7	0.9	0.4	0.6	2.1	1.3	2.3	0.5	1.1	109	82
ELA-B29	0.6	9.9	2.0	1.1	0.7	1.5	2.1	3.2	2.3	0.6	1.4	110	43
ELA-B30	0.6	8.5	2.5	1.2	0.6	1.8	2.1	3.8	2.2	0.9	2.1	106	55
ELA-B31	0.4	7.8	1.2	0.6	0.5	0.4	2.1	0.8	2.3	0.3	0.7	109	91
ELA-B32	0.4	2.8	2.0	1.5	0.3	0.9	2.1	1.9	2.3	1.3	3.0	107	158
ELA-B33	0.5	2.0	1.8	1.9	0.6	2.1	2.1	4.3	2.4	1.2	2.9	116	67
ELA-B34	0.4	1.7	2.4	1.5	0.6	2.2	2.1	4.5	2.3	1.2	2.8	111	61
ELA-B35	0.9	3.5	1.9	1.9	0.4	1.4	2.1	3.0	2.6	1.1	2.7	122	91
ELA-B36	0.9	1.2	1.9	1.0	0.6	1.1	2.1	2.4	2.4	0.5	1.1	113	45
ELA-B37	0.5	1.3	2.2	1.8	0.6	2.4	2.1	5.0	2.3	1.3	3.0	111	59
ELA-B38	0.4	0.7	1.7	1.2	0.6	1.2	2.1	2.6	2.3	0.7	1.6	110	63
ELA-B39	0.4	1.1	2.2	1.7	0.6	2.2	2.1	4.7	2.2	1.2	2.7	107	56
ELA-B40	0.4	1.3	3.0	1.5	0.8	3.6	2.1	7.6	2.3	1.9	4.4	110	58
\bar{X}	0.5	4.1	2.0	1.4	0.6	1.7	2.1	3.5	2.3	1.0	2.3	111	71
SD	0.2	3.6	0.4	0.4	0.1	0.8		1.7	0.1	0.4	1.0	4	29
Area of Katakolo, Peloponnese													
KAT-1	3.1	32.7	2.3	1.8	0.9	3.7	2.5	9.3		2.6	6.5		70
KAT-2	2.8	35.0	2.2	1.4	0.7	2.2	2.5	5.4		1.5	3.8		71
KAT-3	3.0	34.0	1.7	1.3	0.8	1.8	2.5	4.4		1.3	3.3		75
KAT-4	2.8	33.5	1.1	0.8	0.8	0.7	2.5	1.8		0.5	1.3		71
KAT-5	3.0	34.5	1.3	1.3	0.7	1.2	2.5	3.0		1.1	2.8		93
KAT-6	1.5	21.8	2.5	1.8	0.7	3.2	2.5	7.9		2.1	5.4		68
KAT-7	1.4	26.4	0.8	1.1	0.9	0.8	2.5	2.0		0.6	1.5		76
KAT-8	1.4	24.5	1.5	1.3	0.8	1.6	2.5	3.9		1.2	3.0		77
KAT-9	2.6	33.7	1.4	1.3	1.0	1.8	2.5	4.6		1.1	2.8		60
KAT-10	2.7	34.7	1.7	1.6	0.8	2.2	2.5	5.4		1.1	2.7		50
KAT-11	2.9	33.8	1.3	1.7	0.7	1.5	2.5	3.9		0.9	2.3		60
KAT-12	2.8	33.8	1.7	1.3	0.7	1.5	2.5	3.9		1.3	3.3		86
KAT-13	3.8	37.6	1.3	1.2	0.5	0.8	2.5	2.0		0.5	1.3		64
KAT-14	3.5	36.7	1.3	0.8	0.6	0.6	2.5	1.6		0.4	1.0		64
KAT-15	2.8	35.9	1.6	2.2	0.8	2.8	2.5	7.0		1.4	3.6		51
KAT-16	3.4	35.4	0.7	1.4	0.6	0.6	2.5	1.5		0.5	1.3		85
\bar{X}	2.7	32.8	1.5	1.4	0.8	1.7	2.5	4.2		1.1	2.9		70
SD	0.7	4.3	0.5	0.4	0.1	0.9		2.3		0.6	1.5		12
Area of Aghia Pelagia, Cefalonia Island													
PEL-1	4.3	17.9	1.7	1.3	0.7	1.5	2.5	3.9		0.9	2.3		58
PEL-2	4.0	19.9	2.4	2.0	0.7	3.4	2.5	8.4		2.4	6.0		71
PEL-3	3.9	15.8	1.8	1.1	1.0	2.0	2.5	5.0		1.8	4.5		91
PEL-4	3.9	17.2	1.2	0.8	0.5	0.5	2.5	1.2		0.4	1.0		83
PEL-5	3.9	17.5	1.6	1.4	0.7	1.6	2.5	3.9		0.8	2.0		51
PEL-6	4.0	18.5	1.8	1.9	0.6	2.1	2.5	5.1		1.4	3.5		68
PEL-ST	4.2	4.5	2.0	0.9	0.6	1.1	2.5	2.7		0.9	2.3		83
PEL-7	5.1	16.3	2.2	1.6	0.6	2.1	2.5	5.3		1.3	3.3		62
PEL-8	4.0	14.0	2.7	1.7	0.8	3.7	2.5	9.2		2.0	5.0		54
\bar{X}	4.1	15.7	1.9	1.4	0.7	2.0	2.5	5.0		1.3	3.3		67
SD	0.4	4.3	0.4	0.4	0.1	1.0		2.4		0.6	1.5		64

boulder -Id	a.p.s.l. [m]	d.t.s. [m]	a-, b-, c-axis [m]			calc. vol. [m ³]	est. density [g/cm ³]	est. Mass [t]	meas. density [g/cm ³]	3D volume [m ³]	3D mass [t]	ratio meas. to est. density [%]	ratio 3D to est. mass [%]
Area of Cape Geragombos, Cefalonia Island													
GER-ST5	3.2	62.4	3.4	3.2	0.9	9.8	2.3	22.5	2.5	4.5	11.4	110	50
GER-top	1.9	40.3	3.5	2.8	0.9	8.8	2.3	20.3	2.5	5.0	12.5	110	62
GER-base	2.0	41.5	3.0	2.4	1.0	7.2	2.3	16.6	2.5	3.8	9.5	110	57
\bar{X}	2.4	48.1	3.3	2.8	0.9	8.6	2.3	19.8	2.5	4.4	11.1	110	56
SD	0.6	10.1	0.2	0.3	0.0	1.1		2.5		0.5	1.2		5
Area of Cape Schinou, Cefalonia Island													
SCI-1	3.2	11.0	1.7	2.8	0.9	4.3	2.3	9.9		2.9	6.6		67
SCI-2	1.5	15.0	2.6	1.1	0.9	2.6	2.3	5.9		2.0	4.5		76
SCI-3	1.5	16.5	1.3	1.3	1.0	1.7	2.3	3.9		1.1	2.4		63
SCI-4	1.9	28.1	5.3	2.2	1.5	17.5	2.3	40.2		11.1	25.4		63
SCI-5	2.4	29.3	0.7	0.9	0.6	0.4	2.3	0.9		0.4	0.9		106
SCI-6	2.2	27.9	0.7	1.6	0.6	0.7	2.3	1.5		0.7	1.5		100
SCI-7	2.5	27.4	1.0	1.7	0.5	0.9	2.3	2.0		0.9	2.1		108
SCI-8	1.9	27.9	0.9	1.2	0.7	0.7	2.3	1.6		0.5	1.2		73
SCI-9	1.9	29.9	1.7	1.1	1.0	1.9	2.3	4.3		1.2	2.8		65
SCI-10	1.8	28.9	1.4	3.3	0.8	3.8	2.3	8.8		2.8	6.5		74
SCI-11	3.3	37.9	0.9	0.4	0.6	0.2	2.3	0.5		0.3	0.7		148
SCI-12	3.3	39.3	0.9	0.7	0.4	0.3	2.3	0.6		0.2	0.6		95
SCI-13	3.4	40.8	0.9	0.8	0.6	0.4	2.3	1.0		0.2	0.5		51
SCI-14	1.2	28.0	1.5	2.5	1.0	3.8	2.3	8.6		3.0	6.9		80
SCI-15	1.2	34.9	0.8	1.5	0.9	1.1	2.3	2.5		1.0	2.4		96
SCI-16	2.7	36.2	1.8	1.2	1.2	2.6	2.3	6.0		2.0	4.6		77
SCI-17	3.7	43.7	0.7	0.8	0.5	0.3	2.3	0.6		0.3	0.6		100
SCI-18	3.7	35.5	0.8	0.8	0.5	0.3	2.3	0.7		0.7	1.7		228
SCI-19	1.1	26.5	0.7	0.7	0.5	0.2	2.3	0.6		0.2	0.5		90
SCI-20	1.8	32.3	2.0	0.8	0.4	0.6	2.3	1.5		0.6	1.3		91
SCI-21	0.4	22.4	3.0	1.7	1.9	9.7	2.3	22.3		5.8	13.4		60
SCI-22	0.5	25.1	1.9	1.2	1.3	3.0	2.3	6.8		2.2	5.0		74
SCI-23	1.1	29.1	1.6	1.2	0.6	1.2	2.3	2.6		1.1	2.5		93
SCI-24	1.4	31.5	2.5	1.3	0.9	2.9	2.3	6.7		3.2	7.3		109
SCI-25	1.9	31.5	1.3	1.6	0.9	1.9	2.3	4.3		1.5	3.4		78
SCI-26	0.9	27.0	1.6	1.0	1.0	1.6	2.3	3.7		1.1	2.6		69
SCI-27	1.4	21.1	2.0	2.8	0.8	4.5	2.3	10.3		3.2	7.5		72
SCI-28	1.4	28.4	1.8	1.9	1.0	3.4	2.3	7.9		2.3	5.2		66
SCI-29	1.8	25.9	1.6	0.8	1.0	1.3	2.3	2.9		0.9	2.0		68
\bar{X}	2.0	28.9	1.6	1.4	0.8	2.5	2.3	5.8		1.8	4.2		88
SD	0.9	7.2	0.9	0.7	0.3	3.4		7.9		2.1	4.9		33

Table continued from previous page

As a result of the analyses, detailed maps of the study areas were established. These are based on topographical data and created from the point clouds of the TLS surveys. The maps show boulder shapes, the coastline and contour lines, which have all been derived from TLS and RTK-DGPS data (Figure 4-7). Boulders that were selected for the application of wave transport equations can be identified by their boulder ID. Further maps of the other areas can be found in section 4.4.2 in combination with annual change comparisons.

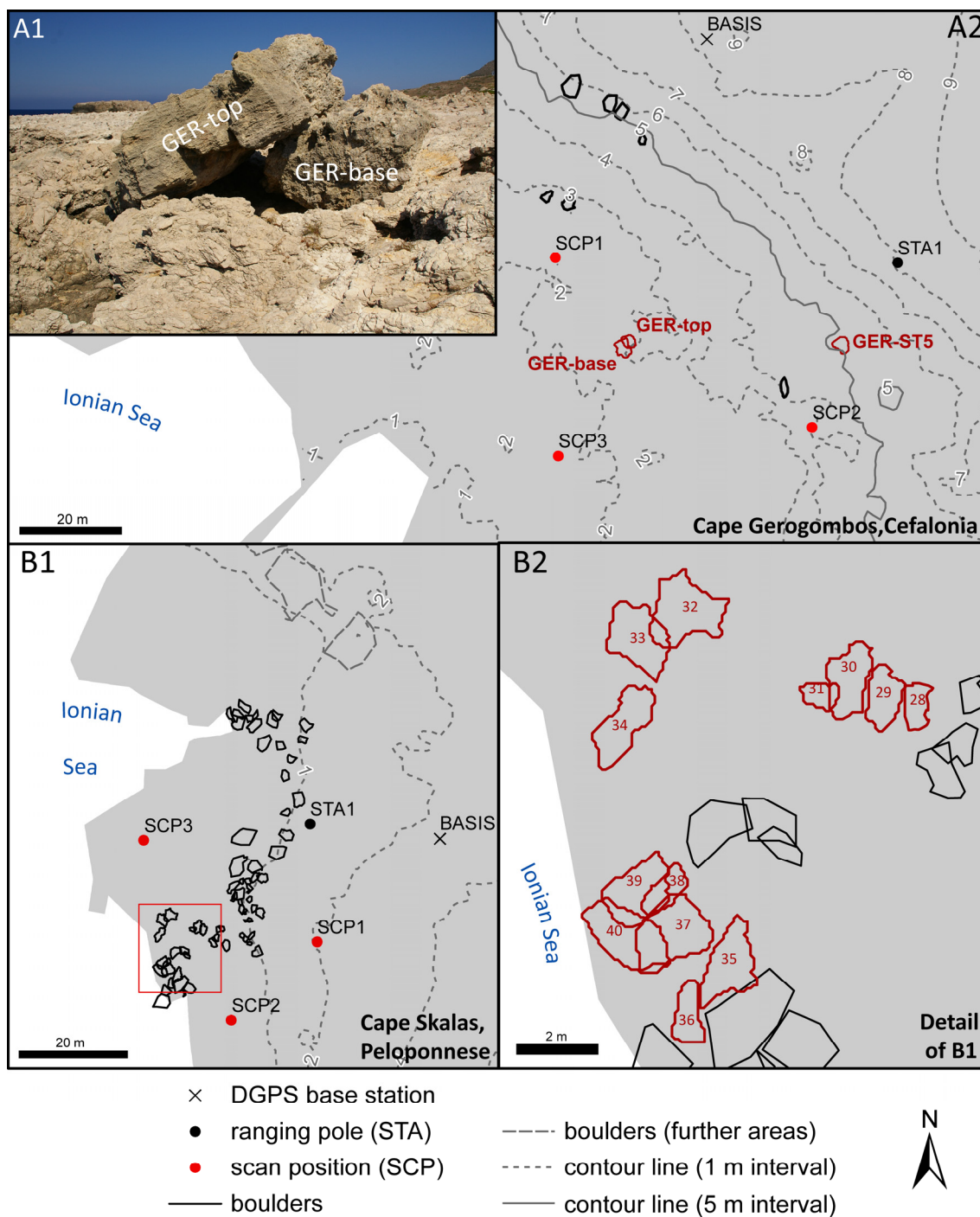


Figure 4-7: Maps of Cape Skalas (Peloponnese) and Cape Gerogombos (Cefalonia Island) based on topographical information and elevation contours created by TLS surveys. The maps also show the arrangements of ranging poles and scan positions for the individual study areas. A1 is a photo of the two dislocated boulders scanned by TLS and depicted in A2. Photo taken by C. Curdt, 2008. A2 shows the survey site of Cape Gerogombos with scan positions (SCP1 to SCP3) and the shape of extracted boulders. B1 gives an overview of the study site at Cape Skalas. B2 displays a detailed map with boulders indicated by numbers (inset box in B1). Modified after Hoffmeister et al. (2013a).

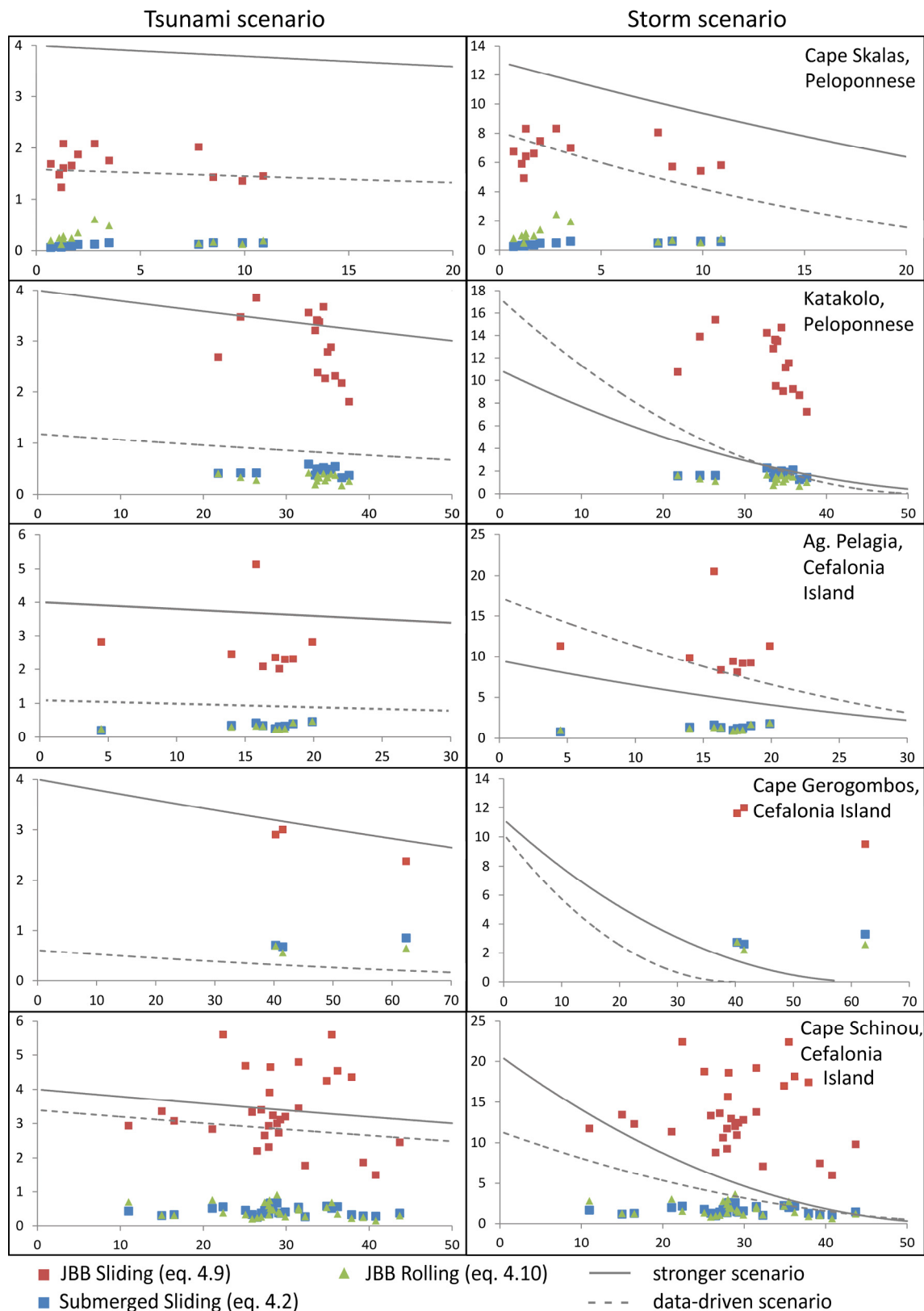


Figure 4-8: Graphs for tsunami and storm cases for all sites in western Greece. The graphs consist of the different minimum wave heights from denoted equations and wave decay curves directly derived from this data as well as estimated, stronger scenarios for the storm and tsunami cases. Note: x-axis = d.t.s. [m]; y-axis = wave height [m].

Figure 4-8 summarizes the main results of the wave transport equations. Wave decay curves for tsunami and storm scenarios were derived by applying eq. 4.11. For each scenario type, two different wave decay curves were computed. One is the data-driven scenario with the highest wave height of the according location derived from eq. 4.9, the other is the stronger scenario regarding a simulated 4 m inundation depth for the tsunami case and the extracted maximum wave heights and periods from buoy data for the storm case. These have been combined with the derived tsunami and storm wave heights for all areas and all boulders in the graphs of Figure 4-8. As expected, all values are relatively small, which is the result of incorporating smaller boulder masses, as well as using generally smaller boulders in comparison to other regions of the world. In the subsequent tables (Table 4-2-Table 4-5), all achieved values are listed with regard to the tsunami and storm cases for each specific site. In addition, the important values of 3D model-based masses, distance to sea and height above present sea-level according to Table 4-1 are shown. For each area, mean values and standard deviations are stated.

Generally, eq. 4.9 yields higher values for the minimum wave heights concerning the joint-bounded pre-transport setting for all scenarios. This is also true for the minimum wave velocities derived by eq. 4.8 regarding an overturning of the boulders. All values derived by the equations of BENNER et al. (2010) are very small, as well as the values of eq. 4.10. Both are equations that show minimum values, where presumably dislocation ends. The other equations focus on the initial processes for transport. Furthermore, the equations of BENNER et al. (2010) take into account how far a dislocated boulder was transported inland (distance from the coast) and to what extent it was up-lifted (elevation above present sea-level), whereas the other equations do not.

Cape Skalas, Peloponnese

The minimum wave heights and velocities calculated for the area of Cape Skalas, Peloponnese (ELA-B28-B40) near Elaphonissos Island are the smallest of all generated values (Table 4-2). This corresponds with the small size of the thirteen boulders (\emptyset 2.3 t) and their location (Figure 4-7). Mostly, the boulders are imbricated. Several boulders, like ELA-B32, ELA-B34 and ELA-B36 show higher values for the derived minimum tsunami velocities of eq. 4.7 and eq. 4.8. The group of boulders ELA-B28 to ELA-B31 lies further inland and shows slightly higher values for the equations of BENNER et al. (2010) (eq. 4.2 and eq. 4.6) with regard to similar sized boulders, e.g. ELA-B36. The heaviest boulder ELA-B40 is not the boulder with the highest values for all equations, which is a result of the incorporation of several factors beside the mass. Although, there is evidence of tsunami impact based on the fine-grained sediment deposits (SCHEFFERS et al., 2008; NTAGERETZIS et al., 2012), the estimated minimum storm wave heights are very small and storms might be capable to move these boulders initially from a joint-bounded location. This is also depicted in the graph in Figure 4-8. All derived values for the minimum tsunami wave heights are below 4 m and below 10 m for the storm scenario.

Table 4-2: Results of different wave transport equations of tsunami and storm scenarios for the area of Cape Skalas, Peloponnese

boulder - id	a.p.s.l. [m]	d.t.s. [m]	3D mass [t]	eq. 4.2 height [m]	eq. 4.9 height [m]	eq.4.10 height [m]	eq. 4.6 vel. [m/s]	eq. 4.7 vel. [m/s]	eq. 4.8 vel. [m/s]	eq. 4.2 height [m]	eq. 4.9 height [m]	eq.4.10 height [m]
			<i>Tsunami scenario</i>						<i>Storm scenario</i>			
ELA-B28	0.5	10.9	1.1	0.1	1.5	0.2	0.8	2.7	5.1	0.6	5.8	0.8
ELA-B29	0.6	9.9	1.4	0.2	1.4	0.1	0.7	2.2	3.4	0.6	5.4	0.5
ELA-B30	0.6	8.5	2.1	0.2	1.4	0.2	0.7	2.6	4.5	0.6	5.7	0.7
ELA-B31	0.4	7.8	0.7	0.1	2.0	0.1	0.7	2.4	3.2	0.5	8.1	0.6
ELA-B32	0.4	2.8	3.0	0.1	2.1	0.6	0.8	4.9	13.6	0.5	8.3	2.4
ELA-B33	0.5	2.0	2.9	0.1	1.9	0.3	0.6	3.7	8.1	0.5	7.5	1.4
ELA-B34	0.4	1.7	2.8	0.1	1.7	0.2	0.5	3.1	6.0	0.3	6.6	1.0
ELA-B35	0.9	3.5	2.7	0.2	1.7	0.5	0.8	4.4	11.8	0.6	7.0	2.0
ELA-B36	0.9	1.2	1.1	0.1	1.2	0.1	0.4	2.2	3.5	0.3	4.9	0.5
ELA-B37	0.5	1.3	3.0	0.1	1.6	0.3	0.5	3.3	7.2	0.4	6.4	1.1
ELA-B38	0.4	0.7	1.6	0.1	1.7	0.2	0.4	2.8	4.9	0.2	6.7	0.8
ELA-B39	0.4	1.1	2.7	0.1	1.5	0.2	0.5	3.1	6.5	0.3	5.9	1.0
ELA-B40	0.4	1.3	4.4	0.1	2.1	0.2	0.5	3.0	5.1	0.4	8.3	0.9
\bar{X}	0.5	4.1	2.3	0.1	1.7	0.3	0.6	3.1	6.4	0.4	6.7	1.0
SD	0.2	3.6	1.0	0.0	0.3	0.1	0.2	0.8	3.1	0.1	1.1	0.6

Katakolo, Peloponnese

The sixteen boulders of the area of Katakolo, western Peloponnese are generally bigger and are lying at a considerably greater distance to the sea (\emptyset 32.8 m) and are more elevated (\emptyset 2.9 m) than the ones discussed earlier (Table 4-3). These conditions result in higher values for all cases, in comparison with the previously presented areas, particularly for the results of eq. 4.9. The site was monitored annually and the map with the annual changes and the boulders is shown in Figure 4-8. Most of the dislocated boulders are arranged along a N-S trending line parallel to the trim line, which can be observed in this area. However, there are three exceptions, namely boulders KAT 6 to 8. These boulders are located at an edge further towards the sea (\emptyset 25 m). This pattern is also depicted in Figure 4-8, where two linear groups are distinguishable. The wave heights necessary for initial transport in a joint-bounded scenario for several boulders are not reached by the stronger tsunami scenario. Hence, the strongest storm scenario is not capable to even initiate such boulder movement. The inundation values of both storm scenarios hardly reach the minimum storm wave heights required for all transport equations, except the previously mentioned group, which may be inundated and moved (eq. 4.2 and eq. 4.10).

Table 4-3: Results of different wave transport equations of tsunami and storm scenarios for the area of Katakolo, Peloponnese.

boulder - id	a.p.s.l. [m]	d.t.s. [m]	3D mass [t]	eq. 4.2 height [m]	eq. 4.9 height [m]	eq.4.10 height [m]	eq. 4.6 vel. [m/s]	eq. 4.7 vel. [m/s]	eq. 4.8 vel. [m/s]	eq. 4.2 height [m]	eq. 4.9 height [m]	eq.4.10 height [m]
Tsunami scenario										Storm scenario		
KAT-1	3.1	32.7	6.5	0.6	3.6	0.4	1.6	4.0	7.1	2.3	14.2	1.7
KAT-2	2.8	35.0	3.8	0.5	2.8	0.3	1.5	3.6	6.3	1.8	11.1	1.3
KAT-3	3.0	34.0	3.3	0.5	3.4	0.3	1.5	3.6	5.6	1.9	13.5	1.3
KAT-4	2.8	33.5	1.3	0.4	3.2	0.2	1.2	2.7	3.4	1.4	12.8	0.8
KAT-5	3.0	34.5	2.8	0.5	3.7	0.4	1.6	4.0	6.7	2.0	14.7	1.6
KAT-6	1.5	21.8	5.4	0.4	2.7	0.4	1.4	4.0	7.9	1.6	10.7	1.6
KAT-7	1.4	26.4	1.5	0.4	3.8	0.3	1.3	3.3	4.5	1.6	15.4	1.1
KAT-8	1.4	24.5	3.0	0.4	3.5	0.3	1.3	3.6	5.7	1.6	13.9	1.3
KAT-9	2.6	33.7	2.8	0.5	3.4	0.3	1.4	3.2	4.5	1.9	13.6	1.0
KAT-10	2.7	34.7	2.7	0.4	2.3	0.3	1.4	3.2	5.7	1.7	9.0	1.1
KAT-11	2.9	33.8	2.3	0.5	2.4	0.3	1.5	3.6	7.0	1.8	9.5	1.4
KAT-12	2.8	33.8	3.3	0.5	3.4	0.4	1.5	3.8	6.4	1.9	13.6	1.5
KAT-13	3.8	37.6	1.3	0.4	1.8	0.3	1.4	3.2	6.1	1.4	7.2	1.0
KAT-14	3.5	36.7	1.0	0.3	2.2	0.2	1.2	2.6	3.7	1.2	8.7	0.7
KAT-15	2.8	35.9	3.6	0.5	2.3	0.4	1.6	3.8	7.9	2.1	9.2	1.5
KAT-16	3.4	35.4	1.3	0.5	2.9	0.4	1.6	3.9	7.5	1.9	11.5	1.6
\bar{X}	2.7	32.8	2.9	0.5	3.0	0.3	1.4	3.5	6.0	1.8	11.8	1.3
SD	0.7	4.3	1.5	0.1	0.6	0.1	0.1	0.4	1.4	0.3	2.4	0.3

Aghia Pelagia, Cefalonia Island

For the area of Ag. Pelagia, Cefalonia Island, nine boulders are presented (Table 4-4), which are located on a cliff-top platform (\emptyset 4 m a.p.s.l.). Again, the boulders are lying in a notional NE-SW trending line parallel to the southeastern fringe of the cliff-top platform, ~17 m away from the present shoreline (Figure 4-12). A second line of dislocated boulders was found to the northwest of the depicted section running perpendicularly in a NW-SE direction parallel to the strike of the ramp-like topography. With regard to this elevated position, the required tsunami wave heights and wave velocities are similar, but slightly larger than those of the previously presented area of Katakolo, Peloponnese. The derived wave heights for initial joint-bounded pre-transport setting, as depicted in Figure 4-8 are within the expected range of the stronger tsunami scenario, but not in the range of the calculated tsunami scenario. This again is similar to the values calculated for Katakolo. Boulder PEL-3 is an outlier, which could not be moved by any of the tsunami and storm scenarios for the joint-bounded pre-transport setting and shows considerably higher values for all equations. Considering a submerged pre-transport scenario all boulders can be moved in all scenarios.

However, the boulder PEL-ST represents another outlier concerning its position close to the fringe of the cliff-top platform. Moreover, its surface is of reddish colour indicating that the boulder has recently been broken out of the weathered bedrock (Figure 4-9). The source area of boulder PEL-ST is easily detectable, as the nearby origin is characterised by the same colour and the fresh-looking fracture. The boulder PEL-ST can be linked to smaller estimated wave heights and velocities using the eq. 4.2 and eq. 4.6 in comparison to the boulder PEL-1, which is of equal weight.

Table 4-4: Results of different wave transport equation of tsunami and storm scenarios for the area of Ag. Pelagia, Cefalonia Island.

boulder - id	a.p.s.l. [m]	d.t.s. [m]	3D mass [t]	eq. 4.2 height [m]	eq. 4.9 height [m]	eq.4.10 height [m]	eq. 4.6 vel. [m/s]	eq. 4.7 vel. [m/s]	eq. 4.8 vel. [m/s]	eq. 4.2 height [m]	eq. 4.9 height [m]	eq.4.10 height [m]
Tsunami scenario										Storm scenario		
PEL-1	4.3	17.9	2.3	0.3	2.3	0.3	1.2	3.1	5.3	1.3	9.2	1.0
PEL-2	4.0	19.9	6.0	0.5	2.8	0.5	1.5	4.3	9.0	1.8	11.3	1.9
PEL-3	3.9	15.8	4.5	0.4	5.1	0.3	1.2	3.6	4.7	1.6	20.5	1.3
PEL-4	3.9	17.2	1.0	0.2	2.4	0.2	1.1	2.9	4.6	1.0	9.4	0.9
PEL-5	3.9	17.5	2.0	0.3	2.0	0.2	1.1	3.0	5.3	1.2	8.1	0.9
PEL-6	4.0	18.5	3.5	0.4	2.3	0.4	1.4	4.1	9.1	1.5	9.2	1.7
PEL-ST	4.2	4.5	2.3	0.2	2.8	0.2	0.9	3.1	4.7	0.8	11.3	1.0
PEL-7	5.1	16.3	3.3	0.3	1.5	0.2	1.3	3.6	7.2	1.3	5.8	0.8
PEL-8	4.0	14.0	5.0	0.3	1.4	0.1	1.2	3.5	6.3	1.3	5.4	0.5
\bar{X}	4.0	15.9	3.1	0.3	2.8	0.3	1.2	3.5	6.1	1.3	11.3	1.3
SD	0.1	4.8	1.6	0.1	1.0	0.1	0.2	0.5	1.9	0.3	3.9	0.4



Figure 4-9: Dislocated boulders encountered at the study site at Aghia Pelaghia (Cefalonia Island). The boulders are arranged in a line (left middleground) except boulder PEL-ST, which lies considerably closer to the cliff (Table 4-4). Pole in front of the boulder line is 2 m long. Modified after HOFFMEISTER et al. (2013b).

Cape Gerogombos and Cape Schinou, Cefalonia Island

Cape Gerogombos on Cefalonia Island (Figure 4-7) and Cape Schinou (Figure A-3) are located in close proximity to one another (Figure 4-3). Both sites comprise bigger boulders, with the largest boulder of all sites being located at Cape Schinou (SCI-4, 25.4 t), as denoted in Table 4-5. The boulders at Cape Schinou showed no movement during the monitoring period. The graphs in Figure 4-8 for the Gerogombos site show that tsunami-induced movement is only possible by the stronger tsunami scenario, whereas storm waves do not reach the boulders in any scenario. For the boulders at Cape

Schinou, initial cracking and dislocation is possible for some of the smaller boulders, but about 10 boulders need higher tsunami wave heights for initial transport from a joint-bounded pre-transport setting. Storm related movement is possible for the smaller boulders of the site.

Table 4-5: Results of different wave transport equation of tsunami and storm scenarios for the area of Cape Gerogombos and Schinou, Peloponnese.

boulder - id	a.p.s.l. [m]	d.t.s. [m]	3D mass [t]	eq. 4.2 height [m]	eq. 4.9 height [m]	eq.4.10 height [m]	eq. 4.6 vel. [m/s]	eq. 4.7 vel. [m/s]	eq. 4.8 vel. [m/s]	eq. 4.2 height [m]	eq. 4.9 height [m]	eq.4.10 height [m]
Tsunami scenario										Storm scenario		
GER-ST5	3.2	62.4	11.4	0.9	2.4	0.6	2.0	5.2	10.0	3.3	9.5	2.6
GER-top	1.9	40.3	12.5	0.7	2.9	0.7	1.8	4.6	7.8	2.7	11.6	2.8
GER-base	2.0	41.5	9.5	0.7	3.0	0.6	1.7	5.2	10.0	2.6	12.0	2.2
\bar{X}	2.4	48.1	11.1	0.7	2.8	0.6	1.8	5.0	9.3	2.9	11.0	2.5
SD	0.6	10.1	1.2	0.1	0.3	0.1	0.1	0.3	1.0	0.3	1.1	0.2
SCI-1	3.2	11.0	6.6	0.1	2.9	0.7	1.3	5.2	10.0	1.7	11.7	2.8
SCI-2	1.5	15.0	4.5	0.1	3.4	0.3	1.0	3.5	4.2	1.2	13.4	1.3
SCI-3	1.5	16.5	2.4	0.1	3.1	0.3	1.0	3.5	4.3	1.3	12.3	1.2
SCI-4	1.9	28.1	25.4	0.9	4.6	0.5	1.5	4.5	5.9	2.6	18.6	2.1
SCI-5	2.4	29.3	0.9	0.7	3.1	0.4	1.3	3.7	5.0	1.4	12.4	1.4
SCI-6	2.2	27.9	1.5	0.7	2.9	0.6	1.5	4.8	8.6	1.8	11.7	2.4
SCI-7	2.5	27.4	2.1	0.4	2.7	0.7	1.6	5.2	10.4	1.7	10.6	2.8
SCI-8	1.9	27.9	1.2	0.3	2.3	0.3	1.3	3.6	5.3	1.3	9.3	1.3
SCI-9	1.9	29.9	2.8	0.3	3.2	0.3	1.2	3.2	3.7	1.6	12.8	1.1
SCI-10	1.8	28.9	6.5	0.7	3.0	0.9	1.8	6.0	12.9	2.6	12.0	3.6
SCI-11	3.3	37.9	0.7	0.4	4.4	0.2	1.2	3.0	2.6	1.3	17.4	0.9
SCI-12	3.3	39.3	0.6	0.5	1.9	0.2	1.3	3.1	4.5	1.1	7.5	1.0
SCI-13	3.4	40.8	0.5	0.4	1.5	0.2	1.1	2.4	3.1	1.1	6.0	0.6
SCI-14	1.2	28.0	6.9	0.3	3.9	0.7	1.6	5.4	9.3	2.5	15.6	3.0
SCI-15	1.2	34.9	2.4	0.4	4.2	0.5	1.6	4.6	6.5	2.2	17.0	2.2
SCI-16	2.7	36.2	4.6	0.7	4.5	0.3	1.4	3.7	4.0	2.2	18.1	1.4
SCI-17	3.7	43.7	0.6	0.3	2.4	0.3	1.4	3.4	4.7	1.4	9.8	1.2
SCI-18	3.7	35.5	1.7	0.3	5.6	0.7	1.8	5.2	7.1	2.0	22.4	2.7
SCI-19	1.1	26.5	0.5	0.3	2.2	0.2	1.1	3.0	3.9	1.0	8.8	0.9
SCI-20	1.8	32.3	1.3	0.6	1.8	0.3	1.2	3.3	5.0	1.0	7.1	1.1
SCI-21	0.4	22.4	13.4	0.6	5.6	0.4	1.2	3.9	4.0	2.2	22.4	1.5
SCI-22	0.5	25.1	5.0	0.6	4.7	0.3	1.2	3.6	3.8	1.8	18.7	1.3
SCI-23	1.1	29.1	2.5	0.4	2.7	0.4	1.4	4.0	6.2	1.5	10.9	1.7
SCI-24	1.4	31.5	7.3	0.5	4.8	0.5	1.5	4.6	5.9	2.1	19.2	2.1
SCI-25	1.9	31.5	3.4	0.2	3.4	0.5	1.5	4.3	6.2	2.0	13.8	1.9
SCI-26	0.9	27.0	2.6	0.3	3.4	0.3	1.1	3.2	3.5	1.4	13.6	1.0
SCI-27	1.4	21.1	7.5	0.6	2.8	0.8	1.5	5.5	11.1	2.0	11.3	3.0
SCI-28	1.4	28.4	5.2	0.5	3.2	0.5	1.4	4.3	6.4	2.0	13.0	1.9
SCI-29	1.8	25.9	2.0	0.4	3.3	0.2	1.0	2.8	2.7	1.3	13.3	0.8
\bar{X}	1.9	31.1	3.6	0.4	3.4	0.4	1.4	3.9	5.6	1.7	13.6	1.7
SD	1.0	5.8	3.1	0.1	1.2	0.2	0.2	0.9	2.6	0.5	4.6	0.8

4.4.2 Annual changes of coastal sites in western Greece

In order to distinguish rare high-energy events from annual changes, seven selected sites were monitored annually between 2009 and 2011. For this purpose, HRDEMs were established by interpolation from the filtered point clouds for each year and each site. These HRDEMs were compared and the results show the annual change. Here the sites of Cape Katakolo (western Peloponnese), Aghia

Pelagia (Cefalonia Island) and Kaminia Beach (Lefkada Island) are presented below and all other sites with similar results are shown in the appendix (Figure A-1 – A-4).

The annual changes of the sediment budget at Kaminia Beach are depicted in Figure 4-10. The sea weed that covered a large part of the beach in 2009, has mostly disappeared in 2010. In the westernmost part of the site, gravel of up to 30-50 cm in diameter was accumulated and transported inland. In total, the eroded volume amounts to $\sim 30 \text{ m}^3$ spreaded over an area of $\sim 93 \text{ m}^2$; in contrast, the accumulated volume amounts to $\sim 3 \text{ m}^3$ within an area of $\sim 14 \text{ m}^2$. Changes in the sediment budget between 2010 and 2011 were smaller. Only $\sim 7 \text{ m}^3$ of material was eroded in an area of $\sim 35 \text{ m}^2$, whereas $\sim 8 \text{ m}^3$ were accumulated in an area of $\sim 45 \text{ m}^2$, particularly in the central part of the study site. Similar results, in particular the stronger erosion between the first years, were detectable for Gialous Skala, located 3 km to the southwest (Figure A-4).

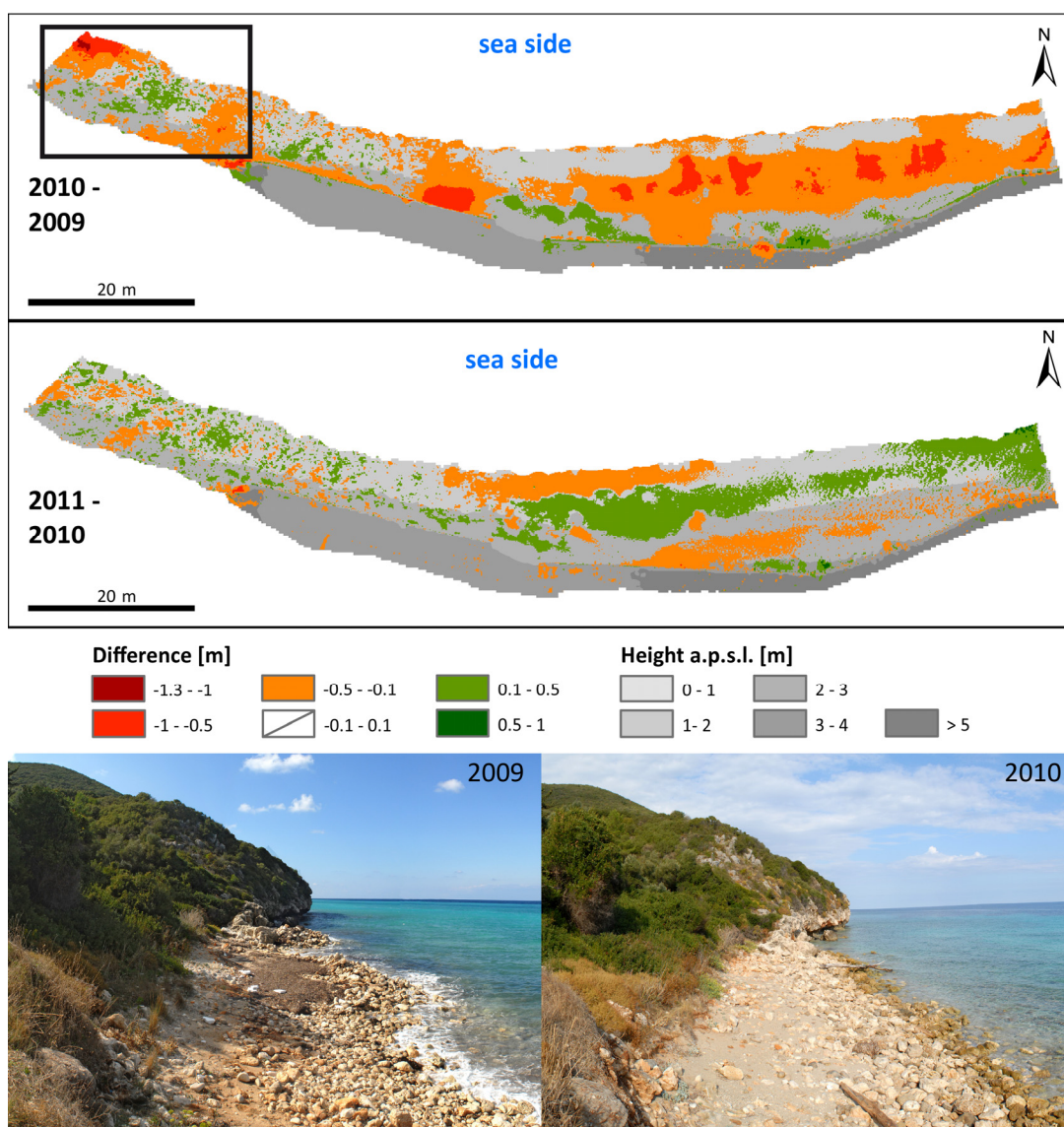


Figure 4-10: Annual sediment budget for the years 2009/2010 and 2010/2011 at Kaminia Beach, Lefkada Island, orange to red colours express erosion in comparison to the previous year, likewise green colors depict accumulation. Results are compared to photos from the western part of the study area (black rectangle), which document the different conditions in 2009 and 2010, respectively. Modified after HOFFMEISTER et al. (2013b).

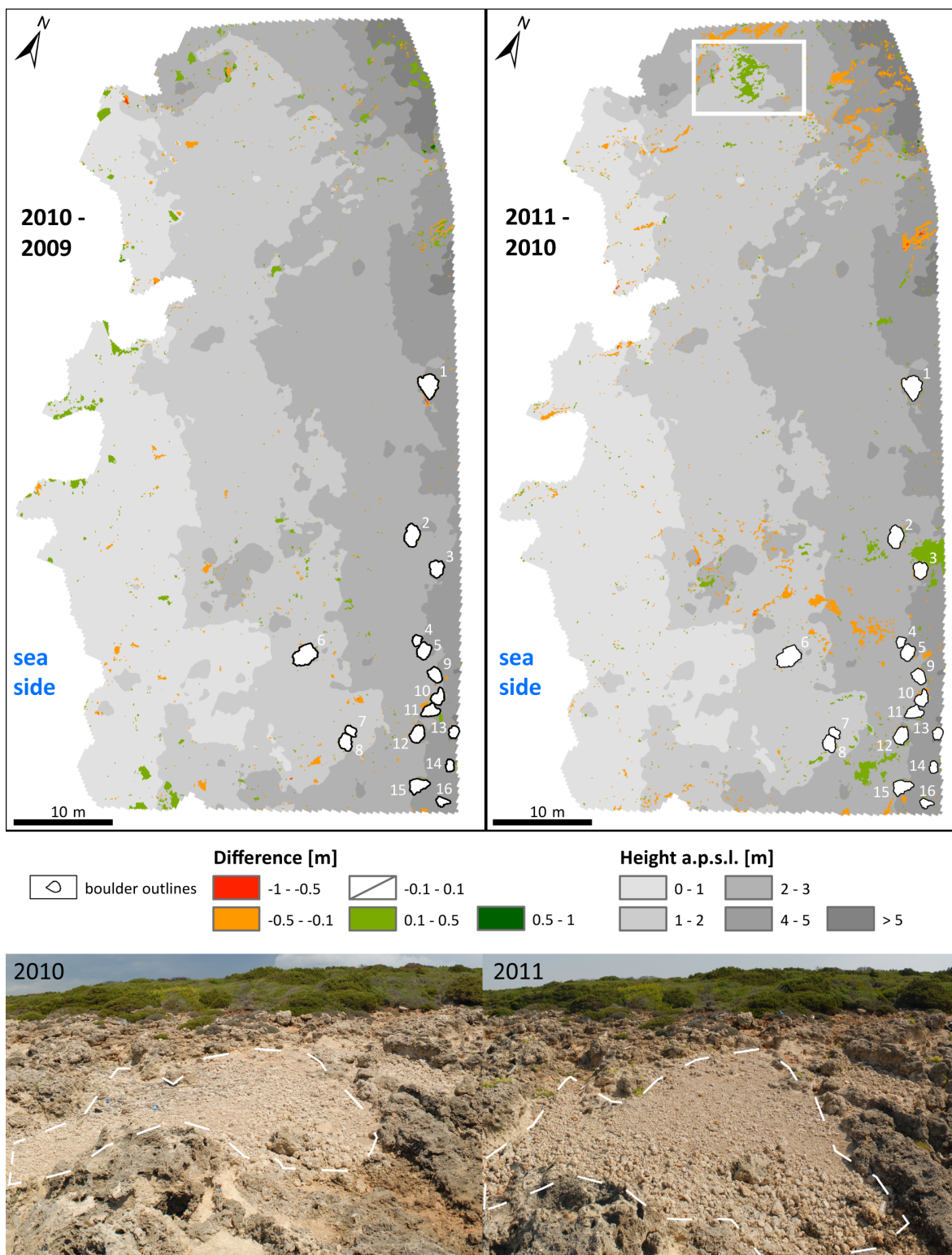


Figure 4-11: Annual sediment budget for the years 2009/2010 and 2010/2011 near Cape Katakolo, western Peloponnese. Photos from the northern part of the study area show the different conditions in 2010 and 2011, respectively, documenting that coarse-grained material was accumulated during backflow after storm-related minor inundation. Modified after HOFFMEISTER et al. (2013b).

The study site near Cape Katakolo, western Peloponnese, shows only minor changes during the observation period of 2009 to 2011. Dislocated boulders that were monitored in this area showed no movement (Figure 4-11). Differences between the high-resolution digital elevation models for 2009 and 2010 are mostly due to wooden jetsam. However, in the northernmost part of the studied section, an increase in elevation in the range of 0.1 to 0.5 m is detected by comparing the years 2010 and 2011. In this case, considerable amounts of gravel were accumulated at the seaward fringe of a small depression. Obviously, the site was completely flooded by sea water during storm events and the material was accumulated during the course of backflow dynamics hindered by the seaward rim of the depression. This matches to the results depicted in Figure 4-8, where boulders are theoretically inundated by both storm scenarios.

In the studied coastal section at Aghia Pelagia on Cefalonia Island, no relevant changes in the annual sediment budget were detected. Slight changes shown in Figure 4-12 are changes of the vegetation. No changes of position and orientation were detected regarding the high-energy dislocated boulders, which were monitored at this site.

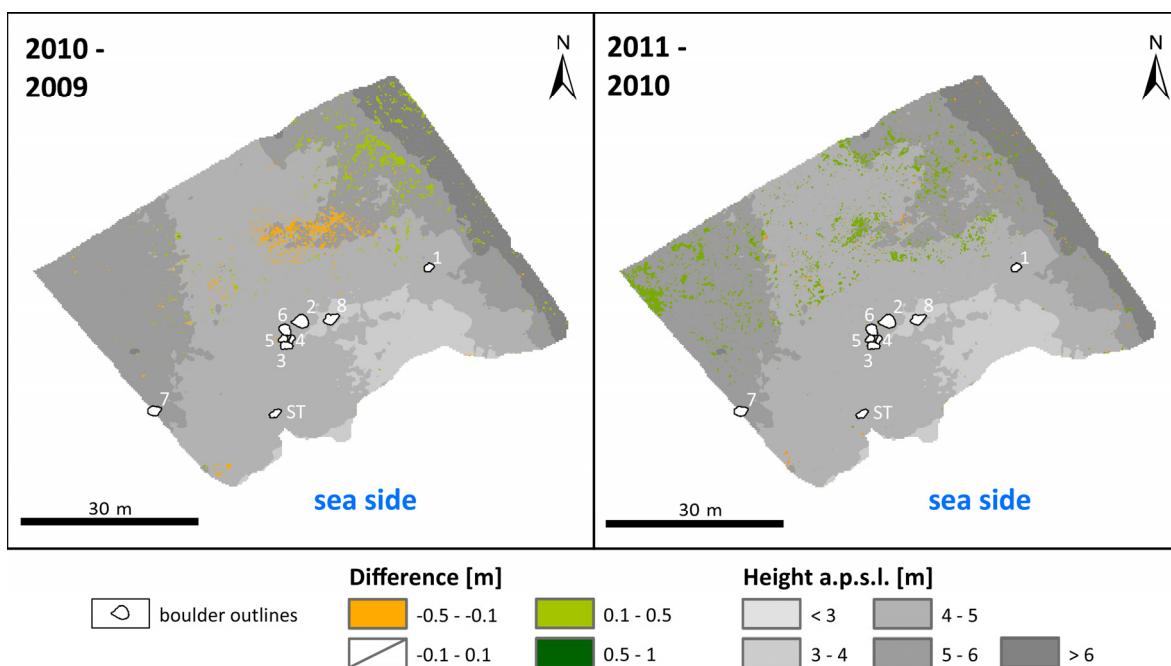


Figure 4-12: Annual sedimentary budget for the years 2009/2010 and 2010/2011 at Aghia Pelagia, Cefalonia Island, expressed by increasing or decreasing elevation data. Modified after HOFFMEISTER et al. (2013b).

Similar results were obtained for the studied coastal sections near Cape Gerogombos and Cape Schinou, which are located approximately 20 km to the northwest of the Aghia Pelagia site (Figure 4-3). The results are shown in the appendix (Figure A-1 – A-3).

4.4.3 Comparison with buoy data

Wave data from two buoys of the Poseidon monitoring system (HCMR, 2013) were analysed for the time period between the end of 2007 and the summer of 2012. The buoys located at Pylos and Zakynthos are the closest ones to the study sites (Figure 4-3). It is important to mention that the buoy data may

include measurement errors. Figure 4-13 shows that the detected average maximum winter storm wave height for the offshore buoy Pylos lies between 5 m and 8 m. During the winter seasons 2008/2009 and 2011/2012, prior to and succeeding our surveys, individual waves higher than 10 m may have occurred.

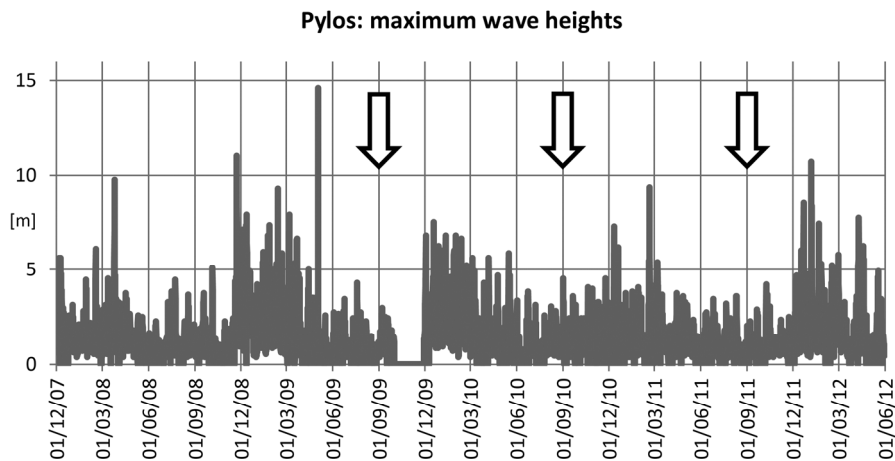


Figure 4-13: Maximum wave heights registered by a buoy offshore Pylos for the time between 1st of December 2007 and 1st of June 2012. Arrows indicate points in time of TLS-based coastal monitoring. Source: HCMR, 2013. Modified after HOFFMEISTER et al. (2013b).

Wave data recorded by the buoy offshore Pylos are in good accordance with changes in the sediment budget found for our study site near Cape Katakolo. Noticeable changes have been found for the time between 2010 and 2011 by comparing TLS-based HRDEM data, which seem to correspond to slightly increased storm wave activity during the 2010/11 winter season (Figure 4-13). Data recorded by the offshore buoy Zakynthos (Figure 4-14) show the same overall tendencies with winter season maximum wave heights between 5 m and 7 m. In addition, the winter seasons 2008/2009 and 2011/2012 seem to show slightly increased wave heights. The extreme wave heights shown for the second half of the year 2008 are most probably due to buoy malfunction.

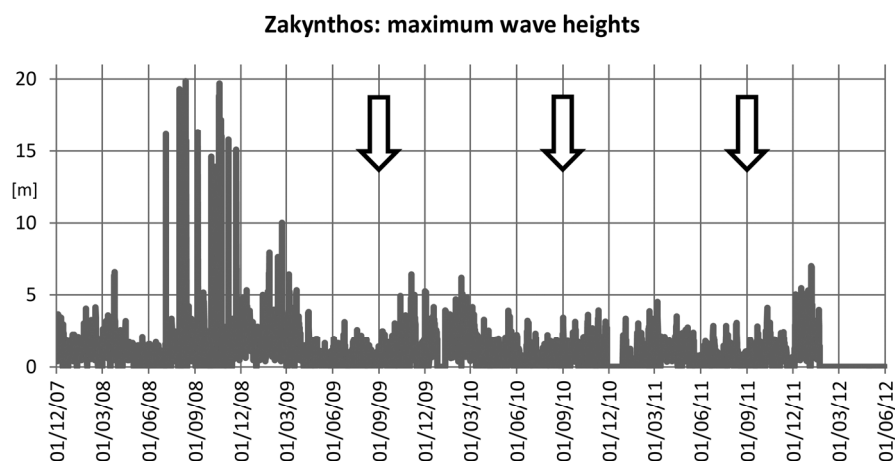


Figure 4-14: Maximum wave heights registered by a buoy offshore Zakynthos for the time between 1st of December 2007 and 1st of June 2012. Arrows indicate points in time of TLS-based coastal monitoring. Source: HCMR, 2013. Modified after HOFFMEISTER et al. (2013b).

4.5 Discussion

The feasibility of the selected method for coastal geomorphology was shown. TLS is an appropriate and reliable tool to achieve various parameters of geomorphological features, such as boulders displaced by high-energy waves. For example, ARMESTO et al. (2009) summarize that TLS is of great value to get detailed, high accurate and fast non-contact measurements of complex objects. Additionally, TLS surveys provide data to create topographic maps, which would be exceedingly tedious to accomplish by stereophotogrammetric approaches (TERRY et al., 2013). With the applied approach it was also possible to monitor the sediment budget of remote and poorly accessible areas. Several hundreds of square meters in a high accuracy and resolution were observable within one day of fieldwork. The method is suitable for an even greater temporal resolution depending on organisational matters and logistics. For instance, PIETRO et al. (2008) successfully use TLS to monitor the performance of a beach nourishment by monthly surveying a beach transect in a similar set-up. The given accuracy and resolution of the TLS system is slightly worse than tachymetric profile surveying, but within the range of DGPS measurements (DORNBUSCH, 2010). As TLS measurements reveal a full coverage of an area, calculations of volume changes are more accurate than volume calculations from profile surveying (PIETRO et al., 2008).

Georeferencing and registration of point clouds by direct measurements of the scan position by the RTK-DGPS, as well as using a further reflector pole turned out to be a practicable and beneficial method for this kind of geomorphological field survey. The accurate transformation of the project coordinate system into a global coordinate system may also be achieved by commercial correction services, like the Greek national correction service HEPOS (GIANNIOU, 2008) or by the PPP correctional method using the carrier phase record of the system (cf. section 2.1.2).

TLS-based high-resolution 3D reconstructions in combination with accurate density measurements of large dislocated boulders yielded more accurate data than previous approaches. Similar results can be found in other publications (MASTRONUZZI & PIGNATELLI, 2011; SCICCHITANO et al., 2012; HOFFMANN et al., 2013). For small boulders (< 2 kg) of more spherical shapes, SPISKE et al. (2008) calculated volumes by multiplying the length of all axes, by using the principle of *Archimedes* and by optical computing and found comparable differences. However, the TLS-based method is susceptible to systematic errors (e.g. accuracy of TLS), calculation errors (e.g. manual 3D reconstruction for areas out of sight) and errors in interpretation (e.g. manual determination of boulder axes in case of complexly shaped boulders). The accuracy can be enhanced by further studies with more accurate laser scanning devices or photogrammetric approaches (TERRY et al., 2013). In order to obtain reliable parameters needed for calculating wave transport equations, minimum values from the 3D models were extracted. For example, the shortest distance of the centre of a boulder to the present sea level was estimated.

Nevertheless, the new information is considered to be more realistic and accurate than data achieved by tape measurements. The comparison of 3D model-based volume and density data with conventional estimations show lower density values by up to 22%. Table 4-1 depicts that the calculations of volume and mass on the basis of tape measurements of the axes result in a mean overestimation of 30% with a 28% variation. Therefore, mass estimations of boulders of this size based on simple measurements of the axes should be multiplied at least with a factor of 0.7. For wave transport equations, which take the mass of a boulder into account (NOORMETS et al., 2004; BENNER et al., 2010; ETIENNE et al., 2011; ENGEL &

MAY, 2012), this correction factor should therefore be applied to avoid an overestimation of wave heights and velocities. However, nowadays wave transport equations on the basis of the parameter “mass” are less common than the equations derived from the approach of NOTT (2003b) using axes as input parameters.

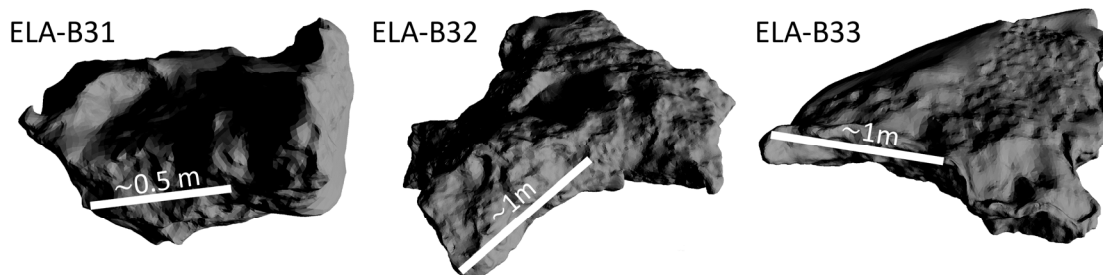


Figure 4-15: Irregularly shaped boulders from Cape Skalas, Peloponnese. Modified after HOFFMEISTER et al. (2013a).

Within the study, very irregularly shaped boulders (Figure 4-15), e.g. ELA-B31, -B32, -B33, lead to an underestimation of the mass by multiplying the axes, when a mean axis is taken. However, the mass would be overestimated quite badly, when maximum axes are used. Hence, multiplying the axes is not suitable for such kind of boulders.

In general, the use of mass values derived from 3D model reconstruction and laboratory density measurements result in smaller wave heights and smaller wave velocities compared to approaches relying on axes and literature-based density values. The differences between estimated and 3D model-based mass values are substantial and vary from 15-45 % as depicted in Table 4-1. Hence, results of all wave transport equations exhibit huge differences ranging from -70 % up to +60 % (Figure 4-16), depending on the boulder. Thus, incorporation of the 3D model-based masses can lead to a significantly different wave height or velocity and better depicts the variety of boulders.

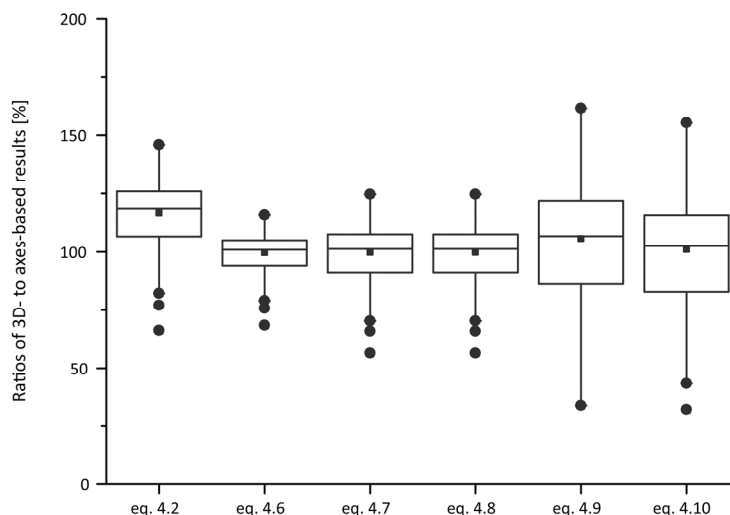


Figure 4-16: Relations between calculated results of wave transport equations from 3D model-based masses and axes-based masses in a box plot. Depending on the size and the dimensions of a boulder, larger differences between both approaches are denoted.

Generally, most of the boulders show minimum tsunami wave heights that are within the range of wave heights from the expected tsunami scenarios, relying on numerical simulations. Minimum wave heights calculated for boulder dislocation of the study sites correspond to the results of SCICCHITANO et al. (2007) reported from southeastern Sicily and of MASTRONUZZI et al. (2007) from southern Apulia, as well as the results of BARBANO et al. (2010). Numerical simulations of tsunami wave propagation in the Gulf of Kyparissia underline the possibility of tsunami wave heights high enough to initiate boulder movement (TSELENTIS et al., 2010; RÖBKE et al., 2013).

Boulders of all areas, except the area of Cape Skalas, Peloponnese, are probably not initially cracked out of sea ward edges by storms, but their transport is possible according to the extracted wave decay curves that are shown in Figure 4-8. In particular, the minimum storm wave heights necessary for the boulder dislocation at the area of Cape Skalas, Peloponnese, are lying within all expected storm wave scenarios. This is in contrast to all other sites that show more consistencies between the derived values and the decay curves. As depicted by the annual comparison of Cape Katakolo, Peloponnese (Figure 4-11), annual changes occur in the surrounding areas of the boulders, but no change in position of the boulders was detected. For every other site, it was not verifiable that the boulders are reached by seawater. Unfortunately, monitoring of the Cape Skalas site was not possible, due to logistic constraints.

It is assumed, that the boulder PEL-ST encountered at Ag. Pelagia, Cefalonia Island (Figure 4-9) was moved by a winter storm event in 2008/2009. This assumption is based on significantly smaller minimum wave heights and velocities derived by equations of BENNER et al. (2010) with regard to the mass of this boulder and compared to other dislocated boulders. BARBANO et al. (2010) mention that boulders were moved during a bigger storm in the 2008/2009 winter season on the Italian side of the Ionian Sea. Additionally, VELLA et al. (2011) report boulder dislocation by storms for the coast of the Provence, France. The TLS-originated elevation data depicted in Figure 4-12 show that the boulder PEL-ST is located directly adjacent to a funnel-type, small indentation of the cliff-top rim, which is believed to have decisively enhanced storm wave influence responsible for boulder dislocation. All the other dislocated boulders studied near Cape Katakolo and Aghia Pelagia are arranged in lines and are lying tens of meters distant from the coast, which may indicate that these were transported by major inundation (GOTO et al., 2010b).

Annual changes in the sediment budget of the study sites are generally negligible or only modest. This is in good agreement with the analysed buoy data, which document no outstanding storm wave activity for the chosen time period. Moreover, the results show that dislocated boulders were not moved at all by winter storm conditions prevailing between 2009 and 2011. However, some methodological problems occurred due to triangulation errors. Occlusions may produce holes in the point clouds that reduce the accuracy of triangulated surfaces (LIM et al., 2005). These occlusions occur in areas with a high surface roughness, like Cape Katakolo, Gerogombos and Cape Schinou. In addition, small variations in the set-up of the scan position of the laser scanner may cause differences that can equally result in triangulation differences. Consequently, results were manually compared with the original point clouds and photos in order to prevent such errors. Areas with considerable occlusion effects were not considered for further analyses. A point cloud to point cloud comparison is more appropriate for these complex areas (LAGUE et al., 2013). These triangulation errors may also occur, when photogrammetric methods are applied. High-resolution photos taken from UAVs, as base for HRDEM comparisons might

be a solution (EISENBEISS & SAUERBIER, 2011). However, acquisition by UAVs can only be applied under calm weather conditions, which is difficult to achieve in these seafront areas.

In general, TLS-derived areal monitoring and 3D-models of dislocated boulders are considered to offer a reliable base to detect the effects of future changes of the sedimentary budget, to determine the dimensions of high-energy impacts and to serve as a base for further hydraulic modelling approaches. Evidence of high-energy impact can only partly be proven, which might also be a consequence of the incorporated wave transport equations. However, for this region and nearby all regarded sites, different kinds of palaeotsunami traces were encountered in near-coast sediment archives (VÖTT et al., 2009; VÖTT et al., 2011; MAY et al., 2012b; NTAGERETZIS et al., 2012; WILLERSHÄUSER et al., 2013). Finally, numeric simulations of tsunami landfall for the Gulf of Kyparissia (western Peloponnese), including Cape Katakolo, show good agreement between inundation scenarios and field evidence (RÖBKE et al., 2013).

5 Case study 2: Agronomy*

5.1 Introduction

For a more sustainable and highly efficient agricultural production, technologic advances are tested and implemented to specifically address spatial-temporal variability on different scales in the whole agricultural system (ZHANG et al., 2002). This technological improvement is called Precision Agriculture (PA) or precision farming. Agronomy already benefits from new technologies like GNSS, GIS and remote sensing. For instance, fertilizers and herbicides are applied “at the right place and the right time” (MULLA, 2013: 358). Overall, crops with their corresponding biomass and yield, are affected by several factors, namely topography, soil, crop type, management and anomalous factors like diseases (ZHANG et al., 2002; KRAVCHENKO et al., 2005). For example, topographic factors like slope, aspect and field boundaries, as well as soil factors like moisture, density, depth and chemical properties affect crops and their development. An accurate mapping of these factors, in particular for the determination of in-field variability is important, as well as accurate measurements of crop height, biomass and yield (STAFFORD, 2000). Furthermore, the accurate determination of the current crop status is also relevant for modeling approaches (LENZ-WIEDEMANN et al., 2010), habitat evaluation, and carbon stock estimation (LEFSKY et al., 2002; OMASA et al., 2007; GARCIA et al., 2010).

The quantification of the effects from these numerous and very variable factors affecting crop development can be conducted by statistical analysis of yield and selected other factors (KRAVCHENKO et al., 2005; MCKINION et al., 2010b; HEUER et al., 2011). For instance, KASPAR et al. (2003) examined the relation between six years of corn yield and topographic values, which were derived by an RTK-DGPS survey, and found that depending on precipitation, yield is correlated to these topographic factors. In this case, in years with lower precipitation the well-known effect of higher yields in low lying areas, which benefit from moisture and better soil properties, can be proven. However, in years with high precipitation or strong precipitation events the pattern is reversed. This knowledge facilitates the establishment of yield stability maps, which can be used for an adjusted management (MCKINION et al., 2010a, b).

In contrast to the mentioned approaches that use yield data, the contemporary status of a crop's structure, -height, -density, -vitality and biomass is important for PA (FIORANI et al., 2012). For instance information about plant vitality can be obtained by multi- and hyperspectral remote sensing (LI et al., 2010; GNYP et al., 2013; YU et al., 2013). Measurements of chlorophyll fluorescence are an additional approach to achieve values on plant vitality (MERONI et al., 2009; RASCHER et al., 2009). Further methods to gather data on crop structure and additional other parameters are photogrammetric approaches conducted from UAVs (OBERTHÜR et al., 2007; BENDIG et al., 2012; LEBOURGEOIS et al., 2012; PRIMICERIO et al., 2012; SAMSEEMOUNG et al., 2012), or balloons (JENSEN et al., 2007; MURAKAMI et al., 2012), as well as

* This chapter an extended version of three articles: HOFFMEISTER et al. (2010); HOFFMEISTER et al. (2012); HOFFMEISTER et al. (2013c).

general imagery (GERTEN & WIESE, 1987), range images (KLOSE et al., 2009) and radar remote sensing (KOPPE et al., 2013).

Laser ranging and laser scanning have also been applied in agronomy by several authors to detect the current plant structure and further parameters. EHLERT et al. (2008; 2009; 2010) and EHLERT & HEISIG (2013) tested several laser scanners at different viewing angles on field machinery to directly derive data on crop height, coverage and density and found correlations between crop height, fresh and dry biomass of oilseed rape, winter rye, winter wheat and grassland ($R^2 > 0.88$). LUMME et al. (2008) investigated growth height of differently fertilized barley, oat and wheat plots with a CW-scanner mounted on a 3 m rack. A correlation between plant height and grain yield was reported ($R^2 > 0.88$) and single ears were successfully detected. HOSOI & OMASA (2009) used a triangulation based scanner for the voxel-based estimation of plant area density, leaf area density and leaf area index of wheat with few errors. The approach was successfully transferred to rice by implementing a mirror above the canopy to accurately estimate the previously stated parameters, which are important for the determination of data concerning for example transpiration, photosynthesis, habitat characteristics and carbon stock (HOSOI & OMASA, 2012). Plant structure and the associated chlorophyll content is derived by the integration of intensity values (section 2.2.5) of a green laser, which are radiometrically corrected (EITEL et al., 2010). Moreover, the nitrogen status in young wheat canopies can also be derived with this approach (EITEL et al., 2011). Further research was conducted by ZHANG & GRIFT (2012), who used a laser scanner for yield prediction of *Miscanthus giganteus*. Weed detection in maize was improved and presented by ANDÚJAR et al. (2013) and SAEYS et al. (2009) describe improvements for harvesting techniques of wheat. 3D monitoring by laser scanning and fluorescence imaging of herbicide effects on a single plant is conducted by KONISHI et al. (2009). Several research has additionally been undertaken in horticulture (TUMBO et al., 2002; WALKLATE et al., 2002; KEIGHTLEY & BAWDEN, 2010; HOSOI et al., 2011; LLORENS et al., 2011).

In contrast to the already mentioned approaches, the application of the presented time-of-flight laser scanner fixed on a tripod was conducted to estimate crop height distribution and variation on a single field of sugar-beet and wheat during two consecutive years by an indirect approach. This approach was successfully transferred for monitoring paddy rice (TILLY et al., 2012). The method was generally enhanced at a second survey operated from a higher scan position of about 4 m to achieve a better point density. For the latter survey, the canopy of contrasting sugar-beet varieties is the focus of attention. In all cases, maps of crop height and crop growth were established, which indirectly evaluate these values by comparison of high-resolution, multi-temporal Crop Surface Models (CSMs) from different time steps. This specific post processing step is introduced in the following (section 5.2). The description and results for the detected in-field variability of crop height in two consecutive years is presented thereafter (section 5.3), followed by an experiment with different types of sugar-beets (section 5.4) and finally concluded with a discussion of the results.

5.2 Main procedure

Generally, the same procedure, as presented in chapter 3 was applied, with multi-temporal surveys having been conducted throughout the vegetation periods in 2008-2010. The derived, registered and

adjusted point clouds were manually reduced by masking the area of interest and removing obstacles and noise, as described in section 3.5. The DTM from the first survey date and the CSMs taken from those surveys conducted at a later date were generated by interpolation of the final point clouds, each with approx. 10 million single measurements. To achieve the Crop Height (CH), a CSM of a certain time step (t) was compared to the initial digital terrain model (DTM) from the first measurement before crop emergence, as depicted in eq. 5-1 and shown in Figure 5-1 A.

$$CH = CSM_t - DTM \tag{eq. 5-1}$$

The resulting CH depicts the current, absolute crop height of the assigned survey date, in accordance with an nDSM or Canopy Height Models in forestry applications, described in section 2.5. In contrast, Crop Growth (CG) can be established by comparing two CSMs from successive dates to retrieve the relative crop growth between those dates, as assigned by eq. 5-2 and depicted in Figure 5-1 B.

$$CG = CSM_{t2} - CSM_{t1} \tag{eq. 5-2}$$

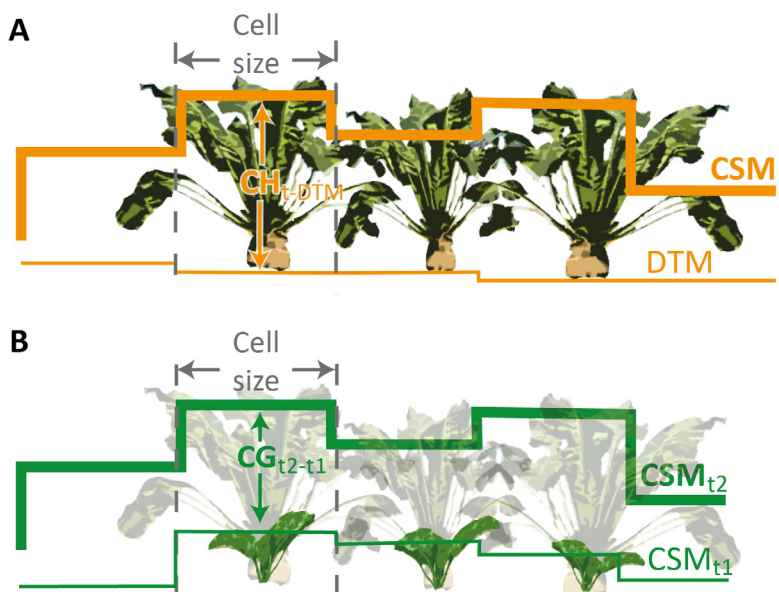


Figure 5-1: Derivation of Crop Height (CH) and Crop Growth (CG) by the comparison of CSMs and the initial DTM.

All surfaces were compared to each other to establish maps of CH and CG. All results were checked for their accuracy using pictures and manual measurements. Further analytical steps are depicted in each individual chapter.

5.3 In-field variability of crop height in two consecutive years

The study was applied within the framework of the Transregional Collaborative Research Centre 32 (CRC/TR32) "Patterns in Soil-Vegetation-Atmosphere (SVA)", which is an interdisciplinary research project, focusing on exchange processes between the soil, vegetation and the adjacent atmospheric boundary layer. The overall research goal of the CRC/TR32 is to achieve improved numerical SVA models

to predict CO₂-, water- and energy transfers by calculating patterns at various spatial and temporal scales. The focus is on the catchment area of the river Rur, situated in western Germany, parts of Belgium, and the Netherlands (CRC/TR32, 2013).

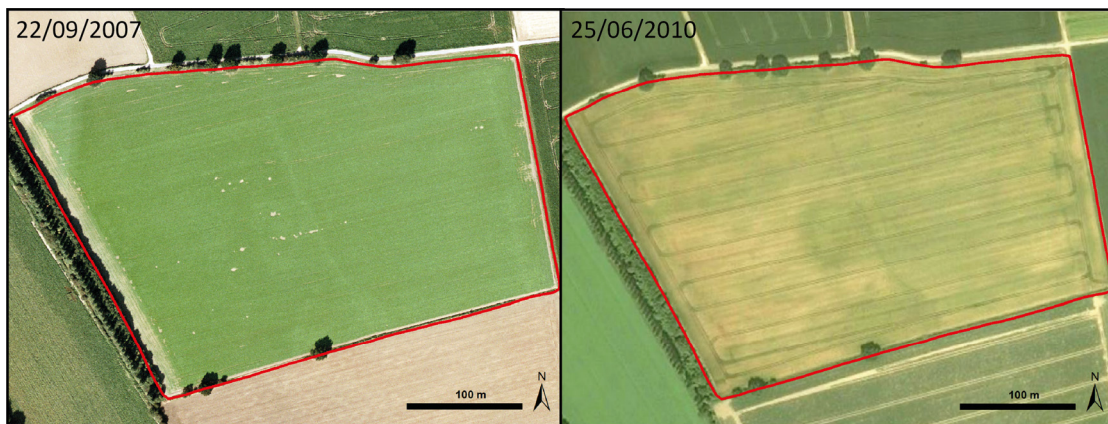


Figure 5-2: Orthophotos of the observed field (red line) from two different years showing the spatial in-field variability of crops. Imagery (left): © Geobasis NRW 2007. Imagery (right): © 2012 Google, Digital Globe, 25.06.2010. Mod. after HOFFMEISTER et al. (2013c).

The survey was conducted on a single field (Figure 5-2), which was observed by different sensors for research issues of the CRC/TR32 (KORRES et al., 2010; KOYAMA et al., 2010; WALDHOFF et al., 2012). The field is situated in an intensively used agricultural area, located about 40 km west of Cologne (N 50°51'58", E 6°26'50"). It is around 405 m by 105 m in size with an area of about 4.3 ha. The field is situated about 102 m-105 m above sea level and has gentle slopes (< 2.5°). The soil of the study field is very heterogeneous. The two most abundant soil types, a gleyic Luvisol and a gleyic Cambisol, change dominance in an east to west direction, with the latter prevailing in the eastern part (GLA, 1995). In addition, some areas with anthropogenic soils with filled or removed material have been identified in the middle part. Overall, the whole field might suffer from poor drainage and therefore promotes gleying processes. In 2008, sugar-beet was planted followed by winter barley flanked by two strips of winter wheat in 2009.

5.3.1 Specific methods and data

GNSS measurements were conducted by establishing a new base point for the base station of the RTK-DGPS that was accurately transformed into the state's surveying network. The base point was marked by a small screw on a wooden pole. For the transformation, six surrounding survey points from the surveying agency were measured by the RTK-DGPS and the transformation was established based on these measured points and their official coordinates. All measurements were executed in DHDN GK2.

The laser scanner was mounted on the tripod at a height of ~1.9 m. Eight scan positions were established around the study field in 2008 and one further scan position was added in 2009 to cover the entire area. Measurements were accomplished three times in 2008 (14/05/08, 26/06/08, 24/07/08) and four times in 2009 (07/04/09, 18/05/09, 24/06/09, 20/07/09).

At first, a general evaluation is conducted by a comparison of the achieved DTM from every year and the DTM of the state's surveying and mapping agency from the year 2012 derived by ALS using a 1 m

resolution (Geobasis NRW, 2012). In addition, the derived plant heights are checked against independently measured plant heights using a tape for 2008. For comparison of the manually measured data, a mean value of a circular 2 m buffer at each measuring point was extracted from the derived crop height data. For 2008, 24 soil moisture measurement points and 3 intensive measurements points existed, where plant heights were measured throughout the year (KORRES et al., 2010). Particular dates for comparison are selected from the soil moisture measurement points (08/07/08, 25/07/08) and the intensive measurement points (24/06/08, 24/07/08). Additionally, biomass samples for further analysis were collected at the latter points.

Secondly, different topographic and soil parameters are prepared, each in different cell sizes (1 m, 5 m, 10 m, 20 m) to determine the causes of the detected variability. The specific parameters are for example, soil moisture, slope and curvature as well as further derivations of the DTM, as depicted in Figure 5-3 and Table 5-1. The data were derived by the according tools of ArcMap, starting with the initial DTM, which is aggregated with mean values to the target cell size. These DEMs and their height values are subsequently used to compute the derivations of the DTM, as described in Table 5-1.

Table 5-1: Parameters incorporated for analysis of the detected variability of crop height (BUCKLEY, 2010; ESRI Inc., 2012)

Parameter	Description
Height	Z-values of the DTM derived from the first measurements of every year.
Aspect	The aspect values assign the direction of the slope in degrees to north.
Slope	Slope is the maximum degree of change between each cell and its neighbours.
Curvature	Curvature is the gradient of the slope. Positive numbers depict convex curvatures, negative values show concave curvatures, zero values are flat.
Plan curvature	Plan curvature is perpendicular to the direction of the maximum slope. Positive values assign sidewardly convex surfaces and negative values denote sidewardly concave surfaces. Zero values are denoted for linear surfaces.
Profile curvature	Profile curvature is in the direction of the maximum slope. A negative value assigns an upwardly convex surface and likewise a positive value indicates a concave surface. Zero values are denoted for linear surfaces.
Soil moisture	Measured mean data from specified date (08/07/2008, 25/07/2008, 07/08/2009), interpolated by ordinary kriging.
Soil depth	Mean soil depth in decimetre from the soil map.
Soil value	Soil value from the soil map.

In addition, soil moisture measurements, here as the ratio of water and soil volume (Vol.-%), were taken with a handheld FDR probe (Delta-T Devices Ltd., Cambridge, UK) at 24 points in a 50 m by 50 m grid (KORRES et al., 2010). The mean of six measurements for each point at the dates, depicted in Table 5-2, was interpolated by ordinary kriging (BRUNSDON, 2009). Mean soil depth (GLA, 1995) and soil value (GLA, 1960) were digitized from the corresponding soil maps of the state's geological agency. For the statistical evaluation of the crop height and crop growth variability, centre points from the DTM raster data were established for each cell size and all data is attached to these points. Generally, a bilinear interpolation function is used to derive accurate values for each point at each resolution. Finally, all point data with all parameters, such as mean plant height, slope value and soil moisture is exported for each resolution and used for correlation and regression analysis in R-statistical software (R-software, 2013).

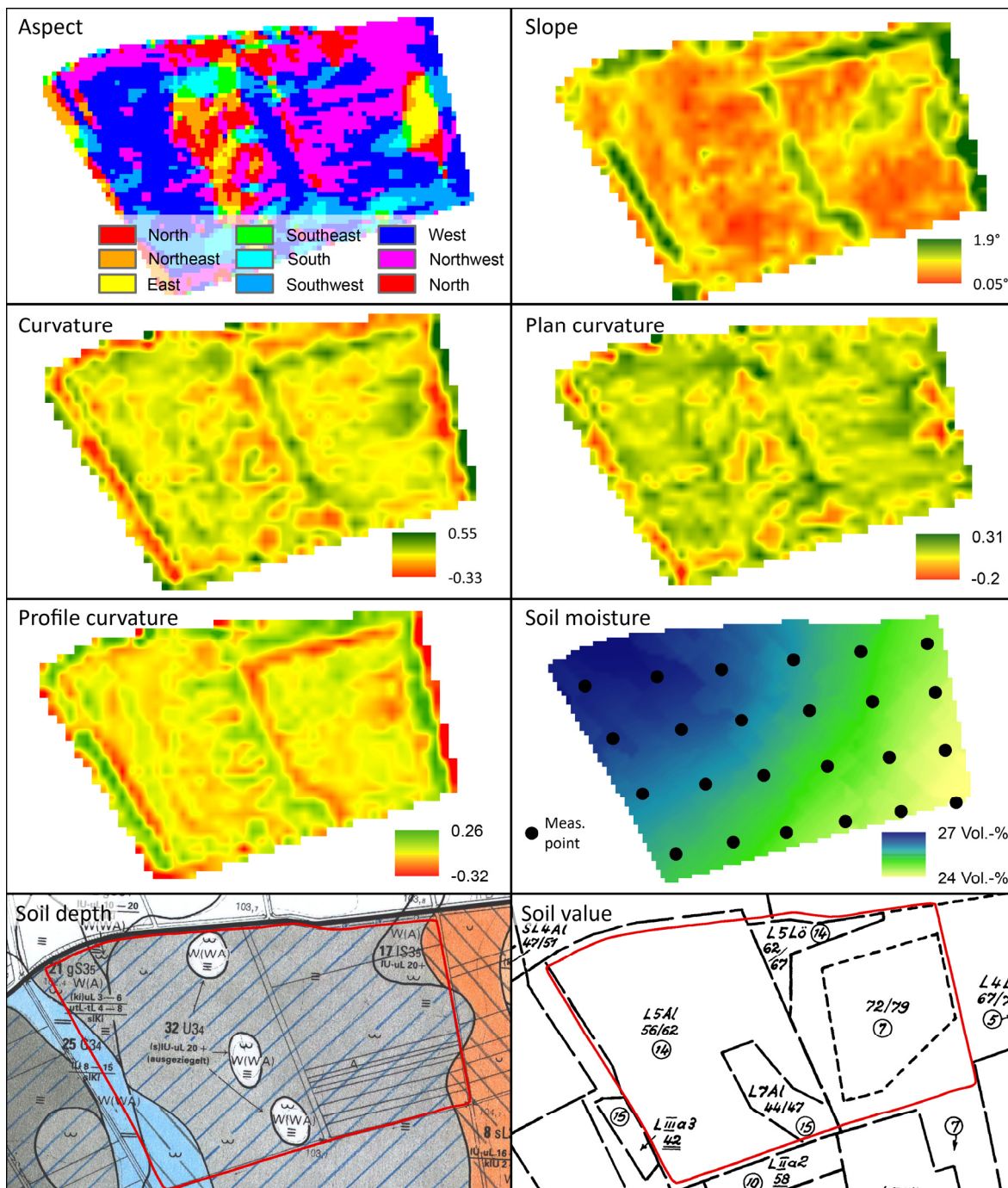


Figure 5-3: Overview of the different, incorporated parameters for correlation analysis. Data is established from the DTM interpolated from TLS measurements and aggregated to the specific cell sizes. The maps generally show a 10 m resolution. Soil value and soil depth is derived from maps of the state’s geological service (GLA, 1960; 1995). Soil moisture is interpolated from the depicted measurement points.

5.3.2 Results

Point clouds with a high density and a very good accuracy were achieved as a primary result. Merging those point clouds of every single scan position was possible by RTK-DGPS measurements and the MSA enhancement (section 3.5.3). Every point cloud of each single scan is colourised by the corresponding pictures, which results in a nearly real perspective of the area (Figure 5-4). The point clouds are reduced to the AOI and noise is filtered as described in section 3.5.4. CH and CG are derived by comparison of the interpolated surfaces.

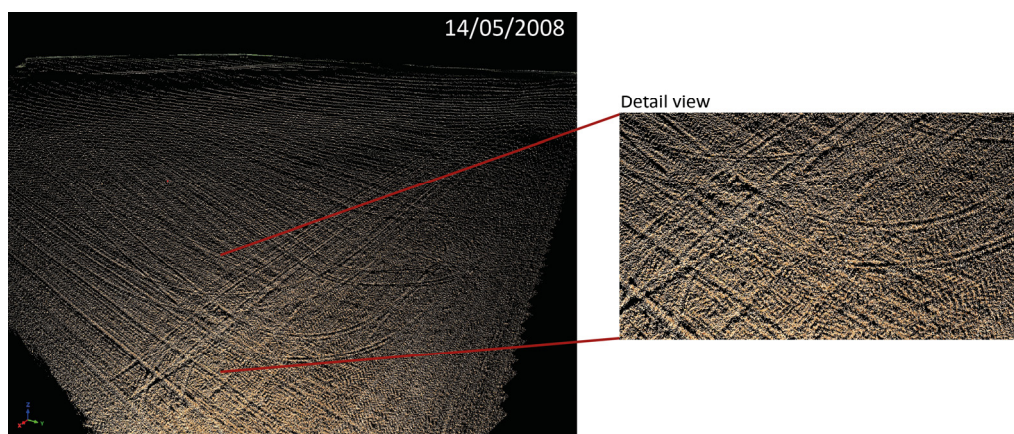


Figure 5-4: Perspective view of a 3D point cloud of one scan position from 14th of May, 2008, illustrating the high resolution and colourisation. Tractor traces are visible.

Results of 2008 and accuracy analysis

The maps of crop height, crop growth and the initial DTM from 2008 are presented in Figure 5-5. The generated DTM (Figure 5-5, top left) shows the major topographic patterns of the field, which is characterized by an east to west downhill trend with several local depressions at the eastern and central parts, as well as a sharp linear edge in the central section. These overall patterns are reflected by the map of crop height from late June, 2008 (Figure 5-5, top right). Particularly, the eastern central part and the whole western edge show inferior crop development. Furthermore, west of the linear edge, several distinctive, circular areas with different crop development can be observed. These patterns appear reversed in the maps of crop growth between late June and late July 2008 (bottom left).

The low lying western part is generally characterized by inferior growth, as well as the small depression in the central eastern part. A panoramic picture generated from the camera on the TLS (Figure 5-6) from the last survey of 2008 shows the poorer development of the sugar-beet plants on the western side. In Figure 5-5, the mainly covered area of the picture is marked. Generally, all observations match with the pictures and manual measurements of crop height.

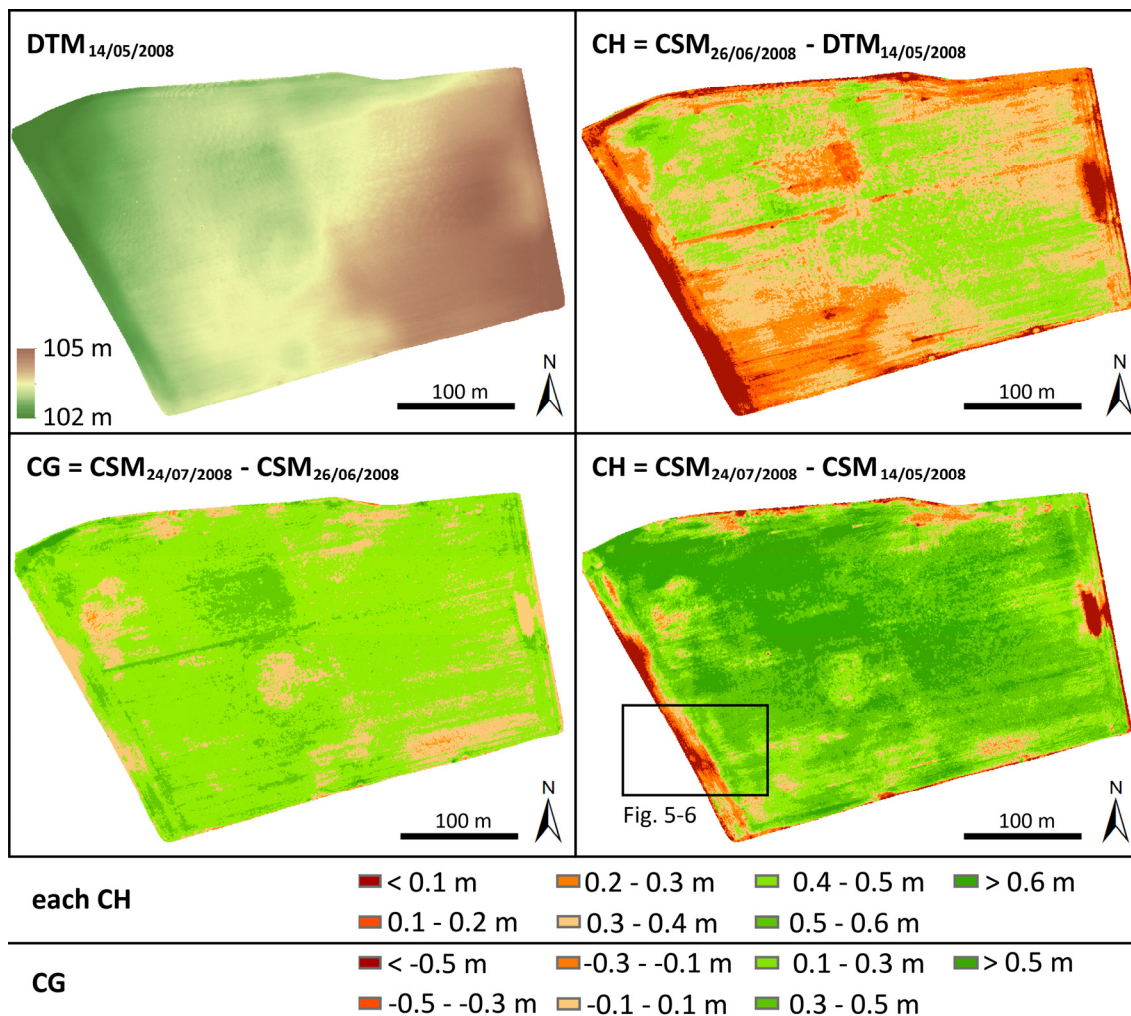


Figure 5-5: Maps of Crop Height (CH), Crop Growth (CG) and the DTM for the year 2008. CH and CG was achieved by comparison of consecutive CSMs and the DTM. Rectangle marks the area of a panoramic picture (Figure 5-6). Modified after HOFFMEISTER et al. (2013c).



Figure 5-6: Panoramic picture from one scan position from 24 July 2008. The western area of inferior growth is visible in the foreground. Modified after HOFFMEISTER et al. (2013c).

The derived DTM was compared to the DGM1L obtained from the state’s surveying agency (Geobasis NRW, 2012) to test the overall accuracy of the approach. For this purpose, the TLS data was aggregated to a 1 m cell size. A regression with a high coefficient of determination ($R^2=0.99$) was found that reveals the precision of the measurements. For the TLS measurements an absolute, slight positive shift of ~80 cm is noticeable, as depicted in Table 5-2.

Table 5-2: Results of the comparison between the derived DTM and the DGM1L of the surveying agency.

	\bar{X}	SD	Min.	Max.
TLS-DTM	103.53	0.53	102.31	105.02
DGM1L	102.86	0.51	101.60	104.23

The calculated plant heights of the CSMs are compared with independent crop height measurements on the field for the year 2008. Unfortunately no independent plant measurements are available for 2009. The manual measurements are in agreement with the derived plant height values as depicted in Table 5-3, and a regression with $R^2=0.53$ was found (Figure 5-7).

Table 5-3: Comparison of mean calculated and manually measured crop heights, also depicted in Figure 5-7.

Derived crop height	n	\bar{X}	SD	Min.	Max.
26/06/2008	27	0.34	0.10	0.04	0.47
25/07/2008	27	0.53	0.09	0.36	0.73
Manual Measurements	n	\bar{X}	SD	Min.	Max.
26/06/2008	27	0.34	0.06	0.21	0.47
25/07/2008	27	0.53	0.13	0.33	0.75

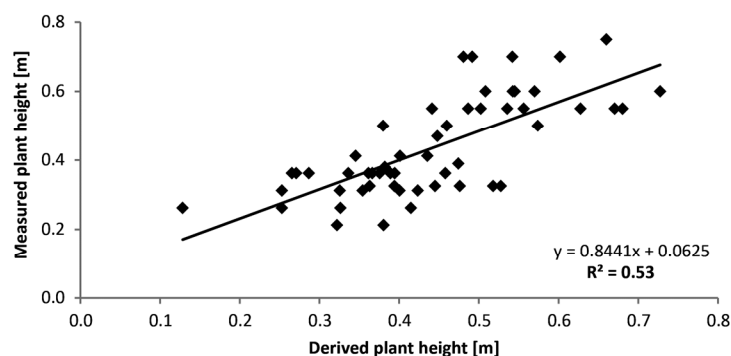


Figure 5-7: Regression of the measured and derived plant heights of 2008.

In addition, biomass sampling of sugar-beet plants was conducted in 2008. Biomass and plant height for the whole growing period are shown in Figure 5-8 A, with the mean crop height of the TLS measurements. Assuming a linear regression (Figure 5-8 B) a coefficient of determination ($R^2=0.47$) can be found. Generally, the quantity of the independent measurements is low.

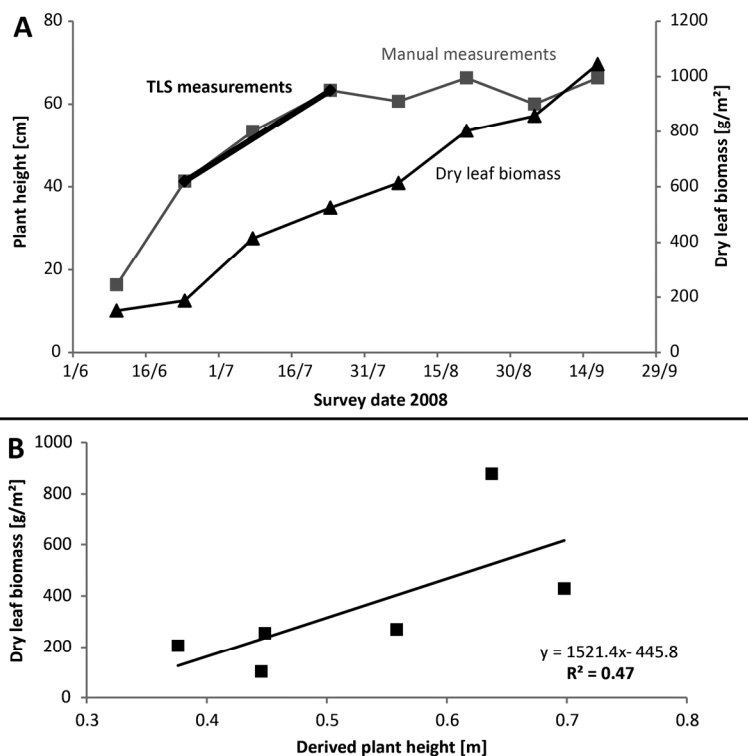


Figure 5-8: Comparison of the manual measured crop heights and dry leaf biomass of the whole vegetation period of 2008 (A) with the derived, mean crop height values. The latter are used in a linear regression with dry leaf biomass (B).

Results of 2009

The survey results of 2009 reveal a DTM similar to the 2008 DTM (Figure 5-9). Wheat and barley exhibit a more uniform growth pattern and crop height distribution as sugar-beet in 2008. Additionally, the pattern of the initial DTM is not recognisable in the later maps of crop height and crop growth. Inferior crop development of barley is detected only for the north-western part. In late July, the crop height has generally decreased, closely to harvest, due to ear development. This is also regarded in the mostly negative crop development between late June and late July (Figure 5-9, bottom right). The narrow strips of wheat show slightly different crop heights, particularly for late June, 2009.

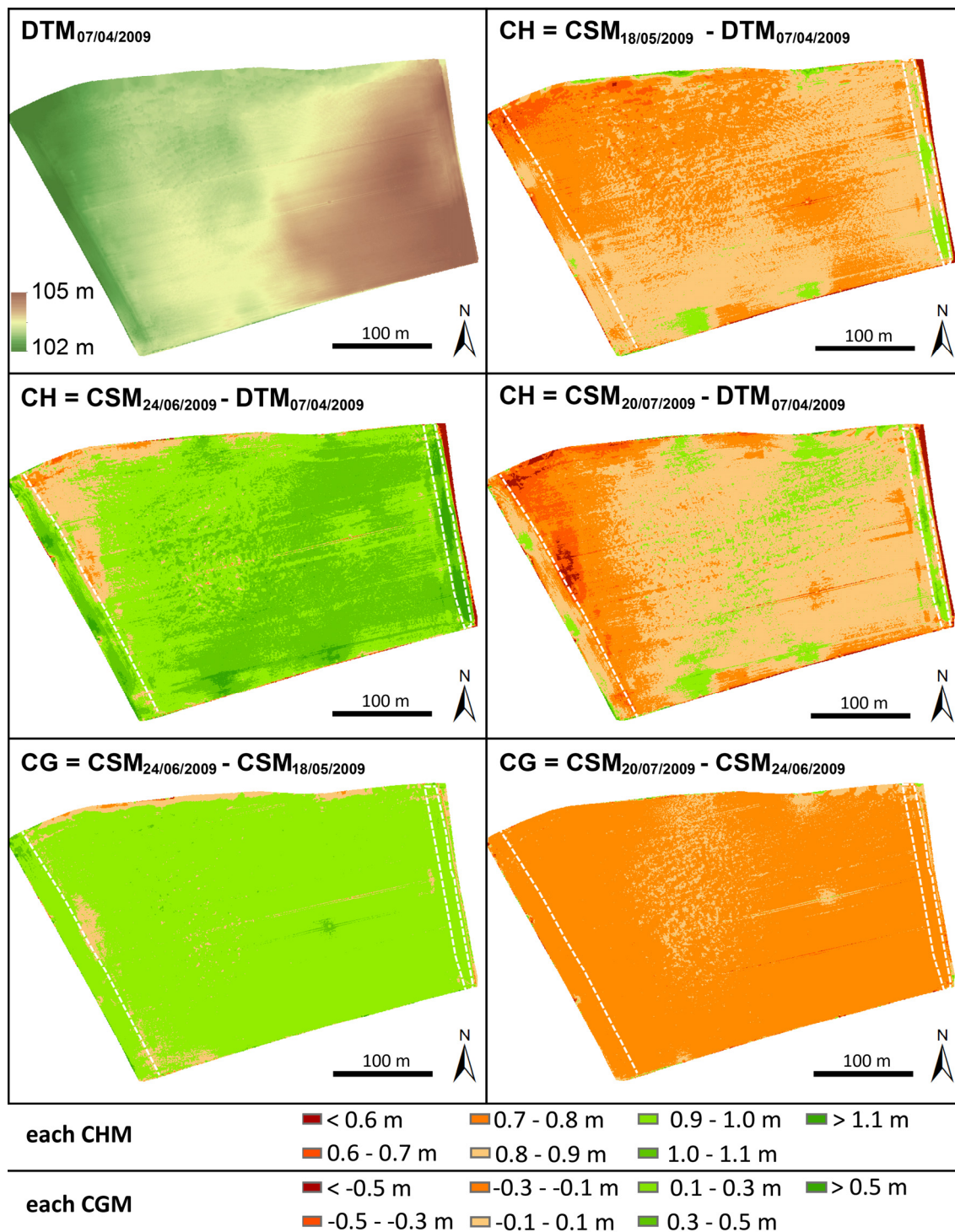


Figure 5-9: Maps of Crop Height (CH), Crop Growth (CG) and the DTM for the year 2009. CH and CG was achieved by comparison of consecutive CSMs and the DTM. The main crop was winter barley with two narrow areas of winter wheat, which are marked by white dashed lines. Mod. after HOFFMEISTER et al. (2013c).

Correlation between crop height variation and selected parameters

The detected variability of crop height and crop growth is compared to the previously stated parameters (section 5.3.1), in order to identify sources for this crop height variation. The mean plant heights were correlated with the stated parameters in R-statistical software (R-software, 2013) with a resolution of 1 m, 5 m, 10 m, and 20 m respectively. Significant parameters were used in a multiple, linear regression in order to retrieve the amount of explanation for this variation. All results are listed in Table 5-4.

Generally, correlations were found with values below 0.55. Some values are increasing with a decreasing resolution. As expected, for the highest resolution most of the parameters are significant, due to the high amount of samples. Examining the results, several patterns can be observed:

- Curvature and the secondary parameters, plane and profile curvature, are usually only correlated to the absolute crop heights and not to the crop growth. The correlation for the curvature and the plane curvature to the plant heights of wheat and barley was found to be mostly negative, whereas profile curvature is positively related. In contrast, profile curvature is negatively related to both sugar-beet crop height stages. The values are generally higher for coarser resolutions.
- Sugar-beet height variety is negatively correlated to slope, whereas wheat and barley show only a minor correlation values.
- The soil value is positively correlated to the earliest crop stage of sugar-beet and the latter stages of wheat and barley (mostly $r \sim 0.15$). In contrast, a negative correlation is depicted for the growth rate of sugar-beet.
- Soil depth is the most important parameter for all CSM values (mostly $r > 0.15$). Similar to the soil value, this parameter shows a negative relation regarding the growth rate of sugar-beet.
- Soil moisture only plays a role for the latest stages of both years, the growth rate of sugar-beet and the latest growth rate of barley and wheat. Furthermore, it is negatively correlated to the early stages of wheat and barley. Higher coefficients were derived ($r > 0.20$).
- The absolute height is the second important parameter, with exceptions for the second growing stage of sugar-beet and the final growing stage in 2009.

In summary, both years show slightly different correlation patterns for the selected parameters. Overall, the resolution of 10 m shows slightly better results than all other resolutions. Significant parameters were used in a multiple linear regression computation for every CH and CG. The adjusted coefficients of determination are generally higher for the earliest stage of sugar-beet ($R^2=0.30-0.41$) and higher for the latest stage of 2009 ($R^2=0.16-0.28$). Overall, about only one third of the variety in crop height can be explained by the selected parameters.

Table 5-4: Derived correlation coefficients (r) and adjusted R^2 values from multiple linear regression analysis of the comparison between crop height (CH) and crop growth (CG) and selected parameters.

Crop	Dates of CH and CG	Height	Aspect	Slope	Curvature	Plan Curvature	Profile Curvature	Soil moisture	Soil depth	Soil value	Multi. lin. regression [adj. R^2]
Resolution 1 m											
Sugar-beet	CH 080624-080525	0.21*	-0.02*	-0.11*	-0.02*	-0.05*	-0.01*	0.00	0.36*	0.20*	0.33
	CH 080725-080525	-0.02*	-0.03*	-0.10*	-0.03*	-0.06*	0.00	0.21*	0.22*	0.03*	0.18
	CG 080725-080624	-0.26*	0.01	-0.01*	-0.02*	-0.02*	0.01*	0.25*	-0.12*	-0.18*	0.07
W. Barley and Wheat	CH 090518-090418	0.20*	0.00	0.03*	-0.02*	-0.02*	0.03*	-0.03*	0.15*	0.06*	0.06
	CH 090624-090418	0.30*	0.01	-0.02*	-0.01*	-0.02*	0.01	0.06*	0.23*	0.16*	0.12
	CH 090720-090418	0.27*	-0.02*	-0.01*	-0.01*	-0.02*	0.00	0.23*	0.35*	0.11*	0.16
	CG 090624-090518	0.20*	0.00	-0.07*	0.01*	0.00	-0.02*	0.08*	0.16*	0.15*	0.08
	CG 090720-090624	-0.03*	-0.03*	0.02*	0.00	0.00	0.00	0.28*	0.22*	-0.08*	0.14
Resolution 5 m											
Sugar-beet	CH 080624-080525	0.21*	-0.06*	-0.18*	0.16*	0.13*	-0.14*	0.00	0.35*	0.19*	0.33
	CH 080725-080525	-0.01	-0.04*	-0.18*	0.07*	0.06*	-0.06*	0.21*	0.22*	0.03	0.20
	CG 080725-080624	-0.25*	0.01	-0.04*	-0.08*	-0.06*	0.08*	0.24*	-0.11*	-0.18*	0.07
W. Barley and Wheat	CH 090518-090418	0.20*	0.00	0.14*	-0.08*	-0.06*	0.14*	-0.05*	0.15*	0.08*	0.12
	CH 090624-090418	0.30*	0.01	0.06*	-0.12*	-0.09*	0.19*	0.02	0.24*	0.18*	0.19
	CH 090720-090418	0.26*	-0.06*	0.04*	-0.08*	-0.05*	0.15*	0.20*	0.35*	0.16*	0.21
	CG 090624-090518	0.20*	0.01	-0.06*	-0.08*	-0.05*	0.10*	0.09*	0.17*	0.17*	0.09
	CG 090720-090624	-0.03*	-0.12*	-0.04*	0.07*	0.05*	-0.09*	0.29*	0.22*	-0.03*	0.17
Resolution 10 m											
Sugar-beet	CH 080624-080525	0.24*	0.05	-0.31*	0.32*	0.30*	-0.25*	-0.01	0.40*	0.19*	0.41
	CH 080725-080525	-0.01	0.00	-0.28*	0.21*	0.21*	-0.16*	0.22*	0.22*	0.03	0.25
	CG 080725-080624	-0.28*	-0.07*	-0.01	-0.08*	-0.06*	0.07*	0.27*	-0.16*	-0.18*	0.11
W. Barley and Wheat	CH 090518-090418	0.25*	0.01	0.09*	-0.16*	-0.07*	0.19*	-0.09*	0.18*	0.10*	0.19
	CH 090624-090418	0.30*	-0.04	-0.09*	-0.18*	-0.08*	0.21*	-0.03	0.23*	0.19*	0.21
	CH 090720-090418	0.29*	-0.06	-0.10*	-0.14*	-0.04	0.18*	0.16*	0.38*	0.17*	0.22
	CG 090624-090518	0.13*	-0.06*	-0.19*	-0.06	-0.04	0.07*	0.05	0.11*	0.13*	0.09
	CG 090720-090624	0.00	-0.04	-0.02	0.04	0.07*	-0.02	0.33*	0.29*	-0.01	0.22
Resolution 20 m											
Sugar-beet	CH 080624-080525	0.26*	0.02	-0.28*	0.33*	0.31*	-0.26*	-0.01	0.36*	0.16*	0.40
	CH 080725-080525	0.02	-0.04	-0.27*	0.25*	0.29*	-0.15*	0.22*	0.22*	0.02	0.24
	CG 080725-080624	-0.26*	-0.07	-0.01	-0.07	0.00	0.11	0.28*	-0.13*	-0.16*	0.12
W. Barley and Wheat	CH 090518-090418	0.26*	-0.10	0.04	-0.20*	-0.09	0.22*	-0.14*	0.17*	0.00	0.22
	CH 090624-090418	0.32*	0.02	-0.09	-0.20*	-0.08	0.24*	-0.14*	0.19*	0.08	0.28
	CH 090720-090418	0.31*	0.00	-0.09	-0.22*	-0.08	0.27*	0.16*	0.38*	0.16*	0.28
	CG 090624-090518	0.14*	0.12	-0.16*	-0.05	0.01	0.07	-0.03	0.07	0.09	0.10
	CG 090720-090624	0.05	-0.03	0.00	-0.05	0.00	0.07	0.55*	0.41*	0.19*	0.44

2-tailed test of significance is used

* : correlation is significant at the 0.05 level

5.4 Detection of crop varieties

The second survey has been conducted at the research campus Klein-Altendorf (N 50°37'18", E 6°59'16"), 20 km southwest of Bonn, Germany. A very fertile Luvisol on loess is the prevailing soil type. All measurements are part of CROP.SENSE.net project (CROP.SENSE.net, 2013), which is an interdisciplinary research network for sensor technology for crop breeding and management. Four different sugar beet cultivars (Maurica, Cesira, Berenika, Pauletta, provided by KWS SAAT AG) have been planted in a factorial block design with four replications. Plot size was ~3 m by 20 m. The cultivars differ mainly in their leaf structure and canopy architecture as well as their drought stress tolerance.

5.4.1 Specific methods and data

The base station of the RTK-DGPS system was set up for every survey on a marked position, without any absolute accuracy corrections or transformations. Thus, a local RTK-network was established in WGS 1984, UTM 32N. The laser scanner was mounted on a tractor with a hydraulic platform at a height of ~4 m (Figure 5-10). To cover the required area six scan positions were established. Measurements were accomplished several times during the growing season in 2010, with four surveys being considered (04/05/10, 23/06/10, 09/07/10, 09/08/10). Biomass samples were continuously taken fortnightly throughout the complete growing season. Six plants were harvested at each sampling. Fresh and dry weight of leaves and roots were measured, as well as the Leaf Area Index (LAI). To link the data of the derived crop heights to the measured biomass and LAI, mean heights of every plot were used. Additionally, a volume based approach was tested. The volume was derived by multiplying the cell height with the cell resolution for three separate square metres in each plot. The mean of the three square metres is compared to the measured values.



Figure 5-10: The platform with the mounted scanner located ~4 m above ground is used on a specifically extended tractor with an axle of 3 m width. Mod. after HOFFMEISTER et al. (2012).

5.4.2 Results

According to the previously stated procedure, HRDEMs were derived and compared to establish maps of crop height. The maps were controlled and analysed. In addition, corrected intensity values were tested to establish single plant points. Table 5-5 depicts, the mean values from the crop heights and the corresponding manual measurements, which were performed for each plot on the same day. The mean values derived from the TLS measurements are generally smaller. The values for the beginning of July 2010 show a higher difference, due to drought stress. Thus, the regression of values from all survey dates depicted in Figure 5-11 A, which show a smaller coefficient of determination ($R^2=0.34$) as the regression with values without the second survey ($R^2=0.72$).

Table 5-5: Height values derived by CSMs and manual measurements.

CSM crop height	n	\bar{x}	SD	Min.	Max.
23/06/2010	16	0.22	0.05	0.13	0.32
09/07/2010	16	0.17	0.07	0.08	0.31
09/08/2010	16	0.37	0.03	0.33	0.43
Manual measurements	n	\bar{x}	SD	Min.	Max.
23/06/2010	16	0.33	0.08	0.20	0.45
09/07/2010	16	0.39	0.09	0.23	0.58
09/08/2010	16	0.43	0.04	0.36	0.48

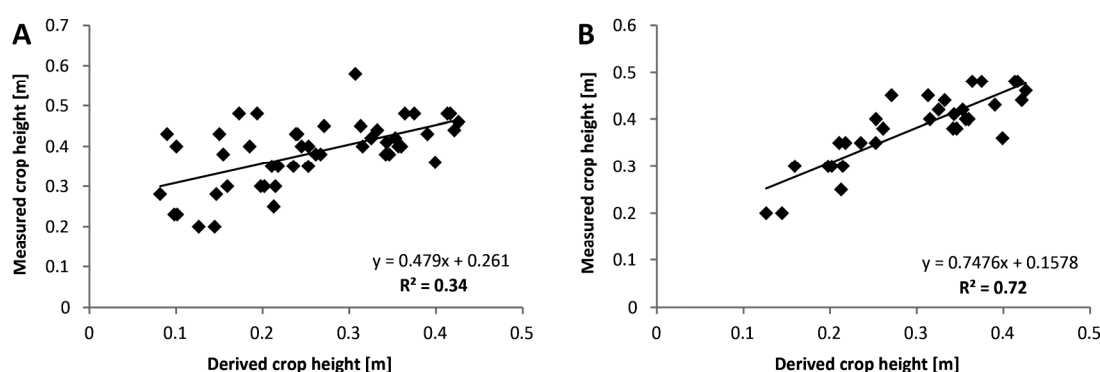


Figure 5-11: Comparison of derived and manually measured crop heights from every survey (A) and without the second survey that showed strong drought stress (B).

Figure 5-12 shows the map of crop heights from the three latter surveying dates. Every northern plot was used for biomass sampling, every southern plot is regarded in all computations here. The map of late June particularly shows the different development of the sugar beet cultivars. At this stage, plots of Berenika show the greatest plant height. Several areas of poor canopy development were precisely detectable. Particularly, the fourth repetition in the western part of the experimental site contains areas of small or no plants. This pattern was confirmed by related pictures, merged to a panoramic image. Those pictures were taken by the camera on top of the laser scanning device (cf. Figure 5-13). The resulting map of plant height of July highlights the drought stress situation. Most of the leaves of the plants showed the well-known symptoms, while Berenika and Cesira apparently suffered the most.

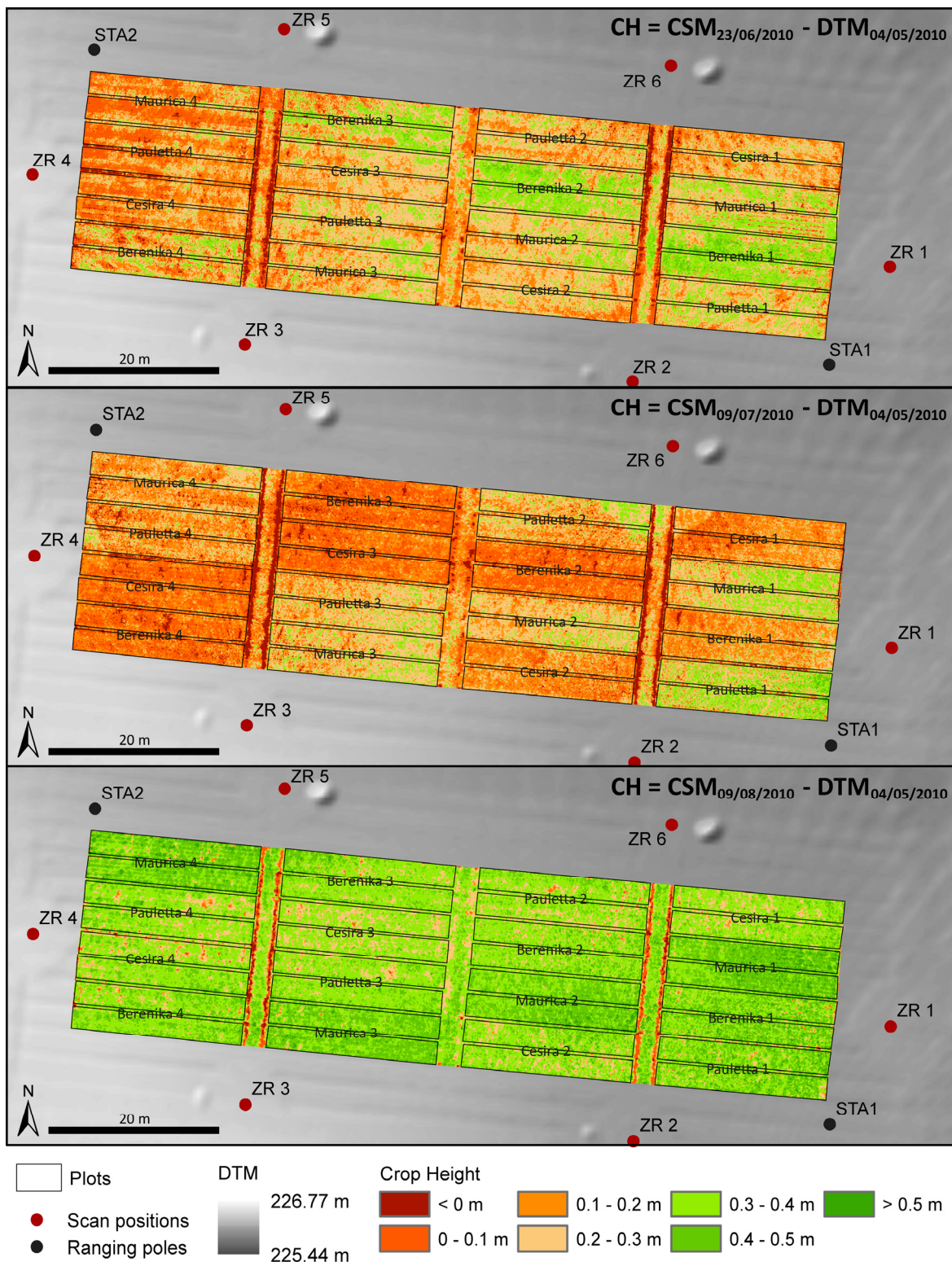


Figure 5-12: Crop Height (CH) for the three surveying dates, achieved by a comparison of the initial DTM from early May and the CSM from June, July and August 2010. Positions of the scanner and ranging poles are indicated by points. Patterns of different heights are visible and fit to the expected characteristics. Red areas indicate inferior canopy height, in particular for the drought stress in July. Mod. after HOFFMEISTER et al. (2012).



Figure 5-13: Panoramic image from the scan position ZR4 looking eastward is achieved by the camera mounted on the TLS. The crops in block four (in front) show poor crop development pattern. The areas correspond to the areas in the map of crop height from 23rd of June (Figure 5-12).

Again, a block influence from east to west is detectable. The CSM shows sharp edges around the scan positions ZR4-ZR6, which are the result of leaf descent during the day. The last map from August confirmed the observed discrepancy among the cultivars. The general trend of the decline of ground height to the west is particularly recognizable for the plots planted with Pauletta and Berenika. Cesira shows the highest overall values in every repetition.

The mean heights for each variety as well as the dried biomass are shown in Figure 5-14. A massive decline due to the significant period of drought is detectable in late June. The sugar beet cultivars responded differently to this drought period. The leaves of Maurica and Pauletta did not droop as much as the leaves of Berenika and Cesira and both cultivars developed higher dry biomass values at the end. This is also detectable in the corresponding maps (Figure 5-12).

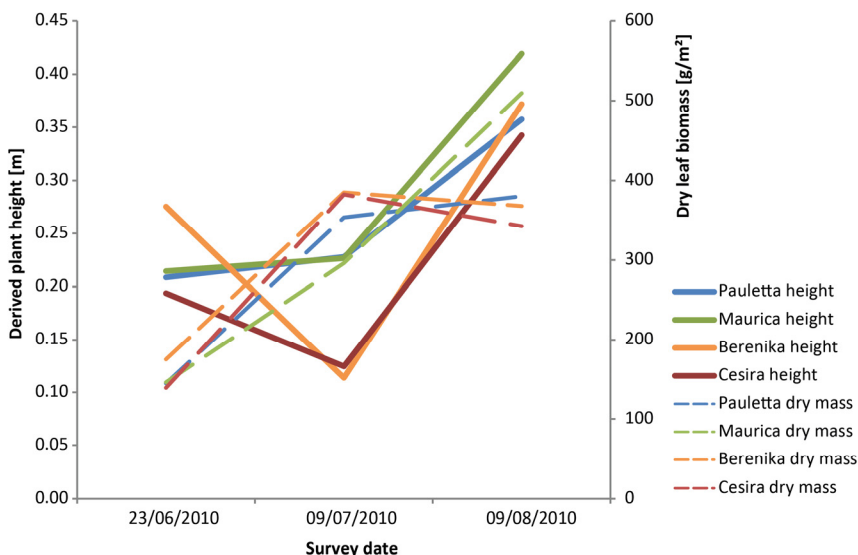


Figure 5-14: Comparison of derived plant height and dry leaf biomass, showing the significant decline for the survey of July, due to draught stress, as well as the late development. Pauletta and Maurica show better drought response.

Biomass and LAI correlation

Mean height values of each plot from each date were correlated to fresh and dry biomass (in g/m²) as well as LAI measurements (Table 5-6). A significant correlation between dry biomass and mean height was only found for the 23rd of June. Due to strong drought stress, no correlation is detectable for July. In August, when the crops did not suffer any more from drought stress, only minor correlation values can be found. Additionally, the results for the whole growth period show no significant correlation, except to dry leaf biomass. The volume approach shows similar values. Considering only the surveys of late June and August, significant correlations were found ($r > 0.87$).

Table 5-6: Correlation coefficients (r) of mean plot heights to fresh leaf biomass, dry leaf biomass, and LAI. Results of the volume based approach in parentheses.

Survey Date	Fresh leaf biomass	Dry leaf biomass	LAI
23/06/2010	0.89* (0.87*)	0.84* (0.83*)	0.71* (0.72*)
09/07/2010	-0.14 (-0.21)	-0.34 (-0.38)	-0.23 (-0.28)
09/08/2010	0.43 (0.45)	0.61* (0.59*)	0.32 (0.30)
All dates	0.21 (0.18)	0.38* (0.36*)	0.12 (0.10)
Only 23/06/2010 & 09/08/2010	0.90* (0.89*)	0.90* (0.88*)	0.89* (0.87*)

2-tailed test of significance is used
 *: correlation is significant at the 0.05 level

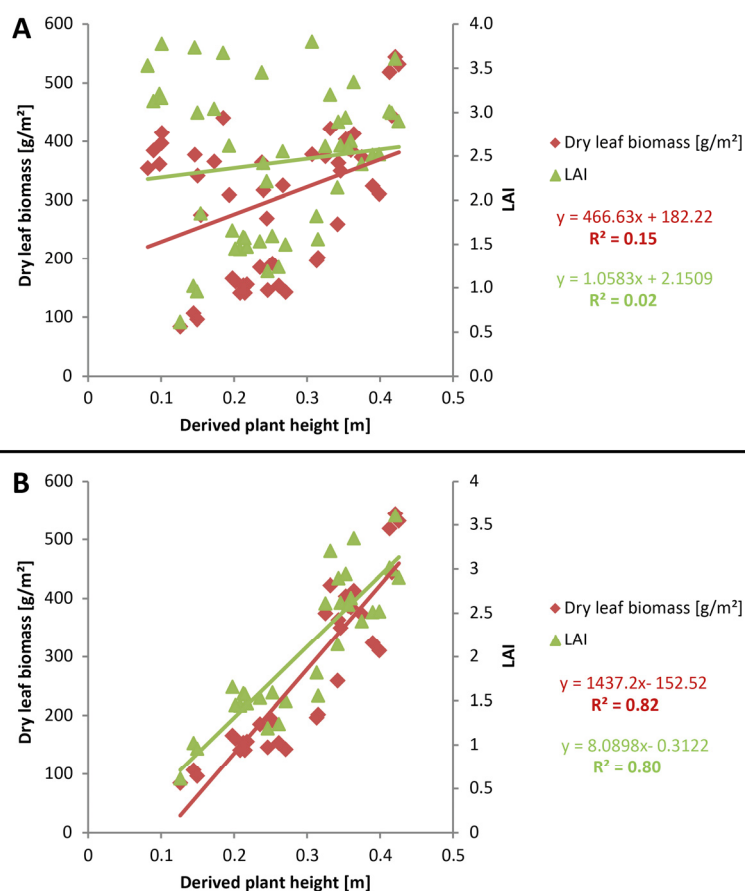


Figure 5-15: Comparison of dry leaf biomass and LAI to derived plant height. Data from all survey dates reveal only very low coefficients of determination (A), regarding only the first and last survey data better results were achieved (B). Similar values are achieved for fresh leaf biomass.

Regressions of the mean plant heights, dry leaf biomass and LAI, for all dates and the dates of late June and beginning of August for all plots are presented in Figure 5-15. Generally, high coefficients of determination without the second survey with drought stress are found for all plots and all values ($R^2 > 0.80$). Similar values were again computed for the volume based approach and for fresh leaf biomass data.

5.5 Discussion

TLS is feasible to derive plant height distribution and plant height development by a multi-temporal surveying method. Considering the method itself, the system and all components worked well under these conditions. Surveys cannot be fulfilled during rain, as most instruments are only splash-water proof. Dust and insects are the cause for noise, which requires filtering processes and manual work.

The method can be applied with a higher temporal resolution depending on organisation and logistics, but the measurement time of about half a day for a field is a major disadvantage. An expansion to an MLS approach by incorporating an INS will enable faster measurements with a more uniform, higher spatial and temporal resolution. Similarly, stereophotogrammetry on UAVs (BENDIG et al., 2012) or balloons (MURAKAMI et al., 2012) can be applied for an accurate, high spatial and temporal resolution.

The resulting point density needs to be taken in consideration. The surveys of the single field conducted with a tripod revealed a lower point density at a distance of ~ 100 m away from each scan position (Figure 5-16). Although, an additional position was established in 2009 within the studied field, a full coverage with a high density was still not acquired. Generally, less than 5 pts./m² were achieved. This problem was resolved by using a raised position from the depicted platform in 2010 (Figure 5-16). The point density increased to 800 pts./m².

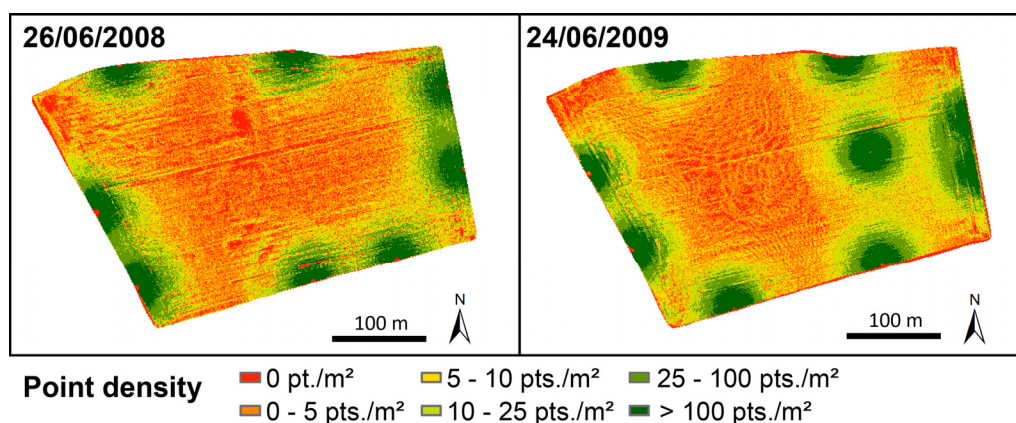


Figure 5-16: Point density per square metre for selected dates of 2008 and 2009 showing the decreasing point density in a distance > 100 m away from each scan position. An additional scan position in 2009 did not reveal a full coverage with a high point density. Modified after HOFFMEISTER et al. (2013c).

This high resolution can enable the automatic establishment of single plant points by using the differences in the intensity values between the small leaves and bare earth during an early stage of crop development (HÖFLE, 2014). A small test of this approach showed the potential, but the crop status of the regarded survey date here was not sufficient, as larger areas showed no crop emergence (Figure

5-17)*. However, single plant points can be modeled by estimation of plant seeding intervals and control points of emerged plants. Thus, the information of the crop height and crop growth can be related to these single plant points.

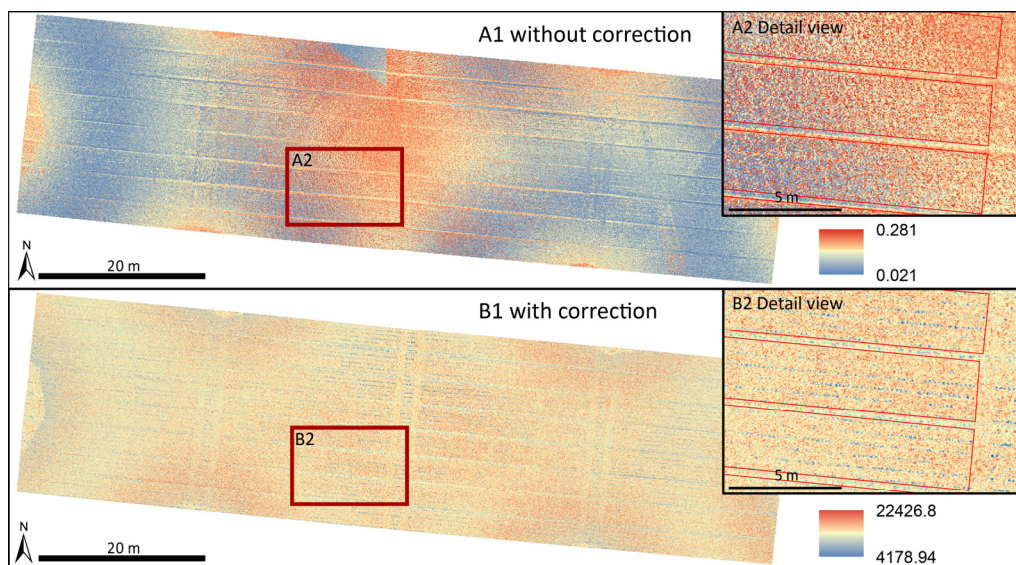


Figure 5-17: Intensity correction of the data. A1 shows the range influence with circular and single linear patterns around every scan position, which leads to very mixed intensity values (A2). The corrected data still shows a weak range influence (B1), but reveals plant patterns (B2).

The georeferencing approach of combining TLS surveys with accurate GNSS-measurements made an analysis and comparison with other georeferenced data possible. This was particularly important in the first study, as other data was incorporated to clarify reasons for crop height variance. In the first example, the RTK-DGPS base station was transformed into the states surveying network, whereas for the second example the base station point was measured by the RTK-solution with the Axio-Net PED correctional service. The comparison to the DTM of the state's surveying agency revealed a shift of about 70 cm, which can be the result of the different measurement methods and according post-processing steps, as well as the temporal difference. However, the relative relation shows a high correlation ($R^2=0.99$). Both measurements are within absolute centimetre accuracy, the second method being slightly less precise (cf. section 3.2).

In this approach, the height of the plants was indirectly derived by a comparison over time. In contrast, EHLERT et al. (2009) applied a height guiding device in front of a carrier that holds the laser sensor at a constant height above the ground. This allows computing the plant height by geometric relations. LUMME et al. (2008) mounted the CW-scanner vertically on a 3 m rack. The resulting data is correlated by an indirect registration of plastic discs, measured by a tachymeter. Thus, in both cases the crop height is directly measured and can be used for the computing of variable-rate farming equipment, e.g. sprayers. However, the comparisons to manually measured crop heights show the accuracy of the approach applied for this study. A similar set-up was applied on paddy rice fields and revealed a high accuracy between manual measurements and mean crop height values (TILLY et al., 2012). For sugar-beet, the

* The equation for correction of the data was established by Jun.-Prof. Dr. B. Höfle, University of Heidelberg.

correspondence is slightly worse, due to the more complex plant structure and the stronger uncertainty of manual crop height measurement (Figure 5-18). The derived crop height is a mean value of the corresponding cell size and the manual measurement is here an absolute, subjective value of a specific point.

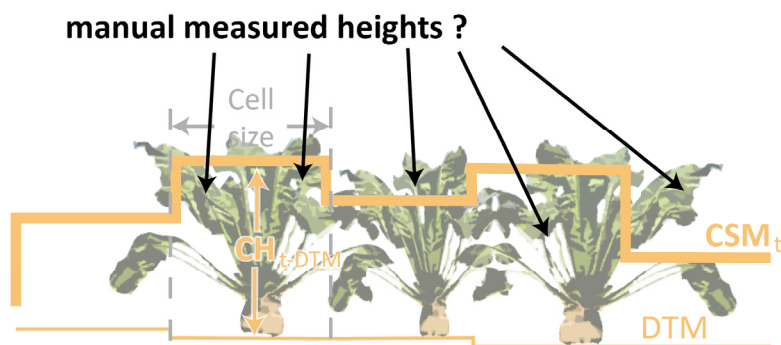


Figure 5-18: The manual measurement problem arises from the difference of the derived mean cell size value and the subjective manual measurement point, depicted by black arrowed lines.

The infield variability of the crop height was detectable for the years 2008 and 2009 (section 5.3). Differences in crop development can be detected and fit to manual measurements and the general distribution is visible in the corresponding pictures. For 2008, mean crop height values of each survey are similar to the independently gathered measurements (KORRES et al., 2010). Thus, the data is a valuable result and input parameter in regard to the aim of CRC-TR32 for the detection of vegetation patterns that influence vertical fluxes of energy, water and carbon.

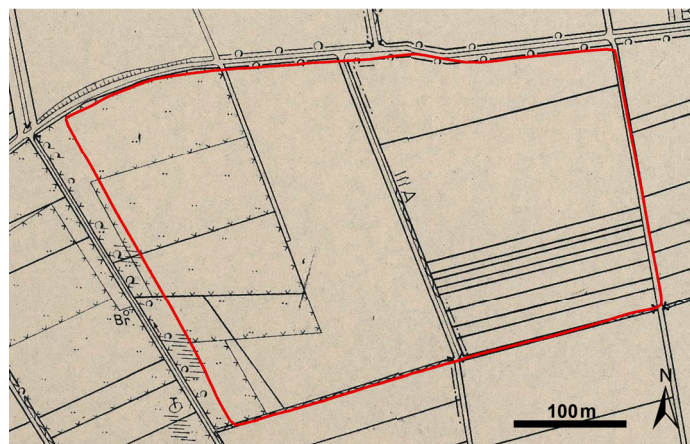


Figure 5-19: Map from 1953 revealing the old pathways and denoted gleyic grass land within the studied field (red line; LVA NRW, 1953).

In particular, the western part of the site showed poor crop establishment and the patterns are also visible in the presented orthophotos. The north-south linear edge in the centre of the site are the remains of old pathways, which existed prior to land reallocation (Figure 5-19). In addition, the whole area is shaped by an inactive palaeo-river system and remains of trenches and bomb craters of World

War II (RUDOLPH et al., 2013), which might be the cause for the circular pattern in the middle of the field. The latter was also denoted in the soil map as a cultural deposit or alteration area.

For correlation purposes, all data were aggregated to raster datasets of 1 m, 5 m, 10 m and 20 m pixel resolution and compared to parameters from topography, soil information and soil moisture. Generally, significant correlations were found ($r < 0.4$), similar to other studies (MCKINION et al., 2010b; HEUER et al., 2011). For instance, MCKINION et al. (2010b), related yield data from five years to topographic parameters and found regression values smaller than 0.11. The selected parameters here do not provide a satisfying explanation for the variation of the derived plant heights ($R^2 > 0.44$). Other processes are probably responsible for the detected variability, for instance management, nutrients, or water availability. The variation might be revealed by applying crop growth models that are additionally capable to acknowledge temporal processes (LENZ-WIEDEMANN et al., 2010). Theoretically, stagnant moisture after heavy rainfall can be a reason for sugar-beet decay, particularly in the gleyic area. This can be a reason for the higher differences in plant development in 2008, in contrast to the more uniform plant development in 2009, as well as an outcome of different plant stress tolerance. These different temporal effects of topography were denoted by the work of KASPAR et al. (2003), as introduced in section 5.1.

An enhancement of the results can be derived by a more sophisticated soil parameterization as using soil depth and soil value data acquired from maps. The soil moisture distributions also represent soil variation. However, the whole area shows a high variability in soil conditions and the spatial heterogeneity might be more accurately revealed by Electromagnetic Induction (EMI), which measures the Electromagnetic Conductivity (EC) of the soil (CORWIN & LESCH, 2005; KITCHEN et al., 2005).

The detection of height differences between various sugar-beet cultivars surveyed in 2010 was also carried out. Again, the results fit to manual measurements, pictures and the expected crop characteristics (section 6.4). The western part of the experimental site once more revealed a poor crop establishment. The long lasting drought stress period in late June and July 2010 accentuates the differences among the four cultivars. Pauletta and Maurica show a better stress response in terms of crop height and biomass.

Biomass samples were extracted for both studies, but more sampling was conducted within the CROP.SENSE.NET project in 2010. Crop height was related to fresh leaf and dry leaf biomass as well as LAI by correlation and regression analysis. Cereal crops show generally a high coefficient of determination to biomass ($R^2 > 0.88$) (EHLERT et al., 2009). The regression between sugar-beet height and biomass shows slightly smaller results ($R^2 > 0.80$). The volume based approach did not show any improvement. Similar results were found for LAI measurements. Voxel-based approaches, as applied by HOSOI & OMASA (2009) for PAD and PAI or in forestry applications, might lead to a further enhancement. A combination with multi- or hyperspectral data might also be useful (WEI et al., 2012; WILLERS et al., 2012).

6 Case study 3: Geoarchaeology

6.1 Introduction

Geoarchaeology is an interdisciplinary research area that applies geoscientific concepts, methods and knowledge for stratigraphical analysis of archaeological sites, as well as the reconstruction of past environments (RAPP & HILL, 2006; BRÜCKNER & GERLACH, 2007). The Collaborative Research Centre 806 (CRC 806) “Our Way to Europe – Culture-Environment Interaction and Human Mobility in the Late Quaternary” funded by the German Research Foundation (DFG) since 2009 (CRC806, 2013), is an interdisciplinary research project involving geoarchaeology, archaeology, geo- and social sciences of the universities of Cologne and Bonn, as well as the RWTH Aachen University. This interdisciplinary large-scale project investigates the complex relationship of chronology, culture, climate and environment during the dispersal of Anatomically Modern Humans (AMH) from Africa into Eurasia during the last 190,000 years (RICHTER et al., 2012). TLS is used here as a method for the accurate documentation of archaeological sites, thereby supporting geoarchaeological research.

After RICHTER et al. (2012), two main migration corridors from the source region mainly in East Africa are assumed. The eastern corridor is leading from East Africa via Northeast Africa into the Middle East, whereas the western corridor is heading via Northwest Africa and Gibraltar to the Iberian Peninsula (Figure 6-1). Several episodes of emergence, settlement, and dispersal, as well as a likely interaction with Neanderthals are examined (e.g. Finlayson et al., 2006).

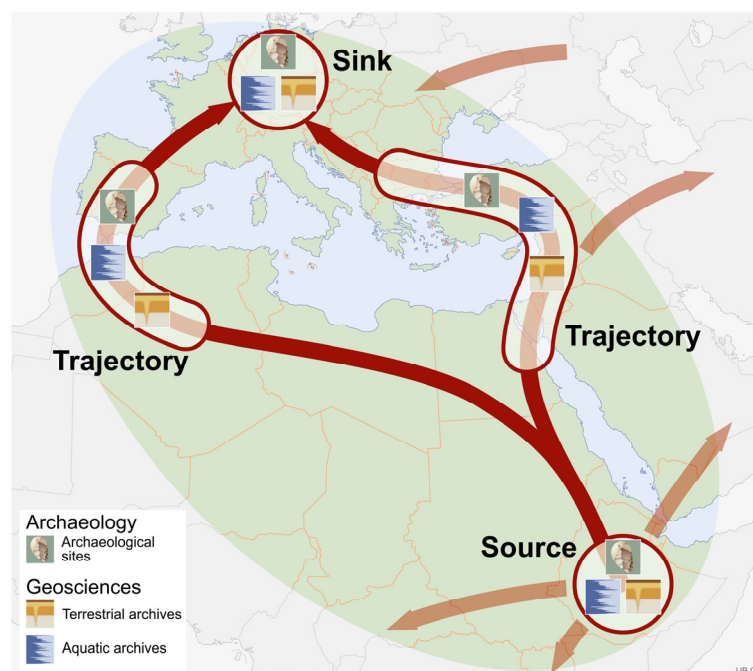


Figure 6-1: Research areas of the CRC 806, tracking the possible dispersal of Anatomically Modern Humans (AMH) from the source, along the trajectories to the sink in central Europe (copyright: U. Beha/University of Cologne 2007).

For that purpose, foci of the CRC 806 are on terrestrial archives and associated archaeological excavations, as well as limnic archives. In order to obtain palaeoenvironmental data of relevant time periods, drillings were carried out on lake Yoa in northern Tschad (BROVKIN & CLAUSSEN, 2008; KROPELIN et al., 2008; KROPELIN et al., 2008), lake Chew Bahir in southern Ethiopia (FOERSTER et al., 2012), lake Iznik in northern Turkey (ROESER et al., 2012; ÜLGEN et al., 2012; VIEHBERG et al., 2012), lake Prespa in the Balkans (AUFGEBAUER et al., 2012; WAGNER et al., 2012) and lake Banyoles in NE-Spain (HÖBIG et al., 2012). Archaeological excavations and intensive geoarchaeological fieldwork was conducted for example at the Mochena Borago Shelter in Ethiopia (BRANDT et al., 2012), the Sodmein Cave in Egypt (MOEYERSONS et al., 2002), and in Wadi Sabra in Jordan (BERTRAMS et al., 2012). This research contributes to the theoretical framework, which was established to understand the different phases of human dispersal and the disappearance of the Neanderthals (BRADTMÖLLER et al., 2012; WIDLÖK et al., 2012; ZIMMERMANN, 2012).

For the purpose of supporting geoarchaeological research, accurate maps and models are required, which can be achieved by laser scanning. In addition, laser scanning is one method to capture and accurately document cultural heritage sites (REMONDINO, 2011). Examples are the survey of historic buildings (HERDT & JONES, 2008; ARMESTO-GONZÁLEZ et al., 2010; ALSHAWABKEH et al., 2011; RIVEIRO et al., 2011) and caves with ancient remains (BUCHROITHNER & GAISECKER, 2009; GONZÁLEZ-AGUILERA et al., 2009; GONZALEZ-AGUILERA et al., 2009; RÜTHER et al., 2009; LERMA et al., 2010; GONZALEZ-AGUILERA et al., 2011a). TLS data can be further used to reconstruct, for example, small missing parts of artifacts, which are printed as 3D objects (FATUZZO et al., 2011) and general CAD models (RÜTHER et al., 2009; LERONES et al., 2010; RÜTHER et al., 2012). ALS surveys are important for a more general detection and documentation of sites (BEWLEY et al., 2005; CRUTCHLEY, 2006; DEVEREUX et al., 2008; LASAPONARA et al., 2010; WERBROUCK et al., 2011; ŠTULAR et al., 2012). Particularly the detection of sites in forests is simplified by an integration of the full-waveform detection (section 2.2.5) and, accordingly, enhanced bare-earth extraction (DONEUS et al., 2008). Furthermore, bathymetric ALS (section 2.2.1) is able to detect and document sites in shallow-water (DONEUS et al., 2013).

As shown by REMONDINO (2011) and NUNEZ ANDRES & BULL POZUELO (2009), most of the available remote sensing methods are employed for the accurate detection and description of geoarchaeological sites and the documentation of cultural heritage. For example, the combination of TLS and UAV-photogrammetry was used for a survey of Pichango Alto, Peru (LAMBERS et al., 2007). As REMONDINO (2011) states, there are still a lot of problems to be solved, which are for example the storage, exchange, quality control and metadata description of 3D models, as well as specific problems with each method.

In this contribution, TLS has been applied for the documentation of research sites within the context of the CRC 806. Similar surveys were carried out to answer specific research questions, as well as for mapping and visualisation purposes. For instance, the accurate determination of specific dimensions, such as size and volume, were important, as well as the integration of already existing data into the 3D-measurement framework.

6.2 Neolithic sites in Jordan

6.2.1 Geoarchaeological background

Geoarchaeological studies in the Levant have related cultural transformation to climate change during the Neolithic period (WENINGER et al., 2006; GEBEL, 2009; ROLLEFSON, 2009; WENINGER, 2009; ZIELHOFER et al., 2012). Variations in precipitation, which have occurred in the mainly arid or semi-arid region can be derived from the amplitudes of the Dead Sea levels (MAYEWSKI et al., 2004). A major drop of the sea-level at 8.6 ka BP is followed by an interval of Rapid Climate Change (RCC) from 8.6-8.0 ka BP and an associated abandonment of Neolithic settlements in Jordan. This phase also matches to a global cold event at 8.2 ka BP, which resulted in an intensification of the global atmospheric circulation. The Levant experienced a colder and drier phase after the optimal Levantine Moist Period (10-8.6 ka BP) (MAHER et al., 2011). During this colder and drier phase with a different circulation, cold Siberian winds from the North could have “interacted strongly with the moist Mediterranean air masses to produce extremely flashy and intensive precipitation” (WENINGER, 2009: 10). This climatic change is also evident in the $\delta^{13}\text{C}$ isotopic relation of the stalagmite record from the Soreq cave in Israel and flash floods may have occurred during this stage (WENINGER, 2009).

Correspondingly, the so-called Yarmoukian* rubble layer (YRL) as a thick, fist-size, angular stone rubble deposit containing re-deposited cultural material (GEBEL, 2009), which covers several of the important Neolithic sites in the Levant and Turkey, might be the result of the assumed flash floods in this phase of climatological change and an assumed reason for the observed cultural decline. However, several authors pointed out that different and combined causes for the occurrence of this stratigraphic layer and the cultural decline exist and that no clear evidence was found (GEBEL, 2009; ROLLEFSON, 2009; WENINGER, 2009). As it turned out, the assumption of a mono-causal decline due to RCC was mainly disproven, because findings in the YRL itself were dated to the Middle to Late Chalcolithic period (6.9-6.2 ka BP) and shows no evidence of a flooding scenario and is most probably of anthropogenic origin (ZIELHOFER et al., 2012). Thus, the YRL is not the reason for abandonment of the sites, but an outcome.

However, in this context, several sites ('Ain Ghazal, 'Ain Jamman, Ba'ja, Basta) in Jordan were visited during spring 2010, in order to investigate this rubble layer phenomenon, as well as to document the archaeological sites from the Pre-Pottery Neolithic B (PPNB). The survey was conducted together with the subproject F1 “Application of Cosmogenic Nuclide Dating (^{14}C and ^{10}Be) in the Construction of High-Resolution Archaeological Chronologies” of the CRC 806. The sites 'Ain Ghazal, 'Ain Jamman and Basta were surveyed with the previously presented approach, combining TLS and direct georeferencing of the point clouds by RTK-DGPS measurements (WGS 1984, UTM 36N).

* The Yarmoukian is the dominant culture in that area during this time (ROLLEFSON, 2009).

6.2.2 Survey description and results

'Ain Ghazal

'Ain Ghazal (N 31°59'9", E 35°58'33") is one of the earliest larger population centres, now situated in the NE suburbs of Amman in the Zarqa River valley (KAFAFI et al., 2009; ZIELHOFER et al., 2012). The area was surveyed in just one day by three scan positions on the upper side of the slope and one additional scan position on the opposite side of the valley, as depicted in Figure 6-2. The extent of the geoarchaeological trenches were measured by RTK-DGPS system.

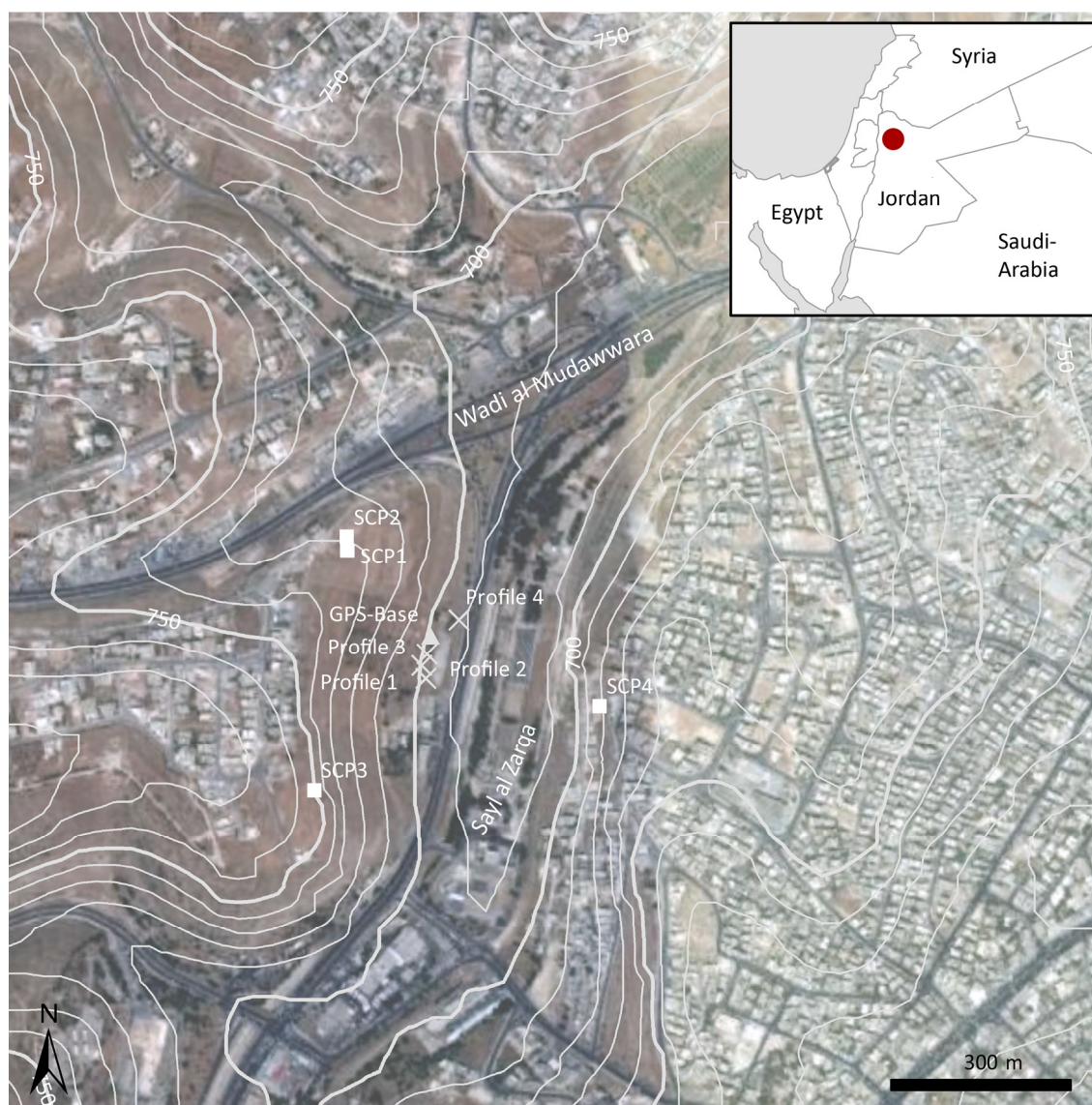


Figure 6-2: Overview map of the Zarqa River valley in NE-Amman with the location of the scan positions (white squares), the RTK-DGPS base station (white triangle), and archaeological profiles (white crosses). Digital elevation model and contours are derived from ASTER-GDEM. Imagery: © 2013 Google, Digital Globe, 27/04/2010. Country data: ArcWorld Supplement. Modified after ZIELHOFER et al. (2012).

An accurate HRDEM of the area, which is obstructed by several buildings, trees and shrubs, is derived by extensive filtering with the manual terrain filter approach (cf. section 3.5.4). Starting with 10 million points overall, the obstruction were removed in three consecutive steps to finally achieve about 5.5 million ground points for the whole area. The removed points are stored in another object file and are visualized accordingly with the final HRDEM in Figure 6-3. The final HRDEM is established as a TIN from the final point cloud and filtered by the Smooth & Decimate-function. Subsequently, the position of the archaeological sections and derived contour lines were added (Figure 6-3, bottom).

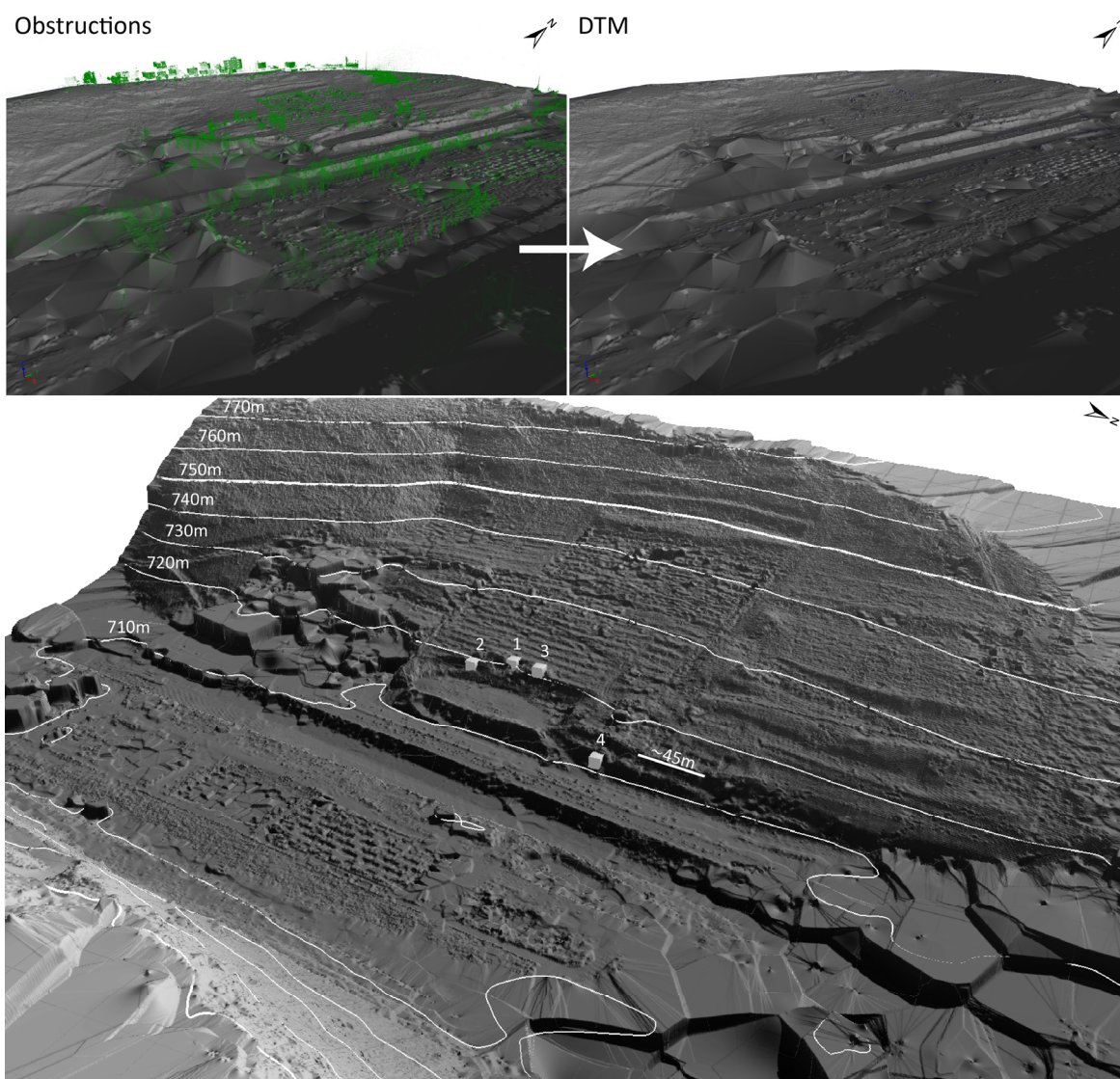


Figure 6-3: Perspective views of the Zarqa river valley and the archaeological site of 'Ain Ghaizal. Upper figures depict the removed obstacles (left) and the derived HRDEM of the valley (right). The perspective view of the valley slope (bottom) with combined contour lines and archaeological profiles (white boxes) reveals no stronger fluvial activity on this side of the valley. Bottom part: ZIELHOFER et al. (2012).

'Ain Jamman

The settlement of 'Ain Jamman (N 30°1'14", E 35°28'5") is located in southern Jordan (ROLLEFSON, 2005; MAKAREWICZ, 2009). The area lies close to the highway from Ma'an to 'Aqaba and was identified during road construction. The site was intensely surveyed by nine different scan positions in two days. At most of the scan positions additional tilted scans were conducted, to cover the site. A detailed plan was established for this site (Figure 6-4) by applying a symbolic reconstruction (cf. section 3.5.4). Single stones in certain areas can be digitised, depending on point density. Additionally, cross sectional profiles of interesting spots of architectural details, like windows, doors and stairs can be derived. The detected walls cover an area of ~30 by 40 m and several rooms can be distinguished.

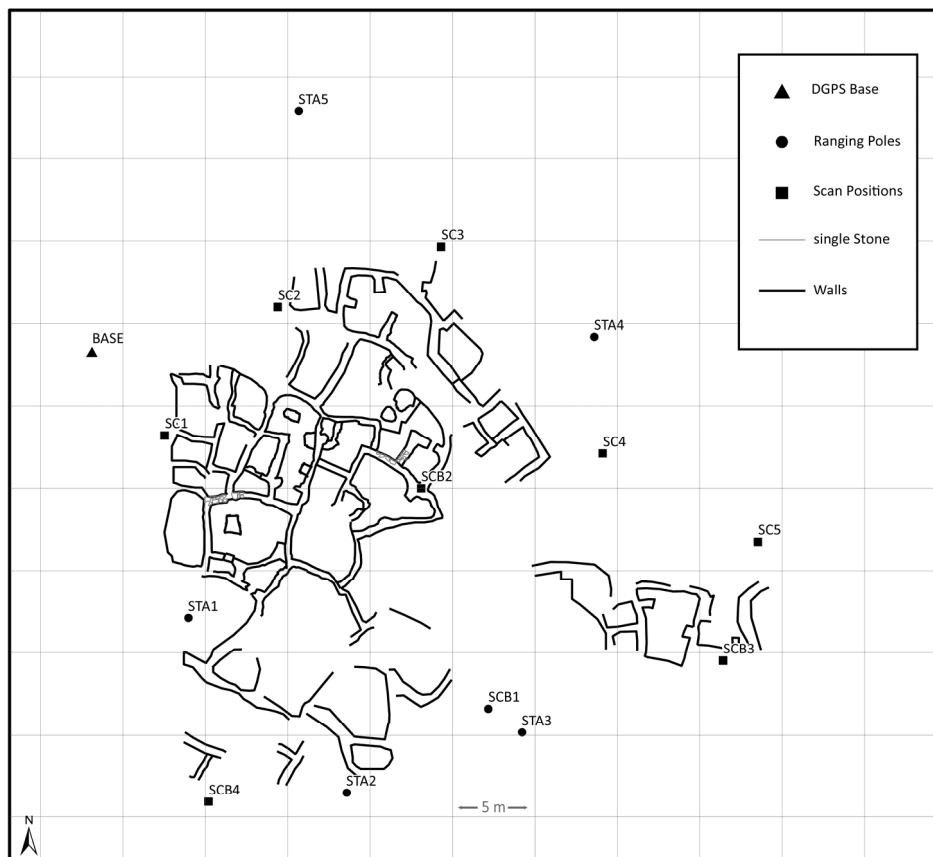


Figure 6-4: Overview map of the archaeological site of 'Ain Jamman, Jordan.

6.3 The Ardales cave (Cueva de Ardales) in Spain

6.3.1 Geoarchaeological background

Research was also conducted in the southern part of the Iberian Peninsula, as well as the north-western part of Africa (LINSTÄDTER et al., 2012). These regions are important for the CRC 806, as a possible, additional bridge or barrier of human dispersal (RICHTER et al., 2012). In addition, the specific area was possibly the last refuge area of the Neanderthals with evidence of their existence until 28 ka BP (FINLAYSON et al., 2006; JENNINGS et al., 2011; LÓPEZ-GARCÍA et al., 2012; BLAIN et al., 2013). Again, RCC has occurred, here with regard to the North Atlantic Heinrich Events (HE), which possibly led to breakdown of

settlements in Southern Iberia (BRADTMÖLLER et al., 2012; SCHMIDT et al., 2012). In this area, numerous caves and rock shelters have been investigated by project members. The focus of the field campaign in spring 2012 was on two caves, the cave of Ardales and the Sima de las Palomas de Teba. The surveys were conducted in the context of the subproject C1 “Continuity or Discontinuity? Patterns of Land Use and Climatic Changes in the Late Pleistocene of the Iberian Peninsula” of the CRC 806.

6.3.2 Survey description

The complexly structured cave of Ardales (N 36°52'22", W 4°49'44") is located south-east of the town of Ardales (RAMOS et al., 1992). Several records verifying the occupation by prehistoric humans have been documented, such as hundreds of Palaeolithic mural paintings and engravings, as well as bones and artifacts. The cave can be divided into the lower parts and the upper parts (Galerías Altas). The latter served as a burial place, which is nowadays only reachable by rock climbing (RAMOS et al., 1992). At least one or possibly several additional entrances must have existed to safely reach those areas. Thus, besides an accurate mapping of the cave, it was an additional task to find evidences for the hypothesis of additional entrances.

Therefore, not only the interior cave was intensively surveyed but also the whole outside hill was recorded by TLS. For the outside area 21 scan positions were established, all recorded by RTK-DGPS measurements and respective reflectors on ranging poles (WGS 1984, UTM 30N). The inside area of the cave was surveyed by 19 scan positions, most of them with additional, tilted scan positions. Supplementary illumination was necessary to achieve better pictures from the mounted camera. This was achieved by an external light mounted onto the camera (Figure 6-5). Further contrast enhancements became necessary for these images. For the inner parts of the site the registration of the scan positions was enabled by an indirect registration with targets (section 2.4.2). A connective registration between the outside RTK-DGPS measurements and the inside local surveying network (Trimble M3 5" total station)* was established at two scan positions. All further scan positions of the inside survey were connected by the introduced small reflectors on flower pots (section 3.3). An accurate integration of all previously measured geoarchaeological data of the total station was possible by the established transformation of both systems.

After removing vegetation from the outside scan position data, a HRDEM with a resolution of 20 cm was interpolated. The 3D model of the inside area was computed by a combination of the polar triangulation and outer surface extraction functions (section 3.5.4). As a result of the post-processing of the collected data, a ground plan was established by applying a symbolic reconstruction (cf. section 3.5.4), and the results were subsequently extended by using data from older maps. For further indications of cave entrances, the outside model and the inside upper shape of the cave were compared, which reflects the ceiling thickness (Figure 6-6). Additionally, the existing modern entrance building and inner entrance door were manually removed and the presumably ancient entrance area was reconstructed.

* Measurements by Dr. A. Pastoors, Neanderthal Museum, Mettmann, Germany.



Figure 6-5: Scan position in the cave of Ardales. An additional light is mounted onto the camera of the laser scanner for better illumination of the pictures. The position is between the geoarchaeological sites 2 and 3.

The assembled 3D model of the whole cave was used to estimate, whether sun-light from the entrance is directly visible at certain places. For every inside area accurate models and detailed maps can be established, mostly in combination with panoramic pictures of the camera or as textured models. For this smaller site only 5 positions were needed with several additional tilted scans. Furthermore, it was possible to align 3D data from a structured-light scanner by a point cloud to point cloud registration (cf. section 2.4.2).

The other site, Sima de las Palomas de Teba (N 36°58'58", W 4°58'58"), was similarly surveyed and the local surveying network was also incorporated and used for registration purposes. Furthermore, the tachymetric measurements of the important karstic rock shelter were used to expand the 3D model for full coverage of the site. As the site is complexly structured, the triangulation was conducted in Geomagic (section 3.5.4). The small chute is filled with sediments containing abundant lithics of Mousterian* affinity as well as bone and charcoal fragments (MEDIANERO et al., 2011).

* Mousterian, the cultural epoch of the Neanderthals, ~120 ka-28 ka BP, Middle Paleolithic.

6.3.3 Results

A 3D model of the cave of Ardales and the outside hill was derived from the accurate TLS measurements (Figure 6-6). The area of the cave shows an extent of ~115 m in a southwestern direction and a maximum width of about 50 m. The great hall, “Sallas de las estrellas”, lies about 20 m below the entrance with a ceiling height of ~20 m. Similar values are depicted for the corridor at the Galeria Altas. The entrance area, the main hall, the corridor and the most southwestern point have a ceiling thickness of about 8 m, whereas other areas reveal differences of up to 47 m between the inner ceiling and the outside surface of the hill.

The entrance to the cave, which is now protected by an entrance building, was virtually reconstructed by removing man-made objects. This new entrance area was integrated into the whole cave model (Figure 6-7). Line-of-sight relations between the entrance areas and the grand hall were estimated. In terms of visibility, as depicted in Figure 6-7, a narrow direct line of sight exists from the entrance to the ground floor of the grand hall.

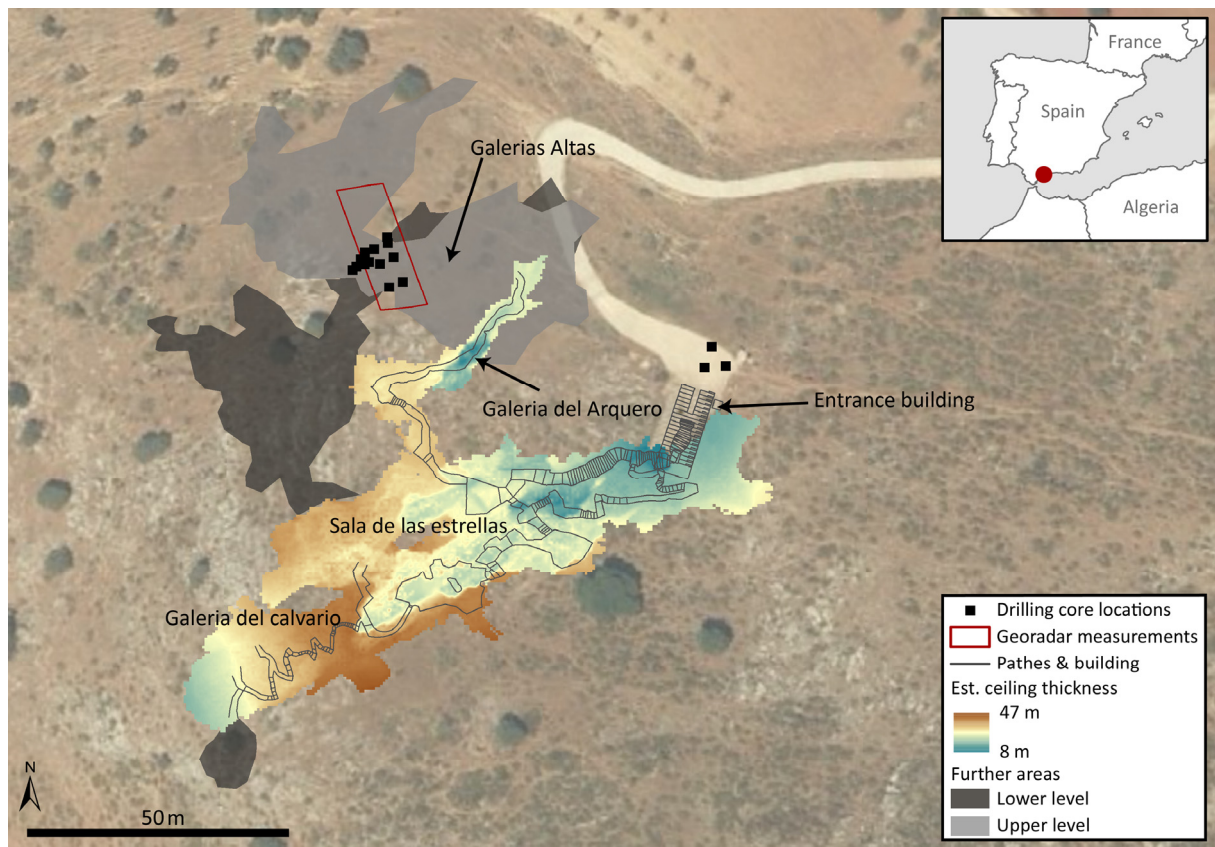


Figure 6-6: Map of the Ardales cave. The ceiling thickness was achieved by comparing the inner and outer 3D model, paths and outlines of the entrance building were derived from the point cloud. Imagery: © 2012 Google, Digital Globe, 21/09/2009. Country data: ArcWorld Supplement.

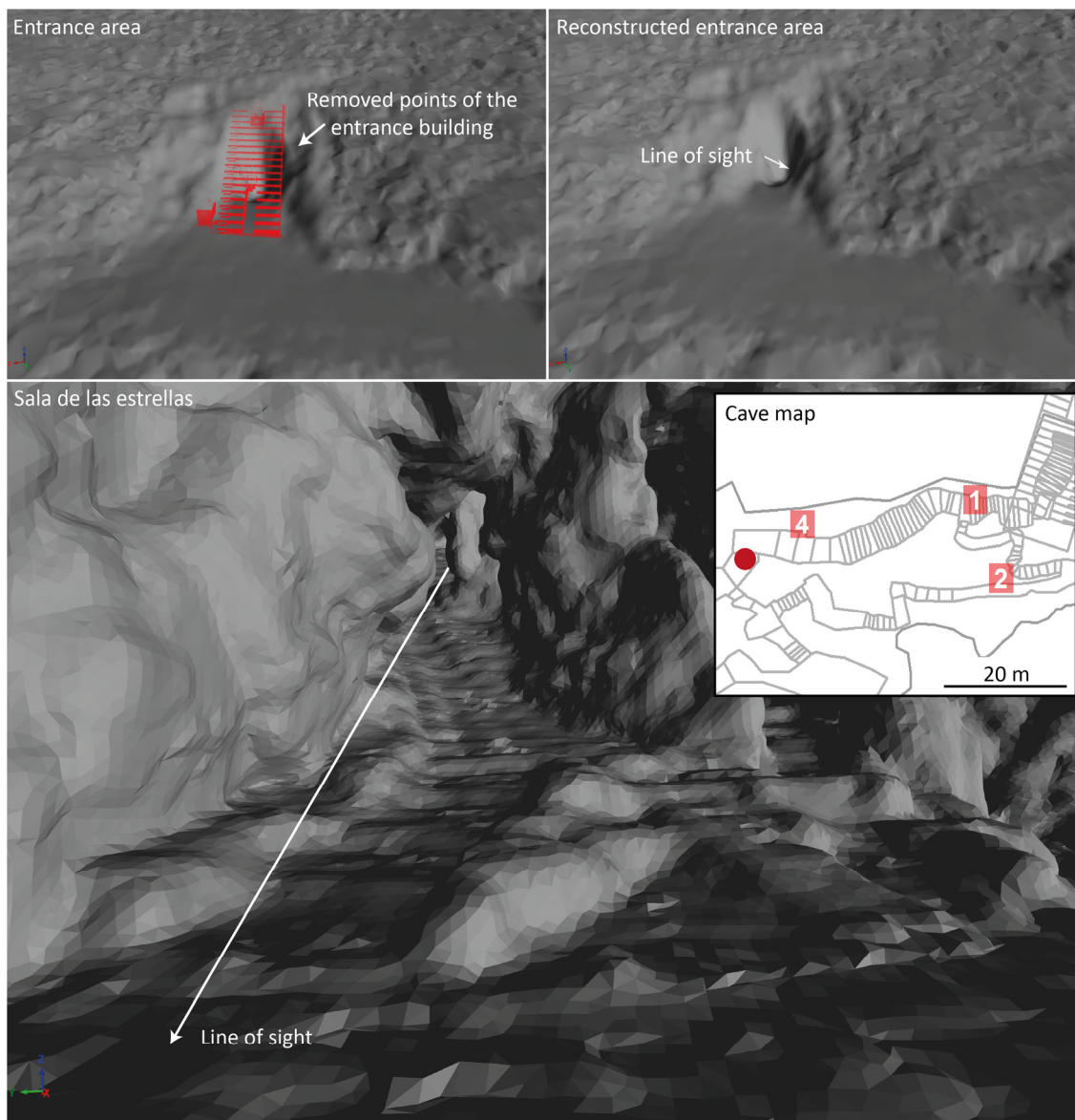


Figure 6-7: Perspective views of the 3D model of the Ardales cave. Top left: Entrance area with removed points of the entrance building (red dots). Top right: Reconstructed entrance to the cave. The arrow indicates the direct line of sight. Bottom: Perspective inside view of the Sala de las estrellas, position marked by red dot in the cave map. The other part of the line of sight assumes that daylight was visible in this area. All views show the 3D cave model in a 20 cm resolution.

Accurate models of specific inner areas can be derived. In Figure 6-8, the geoarchaeological section 2 is depicted in detail with the corresponding panoramic picture of the mounted camera. This part of the cave is filled by a debris cone, consisting of stalagmitic crusts, gravitational debris, rockfall eboulis and fluvial deposits (KEHL, 2013, pers. comm.).

In several sections of the cave, engravings were measured by a structured-light scanner, type Breuckmann smartSCAN^{3D}-DUO, for a high-resolution representation (resolution ~ 0.35 mm/pixel). Restrictions in the cave prevented the use of reflectors on the walls. Thus, a point cloud to point cloud registration (section 2.4.2) was used to achieve an accurate integration of these datasets. The pictures of the TLS camera are utilised to texture these detailed models of the areas 7 and 8 (Figure 6-6), as depicted in Figure 6-9.

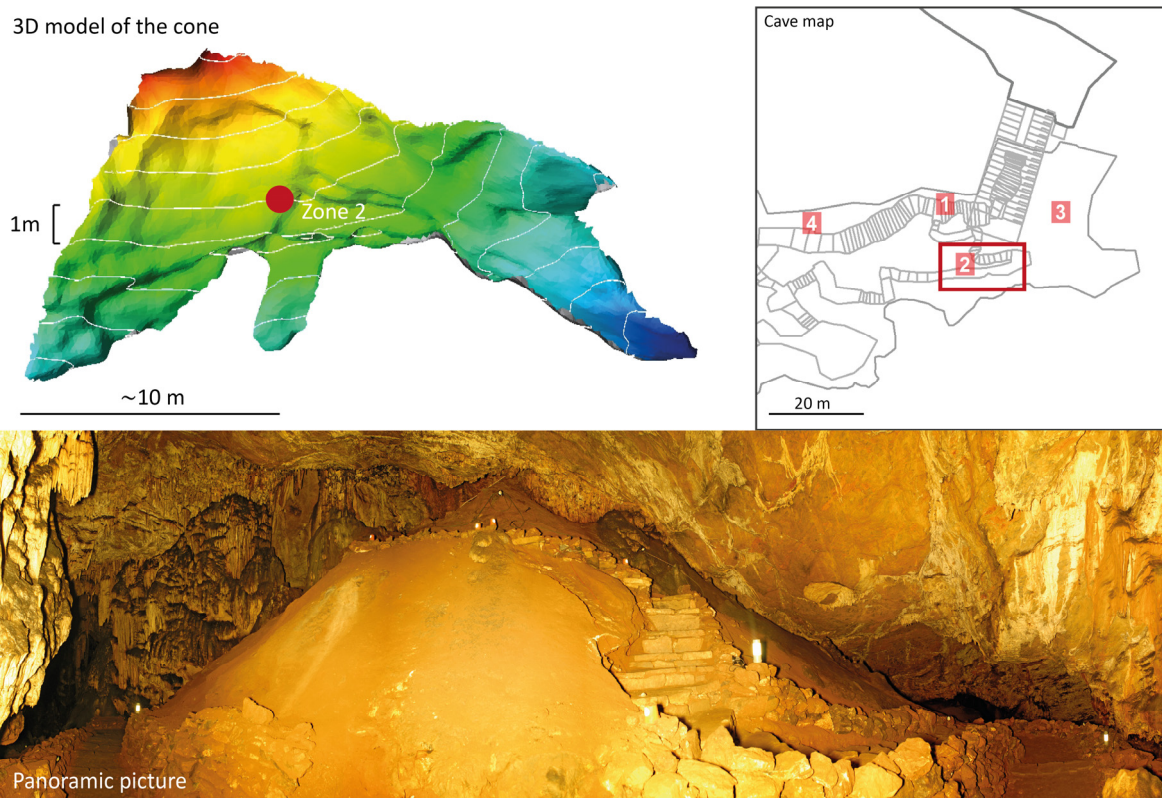


Figure 6-8: 3D model and panoramic picture of the mounted camera from the inside debris cone at geoarchaeological zone 2 (red dot and rectangle).

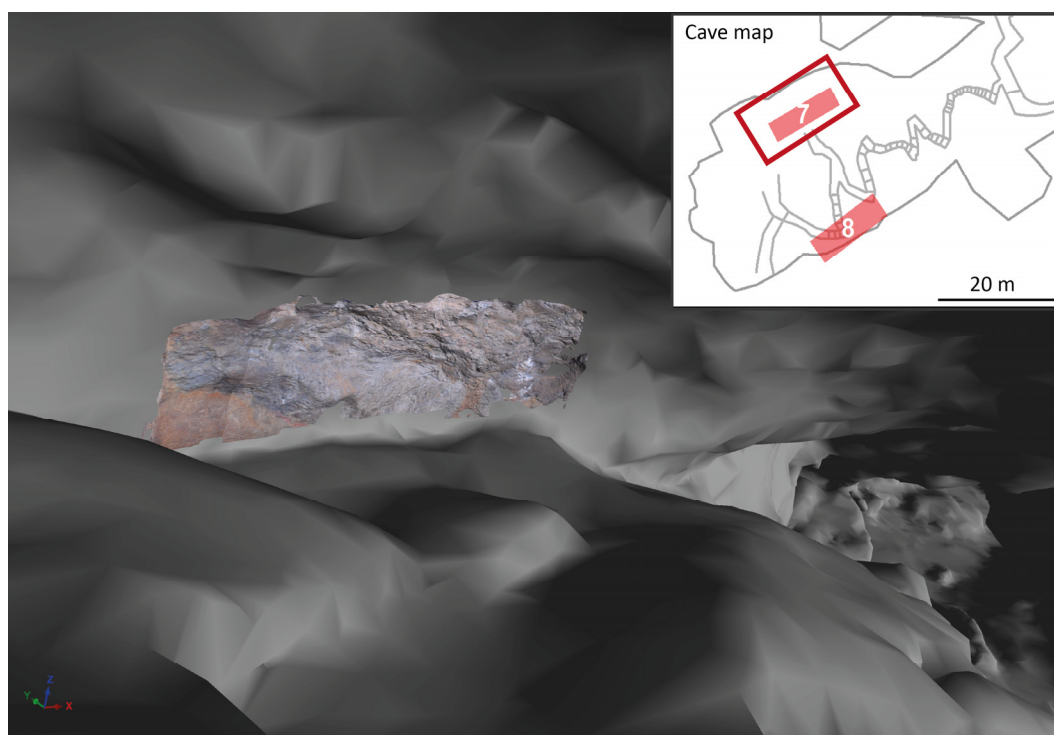


Figure 6-9: Part of the 3D cave model with the accurately positioned and textured high resolution scan of the structured-light scanner. The geoarchaeological zone 7 shows important engravings on the wall of the cave, which can be revealed by the high resolution surveying of a structured-light scanner.

6.4 The Sodmein Cave, Egypt

6.4.1 Geoarchaeological background

The Sodmein Cave (N 26°14'44", E 33°58'24") is located in the Red Sea Mountains of Egypt, around 40 km northwest of Quseir. The cave is situated on the northern flank of the break-through of Wadi Sodmein through the Eocene Limestone of Djebel Duwi. In this cavern more than 4 m of stratified human occupation debris can be identified, spanning from the Late Pleistocene to the Holocene. Therefore, it constitutes a key site for the reconstruction of Late Pleistocene human-environment interaction in Northeast Africa. The lowermost layers have been assigned to 118 ka BP by thermoluminescence dating and give evidence for wetter climate conditions (MERCIER et al., 1999; MOEYERSONS et al., 2002). Thus, the development of the cave in the Eocene Thebes limestone is assigned as karstic, but a system of local faults and associated shear zones with vertical displacement surround the cave, which may have also played an important role in shaping the appearance of the cave. Rock fragments breaking of the roof form a ridge in front of the cave (rockfall wall), in combination with rockfall from other parts of the cliff (MOEYERSONS et al., 2002). The area of interest is located between this frontwall and the backward wall, where several archaeological trenches were excavated (Figure 6-12). A number of archaeological layers with an excellent organic preservation and numerous stone artifacts could be documented in this stratigraphy. Overall, the stratigraphy comprises the Middle Palaeolithic to Neolithic periodes, with the oldest layer J having been dated to 118 ka BP (MERCIER et al., 1999).

In order to identify the dimensions of the Sodmein Cave and the tectonic displacements, as well as the accurate documentation of the current state of the cave and the associated transformation of the local archaeological surveying network, several RTK-DGPS and laser scanning measurements were conducted inside the cave and along the adjacent Wadi Sodmein during a survey field campaign in spring 2012. The research was arranged in cooperation with project A1 "Out of Africa – Late Pleistocene Rock Shelter Stratigraphies and Palaeoenvironments in Northeastern Africa" of the CRC 806. Again, the previously mentioned method for direct georeferencing was used in combination with indirect registration within the cave by tachymetric surveying.

6.4.2 Survey description

The survey of the Sodmein Cave was conducted by three scan positions that were established in front of the cave on the wadi floor and five scan positions were set within the cave. One of the latter was located in one of the main archaeological trenches. The registration of the inner parts was facilitated using an indirect registration by small reflector targets. These were additionally measured by a total station to allow a transformation of the local archaeological surveying system and the RTK-DGPS system (WGS 1984, UTM 36N). Overall, the measurements were carried out in a harsh, warm and dusty environment, but no technical problems occurred. As described in section 3, the usual post-processing steps were conducted to establish a 3D model of the cave, the surrounding cliff, the debris cone in front of the cave and archaeological sections. This model was then used to derive the plan and cross-sectional profiles.

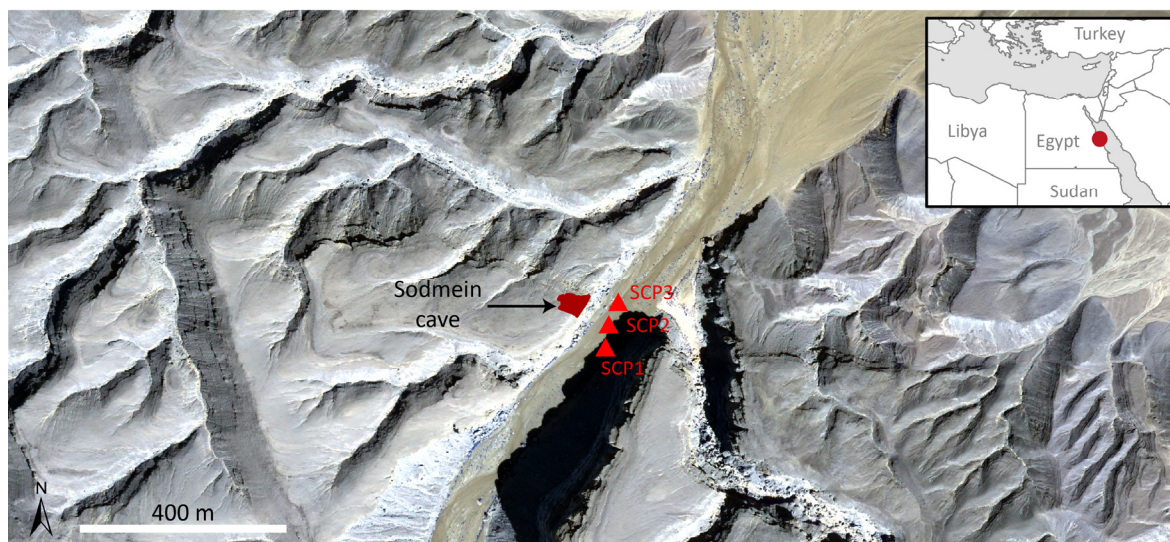


Figure 6-10: Overview map of the Sodmein cave location. Outside scan positions (red triangles) are assigned, and the footprint of the cave. Imagery: DigitalGlobe, 2012. Country data: ArcWorld Supplement.

6.4.3 Results

After successfully establishing the 3D model of the cave and the surrounding cliff wall (Figure 6-11), the detected fault lines and the vertical displacement (> 2 m), were estimated in the model and match to previous investigations (MOEYERSONS et al., 2002). The cave volume ($\sim 12,200$ m³) and the nearly similar debris volume in front of the cave ($\sim 13,200$ m³) was computed by incorporation of virtual planes for closure.

Cross-sectional profiles were established in AutoCAD and all data were integrated in ArcMap (Figure 6-12). The contour lines are directly derived in RiScan Pro and the assigned height was calculated with regard to the WGS 1984 ellipsoid, indicating a height difference between the uppermost part of the cave and the floor of the wadi as ~ 33 m. The main cave measures about 40 m by 25 m and the height at the front of the cave is 13-14 m. The small shafts in the back of the cave reach up to 40 m into the Thebes limestone and have been assigned as solution features (MOEYERSONS et al., 2002).

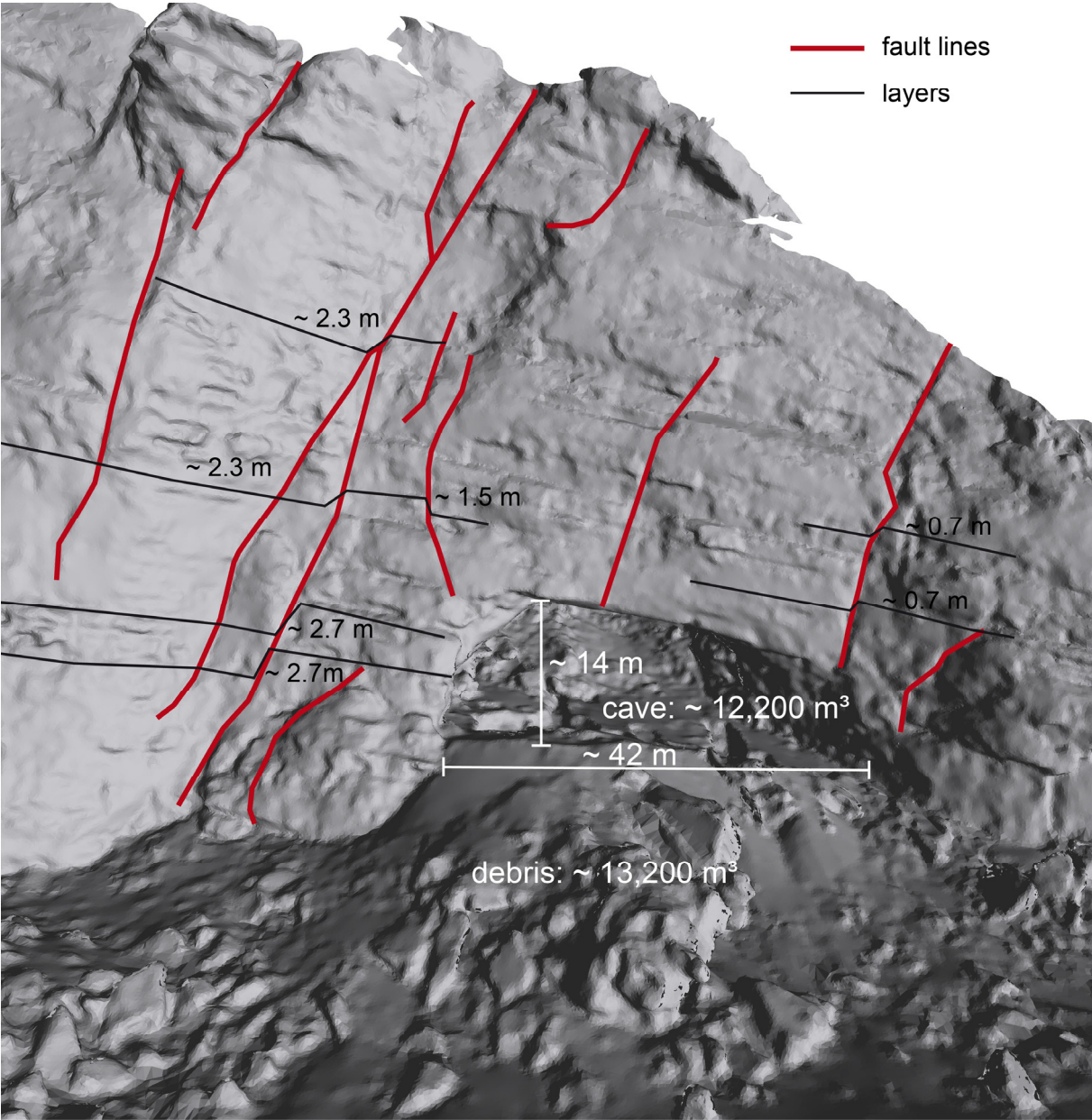
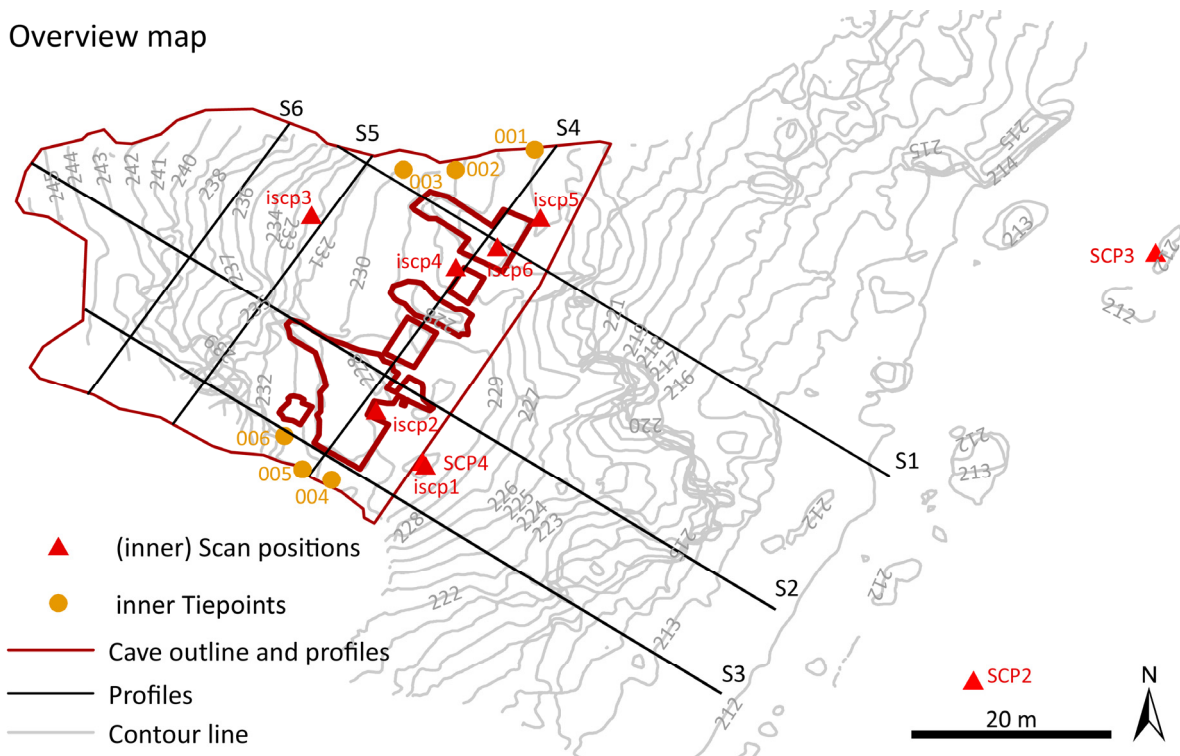


Figure 6-11: Perspective view of the 3D model of the Sodmein Cave. Fault lines and vertical displacement were manually detected and measured, as well as the main dimensions of the cave. The estimated volumes of the cave's interior size and the debris outside appear to be very similar.

Overview map



Cross sections

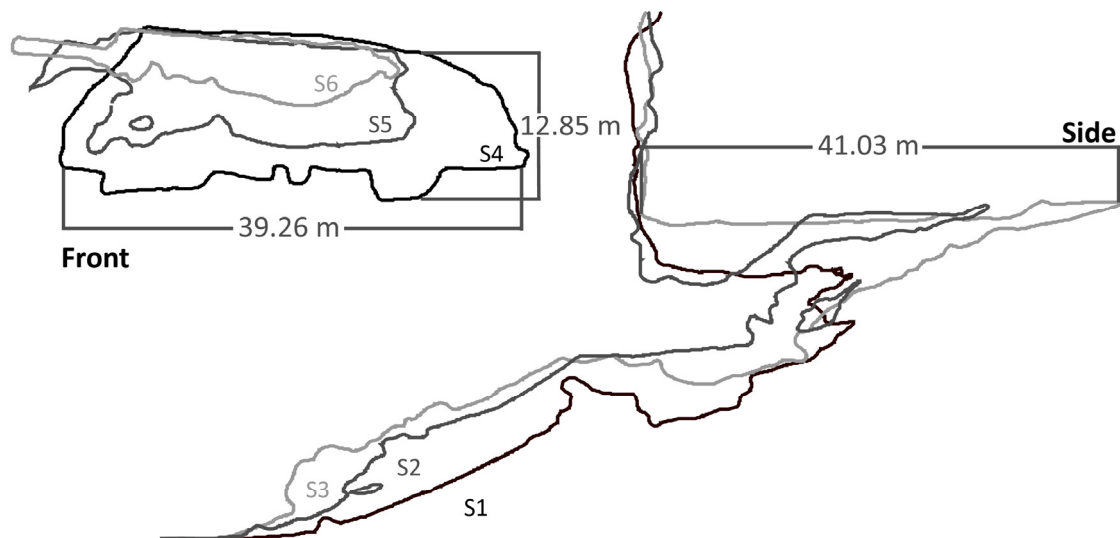


Figure 6-12: Overview map of the Sodmein cave with scan positions, contour lines, archaeological sections, and cross sectional profiles derived from the 3D model.

6.5 Discussion

Field campaigns in Jordan, Spain and Egypt showed that the TLS method is an accurate and reliable tool to support geoarchaeological surveys (REMONDINO, 2011). In particular, it was possible to survey cave sites, which is hardly conductible by other remote sensing methods (BUCHROITHNER & GAISECKER, 2009; RÜTHER et al., 2009). However, the equipment was extensive, heavy, and thus expensive in terms of transport (CHARLTON et al., 2009). In addition, customs regulations played an important role, as the equipment is of high value. However, the solid laser scanner and the other required equipment was reliably usable in the cave sites of Spain, which was also noticed by BUCHROITHNER & GAISECKER (2009) for the same type of scanner, and the dry, dusty and hot sites of Jordan and Egypt. An accurate georeference was established by using the RTK solution in combination with the reflectors on ranging poles for the remote sites. The absolute accuracy of ~1.5 m (section 3.2) can be further enhanced by PPP or other methods, as shown in section 2.1.2. The connection to local surveying networks was enabled by transformation of similar points. This connection was used for the indirect registration by tie points in the caves. Several of these small reflectors were accurately measured by total stations in the local system, which have been transformed later into the global system and were then used for the registration (RÜTHER et al., 2009). Overall, detailed topographic maps, plans and cross-sectional profiles of the archaeological sites were successfully established by the previously stated method and software (section 3.5).

Although a lot of scan positions at each site were established, a full coverage could not be achieved in this time and with the available equipment for several sites. The resolution, measurement time, and minimum distance are a drawback with regard to the complex, sometimes very narrow locations at the selected sites. In particular, the site of Ba'ja in Jordan and the chute at Sima de las Palomas de Teba in Spain, as well as the Galeria Altas and several other parts of the Ardales cave could unfortunately not be reached with this equipment. The main reasons were safety issues regarding the survey team, the size and weight of the instruments and the minimum range of 2 m around the TLS that is omitted during scanning. For such areas, smaller and faster scanners applying the CW-method (section 2.2.2) would be more feasible (RÜTHER et al., 2012). For detailed studies on small structures, the combination with photogrammetric methods was available by using the additionally recorded pictures with various functions of PointCloud Pro, thereby allowing a more detailed reconstruction for several areas. Further photogrammetric approaches (DE REU et al., 2013) or a combination with triangulation-based scanners and structured-light scanners for a more detailed reconstruction of specific objects is generally an option (REMONDINO, 2011). This was successfully shown for the Ardales cave. Accurate texture mapping is still a problem. Research algorithms show faster and more promising results than the incorporated solutions (AL-KHEDERA et al., 2009; ZALAMA et al., 2011).

However, the stated method did achieve accurate results. For example, at the site of 'Ain Ghazal, Jordan, an accurate bare-earth representation of the area could be established. The provided HRDEM indicates no gullies or creeks, which confirms that there was no stronger geomorphological process responsible for the accumulation of the YRL (ZIELHOFER et al., 2012). In addition, maps of the Neolithic sites of 'Ain Jamman and Basta, as well as certain cross-sectional profiles of important, architectural features were successfully established and are now available to serve as a basis for further investigations and excavations. In particular for the sites in Jordan, the established models could be used

for an artificial reconstruction in terms of research on this historic architecture (KINZEL, 2004; KINZEL, 2011).

The ceiling thickness of the cave of Ardales, derived by the comparison of the inner and outer TLS measurements is a valuable result for further geoarchaeological prospection. RÜTHER et al. (2009) present a similar approach, combining inside TLS and tachymetric measurements with outside tachymetric contour measurements. However, several areas of the cave were not reachable, due to the size of the instrument. A further survey with a smaller TLS may reveal additional areas with a lower ceiling thickness. For the chute of the Sima de las Palomas de Teba a similar problem occurred. In this case the incorporated, dense tachymetric measurements of the chute were used here for the 3D reconstruction of this narrow part, as depicted in Figure 6-13. The registration of the point clouds from the inside parts of the Sodmein cave was made possible by tachymetric measurements of the corresponding tie points. In addition, the established transformation allows the integration of all archeological findings, which were measured within this system into the 3D model. This 3D model by itself allows an accurate representation and documentation with regard to possible demolition, as documented for the nearby Tree Shelter area (KINDERMANN et al., 2013).

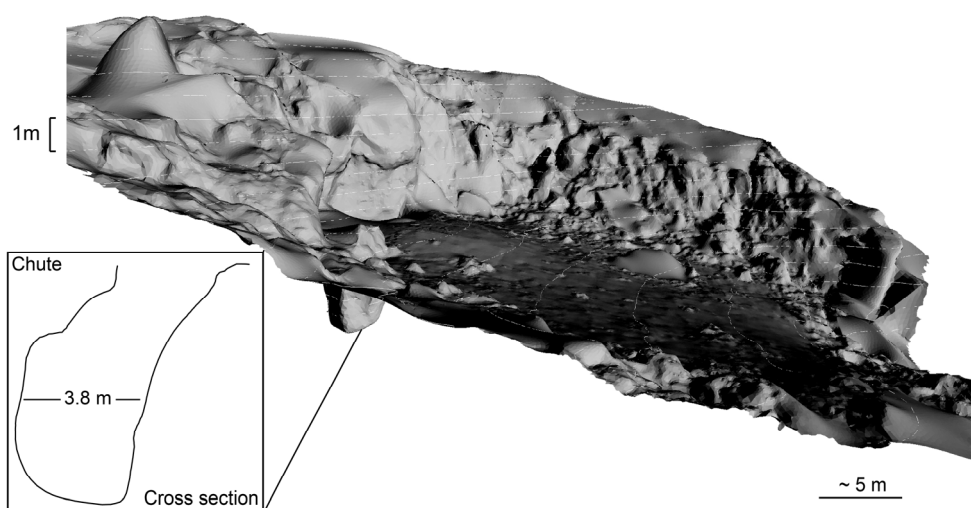


Figure 6-13: 3D model of the Sima de las Palomas de Teba. The small chute was reconstructed by the previously integrated, dense tachymetric measurements.

In general, the combination of tachymetric networks and 3D models derived by TLS measurements is a promising opportunity for further analysis of 3D distributions of archaeological findings and all other geoscientific measurements in a joint 3D-GIS, as conducted by KATSIANIS et al. (2008). This combination allows the representation of all integrated information, an enhanced, interactive visualization of the whole environment by Virtual Reality (VR) (BRUNO et al., 2010; RUA & ALVITO, 2011), and the fusion of the 3D surfaces and further measurements, such as punctual stratigraphic information or georadar transects (SIART et al., 2013). For example, the 3D representation of the distribution of geoscientific and archeological findings of the Sodmein cave might help to understand the complex geological and archeological morphology and illumination analysis for the cave of Ardales can be carried out with regard to living conditions and recorded cave art (PASTOORS & WENIGER, 2011).

Overall, TLS is an appropriate tool for surveying and documenting archaeological sites and can support associated geoarchaeological research. However, some constraints, like the minimum range and measurement time of the TLS need to be considered. In combination with other remote sensing methods, TLS can offer a crucial contribution to the documentation and analysis of such sites (REMONDINO, 2011).

7 Discussion and perspectives

In this contribution several new applications of TLS have been realised for coastal geomorphological, agronomic, and geoarchaeological research and revealed the feasibility of the method. The surveys were conducted with the combination of the time-of-flight laser scanner, type LMS-Z420i by Riegl and the Topcon HiPerPro RTK-DGPS system, described in chapter 3. For an easy georeferencing of the point datasets, the TLS positions were directly measured, as well as a further reflector on a ranging pole being used for point cloud orientation. The point cloud data was registered by these measurements and shows an error of ~1 cm after applying an enhancement of the registration by MSA processing (section 3.5.3). Post-processing of the georeferenced dataset was usually conducted by automatic and manual removal of noise and outliers. Detailed results were achieved by iconic or symbolic processing of the data, depending on the required outcome.

These results were derived by applying the general method, which is briefly discussed in section 7.1. Remarks on the accuracy of the method are also depicted (section 7.2) as well as important aspects of the selected applications are summarized in section 7.3. General future developments of the method, as well as specific advances for each case study are finally described in section 7.4.

7.1 General issues

Overall, laser scanning shows a rapid development since the 1990's as a further remote sensing method (HERITAGE & LARGE, 2009). The actively derived, accurate, dense description of objects by reflectorless measurements is of interest for several (geo-)scientific research areas. ALS is a standard method for the derivation of DSMs and DTMs and a huge amount of research is conducted in the areas of forestry applications and 3D city modeling (PETZOLD et al., 1999; SITHOLE & VOSSELMAN, 2004; HYYPPÄ et al., 2008). For all of these purposes, algorithms are being developed, which automatically structure and segment the point clouds and derive information. MLS or mobile mapping is filling the gap of ALS measurements for vertical facade detection, street inventory recording and clearance measurements (KUTTERER, 2010). Finally, TLS shows extensive applications, in particular in areas where ALS and MLS are expensive or not feasible (section 2.5). All of these applications benefit from the accurate, fast, active and dense measurements of 3D point clouds that allow surveying of new spatial and temporal ranges (HERITAGE et al., 2009). However, the detailed description of the method showed several more complex parts, such as the calculation of the shape of the beam, the final resolution and registration issues (section 2.2-2.4).

Other remote sensing methods show comparable resolutions and accuracies. All methods have particular advantages and disadvantages. For instance, photogrammetry and close-range photogrammetry, as depicted in section 2.1.3, allow retrieving comparable results in all suggested research areas, but depend on illumination and derive the information indirectly (WESTOBY et al., 2012; KOUTSOUDIS et al., 2013). Similarly, radar is also an indirect approach to achieve 3D coordinates (section 2.1.4). For single point measurements, surveying and GNSS solutions need to be considered, depending on the task and accuracy requirements (section 2.1.1-2.1.2). For example the single point measurements

of artifacts in archaeological research are fast and precisely measured by total station surveying in every environment, such as caves. Thus, it is more appropriate to transform these adequate measurements to other data, as conducted in this contribution. Choosing the most appropriate remote sensing method is depends on various factors, like object size, costs and weather. Generally, an appropriate combination of several methods might be the best solution (REMONDINO, 2011). For instance, LAMBERS et al. (2007) conclude that the combination of UAV-borne photogrammetry and TLS is accurate and efficient for the derivation of multi-level documentation products.

In this contribution, TLS was examined particularly with regard to its feasibility for various research areas. On the whole, these laser scanning devices are expensive (CHARLTON et al., 2009) and the equipment used here is fairly bulky and heavy. TLS devices still undergo rapid development towards smaller instrument sizes, better accuracy, higher measurement speed, easier operation, and enhanced functionality of instruments, as well as new algorithms and applications. The devices, for example, are now equipped with flash drives and touchscreens, which enables operation by just one person and shows a lot of further advantages for fieldwork (RÜTHER et al., 2012). For instance, GNSS receivers are additionally integrated for a first estimation of the translation parameters that allow, in combination with the ICP-algorithm, a simple registration. Accurate registration and georeferencing is still the most important task (HERITAGE et al., 2009).

CHARLTON et al. (2009) point out that operation of the devices to carry out basic fieldwork and object surveying is easily taught and comprehensible. Moreover, most objects can be covered within a few hours or days, when the logistic preparation was appropriate. Applying a CW-scanner can lead to over 150 scan positions per day, which leads to a huge amount of data. Hence, post-processing usually takes distinctly more time than the surveying stage (RÜTHER et al., 2012). However, experience is necessary to achieve consistently reliable results with regard to time and quality. Several different software packages are available for accurate results.

7.2 Accuracy of the chosen method

The selected method in this contribution is a direct georeferencing approach using a combined RTK-DGPS measurement. The absolute horizontal accuracy is within decimetres and the vertical accuracy about 1.5 m, which reflects the constraints of precise GNSS measurements of recent GPS and GLONASS signals and the carrier phase of each signal. This absolute accuracy can be enhanced to decimetre or centimetre accuracy by incorporating further corrections utilising additional correction services, transformation into local systems, or by PPP depending on availability (section 2.1.2). The latter is an independent, worldwide available option. Overall, the worldwide availability of the chosen method is the most important advantage for an application of this direct georeferencing approach. Additionally, the easily obtained and small number of measurements of the scanner position and one or several further reflectors on ranging poles are a time-saving and practical fieldwork method, particularly in remote areas. Particularly with regard to the increasing accessibility and accuracy of GNSS by upgrading and additional system availability, this approach shows promising further potential (HOFMANN-WELLENHOF, 2013).

The relative accuracy between the scan positions is dependent on the applied method. In the presented case studies, the direct georeferencing method was usually chosen, leading to an overall accuracy of up to 5 cm in every direction. Enhanced by the MSA approach, an accuracy of ~1 cm is achieved. This relative accuracy can be improved even further, when an indirect approach is chosen for the determination of the laser scanner positions. The targets can be measured by tachymetric surveying. Furthermore, the ICP-algorithm implementation is continuously enhanced and extended (GRESSIN et al., 2013).

For all three application areas such georeferencing was an important factor, as for nearly every other environmental application (CHARLTON et al., 2009). Every case study presented in this contribution considers available maps and other georeferenced data, which can be easily compared and linked to the data achieved by this approach. Accurate documentation of archaeological sites requires a traceable position that should be at least as accurate as consumer-grade GNSS measurements. Local surveying networks have been transformed, thereby enabling the use and comparison of the acquired data in every system. An exact determination of every location was particularly crucial for the results of the coastal geomorphologic research, as devastating impacts will considerably change the landscape. Thus, such areas can be traced much more easily. Furthermore, the linkage of other geoscientific results, like drillings, GPR trenches and simulations becomes a straightforward process. Comparisons to other data were also very important in the agronomic case study, which was enabled by an accurate transformation of the data from the RTK-DGPS base station into the state's surveying network.

As introduced in section 2.2.2, TLS devices applying direct time-of-flight measurements generally show a lesser precision and resolution, but have an extended range. This is particularly the case for the applied laser scanner (section 3.1), which shows range measurements between 2-1000 m and an accuracy of 1 cm. TLS devices applying the continuous wave method, show a lesser maximum range but a better resolution and precision. However, they require different referencing tasks and more processing time, due to newer devices being capable of measuring up to 1 million pts./ sec. instead of 11,000 pts. /sec. for the scanner used in this contribution.

7.3 Case studies

Several different geoscientific applications were investigated with the chosen approach of combining TLS measurements with accurate RTK-DGPS georeferencing. Geoarchaeological research was assisted with the derived models, maps and cross sections within the context of the CRC 806. Important ancient archaeological sites were documented in their current form. The outcome of complex coastal geomorphologic processes were accurately determined by the 3D reconstruction of boulder volumes, the computation of according boulder masses and the measurement of further parameters, as well as the monitoring of annual changes of the sedimentary budget at several sites in western Greece. The current condition and the distribution of crop height were detectable by the multi-temporal CMS approach and a relation to biomass of the complexly structured sugar-beet was established.

Summarizing the results from these investigations (Table 7-1), particular advantages and disadvantages can be presented here. In all described case studies, the instruments worked well and showed robustness in all circumstances, ranging from very cold and wet conditions, to dry, hot and dusty sites

(BUCHROITHNER & GAISECKER, 2009). Apart from a new laptop and a single small cable, all parts of the equipment are still in use. However, the complete equipment is heavy and comprises many parts, which is a major trade-off, but the whole system works without an external power supply. Newer devices, as depicted before, solve several of the less favourable issues.

The pictures taken by the mounted camera deliver important additional information. The accurate assignment of RGB-values to points allows a better orientation in the point clouds. Furthermore, the panoramic pictures from nearly every scan position generate a valuable dataset for controlling, orientation and presentation purposes. In addition, the higher resolution of the pictures enable the modelling of small scale objects, as the inner and outer orientation of the mounted camera is known. Promising research might enhance the density of a point cloud for object reconstruction by automatic incorporation of such dense images (HERBORT et al., 2013). The intensity values, which are captured by the laser scanner provide further reliable information for segmentation and analysis of the point clouds, in particular with regard to vegetation removal and vegetation analysis, respectively (HÖFLE, 2014).

The accurate and dense measurements of the laser scanner and the additional pictures recorded by the mounted camera allow the documentation of objects to a certain grade of resolution. The documentation enables the determination of sizes, distances and volumes of objects and therefore accurate maps, cross sections and 3D models can be generated (RÜTHER et al., 2012). This capacity and the method's accuracy are the main advantages proposed for every case study in every research area in this contribution.

In addition to the accurate description of areas and objects, the multi-temporal approach, which depends in this case mostly on the relative accuracy of the RTK-DGPS measurements, enables the possibility of change detection. This is a major application of laser scanning in geomorphological research. As shown in section 2.5, several research applications exist that deal with multi-temporal laser scanning data to obtain detailed knowledge of processes and further facilitates modelling, verification of models and perhaps corresponding outcomes in particular for hazard assessment.

Furthermore, the digital data allows re-evaluation and reassessment of the results whenever new or other post-processing workflows become available or new project demands arise. For instance, the regarded wave transport equations were expanded throughout the research period and other parameters, e.g. inclination, became necessary, which were easily derived from the datasets.

Overall, this contribution confirms the feasibility of TLS as a method for complex questions in coastal geomorphological, agronomic, and geoarchaeological research, in particular in combination with the chosen georeferencing method.

Table 7-1: Major advantages and disadvantages of the proposed method.

	Advantages	Disadvantages
General method	<ul style="list-style-type: none"> • Fast, accurate and precise measurements • Long range enables surveying of large areas • Established for rough surveying conditions • Combination with RTK-DGPS system, allows to derive accurate georeferenced data • Works without an external power supply, as it is only relying on batteries • Surveying can be easily trained 	<ul style="list-style-type: none"> • Noisy data • Precision and accuracy: medium • Minimum range of 2 m • Slow measurement rate • Heavy system comprising a lot of pieces • Costs (purchase, transport, insurance) • Post-processing time and complexity
Coastal Geomorphology	<ul style="list-style-type: none"> • Accurate modelling of boulders possible • All data can be used for achieving accurate maps • Observations of changes by multi-temporal approach possible • Panoramic pictures important for orientation and control of results • RTK-DGPS measurements allow combination with all other conducted work 	<ul style="list-style-type: none"> • Surface roughness leads to shadowing effects • Similarly, slightly different scan positions caused challenges • No penetration through water and random noise effects on the water's edge
Agronomy	<ul style="list-style-type: none"> • Determination crop height distribution possible and is suitable for biomass detection • System works in a rough agricultural environment, without additional power supply • Combinable with INS for MLS-application 	<ul style="list-style-type: none"> • Not suitable for the accurate description of single plants in this surveying approach • Size, costs and complexity too huge for a saleable sensor • Noise
Geoarchaeology	<ul style="list-style-type: none"> • Accurate description and documentation of sites • Calibrated pictures for detailed reconstruction • Creation of the contextual topography of sites • Combination with archaeological and other important data possible • Specialised measurements possible (e.g. volumes, sections, slopes) 	<ul style="list-style-type: none"> • Minimum range is problematic for complexly structured sites • Manual reconstruction is time-consuming

7.4 Perspectives

As previously stated, laser scanning is under current development, like all remote sensing methods. During the research period of this contribution, newer instruments and methods have been presented. For instance, newer ALS systems incorporate the Multiple Pulse in Air (MPiA) technology that allows the release of several laser beams before receiving the first beams (RIEGER & ULLRICH, 2012). This enables capturing a high point density from greater altitudes. Similarly, space-borne laser scanning will be enhanced by the ICESat-2 mission, which will start in 2016 (NASA, 2013).

Flash Lidar or range imaging (section 2.2.2) appears to be a promising development and will eventually become the low-cost, light-weight solution for UAVs, as proposed by (LIN et al., 2011; ZHOU et al., 2012). UAV measurements are a further method to derive CSMs (BENDIG et al., 2012; BENDIG et al., 2013). For the agronomic application, MLS or mobile mapping is another opportunity for a faster, dense and equally distributed recording of point clouds and is an enhanced surveying method for several research areas, e.g. coastal monitoring (KUKKO et al., 2012) or crop status (EHLERT et al., 2010). Current miniaturization developments allows the first very small laser scanners to be mounted on smaller (L'Avion Jaune, 2013; Velodyne Lidar, 2013) and bigger UAVs .

Additionally, newer TLS instruments from Riegl are now capable to record the full-waveform of the backscattered signal, like ALS systems. By applying methods and algorithms, arisen from ALS research, to point clouds captured by these TLS systems new analysis are possible. Overall, the intensity or amplitude value is helpful information with promising potential, but needs radiometric correction or calibration (EITEL et al., 2011; HÖFLE, 2014).

Fusing laser scanning data with multi- or hyperspectral data is a further possibility with large potential for all geosciences. Combined ALS and hyperspectral imagery generates enhanced land cover classifications (FORZIERI et al., 2013) and hyperspectral images on 3D objects resolve small-scale patterns (KURZ et al., 2011; SIMA et al., 2012; KURZ et al., 2013). The combination of both technologies, as developed and presented by CHEN et al. (2010) and HAKALA et al. (2012) will have a major impact on research.

Apart of these superior enhancements, the presented studies contribute to the specific research questions and document the current state of study sites. Thus, the data will be valuable for further research in these areas. All datasets of the geoarchaeological, coastal geomorphological and agronomic research, will be integrated into corresponding research data repositories for future usage (CURDT et al., 2012; WILLMES et al., 2013). Further investigations can consider the results of this study or enhance the results by newer methods and algorithms.

A revisit of the coastal sites in Greece, in particular after high-energy impacts, may resolve the question of wave transport capabilities. The method can be extended to further sites and a higher temporal resolution. Likewise, the data can be reused for new wave transport equations and hydrologic modelling approaches. Similarly, a revisit of the annually observed agricultural site near Selhausen might reveal the same or different crop height patterns in the field. Currently, the value of the identified patterns is reviewed for ecosystem modelling approaches and further research is conducted on probable causes for the detected patterns. Presumably, similar behaviour of the different sugar-beet cultivars will be observed in the following years. Evidence for the promising correlation between sugar-beet crop heights

and above ground biomass might also be revealed. Finally, a smaller and faster instrument, probably a CW-scanner, will fill the gaps of the survey of the Ardales cave in a future field campaign, as well as becoming a more appropriate tool for the survey of archaeological sites in general.

References

- 3M GmbH, 2013. Technische Informationen - Reflektierende Folien 3M™ Diamond Grade™ DG3 Serie 4090. http://solutions.3m.com/3MContentRetrievalAPI/BlobServlet?locale=de_DE&univid=1176437707020&fallback=true&assetType=MMM_Image&blobAttribute=ImageFile&placeId=7BC6E48B1800BAE180A88E4927002A9E&version=current, 15.08.2013.
- ABELLÁN, A., CALVET, J., VILAPLANA, J.M., BLANCHARD, J., 2010. Detection and spatial prediction of rockfalls by means of terrestrial laser scanner monitoring. *Geomorphology* 119 (3-4), 162-171.
- ABELLÁN, A., VILAPLANA, J.M., CALVET, J., GARCIA-SELLES, D., ASENSIO, E., 2011. Rockfall monitoring by Terrestrial Laser Scanning - case study of the basaltic rock face at Castellfolit de la Roca (Catalonia, Spain). *Natural Hazards and Earth System Sciences* 11, 829-841.
- ADAMS, M.D., PROBERT, P.J., 1996. The interpretation of phase and intensity data from AMCW light detection sensors for reliable ranging. *International Journal of Robotics Research* 15 (5), 441-458.
- AJAJI, A., CHECCHIN, P., TRASSOUDAIN, L., 2013. Segmentation Based Classification of 3D Urban Point Clouds: A Super-Voxel Based Approach with Evaluation. *Remote Sensing* 5 (4), 1624-1650.
- AL-KHEDERA, S., AL-SHAWABKEH, Y., HAALA, N., 2009. Developing a documentation system for desert palaces in Jordan using 3D laser scanning and digital photogrammetry. *Journal of Archaeological Science* 36 (2), 537-546.
- ALBERTZ, J., 2007. Einführung in die Fernerkundung. Wissenschaftliche Buchgesellschaft, Darmstadt, Germany.
- ALEXANDER, C., TANSEY, K., KADUK, J., HOLLAND, D., TATE, N.J., 2010. Backscatter coefficient as an attribute for the classification of full-waveform airborne laser scanning data in urban areas. *ISPRS Journal of Photogrammetry and Remote Sensing* 65 (5), 423-432.
- ALEXANDER, P.S., HOLMAN, R.A., 2004. Quantification of nearshore morphology based on video imaging. *Marine Geology* 208 (1), 101-111.
- ALSHAWABKEH, Y., DOUGLAS, K., MATARYA, M., KHRISAT, B., 2011. Combined Photogrammetric Techniques and Computer Vision: 2D-3D Recording of Gharissa, Jordan. *Journal of Architectural Conservation* 17 (2), 77-92.
- American Society for Photogrammetry and Remote Sensing (ASPRS), 2009. LAS Specification. <http://www.asprs.org/Committee-General/LASer-LAS-File-Format-Exchange-Activities.html>, 15/09/2013.
- ANDERSON, J.M., MIKHAIL, E.M., 1998. Surveying, theory and practice. WCB / McGraw Hill.
- ANDÚJAR, D., ESCOLÀ, A., ROSELL-POLO, J.R., FERNÁNDEZ-QUINTANILLA, C., DORADO, J., 2013. Potential of a terrestrial LiDAR-based system to characterise weed vegetation in maize crops. *Computers and Electronics in Agriculture* 92, 11-15.
- ANTONARAKIS, A.S., RICHARDS, K.S., BRASINGTON, J., 2008. Object-based land cover classification using airborne LiDAR. *Remote Sensing of Environment* 112 (6), 2988-2998.
- APONTE, J., MENG, X., HILL, C., MOORE, T., BURBIDGE, M., DODSON, A., 2009. Quality assessment of a network-based RTK GPS service in the UK. *Journal of Applied Geodesy* 3 (1).
- ARMAROLI, C., CIAVOLA, P., 2011. Dynamics of a nearshore bar system in the northern Adriatic: A video-based morphological classification. *Geomorphology* 126 (1-2), 201-216.
- ARMESTO-GONZÁLEZ, J., RIVEIRO-RODRÍGUEZ, B., GONZÁLEZ-AGUILERA, D., RIVAS-BREA, M.T., 2010. Terrestrial laser scanning intensity data applied to damage detection for historical buildings. *Journal of Archaeological Science* 37 (12), 3037-3047.
- ARMESTO, J., ORDÓÑEZ, C., ALEJANO, L., ARIAS, P., 2009. Terrestrial laser scanning used to determine the geometry of a granite boulder for stability analysis purposes. *Geomorphology* 106 (3-4), 271-277.
- ARP, H., GRIESBACH, J.C., 1982. Mapping in tropical forests - a new approach using the laser APR. *Photogrammetric engineering and remote sensing* 48 (1), 91-100.
- AUFGEBAUER, A., PANAGIOTOPOULOS, K., WAGNER, B., SCHÄBITZ, F., VIEHBERG, F.A., VOGEL, H., ZANCHETTA, G., Sulpizio, R., LENG, M.J., DAMASCHKE, M., 2012. Climate and environmental change in the Balkans over the last 17 ka recorded in sediments from Lake Prespa (Albania/F.Y.R. of Macedonia/Greece). *Quaternary International* 274, 122-135.
- Autodesk Inc., 2013. Autodesk Autocad Civil 3D. <http://www.autodesk.de/products/autodesk-autocad-civil-3d/overview>, 15/09/2013.
- AVIAN, M., KELLERER-PIRKLBAUER, A., BAUER, A., 2009. LiDAR for monitoring mass movements in permafrost environments at the cirque Hinteres Langtal, Austria, between 2000 and 2008. *Natural Hazards and Earth System Sciences* 9 (4), 1087-1094.

References

- AXIO-NET GmbH, 2013. AXIO-NET PED - der Präzise Echtzeitdienst mit einer Messgenauigkeit von +/- 2 cm. <http://www.axio-net.eu/produkte-loesungen/d/axio-net-ped/>, 15/09/2013.
- BAE, K.H., LICHTI, D.D., 2008. A method for automated registration of unorganised point clouds. *ISPRS Journal of Photogrammetry and Remote Sensing* 63 (1), 36-54.
- BAE, K.H., 2009. Evaluation of the Convergence Region of an Automated Registration Method for 3D Laser Scanner Point Clouds. *Sensors* 9 (1), 355-375.
- BAEWERT, H., BRYK, A., RASCHER, E., SCHMIDT, K.-H., MORCHE, D., 2013. Roughness determination of coarse grained alpine river bed surfaces using Terrestrial Laser Scanning data. *Zeitschrift für Geomorphologie, Supplementary Issues* (in print).
- BALTSAVIAS, E.P., 1999a. Airborne laser scanning: basic relations and formulas. *ISPRS Journal of Photogrammetry and Remote Sensing* 54 (2-3), 199-214.
- BALTSAVIAS, E.P., 1999b. A Comparison between Photogrammetry and Laser Scanning. *ISPRS Journal of Photogrammetry and Remote Sensing* 54 (2-3), 83-94.
- BAPTISTA, P., BASTOS, L., BERNARDES, C., CUNHA, T., DIAS, J., 2008. Monitoring Sandy Shores Morphologies by DGPS-A Practical Tool to Generate Digital Elevation Models. *Journal of Coastal Research* 24 (6), 1516-1528.
- BARBANO, M.S., PIRROTTA, C., GERARDI, F., 2010. Large boulders along the south-eastern Ionian coast of Sicily: Storm or tsunami deposits? *Marine Geology* 275 (1-4), 140-154.
- BAUER, M., 2003. Vermessung und Ortung mit Satelliten. Wichmann, Heidelberg, Germany.
- BECEK-GERBER, B., JAZIZADEH, F., KAVULYA, G., CALIS, G., 2011. Assessment of target types and layouts in 3D laser scanning for registration accuracy. *Automation in Construction* 20 (5), 649-658.
- BECKER, S., HAALA, N., 2008. Integrated LIDAR and Image Processing for the Modelling of Building Facades. *Photogrammetrie - Fernerkundung - Geoinformation* 2008 (2), 65-81.
- BELAND, M., WIDLÓWSKI, J.-L., FOURNIER, R.A., COTE, J.-F., VERSTRAETE, M.M., 2011. Estimating leaf area distribution in savanna trees from terrestrial LiDAR measurements. *Agricultural and Forest Meteorology* 151 (9), 1252-1266.
- BENDIG, J., BOLTEN, A., BARETH, G., 2012. Introducing a low-cost mini-UAV for thermal- and multispectral imaging. *International Archives of the Photogrammetry, Remote Sensing and Spatial Information Sciences, Volume XXXIX-B1, XXII ISPRS Congress (AUG-SEP 25-01, 2012)*, Melbourne, Australia. Copernicus Publications, Göttingen, Germany, 345-349.
- BENDIG, J., WILLKOMM, M., TILLY, N., GNYP, M.L., BENNERTZ, S., QIANG, C., MIAO, Y., LENZ-WIEDEMANN, V.I.S., BARETH, G., 2013. Very high resolution crop surface models (CSMs) from UAV-based stereo images for rice growth monitoring in Northeast China. *International Archives of the Photogrammetry, Remote Sensing and Spatial Information Sciences, Volume XL-1/W2, UAV-g2013, Rostock, Germany (SEP 04-06, 2013)*. Copernicus Publications, Göttingen, Germany.
- BENNER, R., BROWNE, T., BRÜCKNER, H., KELLETAT, D., SCHEFFERS, A., 2010. Boulder Transport by Waves: Progress in Physical Modelling. *Zeitschrift für Geomorphologie, Supplementary Issues* 54 (3), 127-146.
- BERALDIN, J.-A., BLAIS, F., LOHR, U., 2010. Laser Scanning Technology. In: VOSSelman, G., MAAS, H.G. (Eds.), *Airborne and terrestrial laser scanning*. Whittles Publishing, Dunbeath, UK, 1-42.
- BERTONI, D., SARTI, G., BENELLI, G., POZZEBON, A., RAGUSEO, G., 2012. Transport trajectories of "smart" pebbles on an artificial coarse-grained beach at Marina di Pisa (Italy): Implications for beach morphodynamics. *Marine Geology* 291-294, 227-235.
- BERTRAMS, M., PROTZE, J., LÖHRER, R., SCHYLE, D., RICHTER, J., HILGERS, A., KLASEN, N., SCHMIDT, C., LEHMKUHL, F., 2012. Multiple environmental change at the time of the Modern Human passage through the Middle East: First results from geoarchaeological investigations on Upper Pleistocene sediments in the Wadi Sabra (Jordan). *Quaternary International* 274, 55-72.
- BESL, P.J., MCKAY, N.D., 1992. A method for registration of 3-D shapes. *IEEE Transactions on Pattern Analysis and Machine Intelligence* 14 (2), 239-256.
- BEWLEY, R.H., CRUTCHLEY, S.P., SHELL, C.A., 2005. New light on an ancient landscape: Lidar survey in the Stonehenge World Heritage Site. *Antiquity* 79 (305), 636-647.
- BILL, R., 1999. Grundlagen der Geo-Informationssysteme. Band 1: Hardware, Software und Daten. Wichmann, Heidelberg, Germany.
- BLAIN, H.A., GLEED-OWEN, C.P., LOPEZ-GARCIA, J.M., CARRION, J.S., JENNINGS, R., FINLAYSON, G., FINLAYSON, C., GILES-PACHECO, F., 2013. Climatic conditions for the last Neanderthals: Herpetofaunal record of Gorham's Cave, Gibraltar. *J Hum Evol* 64 (4), 289-99.
- BLAIS, F., 2004. Review of 20 years of range sensor development. *Journal of Electronic Imaging* 13 (1), 231-243.
- BOEHLER, W., VICENT, M.B., MARBS, A., 2003. Investigation laser scanner accuracy. *Proc. of XIX. CIPA Symposium Antalya, Turkey (SEP-OCT 30-04, 2003)*, 9.
- BOGUSZ, J., FIGURSKI, M., NYKIEL, G., SZOLUCHA, M., WRONA, M., 2012. GNSS-based multi-sensor system for structural monitoring applications. *Journal of Applied Geodesy* 6 (1), 55-64.

References

- BRADTMÖLLER, M., PASTOORS, A., WENINGER, B., WENIGER, G.-C., 2012. The repeated replacement model – Rapid climate change and population dynamics in Late Pleistocene Europe. *Quaternary International* 247, 38-49.
- BRANDT, S.A., FISHER, E.C., HILDEBRAND, E.A., VOGELSANG, R., AMBROSE, S.H., LESUR, J., WANG, H., 2012. Early MIS 3 occupation of Mochena Borago Rockshelter, Southwest Ethiopian Highlands: Implications for Late Pleistocene archaeology, paleoenvironments and modern human dispersals. *Quaternary International* 274, 38-54.
- BRENNER, C., 2008. Interpretation terrestrischer Scandaten. *zfv - Zeitschrift für Geodäsie, Geoinformation und Landmanagement* 2008 (3), 170-180.
- BRENNER, C., 2010. Building extraction. In: VOSSELMAN, G., MAAS, H.G. (Eds.), *Airborne and terrestrial laser scanning*. Whittles Publishing, Dunbeath, UK, 169-212.
- BRIESE, C., 2010. Extraction of digital terrain models. In: VOSSELMAN, G., MAAS, H.G. (Eds.), *Airborne and terrestrial laser scanning*. Whittles Publishing, Dunbeath, UK, 135-168.
- BRILL, D., BRÜCKNER, H., JANKAEW, K., KELLETAT, D., SCHEFFERS, A., SCHEFFERS, S., 2011. Potential predecessors of the 2004 Indian Ocean Tsunami – Sedimentary evidence of extreme wave events at Ban Bang Sak, SW Thailand. *Sedimentary Geology* 239 (3-4), 146-161.
- BRILL, D., 2012. The tsunami history of southwest Thailand – Recurrence, magnitude and impact of palaeo-tsunamis inferred from onshore deposits. Dissertation, Geographisches Institut, Universität zu Köln, Germany.
- BROVKIN, V., CLAUSSEN, M., 2008. Comment on "Climate-driven ecosystem succession in the Sahara: the past 6000 years". *Science* 322 (5906), 1326.
- BRÜCKNER, H., GERLACH, R., 2007. Geoarchäologie. In: GEBHARDT, H., GLASER, R., RADKTE, U., REUBER, P. (Eds.), *Geographie – Physische Geographie und Humangeographie*. Elsevier GmbH, München, Germany, 513-516.
- BRÜCKNER, H., KELTERBAUM, D., MARUNCHAK, O., POROTOV, A., VÖTT, A., 2010. The Holocene sea level story since 7500 BP – Lessons from the Eastern Mediterranean, the Black and the Azov Seas. *Quaternary International* 225 (2), 160-179.
- BRUNO, F., BRUNO, S., DE SENSI, G., LUCHI, M.-L., MANCUSO, S., MUZZUPAPPA, M., 2010. From 3D reconstruction to virtual reality: A complete methodology for digital archaeological exhibition. *Journal of Cultural Heritage* 11 (1), 42-49.
- BRUNSDON, C., 2009. Geostatistical analysis of Lidar data. In: HERITAGE, G.L., LARGE, A.R.G. (Eds.), *Laser scanning for the Environmental Sciences*. Wiley-Blackwell, Chichester, UK., 66-81.
- BRYANT, E., 2008. *Tsunami. The underrated hazard*. Springer, Chichester, UK.
- BUBENZER, O., BOLTEN, A., 2008. The use of new elevation data (SRTM/ASTER) for the detection and morphometric quantification of Pleistocene megadunes (draa) in the eastern Sahara and the southern Namib. *Geomorphology* 102 (2), 221-231.
- BUCHROITHNER, M.F., GAISECKER, T., 2009. Terrestrial laser scanning for the visualization of complex dome in an extreme alpine cave system. *Photogrammetrie - Fernerkundung – Geoinformation* 2009 (4), 329-339.
- BUCKLEY, A., 2010. Understanding curvature rasters. <http://blogs.esri.com/esri/arcgis/2010/10/27/understanding-curvature-rasters/>, 15/09/2013.
- BUCKLEY, S.J., HOWELL, J.A., ENGE, H.D., KURZ, T.H., 2008. Terrestrial laser scanning in geology: data acquisition, processing and accuracy considerations. *Journal of the Geological Society* 165, 625-638.
- BUFTON, J.L., GARVIN, J.B., CAVANAUGH, J.F., RAMOSIZQUIERDO, L., CLEM, T.D., KRABILL, W.B., 1991. Airborne Lidar for profiling of surface-topography. *Optical Engineering* 30 (1), 72-78.
- BURTON, D., DUNLAP, D.B., WOOD, L.J., FLAIG, P.P., 2011. Lidar Intensity as a Remote Sensor of Rock Properties. *Journal of Sedimentary Research* 81 (5), 339-347.
- CAI, C., GAO, Y., 2012. Modeling and assessment of combined GPS/GLONASS precise point positioning. *GPS Solutions* 17 (2), 223-236.
- CAMPBELL, J.B., WYNNE, R.H., 2011. *Introduction to Remote Sensing*. The Guilford Press, New York, NY, USA.
- CAMPBELL, R.J., FLYNN, P.J., 2001. A Survey Of Free-Form Object Representation and Recognition Techniques. *Computer Vision and Image Understanding* 81 (2), 166-210.
- CHARLTON, M.E., COVENEY, S.J., MCCARTHY, T., 2009. Issues in laser scanning. In: HERITAGE, G.L., LARGE, A.R.G. (Eds.), *Laser scanning for the Environmental Sciences*. Wiley-Blackwell, Chichester, UK., 35-48.
- CHEN, Y., MEDIONI, G., 1992. Object modeling by registration of multiple range images. *Image and Vision Computing* 10 (3), 145-155.
- CHEN, Y., RAIKKONEN, E., KAASALAINEN, S., SUOMALAINEN, J., HAKALA, T., HYYPPA, J., CHEN, R., 2010. Two-channel Hyperspectral LiDAR with a Supercontinuum Laser Source. *Sensors* 10 (7), 7057-7066.
- CHMELINA, K., JANSKA, J., HESINA, G., TRAXLER, C., 2012. A 3-d laser scanning system and scan data processing method for the monitoring of tunnel deformations. *Journal of Applied Geodesy* 6 (3-4), 177-185.
- CHOW, J.C.K., EBELING, A., TESKEY, W.F., 2012. Point-based and plane-based deformation monitoring of indoor environments using terrestrial laser scanners. *Journal of Applied Geodesy* 6 (3-4), 193-202.

References

- CLAWGES, R., VIERLING, L., CALHOON, M., TOOMEY, M., 2007. Use of a ground-based scanning lidar for estimation of biophysical properties of western larch (*Larix occidentalis*). *International Journal of Remote Sensing* 28, 4331-4344.
- CLEMENT, C., HIRN, A., CHARVIS, P., SACHPAZI, M., MARNELIS, F., 2000. Seismic structure and the active Hellenic subduction in the Ionian islands. *Tectonophysics* 329 (1-4), 141-156.
- CORWIN, D.L., LESCH, S.M., 2005. Apparent soil electrical conductivity measurements in agriculture. *Computers and Electronics in Agriculture* 46 (1-3), 11-43.
- CÔTÉ, J.-F., FOURNIER, R.A., FRAZER, G.W., NIEMANN, K.O., 2012. A fine-scale architectural model of trees to enhance LiDAR-derived measurements of forest canopy structure. *Agricultural and Forest Meteorology* 166-167, 72-85.
- CRC806, 2013. Collaborative Research Centre 806 : Our way to Europe. Culture-Environment Interaction and Human Mobility in the Late Quaternary. <http://www.sfb806.uni-koeln.de/>, 15/09/2013.
- CRC/TR32, 2013. Transregional Collaborative Research Centre 32 : Patterns in Soil-Vegetation-Atmosphere-Systems. <http://www.tr32.uni-koeln.de/index.php>, 15/09/2013.
- CROP.SENSE.net, 2013. CROP.SENSE.net - Competence network for phenotyping science <http://www.cropsense.uni-bonn.de/>, 15/09/2013.
- CRUSLOCK, E.M., NAYLOR, L.A., FOOTE, Y.L., SWANTESSON, J.O.H., 2010. Geomorphologic equifinality: A comparison between shore platforms in Hôga Kusten and Fårö, Sweden and the Vale of Glamorgan, South Wales, UK. *Geomorphology* 114 (1-2), 78-88.
- CRUTCHLEY, S., 2006. Light detection and ranging (lidar) in the Witham Valley, Lincolnshire: an assessment of new remote sensing techniques. *Archaeological Prospection* 13 (4), 251-257.
- CURDT, C., HOFFMEISTER, D., WALDHOF, G., JEKEL, C., BARETH, G., 2012. Scientific Research Data Management for Soil-Vegetation-Atmosphere Data: The TR32DB. *Scientific Research Data* 7 (2), 68-80.
- DAWSON, A.G., 1994. Geomorphological Effects of Tsunami Run-up and Backwash. *Geomorphology* 10 (1-4), 83-94.
- DAWSON, A.G., STEWART, I., 2007. Tsunami deposits in the geological record. *Sedimentary Geology* 200 (3-4), 166-183.
- DE REU, J., PLETS, G., VERHOEVEN, G., DE SMEDT, P., BATS, M., CHERRETTÉ, B., DE MAEYER, W., DECONYNCK, J., HERREMANS, D., LALOO, P., VAN MEIRVENNE, M., DE CLERCQ, W., 2013. Towards a three-dimensional cost-effective registration of the archaeological heritage. *Journal of Archaeological Science* 40 (2), 1108-1121.
- DEL RÍO, L., GRACIA, F.J., BENAVENTE, J., 2013. Shoreline change patterns in sandy coasts. A case study in SW Spain. *Geomorphology* 196, 252-266.
- derletztekick, 2013. Java Graticule 3D (OpenAdjustment) - An OpenSource Least-Squares-Adjustment Tool. <http://sourceforge.net/projects/javagraticule3d/>, 15/09/2013.
- DEVEREUX, B.J., AMABLE, G.S., CROW, P., 2008. Visualisation of LiDAR terrain models for archaeological feature detection. *Antiquity* 82 (316), 470-479.
- DONEUS, M., BRIESE, C., FERA, M., JANNER, M., 2008. Archaeological prospection of forested areas using full-waveform airborne laser scanning. *Journal of Archaeological Science* 35 (4), 882-893.
- DONEUS, M., DONEUS, N., BRIESE, C., PREGESBAUER, M., MANDLBURGER, G., VERHOEVEN, G., 2013. Airborne laser bathymetry – detecting and recording submerged archaeological sites from the air. *Journal of Archaeological Science* 40 (4), 2136-2151.
- DORNBUSCH, U., 2010. Ground Survey Methods for Mixed Sand and Gravel Beaches in Intertidal Environments: A Comparison. *Journal of Coastal Research* 263, 451-464.
- DOS SANTOS, D.R., DAL POZ, A.P., KHOSHELHAM, K., 2013. Indirect Georeferencing of Terrestrial Laser Scanning Data using Control Lines. *The Photogrammetric Record* 28 (143), 276-292.
- DUONG, V.H., LINDENBERGH, R., PFEIFER, N., VOSSelman, G., 2008. Single and two epoch analysis of ICESat full waveform data over forested areas. *International Journal of Remote Sensing* 29 (5), 1453-1473.
- EHLERT, D., HORN, H.J., ADAMEK, R., 2008. Measuring crop biomass density by laser triangulation. *Computers and Electronics in Agriculture* 61 (2), 117-125.
- EHLERT, D., ADAMEK, R., HORN, H.-J., 2009. Laser rangefinder-based measuring of crop biomass under field conditions. *Precision Agriculture* 10 (5), 395-408.
- EHLERT, D., HEISIG, M., ADAMEK, R., 2010. Suitability of a laser rangefinder to characterize winter wheat. *Precision Agriculture* 11 (6), 650-663.
- EHLERT, D., HEISIG, M., 2013. Sources of angle-dependent errors in terrestrial laser scanner-based crop stand measurement. *Computers and Electronics in Agriculture* 93, 10-16.
- EISENBEISS, H., SAUERBIER, M., 2011. Investigation of uav systems and flight modes for photogrammetric applications. *The Photogrammetric Record* 26 (136), 400-421.
- EITEL, J.U.H., VIERLING, L.A., LONG, D.S., 2010. Simultaneous measurements of plant structure and chlorophyll content in broadleaf saplings with a terrestrial laser scanner. *Remote Sensing of Environment* 114 (10), 2229-2237.

References

- EITEL, J.U.H., VIERLING, L.A., LONG, D.S., HUNT, E.R., 2011. Early season remote sensing of wheat nitrogen status using a green scanning laser. *Agricultural and Forest Meteorology* 151 (10), 1338-1345.
- EL-MOWAFY, A., 2000. Performance analysis of the RTK technique in an urban environment. *Australian Surveyor* 45 (1), 47-54.
- EL-MOWAFY, A., 2002. Impact of augmenting GPS by GLONASS on determination of horizontal control networks. *Survey Review* (36), 351-361.
- ELSEBERG, J., BORRMANN, D., NÜCHTER, A., 2013. One billion points in the cloud – an otree for efficient processing of 3D laser scans. *ISPRS Journal of Photogrammetry and Remote Sensing* 76, 76-88.
- ENGEL, M., KNIPPING, M., BRÜCKNER, H., KIDERLEN, M., KRAFT, J.C., 2009. Reconstructing middle to late Holocene palaeogeographies of the lower Messenian plain (southwestern Peloponnese, Greece): Coastline migration, vegetation history and sea level change. *Palaeogeography, Palaeoclimatology, Palaeoecology* 284 (3-4), 257-270.
- ENGEL, M., BRÜCKNER, H., MESSENZEHL, K., FRENZEL, P., MAY, S.M., SCHEFFERS, A., SCHEFFERS, S., WENNRICH, V., KELLETAT, D., 2012. Shoreline changes and high-energy wave impacts at the leeward coast of Bonaire (Netherlands Antilles). *Earth, Planets and Space* 64 (10), 905-921.
- ENGEL, M., MAY, S.M., 2012. Bonaire's boulder fields revisited: evidence for Holocene tsunami impact on the Leeward Antilles. *Quaternary Science Reviews* 54, 126-141.
- ENTWISTLE, J.A., MCCAFFREY, K.J.W., ABRAHAMS, P.W., 2009. Three-dimensional (3D) visualisation: the application of terrestrial laser scanning in the investigation of historical Scottish farming townships. *Journal of Archaeological Science* 36 (3), 860-866.
- ESRI Inc., 2012. ESRI ArcGIS Resource Center, Desktop 10, Professional Library. http://help.arcgis.com/en/arcgisdesktop/10.0/help/index.html#/What_s_in_the_Professional_Library/00r900000092000000/, 15/09/2013.
- ESRI Inc., 2013. ArcGIS for Desktop. <http://www.esri.com/software/arcgis/arcgis-for-desktop>, 15/09/2013.
- ETIENNE, S., BUCKLEY, M., PARIS, R., NANDASENA, A.K., CLARK, K., STROTZ, L., CHAGUÉ-GOFF, C., GOFF, J., RICHMOND, B., 2011. The use of boulders for characterising past tsunamis: Lessons from the 2004 Indian Ocean and 2009 South Pacific tsunamis. *Earth-Science Reviews* 107 (1-2), 76-90.
- FATUZZO, G., MUSSUMECI, G., OLIVERI, S.M., SEQUENZIA, G., 2011. The “Guerriero di Castiglione”: reconstructing missing elements with integrated non-destructive 3D modelling techniques. *Journal of Archaeological Science* 38 (12), 3533-3540.
- Federal Space Agency (FDA), 2013. Glonass status. <http://glonass-iac.ru/en/>, 15/09/2013.
- FICHAUT, B., SUANEZ, S., 2011. Quarrying, transport and deposition of cliff-top storm deposits during extreme events: Banneg Island, Brittany. *Marine Geology* 283 (1-4), 36-55.
- FINLAYSON, C., GILES PACHECO, F., RODRIGUEZ-VIDAL, J., FA, D.A., GUTIERREZ LOPEZ, J.M., SANTIAGO PEREZ, A., FINLAYSON, G., ALLUE, E., PREYSLER, J.B., CACERES, I., CARRION, J.S., FERNANDEZ JALVO, Y., GLEED-OWEN, C.P., JIMENEZ ESPEJO, F.J., LOPEZ, P., LOPEZ SAEZ, J.A., RIQUELME CANTAL, J.A., SANCHEZ MARCO, A., GILES GUZMAN, F., BROWN, K., FUENTES, N., VALARINO, C.A., VILLALPANDO, A., STRINGER, C.B., MARTINEZ RUIZ, F., SAKAMOTO, T., 2006. Late survival of Neanderthals at the southernmost extreme of Europe. *Nature* 443 (7113), 850-853.
- FIORANI, F., RASCHER, U., JAHNKE, S., SCHURR, U., 2012. Imaging plants dynamics in heterogenic environments. *Current Opinion in Biotechnology* 23 (2), 227-35.
- FISCHER, R.E., TADIC-GALEB, B., YODER, P.R., 2008. *Optical System Design*. McGraw-Hill Professional.
- FISCHLER, M.A., BOLLES, R.C., 1981. Random Sample Consensus - a Paradigm for Model-Fitting with Applications to Image-Analysis and Automated Cartography. *Communications of the Acm* 24 (6), 381-395.
- FOERSTER, V., JUNGINGER, A., LANGKAMP, O., GEBRU, T., ASRAT, A., UMER, M., LAMB, H.F., WENNRICH, V., RETHEMEYER, J., NOWACZYK, N., TRAUTH, M.H., SCHAEBITZ, F., 2012. Climatic change recorded in the sediments of the Chew Bahir basin, southern Ethiopia, during the last 45,000 years. *Quaternary International* 274, 25-37.
- FOLEY, J.D., DAM, A.V., FEINER, S.K., HUGHES, J.F., PHILLIPS, R.L., 1999. *Grundlagen der Computergraphik: Einführung, Methoden, Prinzipien*. Addison Wesley, Bonn, Germany.
- FORLANI, G., NARDINOCCHI, C., SCAIONI, M., ZINGARETTI, P., 2006. Complete classification of raw LIDAR data and 3D reconstruction of buildings. *Pattern Analysis and Applications* 8 (4), 357-374.
- FORZIERI, G., TANTERI, L., MOSER, G., CATANI, F., 2013. Mapping natural and urban environments using airborne multi-sensor ADS40–MIVIS–LiDAR synergies. *International Journal of Applied Earth Observation and Geoinformation* 23, 313-323.
- FUKUI, Y., NAKAMURA, M., SHIRAISHI, Y., SASAKI, Y., 1963. Hydraulic study on tsunami action against dikes and their preservation (II) - influence of tsunamis on dikes. *Trans. Agr. Eng. Soc. Japan* 1963 (5), 31-36.
- GARCÍA-SAN-MIGUEL, D., LERMA, J.L., 2013. Geometric calibration of a terrestrial laser scanner with local additional parameters: An automatic strategy. *ISPRS Journal of Photogrammetry and Remote Sensing* 79, 122-136.
- GARCIA, M., RIANO, D., CHUVIECO, E., DANSON, F.M., 2010. Estimating biomass carbon stocks for a Mediterranean forest in central Spain using LiDAR height and intensity data. *Remote Sensing of Environment* 114 (4), 816-830.

References

- GARVIN, J., BUFTON, J., BLAIR, J., HARDING, D., LUTHCKE, S., FRAWLEY, J., ROWLANDS, D., 1998. Observations of the Earth's Topography from the Shuttle Laser Altimeter (SLA): Laser-pulse Echo-recovery Measurements of Terrestrial Surfaces. *Physics and Chemistry of the Earth* 23 (9-10), 1053-1068.
- GEBEL, H.-G.K., 2009. The Intricacy of Neolithic Rubble Layers. The Ba'ja, Basta, and 'Ain Rahub Evidence. *Neo-Lithics* (1), 32-48.
- GENS, R., 2010. Remote sensing of coastlines: detection, extraction and monitoring. *International Journal of Remote Sensing* 31 (7), 1819-1836.
- Geobasisdaten der Kommunen und des Landes NRW (Geobasis NRW) 2012. Digitales Gelände Modell (DGM) 1L.
- Geologisches Landesamt Nordrhein-Westfalen (GLA), 1960. Bodenkarte auf Grundlage der Bodenschätzung, Selhausen 5104, 1:5,000.
- Geologisches Landesamt Nordrhein-Westfalen (GLA), 1995. Landwirtschaftliche Standorterkundung, Oberzier/Kreis Düren, Bodenkarte L9410 5104, 1:5,000.
- Geomagic Inc., 2013. Geomagic Studio. <http://www.geomagic.com/en/products/studio/overview/>, 15/09/2013.
- GERTEN, D.M., WIESE, M.V., 1987. Microcomputer-Assisted Video Image Analysis of Lodging in Winter Wheat. *Photogrammetric engineering and remote sensing* 53 (1), 83-88.
- GIANNIOU, M., 2008. HEPOS: Designing and Implementing an RTK network. *Geoinformatics* (1), 10-13.
- GIRARDEAU-MONTAUT, D., 2013. Cloudcompare (version 2.4) (gpl software). – EDF R&D, Telecom Paris-Tech. <http://www.danielgm.net/cc/>, 15/09/2013.
- GLENNIE, C., LICHTI, D.D., 2011. Temporal Stability of the Velodyne HDL-64E S2 Scanner for High Accuracy Scanning Applications. *Remote Sensing* 3 (3), 539-553.
- GNYP, M.L., YU, K., AASEN, H., YAO, Y., HUANG, S., MIAO, Y., BARETH, G., 2013. Analysis of Crop Reflectance for Estimating Biomass in Rice Canopies at Different Phenological Stages. *Photogrammetrie - Fernerkundung - Geoinformation* 2013 (4), 351-365.
- GOFF, J., CHAGUÉ-GOFF, C., NICHOL, S., JAFFE, B., DOMINEY-HOWES, D., 2012. Progress in palaeotsunami research. *Sedimentary Geology* 243-244, 70-88.
- GOLDSTEIN, R.M., ZEBKER, H.A., WERNER, C.L., 1988. Satellite radar interferometry - two-dimensional phase unwrapping. *Radio Science* 23 (4), 713-720.
- GONZALEZ-AGUILERA, D., MUNOZ, A.L., LAHOZ, J.G., HERRERO, J.S., CORCHON, M.S., GARCIA, E., 2009. Recording and modeling Paleolithic caves through laser scanning. In: DRAGICEVIC, S., ROMAN, D., TANASESCU, V. (Eds.), *Proc. of International Conference on Advanced Geographic Information Systems and Web Services: Geows 2009*, 19-26.
- GONZALEZ-AGUILERA, D., MUÑOZ-NIETO, A., RODRIGUEZ-GONZALVEZ, P., MENÉNDEZ, M., 2011a. New tools for rock art modelling: automated sensor integration in Pindal Cave. *Journal of Archaeological Science* 38 (1), 120-128.
- GONZALEZ-AGUILERA, D., RODRIGUEZ-GONZALVEZ, P., ARMESTO, J., ARIAS, P., 2011b. Trimble GX200 and RiegI LMS-Z390i sensor self-calibration. *Optics Express* 19 (3), 2676-2693.
- GONZALEZ-AGUILERA, D., DEL POZO, S., LOPEZ, G., RODRIGUEZ-GONZALVEZ, P., 2012. From point cloud to CAD models: Laser and optics geotechnology for the design of electrical substations. *Optics & Laser Technology* 44 (5), 1384-1392.
- GONZALEZ-AGUILERA, D., MUÑOZ-NIETO, A., GÓMEZ-LAHOZ, J., HERRERO-PASCUAL, J., GUTIERREZ-ALONSO, G., 2009. 3D Digital Surveying and Modelling of Cave Geometry: Application to Paleolithic Rock Art. *Sensors* (9), 1108-1127.
- GOTO, K., KAWANA, T., IMAMURA, F., 2010a. Historical and geological evidence of boulders deposited by tsunamis, southern Ryukyu Islands, Japan. *Earth-Science Reviews* 102 (1-2), 77-99.
- GOTO, K., MIYAGI, K., KAWAMATA, H., IMAMURA, F., 2010b. Discrimination of boulders deposited by tsunamis and storm waves at Ishigaki Island, Japan. *Marine Geology* 269 (1-2), 34-45.
- GOTO, K., CHAGUÉ-GOFF, C., GOFF, J., JAFFE, B., 2012. The future of tsunami research following the 2011 Tohoku-oki event. *Sedimentary Geology* 282, 1-13.
- GRAHAM, L., 2009. Management of Lidar data. In: SHAN, J., TOTH, C.K. (Eds.), *Topographic Laser Ranging and Scanning*. Taylor & Francis Group, Boca Raton, Florida, USA, 295-306.
- GRANT, D., BETHEL, J., CRAWFORD, M., 2012. Point-to-plane registration of terrestrial laser scans. *ISPRS Journal of Photogrammetry and Remote Sensing* 72, 16-26.
- GRESSIN, A., MALLET, C., DEMANTKÉ, J., DAVID, N., 2013. Towards 3D lidar point cloud registration improvement using optimal neighborhood knowledge. *ISPRS Journal of Photogrammetry and Remote Sensing* 79, 240-251.
- GRUEN, A., AKCA, D., 2005. Least squares 3D surface and curve matching. *ISPRS Journal of Photogrammetry and Remote Sensing* 59 (3), 151-174.
- GÜLCH, E., 2005. Erfassung von 3D-Daten mit Digitaler Photogrammetrie. In: CORRS, V., ZIPF, A. (Eds.), *3D-Geoinformationssysteme - Grundlagen und Anwendungen*. Wichmann, Heidelberg, Germany, 4-25.
- HAALA, N., ROTHERMEL, M., 2012. Dense Multi-Stereo Matching for High Quality Digital Elevation Models. *Photogrammetrie – Fernerkundung - Geoinformation* 2012 (4), 331-343.

References

- HAKALA, T., SUOMALAINEN, J., KAASALAINEN, S., CHEN, Y., 2012. Full waveform hyperspectral LiDAR for terrestrial laser scanning. *Optics Express* 20 (7), 7119-7127.
- HAN, J.-Y., GUO, J., JIANG, Y.-S., 2013. Monitoring tunnel profile by means of multi-epoch dispersed 3-D LiDAR point clouds. *Tunnelling and Underground Space Technology* 33, 186-192.
- HARING, A., BRIESE, C., PFEIFER, N., 2003. Modellierung terrestrischer Laserscanner-Daten am Beispiel der Marc-Anton-Plastik. *Österreichische Zeitschrift für Vermessung und Geoinformation (VGI)* 91 (4), 281-287.
- HARLEY, M.D., TURNER, I.L., SHORT, A.D., RANASINGHE, R., 2011. Assessment and integration of conventional, RTK-GPS and image-derived beach survey methods for daily to decadal coastal monitoring. *Coastal Engineering* 58 (2), 194-205.
- HARWIN, S., LUCIEER, A., 2012. Assessing the Accuracy of Georeferenced Point Clouds Produced via Multi-View Stereopsis from Unmanned Aerial Vehicle (UAV) Imagery. *Remote Sensing* 4 (12), 1573-1599.
- HEBERT, M., KROTKOV, E., 1992. 3D measurements from imaging laser radars - how good are they? *Image and Vision Computing* 10 (3), 170-178.
- Hellenic Centre for Marine Research (HCMR), 2013. Poseidon Operational Oceanography System. <http://www.poseidon.hcmr.gr>, 15/09/2013.
- HENNING, J.G., RADTKE, P.J., 2006. Detailed stem measurements of standing trees from ground-based scanning lidar. *Forest Science* 52 (1), 67-80.
- HENRY, P., KRAININ, M., HERBST, E., REN, X., FOX, D., 2012. RGB-D mapping: Using Kinect-style depth cameras for dense 3D modeling of indoor environments. *The International Journal of Robotics Research* 31 (5), 647-663.
- HERBORT, S., GERKEN, B., SCHUGK, D., WÖHLER, C., 2013. 3D range scan enhancement using image-based methods. *ISPRS Journal of Photogrammetry and Remote Sensing* 84, 69-84.
- HERDT, G., JONES, M.W., 2008. Scanning Ancient Buildings. *Photogrammetrie - Fernerkundung - Geoinformation* (4), 245-251.
- HERITAGE, G., HETHERINGTON, D., 2007. Towards a protocol for laser scanning in fluvial geomorphology. *Earth Surface Processes and Landforms* 32 (1), 66-74.
- HERITAGE, G.L., LARGE, A.R.G., 2009. Laser scanning - Evolution of a discipline. In: HERITAGE, G.L., LARGE, A.R.G. (Eds.), *Laser scanning for the Environmental Sciences*. Wiley-Blackwell, Chichester, UK., 1-20.
- HERITAGE, G.L., LARGE, A.R.G., CHARLTON, M.E., 2009. Laser scanning: the future. In: HERITAGE, G.L., LARGE, A.R.G. (Eds.), *Laser scanning for the Environmental Sciences*. Wiley-Blackwell, Chichester, UK., 262-271.
- HERITAGE, G.L., MILAN, D.J., 2009. Terrestrial Laser Scanning of grain roughness in a gravel-bed river. *Geomorphology* 113 (1-2), 4-11.
- HEUER, A., CASPER, M.C., HERBST, M., 2011. Correlation of topography, soil properties and spatial variability of biomass – application of the self-organizing map method. *Zeitschrift für Geomorphologie, Supplementary Issues* 55 (3), 169-178.
- HICKMAN, G.D., HOGG, J.E., 1969. Application of an airborne pulsed laser for near shore bathymetric measurements. *Remote Sensing of Environment* 1 (1), 47-58.
- HIRSCHMÜLLER, H., 2008. Stereo Processing by Semiglobal Matching and Mutual Information. *Pattern Analysis and Machine Intelligence, IEEE Transactions on* 30 (2), 328-341.
- HÖBIG, N., WEBER, M.E., KEHL, M., WENIGER, G.-C., JULIÀ, R., MELLES, M., FÜLÖP, R.-H., VOGEL, H., REICHERTER, K., 2012. Lake Banyoles (northeastern Spain): A Last Glacial to Holocene multi-proxy study with regard to environmental variability and human occupation. *Quaternary International* 274, 205-218.
- HOFFMANN, G., REICHERTER, K., WIATR, T., GRÜTZNER, C., RAUSCH, T., 2013. Block and boulder accumulations along the coastline between Fins and Sur (Sultanate of Oman): tsunamigenic remains? *Natural Hazards* 65 (1), 851-873.
- HOFFMEISTER, D., BOLTEN, A., CURDT, C., WALDHOFF, G., BARETH, G., 2010. High resolution Crop Surface Models (CSM) and Crop Volume Models (CVM) on field level by terrestrial laser scanning. In: GUO, H., WANG, C. (Eds.), *Proceedings of SPIE-7840, 6th International Symposium on Digital Earth: Models, Algorithms, and Virtual Reality (SEP 09-12, 2009)*, Beijing, China, 78400E.
- HOFFMEISTER, D., TILLY, N., BENDIG, J., CURDT, C., BARETH, G., 2012. Detektion von Wachstumsvariabilität in vier Zuckerrübensorten durch multi-temporales terrestrisches Laserscanning. In: CLASEN, M., FRÖHLICH, G., BERNHARDT, H., HILDEBRAND, K., THEUVSEN, B. (Eds.), *Informationstechnologie für eine nachhaltige Landwirtschaft, 32. GIL Jahrestagung (FEB-MAR 29-1, 2012)*, Freising, Germany. Köllen Verlag, Bonn, Germany, 135-138.
- HOFFMEISTER, D., NTAGERETZIS, K., AASEN, H., CURDT, C., HADLER, H., WILLERSHÄUSER, T., BARETH, G., BRÜCKNER, H., VÖTT, A., 2013a. 3D model-based estimations of volume and mass of high-energy dislocated boulders in coastal areas of Greece by terrestrial laser scanning. *Zeitschrift für Geomorphologie, Supplementary Issues* (in print).
- HOFFMEISTER, D., TILLY, N., CURDT, C., NTAGERETZIS, K., BARETH, G., VÖTT, A., 2013b. Monitoring annual changes of the coastal sedimentary budget in western Greece by terrestrial laser scanning. *Zeitschrift für Geomorphologie, Supplementary Issues* 57 (4), 47-67.

References

- HOFFMEISTER, D., WALDHOF, G., CURDT, C., TILLY, N., BENDIG, J., BARETH, G., 2013c. Spatial variability detection of crop height in a single field by terrestrial laser scanning. In: STAFFORD, J.V. (Ed.), Precision agriculture '13, 9th European Conference on Precision Agriculture (JUL 07-11, 2013), Lleida, Spain. Wageningen Academic Publishers, Wageningen, the Netherlands, 267-274.
- HÖFLE, B., PFEIFER, N., 2007. Correction of laser scanning intensity data: Data and model-driven approaches. *ISPRS Journal of Photogrammetry and Remote Sensing* 62 (6), 415-433.
- HÖFLE, B., HOLLAUS, M., HAGENAUER, J., 2012. Urban vegetation detection using radiometrically calibrated small-footprint full-waveform airborne LiDAR data. *ISPRS Journal of Photogrammetry and Remote Sensing* 67, 134-147.
- HÖFLE, B., 2014. Radiometric Correction of Terrestrial LiDAR Point Cloud Data for Individual Maize Plant Detection. *IEEE Geoscience and Remote Sensing Letters* 11, 94-98.
- HOFMANN-WELLENHOF, B., LICHTENEGGER, H., WASLE, E., 2008. GNSS - Global Navigation Satellite Systems. Springer, Wien, Austria.
- HOFMANN-WELLENHOF, B., 2013. Kommt Galileo zu spät? *zfv - Zeitschrift für Geodäsie, Geoinformation und Landmanagement* 138 (4), 241-248.
- HÖGE, F.E., SWIFT, R.N., 1979. Wide area airborne laser bathymetry mapping. *IEEE Journal of Quantum Electronics* 15 (9), D14-D15.
- HÖGE, F.E., SWIFT, R.N., 1980. Oil film thickness measurement using airborne laser-induced water Raman backscatter. *Applied Optics* 19 (19), 3269-3281.
- HÖGE, F.E., SWIFT, R.N., FREDERICK, E.B., 1980. Water depth measurement using an airborne pulsed neon laser system. *Applied Optics* 19 (6), 871-883.
- HOHENTHAL, J., ALHO, P., HYYPPÄ, J., HYYPPÄ, H., 2011. Laser scanning applications in fluvial studies. *Progress in Physical Geography* 35 (6), 782-809.
- HOSOI, F., OMASA, K., 2006. Voxel-based 3-D modeling of individual trees for estimating leaf area density using high-resolution portable scanning lidar. *IEEE Transactions on Geoscience and Remote Sensing* 44 (12), 3610-3618.
- HOSOI, F., OMASA, K., 2009. Estimating vertical plant area density profile and growth parameters of a wheat canopy at different growth stages using three-dimensional portable lidar imaging. *ISPRS Journal of Photogrammetry and Remote Sensing* 64 (2), 151-158.
- HOSOI, F., NAKABAYASHI, K., OMASA, K., 2011. 3-D modeling of tomato canopies using a high-resolution portable scanning lidar for extracting structural information. *Sensors* 11 (2), 2166-74.
- HOSOI, F., OMASA, K., 2012. Estimation of vertical plant area density profiles in a rice canopy at different growth stages by high-resolution portable scanning lidar with a lightweight mirror. *ISPRS Journal of Photogrammetry and Remote Sensing* 74, 11-19.
- HUBER, D., 2011. The ASTM E57 File Format for 3D Imaging Data Exchange. SPIE Vol. 7864A, Proc. of Electronic Imaging - Science and Technology Conference (IS&T) (JAN 23-27, 2011), San Francisco, CA, USA.
- HUISMAN, L., TEUNISSEN, P., HU, C., 2012. GNSS precise point positioning in regional reference frames using real-time broadcast corrections. *Journal of Applied Geodesy* 6 (1), 15-23.
- HYYPPÄ, J., HYYPPÄ, H., LECKIE, D., GOUGEON, F., YU, X., MALTAMO, M., 2008. Review of methods of small-footprint airborne laser scanning for extracting forest inventory data in boreal forests. *International Journal of Remote Sensing* 29 (5), 1339-1366.
- HYYPPÄ, J., HYYPPÄ, H., XIAOWEI, Y., KAARTINEN, H., KUKKO, A., HOLOPAINEN, M., 2009. Forest inventory using small-footprint airborne Lidar. In: SHAN, J., TOH, C.K. (Eds.), *Topographic Laser Ranging and Scanning*. Taylor & Francis Group, Boca Raton, Florida, USA, 336-370.
- IMAMURA, F., GOTO, K., OHKUBO, S., 2008. A numerical model for the transport of a boulder by tsunami. *Journal of Geophysical Research-Oceans* 113 (C1), 1-12.
- Institute of Geology and Mineral Exploration (IGME), 1963. Geological map of Greece, Lefkas sheet, 1:50,000, Athens, Greece.
- Institute of Geology and Mineral Exploration (IGME), 1985. Geological map of Greece, Cephalonia Island sheet (southern part), 1:50,000, Athens, Greece.
- Institute of Geology and Mineral Exploration (IGME), 2002. Geological map of Greece, Pappadhuanika-Potamos sheet, 1:50,000, Athens, Greece.
- Institute of Geology and Mining Research (IGMR), 1980. Geological map of Greece, Pyrgos sheet, 1:50,000, Athens, Greece.
- International Electrotechnical Commission (IEC), 2007. IEC 60825-1:2007 Safety of Laser Products - Part1: Equipment classification and requirements., Geneva.
- IRISH, J.L., LILLYCROP, W.J., 1999. Scanning laser mapping of the coastal zone: the SHOALS system. *ISPRS Journal of Photogrammetry and Remote Sensing* 54 (2-3), 123-129.
- JEKELI, C., 2001. Inertial navigation systems with geodetic applications. de Gruyter, Berlin, Germany.
- JENNINGS, R., FINLAYSON, C., FA, D., FINLAYSON, G., 2011. Southern Iberia as a refuge for the last Neanderthal populations. *Journal of Biogeography* 38 (10), 1873-1885.

References

- JENSEN, J.R., 2007. Remote Sensing of the environment: an earth resource perspective. Pearson Prentice Hall, Upper Saddle River, NJ, USA.
- JENSEN, T., APAN, A., YOUNG, F., ZELLER, L., 2007. Detecting the attributes of a wheat crop using digital imagery acquired from a low-altitude platform. *Computers and Electronics in Agriculture* 59 (1-2), 66-77.
- JOECKEL, R., STOBER, M., HUEP, W., 2008. Elektronische Entfernungs- und Richtungsmessung und ihre Integration in aktuelle Positionierungsverfahren. Wichmann, Heidelberg, Germany.
- KAARTINEN, H., HYYPPÄ, J., YU, X., VASTARANTA, M., HYYPPÄ, H., KUKKO, A., HOLOPAINEN, M., HEIPKE, C., HIRSCHMUGL, M., MORSODORF, F., NÆSSET, E., PITKÄNEN, J., POPESCU, S., SOLBERG, S., WOLF, B.M., WU, J.-C., 2012. An International Comparison of Individual Tree Detection and Extraction Using Airborne Laser Scanning. *Remote Sensing* 4 (12), 950-974.
- KAASALAINEN, S., KROOKS, A., KUKKO, A., KAARTINEN, H., 2009. Radiometric Calibration of Terrestrial Laser Scanners with External Reference Targets. *Remote Sensing* 1 (3), 144-158.
- KAASALAINEN, S., JAAKKOLA, A., KAASALAINEN, M., KROOKS, A., KUKKO, A., 2011. Analysis of Incidence Angle and Distance Effects on Terrestrial Laser Scanner Intensity: Search for Correction Methods. *Remote Sensing* 3 (10), 2207-2221.
- KAFABI, Z., LUCKE, B., BÄUMLER, R., 2009. Environment and Architectural Change at the Neolithic Site of 'Ain Ghazal. *Neo-Lithics* (1), 22-32.
- KAHMEN, H., 2006. Angewandte Geodäsie: Vermessungskunde. de Gruyter, New York, USA.
- KASPAR, T.C., COLVIN, T.S., JAYNES, D.B., KARLEN, D.L., JAMES, D.E., MEEK, D.W., 2003. Relationship Between Six Years of Corn Yields and Terrain Attributes. *Precision Agriculture* 4, 87-101.
- KATSIANIS, M., TSIPIDIS, S., KOTSAKIS, K., KOUSOULAKOU, A., 2008. A 3D digital workflow for archaeological intra-site research using GIS. *Journal of Archaeological Science* 35 (3), 655-667.
- KAZHDAN, M., BOLITHO, M., HOPPE, H., 2006. Poisson Surface Reconstruction. In: POLTHIER, K., SHEFFER, A. (Eds.), *Proc. of the 4th Eurographics Symposium on Geometry Processing* (2006).
- KEHL, M., 2013. Personal communication (15/09/2013). Institute of Geography, University of Cologne.
- KEIGHTLEY, K.E., BAWDEN, G.W., 2010. 3D volumetric modeling of grapevine biomass using Tripod LiDAR. *Computers and Electronics in Agriculture* 74 (2), 305-312.
- KELLER, K., CASASSA, G., RIVERA, A., FORSBERG, R., GUNDESTRUP, N., 2007. Airborne laser altimetry survey of Glaciar Tyndall, Patagonia. *Global and Planetary Change* 59 (1-4), 101-109.
- KELLETAT, D., 2013. Physische Geographie der Meere und Küsten. Gebr. Borntraeger, Stuttgart, Germany.
- KERN, F., 2003. Automatisierte Modellierung von Bauwerksgeometrien aus 3D-Laserscanner-Daten. Dissertation, Fachbereich Bauingenieurwesen, TU Braunschweig, Germany.
- KIM, J., LEE, S., AHN, H., SEO, D., PARK, S., CHOI, C., 2013. Feasibility of employing a smartphone as the payload in a photogrammetric UAV system. *ISPRS Journal of Photogrammetry and Remote Sensing* 79, 1-18.
- KINDERMANN, K., BUBENZER, O., PEER, P.V., 2013. Geo-archaeological research on the Late Pleistocene of the Egyptian Eastern Desert: recent threats to the Sodmein Cave. *Antiquity* 87 (337).
- KINZEL, M., 2004. Some Notes on the Reconstruction of PPNB Architecture. *Neo-Lithics* (2), 18-22.
- KINZEL, M.G.F., 2011. Am Beginn des Hausbaus. Studien zur PPNB-Architektur von Shkārāt Msaied und Ba'ja in der Petra-Region, SüdJordanien. Dissertation, Technische Universität Berlin, Fakultät VI Planen | Bauen | Umwelt, Germany.
- KITCHEN, N.R., SUDDUTH, K.A., MYERS, D.B., DRUMMOND, S.T., HONG, S.Y., 2005. Delineating productivity zones on claypan soil fields using apparent soil electrical conductivity. *Computers and Electronics in Agriculture* 46 (1-3), 285-308.
- KLEMAS, V., 2011. Beach Profiling and LiDAR Bathymetry: An Overview with Case Studies. *Journal of Coastal Research* 27 (6), 1019-1028.
- KLOSE, R., PENLINGTON, J., RUCKELSHAUSEN, A., 2009. Usability study of 3D Time-of-Flight cameras for automatic plant phenotyping. *Bornimer Agrartechnische Berichte* 69.
- KNIGHT, J., BURNINGHAM, H., 2011. Boulder dynamics on an Atlantic-facing rock coastline, northwest Ireland. *Marine Geology* 283 (1-4), 56-65.
- KOETZ, B., MORSODORF, F., SUN, G., RANSON, K.J., ITTEN, K., ALLGOWER, B., 2006. Inversion of a lidar waveform model for forest biophysical parameter estimation. *Ieee Geoscience and Remote Sensing Letters* 3 (1), 49-53.
- KOGELNIK, H., LI, T., 1966. Laser Beams and Resonators. *Applied Optics* 5 (10), 1550-1567.
- KONISHI, A., EGUCHI, A., HOSOI, F., OMASA, K., 2009. 3D monitoring spatio-temporal effects of herbicide on a whole plant using combined range and chlorophyll a fluorescence imaging. *Functional Plant Biology* 36 (10-11), 874-879.
- KOPPE, W., GNYP, M.L., HUTT, C., YAO, Y.K., MIAO, Y.X., CHEN, X.P., BARETH, G., 2013. Rice monitoring with multi-temporal and dual-polarimetric TerraSAR-X data. *International Journal of Applied Earth Observation and Geoinformation* 21, 568-576.
- KORRES, W., KOYAMA, C.N., FIENER, P., SCHNEIDER, K., 2010. Analysis of surface soil moisture patterns in agricultural landscapes using Empirical Orthogonal Functions. *Hydrology and Earth System Sciences* 14 (5), 751-764.

References

- KORTEKAAS, S., DAWSON, A.G., 2007. Distinguishing tsunami and storm deposits: An example from Martinhal, SW Portugal. *Sedimentary Geology* 200 (3-4), 208-221.
- KOUTSOUDIS, A., VIDMAR, B., IOANNAKIS, G., ARNAOUTOGLU, F., PAVLIDIS, G., CHAMZAS, C., 2013. Multi-image 3D reconstruction data evaluation. *Journal of Cultural Heritage* (in press).
- KOYAMA, C.N., 2010. A novel approach to estimate soil moisture. *International Archives of the Photogrammetry, Remote Sensing and Spatial Information Science*, Volume XXXVIII, Part 8, Kyoto Japan 2010, 421-426.
- KOYAMA, C.N., KORRES, W., FIENER, P., SCHNEIDER, K., 2010. Variability of Surface Soil Moisture Observed from Multitemporal C-Band Synthetic Aperture Radar and Field Data. *Vadose Zone Journal* 9 (4), 1014.
- KRABILL, W., FREDERICK, E., MANIZADE, S., MARTIN, C., SONNTAG, J., SWIFT, R., THOMAS, R., WRIGHT, W., YUNGEL, J., 1999. Rapid Thinning of Parts of the Southern Greenland Ice Sheet. *Science* 283 (5407), 1522.
- KRABILL, W., ABDALATI, W., FREDERICK, E., MANIZADE, S., MARTIN, C., SONNTAG, J., SWIFT, R., THOMAS, R., WRIGHT, W., YUNGEL, J., 2000a. Greenland ice sheet: High-elevation balance and peripheral thinning. *Science* 289 (5478), 428-430.
- KRABILL, W.B., COLLINS, J.G., LINK, L.E., SWIFT, R.N., BUTLER, M.L., 1984. Airborne laser topographic mapping results. *Photogrammetric engineering and remote sensing* 50 (6), 685-694.
- KRABILL, W.B., WRIGHT, C.W., SWIFT, R.N., FREDERICK, E.B., MANIZADE, S.S., YUNGEL, J.K., MARTIN, C.F., SONNTAG, J.G., DUFFY, M., HULSLANDER, W., BROCK, J.C., 2000b. Airborne laser mapping of Assateague National Seashore beach. *Photogrammetric engineering and remote sensing* 66 (1), 65-71.
- KRAFT, J.C., ASCHENBRENNER, S.E., RAPP, G., JR., 1977. Paleogeographic reconstructions of coastal aegean archaeological sites. *Science* 195 (4282), 941-7.
- KRAUS, K., PFEIFER, N., 1998. Determination of terrain models in wooded areas with airborne laser scanner data. *ISPRS Journal of Photogrammetry and Remote Sensing* 53 (4), 193-203.
- KRAUS, K., 2004. *Photogrammetrie*. de Gruyter, Berlin, Germany.
- KRAVCHENKO, A.N., ROBERTSON, G.P., THELEN, K.D., HARWOOD, R.R., 2005. Management, topographical, and weather effects on spatial variability of crop grain yields. *Agronomy Journal* 97 (2), 514-523.
- KRIEGER, G., MOREIRA, A., FIEDLER, H., HAJSEK, I., WERNER, M., YOUNIS, M., ZINK, M., 2007. TanDEM-X: A satellite formation for high-resolution SAR interferometry. *IEEE Transactions on Geoscience and Remote Sensing* 45 (11), 3317-3341.
- KROEPPELIN, S., VERSCHUREN, D., LEZINE, A.M., EGGERMONT, H., COCQUYT, C., FRANCOUS, P., CAZET, J.P., FAGOT, M., RUMES, B., RUSSELL, J.M., DARIUS, F., CONLEY, D.J., SCHUSTER, M., VON SUCHODOLETZ, H., ENGSTROM, D.R., 2008. Climate-driven ecosystem succession in the Sahara: The past 6000 years. *Science* 320 (5877), 765-768.
- KROPELIN, S., VERSCHUREN, D., LEZINE, A.M., 2008. Response to Comment on "Climate-Driven Ecosystem Succession in the Sahara: The Past 6000 Years". *Science* 322 (5906).
- Kubit GmbH, 2013. PointSense Pro - 3D-Laserscandaten in AutoCAD. http://www.kubit.de/CAD/Produkte/PointSense/3D_Laser_Scanner_Basic_Pro.php, 15/09/2013.
- KUKKO, A., KAARTINEN, H., HYYPPÄ, J., CHEN, Y., 2012. Multiplatform mobile laser scanning: usability and performance. *Sensors* 12 (9), 11712-33.
- KURZ, T.H., BUCKLEY, S.J., HOWELL, J.A., SCHNEIDER, D., 2011. Integration of panoramic hyperspectral imaging with terrestrial lidar data. *Photogrammetric Record* 26 (134), 212-228.
- KURZ, T.H., BUCKLEY, S.J., HOWELL, J.A., 2013. Close-range hyperspectral imaging for geological field studies: workflow and methods. *International Journal of Remote Sensing* 34 (5), 1798-1822.
- KUTTERER, H., 2010. *Mobile Mapping*. In: VOSSELMAN, G., MAAS, H.G. (Eds.), *Airborne and terrestrial laser scanning*. Whittles Publishing, Dunbeath, UK, 293-311.
- L'Avion Jaune, 2013. Yellow Scan. <http://yellowscan.lavionjaune.com/>, 15/09/2013.
- LAFARGE, F., DESCOMBES, X., ZERUBIA, J., PIERROT-DESEILLIGNY, M., 2008. Automatic building extraction from DEMs using an object approach and application to the 3D-city modeling. *ISPRS Journal of Photogrammetry and Remote Sensing* 63 (3), 365-381.
- LAGUE, D., BRODU, N., LEROUX, J., 2013. Accurate 3D comparison of complex topography with terrestrial laser scanner: Application to the Rangitikei canyon (N-Z). *ISPRS Journal of Photogrammetry and Remote Sensing* 82, 10-26.
- LAIGLE, M., HIRN, A., SACHPAZI, M., CLEMENT, C., 2002. Seismic coupling and structure of the Hellenic subduction zone in the Ionian Islands region. *Earth and Planetary Science Letters* 200 (3-4), 243-253.
- LAMBERS, K., EISENBEISS, H., SAUERBIER, M., KUPPERSCHMIDT, D., GAISECKER, T., SOTOODEH, S., HANUSCH, T., 2007. Combining photogrammetry and laser scanning for the recording and modelling of the Late Intermediate Period site of Pinchango Alto, Palpa, Peru. *Journal of Archaeological Science* 34 (10), 1702-1712.
- LAMBROU, E., PANTAZIS, G., 2010. Evaluation of the Credibility of Reflectorless Distance Measurement. *Journal of Surveying Engineering* 136 (4), 165-171.
- Landesvermessungsamt Nordrhein-Westfalen (LVA NRW), 1953. *Deutsche Grundkarte, Selhausen 5104, 1:5,000*.

References

- LANGE, R., SEITZ, P., 2001. Solid-state time-of-flight range camera. *IEEE Journal of Quantum Electronics* 37 (3), 390-397.
- LASAPONARA, R., COLUZZI, R., GIZZI, F.T., MASINI, N., 2010. On the LiDAR contribution for the archaeological and geomorphological study of a deserted medieval village in Southern Italy. *Journal of Geophysics and Engineering* 7 (2), 155-163.
- LEBOURGEOIS, V., BEGUE, A., LABBE, S., HOULES, M., MARTINE, J.F., 2012. A light-weight multi-spectral aerial imaging system for nitrogen crop monitoring. *Precision Agriculture* 13 (5), 525-541.
- LEFSKY, M.A., COHEN, W.B., PARKER, G.G., HARDING, D.J., 2002. Lidar remote sensing for ecosystem studies. *Bioscience* 52 (1), 19-30.
- LEFSKY, M.A., HARDING, D.J., KELLER, M., COHEN, W.B., CARABAJAL, C.C., DEL BOM ESPIRITO-SANTO, F., HUNTER, M.O., DE OLIVEIRA, R., 2005. Estimates of forest canopy height and aboveground biomass using ICESat. *Geophysical Research Letters* 32 (22).
- LENZ-WIEDEMANN, V.I.S., KLAR, C.W., SCHNEIDER, K., 2010. Development and test of a crop growth model for application within a Global Change decision support system. *Ecological Modelling* 221 (2), 314-329.
- LERMA, J.L., NAVARRO, S., CABRELLES, M., VILLAVARDE, V., 2010. Terrestrial laser scanning and close range photogrammetry for 3D archaeological documentation: the Upper Palaeolithic Cave of Parpallo as a case study. *Journal of Archaeological Science* 37 (3), 499-507.
- LERMA, J.L., NAVARRO, S., CABRELLES, M., SEGUI, A.E., HERNANDEZ-LOPEZ, D., 2013. Automatic orientation and 3D modelling from markerless rock art imagery. *ISPRS Journal of Photogrammetry and Remote Sensing* 76, 64-75.
- LERONES, P.M., FERNANDEZ, J.L., GIL, A.M., GOMEZ-GARCIA-BERMEJO, J., CASANOVA, E.Z., 2010. A practical approach to making accurate 3D layouts of interesting cultural heritage sites through digital models. *Journal of Cultural Heritage* 11 (1), 1-9.
- LEWIS, A.J., HENDERSON, F.M., 1998. Radar fundamentals: the geoscience perspective. In: HENDERSON, F.M., LEWIS, A.J. (Eds.), *Principles and applications of imaging radar*. Jon Wiley & Sons, 131-181.
- LI, F., MIAO, Y., HENNIG, S.D., GNYP, M.L., CHEN, X., JIA, L., BARETH, G., 2010. Evaluating hyperspectral vegetation indices for estimating nitrogen concentration of winter wheat at different growth stages. *Precision Agriculture* 11 (4), 335-357.
- LICHTI, D.D., GORDON, S.J., TIPDECHO, T., 2005. Error models and propagation in directly georeferenced terrestrial laser scanner networks. *Journal of Surveying Engineering* 131 (4), 135-142.
- LICHTI, D.D., 2007. Error modelling, calibration and analysis of an AM-CW terrestrial laser scanner system. *ISPRS Journal of Photogrammetry and Remote Sensing* 61 (5), 307-324.
- LICHTI, D.D., 2010. A Review of Geometric Models and Self-Calibration Methods for Terrestrial Laser Scanners. *Boletim De Ciencias Geodesicas* 16 (1), 3-19.
- LICHTI, D.D., SKALLOUD, J., 2010. Registration and calibration. In: VOSSELMAN, G., MAAS, H.G. (Eds.), *Airborne and terrestrial laser scanning*. Whittles Publishing, Dunbeath, UK, 83-134.
- LICHTI, D.D., CHOW, J., LAHAMY, H., 2011. Parameter de-correlation and model-identification in hybrid-style terrestrial laser scanner self-calibration. *ISPRS Journal of Photogrammetry and Remote Sensing* 66 (3), 317-326.
- LICHTI, D.D., JAMTSHO, S., EL-HALAWANY, S.I., LAHAMY, H., CHOW, J., CHAN, T.O., EL-BADRY, M., 2012. Structural Deflection Measurement with a Range Camera. *Journal of Surveying Engineering-Asce* 138 (2), 66-76.
- LILLESAND, T.M., KIEFER, R.W., CHIPMAN, J.W., 2008. *Remote Sensing and Image Interpretation*. Wiley, New York, USA.
- LIM, M., PETLEY, D.N., ROSSER, N.J., ALLISON, R.J., LONG, A.J., PYBUS, D., 2005. Combined digital photogrammetry and time-of-flight laser scanning for monitoring cliff evolution. *Photogrammetric Record* 20 (110), 109-129.
- LIM, M., ROSSER, N.J., PETLEY, D.N., KEEN, M., 2011. Quantifying the Controls and Influence of Tide and Wave Impacts on Coastal Rock Cliff Erosion. *Journal of Coastal Research* 27 (1), 46-56.
- LIN, Y., HYYPPÄ, J., JAAKKOLA, A., 2011. Mini-UAV-Borne LIDAR for Fine-Scale Mapping. *Ieee Geoscience and Remote Sensing Letters* 8 (3), 426-430.
- LINDENBERGH, R., 2010. Engineering applications. In: VOSSELMAN, G., MAAS, H.G. (Eds.), *Airborne and terrestrial laser scanning*. Whittles Publishing, Dunbeath, UK, 237-269.
- LINDENBERGH, R.C., SOUDARISSANANE, S.S., DE VRIES, S., GORTE, B.G.H., DE SCHIPPER, M.A., 2011. Aeolian Beach Sand Transport Monitored by Terrestrial Laser Scanning. *Photogrammetric Record* 26 (136), 384-399.
- LINSTÄDTER, J., EIWANGER, J., MIKDAD, A., WENIGER, G.-C., 2012. Human occupation of Northwest Africa: A review of Middle Palaeolithic to Epipalaeolithic sites in Morocco. *Quaternary International* 274, 158-174.
- LLORENS, J., GIL, E., LLOP, J., ESCOLA, A., 2011. Ultrasonic and LIDAR sensors for electronic canopy characterization in vineyards: advances to improve pesticide application methods. *Sensors* 11 (2), 2177-94.
- LÓPEZ-GARCÍA, J.M., BLAIN, H.-A., BURJACHS, F., BALLESTEROS, A., ALLUÉ, E., CUEVAS-RUIZ, G.E., RIVALS, F., BLASCO, R., MORALES, J.I., HIDALGO, A.R., CARBONELL, E., SERRAT, D., ROSELL, J., 2012. A multidisciplinary approach to reconstructing the chronology and environment of southwestern European Neanderthals: the contribution of Teixonerres cave (Moià, Barcelona, Spain). *Quaternary Science Reviews* 43, 33-44.
- LORANG, M.S., 2011. A wave-competence approach to distinguish between boulder and megaclast deposits due to storm waves versus tsunamis. *Marine Geology* 283 (1-4), 90-97.
- LUHMANN, T., 2003. *Nahbereichsphotogrammetrie*. Wichmann, Heidelberg, Germany.

References

- LUMME, J., KARJALAINEN, M., KAARTINEN, H., KUKKO, A., HYYPPÄ, J., HYYPPÄ, H., JAAKOLA, A., KLEEMOLA, J., 2008. Terrestrial Laser Scanning of agricultural crops. In: CHEN, J., JIANG, J., MAAS, H.-G. (Eds.), ISPRS Archives – Volume XXXVII Part B5, Proc. XXI. ISPRS Conference (JUL 03-11, 2008), Beijing, China, 563-566.
- LUZI, G., NOFERINI, L., MECATTI, D., MACALUSO, G., PIERACCINI, M., ATZENI, C., SCHAFFHAUSER, A., FROMM, R., NAGLER, T., 2009. Using a Ground-Based SAR Interferometer and a Terrestrial Laser Scanner to Monitor a Snow-Covered Slope: Results From an Experimental Data Collection in Tyrol (Austria). *IEEE Transactions on Geoscience and Remote Sensing* 47 (2), 382-393.
- MAAS, H.G., 2000. Least-Squares Matching with Airborne Laserscanning Data in a TIN Structure. In: SCHENK, T., VOSSELMAN, G. (Eds.), ISPRS Archives – Volume XXXIII Part B3, Proc. XIX. ISPRS Conference (JUL 16-26, 2000), Amsterdam, the Netherlands, 548-555.
- MAAS, H.G., 2010. Forestry applications. In: VOSSELMAN, G., MAAS, H.G. (Eds.), *Airborne and terrestrial laser scanning*. Whittles Publishing, Dunbeath, UK, 213-236.
- MACLEAN, G., KRABILL, W., 1986. Gross-merchantable timber volume estimation using an airborne lidar system. *Canadian Journal of Remote Sensing* 12, 7-18.
- MAHER, L.A., BANNING, E.B., CHAZAN, M., 2011. Oasis or Mirage? Assessing the Role of Abrupt Climate Change in the Prehistory of the Southern Levant. *Cambridge Archaeological Journal* 21 (01), 1-30.
- MAIMAN, T.H., 1960. Stimulated Optical Radiation in Ruby. *Nature* 187 (4736), 493-494.
- MAKAREWICZ, C.A., 2009. Complex caprine harvesting practices and diversified hunting strategies: Integrated animal exploitation systems at Late Pre-Pottery Neolithic B 'Ain Jamman. *Anthropozoologica* 44 (1), 79-101.
- MAKROPOULOS, K., KAVIRIS, G., KOUSKOUNA, V., 2012. An updated and extended earthquake catalogue for Greece and adjacent areas since 1900. *Natural Hazards and Earth System Science* 12 (5), 1425-1430.
- MALLET, C., BRETAR, F., 2009. Full-Waveform topographic lidar: State-of-the-art. *ISPRS Journal of Photogrammetry and Remote Sensing* 64 (1), 1-16.
- MANSFELD, W., 2010. *Satellitenortung und Navigation*. Vieweg & Sohn Verlag, Wiesbaden, Germany.
- MAOUCHE, S., MORHANGE, C., MEGHRAOUI, M., 2009. Large boulder accumulation on the Algerian coast evidence tsunami events in the western Mediterranean. *Marine Geology* 262 (1-4), 96-104.
- MÄRTENSSON, S.-G., RESHETYUK, Y., JIVALL, L., 2012. Measurement uncertainty in network RTK GNSS-based positioning of a terrestrial laser scanner. *Journal of Applied Geodesy* 6 (1).
- MARTÍNEZ, J., SORIA-MEDINA, A., ARIAS, P., BUFFARA-ANTUNES, A.F., 2012. Automatic processing of Terrestrial Laser Scanning data of building façades. *Automation in Construction* 22, 298-305.
- MASSONNET, D., FEIGL, K.L., 1998. Radar interferometry and its application to changes in the earth's surface. *Reviews of Geophysics* 36 (4), 441-500.
- MASTRONUZZI, G., SANSÒ, P., 2004. Large boulder accumulations by extreme waves along the Adriatic coast of southern Apulia (Italy). *Quaternary International* 120 (1), 173-184.
- MASTRONUZZI, G., PIGNATELLI, C., SANSÒ, P., SELLERI, G., 2007. Boulder accumulations produced by the 20th of February, 1743 tsunami along the coast of southeastern Salento (Apulia region, Italy). *Marine Geology* 242 (1-3), 191-205.
- MASTRONUZZI, G., PIGNATELLI, C., 2011. Determination of Tsunami Inundation Model Using Terrestrial Laser Scanner Techniques. In: MÖRNER, N.-A. (Ed.), *The Tsunami Threat - Research and Technology*. InTech, 219-236.
- MASTRONUZZI, G., PIGNATELLI, C., 2012. The boulder berm of Punta Saguerra (Taranto, Italy): a morphological imprint of the Rossano Calabro tsunami of April 24, 1836? *Earth Planets and Space* 64 (10), 829-842.
- MAY, S.M., VÖTT, A., BRÜCKNER, H., GRAPMAYER, R., HANDL, M., WENNRICH, V., 2012a. The Lefkada barrier and beachrock system (NW Greece) - Controls on coastal evolution and the significance of extreme wave events. *Geomorphology* 139, 330-347.
- MAY, S.M., VÖTT, A., BRÜCKNER, H., SMEDILE, A., 2012b. The Gyra washover fan in the Lefkada Lagoon, NW Greece—possible evidence of the 365 AD Crete earthquake and tsunami. *Earth, Planets and Space* 64 (10), 859-874.
- MAYEWSKI, P.A., ROHLING, E.E., CURT STAGER, J., KARLÉN, W., MAASCH, K.A., DAVID MEEKER, L., MEYERSON, E.A., GASSE, F., VAN KREVELD, S., HOLMGREN, K., LEE-THORP, J., ROSQVIST, G., RACK, F., STAUBWASSER, M., SCHNEIDER, R.R., STEIG, E.J., 2004. Holocene climate variability. *Quaternary Research* 62 (3), 243-255.
- MAYR, W., 2002. Bemerkungen zum Thema "True Orthoimage". *Photogrammetrie - Fernerkundung - Geoinformation* (3), 237-244.
- MCCAFFREY, K.J.W., FEELY, M., HENNESSY, R., THOMPSON, J., 2008. Visualization of folding in marble outcrops, Connemara, western Ireland: An application of virtual outcrop technology. *Geosphere* 4 (3), 588-599.
- McKINION, J.M., WILLERS, J.L., JENKINS, J.N., 2010a. Comparing high density LIDAR and medium resolution GPS generated elevation data for predicting yield stability. *Computers and Electronics in Agriculture* 74 (2), 244-249.
- McKINION, J.M., WILLERS, J.L., JENKINS, J.N., 2010b. Spatial analyses to evaluate multi-crop yield stability for a field. *Computers and Electronics in Agriculture* 70 (1), 187-198.

References

- MEDIANERO, F.J., RAMOS, J., PALMQVIST, P., WENIGER, G., RIQUELME, J.A., ESPEJO, M., CANTALEJO, P., ARANDA, A., PÉREZ-CLAROS, J.A., FIGUEIRIDO, B., ESPIGARES, P., ROS-MONTOYA, S., TORREGROSA, V., LINSTÄDTER, J., CABELLO, L., BECERRA, S., LEDESMA, P., MEVDEV, I., CASTRO, A., ROMERO, M., MARTÍNEZ-NAVARRO, B., 2011. The karst site of Las Palomas (Guadalteba County, Málaga, Spain): A preliminary study of its Middle–Late Pleistocene archaeopaleontological record. *Quaternary International* 243 (1), 127-136.
- MEKIK, C., ARSLANOGLU, M., 2009. Investigation on Accuracies of Real Time Kinematic GPS for GIS Applications. *Remote Sensing* 1 (1), 22-35.
- MERCIER, N., VALLADAS, H., FROGET, L., 1999. Thermoluminescence Dating of a Middle Palaeolithic Occupation at Sodmein Cave, Red Sea Mountains (Egypt). *Journal of Archaeological Science* 26, 1339–1345.
- MERONI, M., ROSSINI, M., GUANTER, L., ALONSO, L., RASCHER, U., COLOMBO, R., MORENO, J., 2009. Remote sensing of solar-induced chlorophyll fluorescence: Review of methods and applications. *Remote Sensing of Environment* 113 (10), 2037-2051.
- MESAS-CARRASCOSA, F.J., CASTILLEJO-GONZÁLEZ, I.L., DE LA ORDEN, M.S., PORRAS, A.G.-F., 2012. Combining LiDAR intensity with aerial camera data to discriminate agricultural land uses. *Computers and Electronics in Agriculture* 84, 36-46.
- MILLER, B., 1965. Laser Altimeter may aid photo mapping. *Aviation Week & Space Technology*, March 29, 60-65.
- MILLER, I.M., WARRICK, J.A., 2012. Measuring sediment transport and bed disturbance with tracers on a mixed beach. *Marine Geology* 299, 1-17.
- MILLER, P., MILLS, J., EDWARDS, S., BRYAN, P., MARSH, S., MITCHELL, H., HOBBS, P., 2008. A robust surface matching technique for coastal geohazard assessment and management. *ISPRS Journal of Photogrammetry and Remote Sensing* 63 (5), 529-542.
- MOEYERSONS, J., VERMEERSCH, P.M., VAN PEER, P., 2002. Dry cave deposits and their palaeoenvironmental significance during the last 115 ka, Sodmein Cave, Red Sea Mountains, Egypt. *Quaternary Science Reviews* 21 (7), 837-851.
- MOHAMED, A., WILKINSON, B., 2009. Direct Georeferencing of Stationary LiDAR. *Remote Sensing* 1 (4), 1321-1337.
- MONTENBRUCK, O., HAUSCHILD, A., STEIGENBERGER, P., HUGENTOBLE, U., TEUNISSEN, P., NAKAMURA, S., 2012. Initial assessment of the COMPASS/BeiDou-2 regional navigation satellite system. *GPS Solutions* 17 (2), 211-222.
- MORSORF, F., MEIER, E., KOTZ, B., ITTEN, K.I., DOBBERTIN, M., ALLGOWER, B., 2004. LIDAR-based geometric reconstruction of boreal type forest stands at single tree level for forest and wildland fire management. *Remote Sensing of Environment* 92 (3), 353-362.
- MULLA, D.J., 2013. Twenty five years of remote sensing in precision agriculture: Key advances and remaining knowledge gaps. *Biosystems Engineering* 114 (4), 358-371.
- MURAKAMI, T., YUI, M., AMAHA, K., 2012. Canopy height measurement by photogrammetric analysis of aerial images: Application to buckwheat (*Fagopyrum esculentum* Moench) lodging evaluation. *Computers and Electronics in Agriculture* 89, 70-75.
- NAESSET, E., 1997. Estimating timber volume of forest stands using airborne laser scanner data. *Remote Sensing of Environment* 61 (2), 246-253.
- NAESSET, E., 2009. Effects of different sensors, flying altitudes, and pulse repetition frequencies on forest canopy metrics and biophysical stand properties derived from small-footprint airborne laser data. *Remote Sensing of Environment* 113 (1), 148-159.
- NANDASENA, N.A.K., PARIS, R., TANAKA, N., 2011. Reassessment of hydrodynamic equations: Minimum flow velocity to initiate boulder transport by high energy events (storms, tsunamis). *Marine Geology* 281 (1-4), 70-84.
- NANDASENA, N.A.K., TANAKA, N., 2013. Boulder transport by high energy: Numerical model-fitting experimental observations. *Ocean Engineering* 57, 163-179.
- National Aeronautics and Space Administration (NASA), 2013. ICESat-2. <http://icesat.gsfc.nasa.gov/icesat2/>, 15/09/2013.
- NELSON, R., KRABILL, W., MACLEAN, G., 1984. Determining Forest Canopy Characteristics Using Airborne Laser Data. *Remote Sensing of Environment* 15 (3), 201-212.
- NELSON, R., KRABILL, W., TONELLI, J., 1988. Estimating Forest Biomass and Volume Using Airborne Laser Data. *Remote Sensing of Environment* 24 (2), 247-267.
- NELSON, R., ODERWALD, R., GREGOIRE, T.G., 1997. Separating the ground and airborne laser sampling phases to estimate tropical forest basal area, volume, and biomass. *Remote Sensing of Environment* 60 (3), 311-326.
- NGUYEN, H.T., FERNANDEZ-STEGER, T.M., WIATR, T., RODRIGUES, D., AZZAM, R., 2011. Use of terrestrial laser scanning for engineering geological applications on volcanic rock slopes – an example from Madeira island (Portugal). *Natural Hazards and Earth System Science* 11 (3), 807-817.
- NICHOLLS, R.J., WONG, P.P., BURKETT, V.R., CODIGNOTTO, J.O., HAY, J.E., MCLEAN, R.F., RAGOONADEN, S., WOODROFFE, C.D., 2007. Coastal systems and low-lying areas. In: PARRY, M.L., CANZIANI, O.F., PALUTIKOF, J.P., LINDEN, P.J.V.D., HANSON, C.E. (Eds.), *Climate Change 2007: Impacts, Adaptation and Vulnerability. Contribution of Working Group II to the Fourth Assessment Report of the Intergovernmental Panel on Climate Change*, Cambridge University Press, Cambridge, UK, 315-356.

References

- NICO, G., LEVA, D., ANTONELLO, G., TARCHI, D., 2004. Ground-based SAR interferometry for terrain mapping: Theory and sensitivity analysis. *IEEE Transactions on Geoscience and Remote Sensing* 42 (6), 1344-1350.
- NIEMEIER, W., 2002. Ausgleichsrechnung. de Gruyter, Berlin, Germany.
- NILSSON, M., 1996. Estimation of tree heights and stand volume using an airborne lidar system. *Remote Sensing of Environment* 56 (1), 1-7.
- NOFERINI, L., PIERACCINI, M., MECATTI, D., MACALUSO, G., LUZI, G., ATZENI, C., 2006. Long term landslide monitoring by ground-based synthetic aperture radar interferometer. *International Journal of Remote Sensing* 27 (10), 1893-1905.
- NOORMETS, R., CROOK, K.A.W., FELTON, E.A., 2004. Sedimentology of rocky shorelines: 3. Hydrodynamics of megaclast emplacement and transport on a shore platform, Oahu, Hawaii. *Sedimentary Geology* 172 (1-2), 41-65.
- NOTT, J., 2003a. Tsunami or storm waves? - Determining the origin of a spectacular field of wave emplaced boulders using numerical storm surge and wave models and hydrodynamic transport equations. *Journal of Coastal Research* 19 (2), 348-356.
- NOTT, J., 2003b. Waves, coastal boulder deposits and the importance of the pre-transport setting. *Earth and Planetary Science Letters* 210 (1-2), 269-276.
- NOTT, J., 2004. Palaeotempestology: the study of prehistoric tropical cyclones-a review and implications for hazard assessment. *Environment International* 30 (3), 433-47.
- NTAGERETZIS, K., 2009. Geomorphologische und sedimentologische Untersuchungen zu holozänen Extremereignissen im Golf von Lakonien (Peloponnes) und auf Kephallonia (Ionische Inseln), Griechenland. Diploma thesis (unpublished), University of Cologne, Germany.
- NTAGERETZIS, K., VÖTT, A., HADLER, H., HENNING, P., WILLERSHÄUSER, T., 2012. In search of tsunami fingerprints in geo-archives of southeastern Lakonia (southern Peloponnese, Greece). In: VÖTT, A., VENZKE, J.-F. (Eds.), *Bremer Beiträge zur Geographie u. Raumplanung Heft 44: 29. Jahrestagung des Arbeitskreises „Geographie der Meere und Küsten“*, Bremen, Germany, 16-226.
- NUNEZ ANDRES, M.A., BUILL POZUELO, F., 2009. Evolution of the architectural and heritage representation. *Landscape and Urban Planning* 91 (2), 105-112.
- OBERTHÜR, T., COCK, J., ANDERSSON, M.S., NARANJO, R.N., CASTAÑEDA, D., BLAIR, M., 2007. Acquisition of low altitude digital imagery for local monitoring and management of genetic resources. *Computers and Electronics in Agriculture* 58 (1), 60-77.
- OMASA, K., HOSOI, F., KONISHI, A., 2007. 3D lidar imaging for detecting and understanding plant responses and canopy structure. *Journal of Experimental Botany* 58 (4), 881-898.
- PAPAZACHOS, B.C., DIMITRIU, P.P., 1991. Tsunamis in and near Greece and their relation to the earthquake focal mechanisms. *Natural Hazards* 4 (2), 161-170.
- PAPAZACHOS, C.B., KIRATZI, A.A., 1996. A detailed study of the active crustal deformation in the Aegean and surrounding area. *Tectonophysics* 253 (1-2), 129-153.
- PARIS, R., WASSMER, P., SARTOHADI, J., LAVIGNE, F., BARTHOMEUF, B., DESGAGES, E., GRANCHER, D., BAUMERT, P., VAUTIER, F., BRUNSTEIN, D., GOMEZ, C., 2009. Tsunamis as geomorphic crises: Lessons from the December 26, 2004 tsunami in Lhok Nga, West Banda Aceh (Sumatra, Indonesia). *Geomorphology* 104 (1-2), 59-72.
- PARIS, R., FOURNIER, J., POIZOT, E., ETIENNE, S., MORIN, J., LAVIGNE, F., WASSMER, P., 2010. Boulder and fine sediment transport and deposition by the 2004 tsunami in Lhok Nga (western Banda Aceh, Sumatra, Indonesia): A coupled offshore-onshore model. *Marine Geology* 268 (1-4), 43-54.
- PARIS, R., NAYLOR, L.A., STEPHENSON, W.J., 2011. Boulders as a signature of storms on rock coasts. *Marine Geology* 283 (1-4), 1-11.
- PASTOORS, A., WENIGER, G.-C., 2011. Cave Art in Context: Methods for the Analysis of the Spatial Organization of Cave Sites. *Journal of Archaeological Research* 19 (4), 377-400.
- PETRIE, G., TOTH, C.K., 2009a. Introduction to Laser Ranging, Profiling, and Scanning. In: SHAN, J., TOTH, C.K. (Eds.), *Topographic Laser Ranging and Scanning*. Taylor & Francis Group, Boca Raton, Florida, USA, 1-29.
- PETRIE, G., TOTH, C.K., 2009b. Airborne and spaceborne laser profilers and scanners. In: SHAN, J., TOTH, C.K. (Eds.), *Topographic Laser Ranging and Scanning*. Taylor & Francis Group, Boca Raton, Florida, USA, 29-87.
- PETRIE, G., TOTH, C.K., 2009c. Terrestrial laser scanners. In: SHAN, J., TOTH, C.K. (Eds.), *Topographic Laser Ranging and Scanning*. Taylor & Francis Group, Boca Raton, Florida, USA, 87-128.
- PETZOLD, B., REISS, P., STÖSSEL, W., 1999. Laser scanning - surveying and mapping agencies are using a new technique for the derivation of digital terrain models. *ISPRS Journal of Photogrammetry and Remote Sensing* 54 (2-3), 95-104.
- PFEIFER, N., HÖFLE, B., BRIESE, C., RUTZINGER, M., HARING, A., 2008. Analysis of the backscattered energy in terrestrial laser scanning data. In: CHEN, J., JIANG, J., MAAS, H.-G. (Eds.), *ISPRS Archives – Volume XXXVII Part B5, Proc. XXI. ISPRS Conference, Beijing, China (JUL 03-11, 2008)*.
- PFEIFER, N., MANDLBURGER, G., 2009. Lidar data filtering and DTM generation. In: SHAN, J., TOTH, C.K. (Eds.), *Topographic Laser Ranging and Scanning*. Taylor & Francis Group, Boca Raton, Florida, USA, 308-333.

References

- PFLUGMACHER, A., HEISTER, H., HEUNECKE, O., 2009. Global investigations of the satellite-based Fugro OmniSTAR HP service. *Journal of Applied Geodesy* 3 (4).
- PIETRO, L.S., O'NEAL, M.A., PULEO, J.A., 2008. Developing Terrestrial-LIDAR-Based Digital Elevation Models for Monitoring Beach Nourishment Performance. *Journal of Coastal Research* 246, 1555-1564.
- PIGNATELLI, C., SANSÒ, P., MASTRONUZZI, G., 2009. Evaluation of tsunami flooding using geomorphologic evidence. *Marine Geology* 260 (1-4), 6-18.
- PLETS, G., GHEYLE, W., VERHOEVEN, G., DE REU, J., BOURGEOIS, J., VERHEGGE, J., STICHELBAUT, B., 2012. Three-dimensional recording of archaeological remains in the Altai Mountains. *Antiquity* 86 (333), 884-897.
- PRIMICERIO, J., DI GENNARO, S.F., FIORILLO, E., GENESIO, L., LUGATO, E., MATESE, A., VACCARI, F.P., 2012. A flexible unmanned aerial vehicle for precision agriculture. *Precision Agriculture* 13 (4), 517-523.
- PU, S., VOSSELMAN, G., 2009. Knowledge based reconstruction of building models from terrestrial laser scanning data. *ISPRS Journal of Photogrammetry and Remote Sensing* 64 (6), 575-584.
- R-software, 2013. R-statistical software. <http://www.r-project.org/>, 15/09/2013.
- RABATEL, A., DELINE, P., JAILLET, S., RAVANEL, L., 2008. Rock falls in high-alpine rock walls quantified by terrestrial lidar measurements: A case study in the Mont Blanc area. *Geophysical Research Letters* 35 (10), 1-5.
- RABBANI, T., DIJKMAN, S., VAN DEN HEUVEL, F., VOSSELMAN, G., 2007. An integrated approach for modelling and global registration of point clouds. *ISPRS Journal of Photogrammetry and Remote Sensing* 61 (6), 355-370.
- RAMOS, J., ESPEJO, M.M., CANTALEJO, P., 1992. Cueva de Ardales. Su recuperación y estudio. Ayuntamiento de Ardales, Málaga.
- RAPP, G.R., HILL, C.L., 2006. *Geoarchaeology: The Earth-Science Approach to Archaeological Interpretation*. Yale University Press, New Haven, CT, USA.
- RASCHER, U., AGATI, G., ALONSO, L., CECCHI, G., CHAMPAGNE, S., COLOMBO, R., DAMM, A., DAUMARD, F., DE MIGUEL, E., FERNANDEZ, G., FRANCH, B., FRANKE, J., GERBIG, C., GIOLI, B., GOMEZ, J.A., GOULAS, Y., GUANTER, L., GUTIERREZ-DE-LA-CAMARA, O., HAMDI, K., HOSTERT, P., JIMENEZ, M., KOSVANCOVA, M., LOGNOLI, D., MERONI, M., MIGLIETTA, F., MOERSCH, A., MORENO, J., MOYA, I., NEININGER, B., OKUJENI, A., OUNIS, A., PALOMBI, L., RAIMONDI, V., SCHICKLING, A., SOBRINO, J.A., STELLMES, M., TOCI, G., TOSCANO, P., UDELHOVEN, T., VAN DER LINDEN, S., ZALDEI, A., 2009. CEFLES2: the remote sensing component to quantify photosynthetic efficiency from the leaf to the region by measuring sun-induced fluorescence in the oxygen absorption bands. *Biogeosciences* 6 (7), 1181-1198.
- REITBERGER, J., SCHNORR, C., KRZYSZEK, P., STILLA, U., 2009. 3D segmentation of single trees exploiting full waveform LIDAR data. *ISPRS Journal of Photogrammetry and Remote Sensing* 64 (6), 561-574.
- REMONDINO, F., 2011. Heritage Recording and 3D Modeling with Photogrammetry and 3D Scanning. *Remote Sensing* 3 (6), 1104-1138.
- RESHETYUK, Y., 2010. A unified approach to self-calibration of terrestrial laser scanners. *ISPRS Journal of Photogrammetry and Remote Sensing* 65 (5), 445-456.
- RESOP, J.P., HESSION, W.C., 2010. Terrestrial Laser Scanning for Monitoring Streambank Retreat: Comparison with Traditional Surveying Techniques. *Journal of Hydraulic Engineering* 136 (10), 794-798.
- RICHTER, A., FAUST, D., MAAS, H.G., 2013. Dune cliff erosion and beach width change at the northern and southern spits of Sylt detected with multi-temporal Lidar. *Catena* 103, 103-111.
- RICHTER, J., MELLES, M., SCHÄBITZ, F., 2012. Temporal and spatial corridors of Homo sapiens sapiens population dynamics during the Late Pleistocene and early Holocene. *Quaternary International* 274, 1-4.
- RIEGER, P., ULLRICH, A., 2012. Resolving range ambiguities in high-repetition rate airborne light detection and ranging applications. *Journal of Applied Remote Sensing* 6 (1), 063552.
- RiegL LMS GmbH, 2008. RiSCAN PRO Manual 1.4.3, Horn, Österreich.
- RiegL LMS GmbH, 2013a. Datasheet LMS-Z420i. http://riegl.com/uploads/tx_pxpriegl/downloads/10_DataSheet_Z420i_03-05-2010.pdf, 15/09/2013.
- RiegL LMS GmbH, 2013b. Integrated inclination sensors for RIEGL terrestrial laser scanners. http://www.riegl.com/uploads/tx_pxpriegl/downloads/10_DataSheet_Inclination-Sensors_LMS-Zxxx_08-02-2008.pdf, 15/09/2013.
- RIGNOT, E., KANAGARATNAM, P., 2006. Changes in the velocity structure of the Greenland ice sheet. *Science* 311 (5763), 986-990.
- RITCHIE, J.C., 1995. Airborne Laser Altimeter Measurements of Landscape Topography. *Remote Sensing of Environment* 53 (2), 91-96.
- RITCHIE, J.C., MENENTI, M., WELTZ, M.A., 1996. Measurements of land surface features using an airborne laser altimeter: the HAPEX-Sahel experiment. *International Journal of Remote Sensing* 17 (18), 3705-3724.
- RIVEIRO, B., MORER, P., ARIAS, P., DE ARTEAGA, I., 2011. Terrestrial laser scanning and limit analysis of masonry arch bridges. *Construction and Building Materials* 25 (4), 1726-1735.

References

- RÖBKE, B.R., SCHÜTTRUMPF, H., WÖFFLER, T., FISCHER, P., HADLER, H., NTAGERETZIS, K., WILLERSHÄUSER, T., VÖTT, A., 2013. Tsunami inundation scenarios for the Gulf of Kyparissia (western Peloponnese, Greece) derived from numerical simulations and geoscientific field evidence. *Zeitschrift für Geomorphologie, Supplementary Issues* 57 (4), 69-104.
- ROESER, P.A., FRANZ, S.O., LITT, T., ÜLGEN, U.B., HILGERS, A., WULF, S., WENNRICH, V., AKÇER ÖN, S., VIEHBERG, F.A., ÇAĞATAY, M.N., MELLES, M., 2012. Lithostratigraphic and geochronological framework for the paleoenvironmental reconstruction of the last ~36 ka cal BP from a sediment record from Lake Iznik (NW Turkey). *Quaternary International* 274, 73-87.
- ROLLEFSON, G.O., 2005. Stone Tools from 'Ayn Jammam, near Ras en-Naqb, Southern Jordan. *Neo-Lithics* (1), 17-23.
- ROLLEFSON, G.O., 2009. Slippery Slope: The Late Neolithic Rubble Layer in the Southern Levant. *Neo-Lithics* (1), 12-18.
- ROSSER, N.J., PETLEY, D.N., LIM, M., DUNNING, S.A., ALLISON, R.J., 2005. Terrestrial laser scanning for monitoring the process of hard rock coastal cliff erosion. *Quarterly Journal of Engineering Geology and Hydrogeology* 38 (4), 363-375.
- RUA, H., ALVITO, P., 2011. Living the past: 3D models, virtual reality and game engines as tools for supporting archaeology and the reconstruction of cultural heritage – the case-study of the Roman villa of Casal de Freiria. *Journal of Archaeological Science* 38 (12), 3296-3308.
- RUDOLPH, S., HEBEL, C.V., ALI, M., STADLER, A., HERBST, M., MONTZKA, C., PÄTZOLD, S., WEIHERMÜLLER, L., KRUK, J.V.D., VERECKEN, H., 2013. Validation of a paleo river system derived by ground based electromagnetic induction measurements with satellite based RapidEye images. *Proc. EGU 2013, Geophysical Research Abstracts*, Vienna, Austria.
- RÜTHER, H., CHAZAN, M., SCHROEDER, R., NEESER, R., HELD, C., WALKER, S.J., MATMON, A., HORWITZ, L.K., 2009. Laser scanning for conservation and research of African cultural heritage sites: the case study of Wonderwerk Cave, South Africa. *Journal of Archaeological Science* 36 (9), 1847-1856.
- RÜTHER, H., BHURTHA, R., HELD, C., SCHROEDER, R., WESSELS, S., 2012. Laser Scanning in Heritage Documentation: The Scanning Pipeline and its Challenges. *Photogrammetric engineering and remote sensing* 78 (4), 309-316.
- SAEYS, W., LENAERTS, B., CRAESSAERTS, G., DE BAERDEMAEKER, J., 2009. Estimation of the crop density of small grains using LiDAR sensors. *Biosystems Engineering* 102 (1), 22-30.
- SALLENGER, A.H., KRABILL, W.B., SWIFT, R.N., BROCK, J., LIST, J., HANSEN, M., HOLMAN, R.A., MANIZADE, S., SONTAG, J., MEREDITH, A., MORGAN, K., YUNKEL, J.K., FREDERICK, E.B., STOCKDON, H., 2003. Evaluation of airborne topographic lidar for quantifying beach changes. *Journal of Coastal Research* 19 (1), 125-133.
- SAMSEEMOUNG, G., SONI, P., JAYASURIYA, H.P.W., SALOKHE, V.M., 2012. Application of low altitude remote sensing (LARS) platform for monitoring crop growth and weed infestation in a soybean plantation. *Precision Agriculture* 13 (6), 611-627.
- SCHIEFFERS, A., KELLETAT, D., 2003. Sedimentologic and geomorphologic tsunami imprints worldwide - a review. *Earth-Science Reviews* 63 (1-2), 83-92.
- SCHIEFFERS, A., KELLETAT, D., VÖTT, A., MAY, S.M., SCHIEFFERS, S., 2008. Late Holocene tsunami traces on the western and southern coastlines of the Peloponnese (Greece). *Earth and Planetary Science Letters* 269 (1-2), 271-279.
- SCHERER, M., LERMA, J.L., 2009. From the Conventional Total Station to the Prospective Image Assisted Photogrammetric Scanning Total Station: Comprehensive Review. *Journal of Surveying Engineering* 135 (4), 173-178.
- SCHMIDT, I., BRADTMÖLLER, M., KEHL, M., PASTOORS, A., TAFELMAIER, Y., WENINGER, B., WENIGER, G.-C., 2012. Rapid climate change and variability of settlement patterns in Iberia during the Late Pleistocene. *Quaternary International* 274, 179-204.
- SCHNEIDER, D., 2009. Calibration of a Riegl LMS-Z420i based on a multi-station adjustment and a geometric model with additional parameters. *International Archives of Photogrammetry, Remote Sensing and Spatial Information Sciences. Proc. of ISPRS Workshop Laserscanning 2009, Paris, France (SEP 01-02, 2009)*. 177-182.
- SCHREIER, H., LOUGHEED, J., GIBSON, J.R., RUSSELL, J., 1984. Calibrating an airborne laser profiling system. *Photogrammetric engineering and remote sensing* 50 (11), 1591-1598.
- SCHREIER, H., LOUGHEED, J., TUCKER, C., LECKIE, D., 1985. Automated measurements of terrain reflection and height variations using an airborne infrared-laser system. *International Journal of Remote Sensing* 6 (1), 101-113.
- SCHÜLER, T., WALLNER, S., EISSFELLER, B., 2009. Entwicklungsstand GALILEO mit einem Ausblick auf die Kombination mit GPS für die schnelle RTK-Positionierung. *zfv - Zeitschrift für Geodäsie, Geoinformation und Landmanagement* 134 (6), 363-371.
- SCHUTZ, B.E., ZWALLY, H.J., SHUMAN, C.A., HANCOCK, D., DIMARZIO, J.P., 2005. Overview of the ICESat Mission. *Geophysical Research Letters* 32 (21).
- SCICCHITANO, G., MONACO, C., TORTORICI, L., 2007. Large boulder deposits by tsunami waves along the Ionian coast of south-eastern Sicily (Italy). *Marine Geology* 238 (1-4), 75-91.
- SCICCHITANO, G., PIGNATELLI, C., SPAMPINATO, C.R., PISCITELLI, A., MILELLA, M., MONACO, C., MASTRONUZZI, G., 2012. Terrestrial Laser Scanner techniques in the assessment of tsunami impact on the Maddalena peninsula (south-eastern Sicily, Italy). *Earth, Planets and Space* 64 (10), 889-903.
- SEEBER, G., 2003. *Satellite geodesy*. Walter de Gruyter, Berlin, Germany.
- SHAH-HOSSEINI, M., MORHANGE, C., NADERI BENI, A., MARRINER, N., LAHIJANI, H., HAMZEH, M., SABATIER, F., 2011. Coastal boulders as evidence for high-energy waves on the Iranian coast of Makran. *Marine Geology* 290 (1-4), 17-28.

References

- SHAN, J., TOTH, C.K., 2009. Topographic laser ranging and scanning. Principles and processing. CRC Press, Boca Raton, USA.
- SHEPHERD, E.C., 1965. Laser to watch height. *New Scientist* 1 (April), 33.
- SIART, C., FORBRIGER, M., NOWACZINSKI, E., HECHT, S., HOFLE, B., 2013. Fusion of multi-resolution surface (terrestrial laser scanning) and subsurface geodata (ERT, SRT) for karst landform investigation and geomorphometric quantification. *Earth Surface Processes and Landforms* 38 (10), 1135-1147.
- SIEGMAN, A.E., 1986. Lasers. University Science Books.
- SILVIA, E.P., OLSEN, M.J., 2012. To Level or Not to Level: Laser Scanner Inclination Sensor Stability and Application. *Journal of Surveying Engineering* 138 (3), 117-125.
- SIMA, A., BUCKLEY, S.J., KURZ, T.H., SCHNEIDER, D., 2012. Semi-automatic Integration of Panoramic Hyperspectral Imagery with Photorealistic Lidar Models. *Photogrammetrie – Fernerkundung - Geoinformation* (4), 443-454.
- SITHOLE, G., VOSSELMAN, G., 2004. Experimental comparison of filter algorithms for bare-Earth extraction from airborne laser scanning point clouds. *ISPRS Journal of Photogrammetry and Remote Sensing* 59 (1-2), 85-101.
- SMITH, G.F., 1984. The Early Laser Years at Hughes-Aircraft-Company. *IEEE Journal of Quantum Electronics* 20 (6), 577-584.
- SOLOVIEV, S.L., SOLOVIEVA, O.N., GO, C.N., KIM, K.S., SHCHETNIKOV, N.A., 2000. Tsunamis in the Mediterranean Sea 2000 B.C. - 2000 A.D. Kluwer, Dordrecht, the Netherlands.
- SPISKE, M., BOROCZ, Z., BAHLBURG, H., 2008. The role of porosity in discriminating between tsunami and hurricane emplacement of boulders - A case study from the Lesser Antilles, southern Caribbean. *Earth and Planetary Science Letters* 268 (3-4), 384-396.
- STAFFORD, J.V., 2000. Implementing precision agriculture in the 21st century. *Journal of Agricultural Engineering Research* 76 (3), 267-275.
- STEINLE, E., 2005. Gebäudemodellierung und -änderungserkennung aus multitemporalen Laserscanningdaten. Dissertation, Bauingenieur-, Geo- und Umweltwissenschaften, TH Karlsruhe, Germany.
- STEPHENSON, W.J., NAYLOR, L.A., 2011. Geological controls on boulder production in a rock coast setting: Insights from South Wales, UK. *Marine Geology* 283 (1-4), 12-24.
- STONE, G.W., LIU, B., PEPPER, D.A., WANG, P., 2004. The importance of extratropical and tropical cyclones on the short-term evolution of barrier islands along the northern Gulf of Mexico, USA. *Marine Geology* 210 (1-4), 63-78.
- ŠTULAR, B., KOKALJ, Ž., OŠTIR, K., NUNINGER, L., 2012. Visualization of lidar-derived relief models for detection of archaeological features. *Journal of Archaeological Science* 39 (11), 3354-3360.
- SWITZER, A.D., BURSTON, J.M., 2010. Competing mechanisms for boulder deposition on the southeast Australian coast. *Geomorphology* 114 (1-2), 42-54.
- TANG, P., AKINCI, B., HUBER, D., 2009. Quantification of edge loss of laser scanned data at spatial discontinuities. *Automation in Construction* 18 (8), 1070-1083.
- TAPPIN, D.R., EVANS, H.M., JORDAN, C.J., RICHMOND, B., SUGAWARA, D., GOTO, K., 2012. Coastal changes in the Sendai area from the impact of the 2011 Tōhoku-oki tsunami: Interpretations of time series satellite images, helicopter-borne video footage and field observations. *Sedimentary Geology* 282, 151-174.
- TERRY, J.P., LAU, A.Y.A., ETIENNE, S., 2013. Reef-Platform Coral Boulders. Evidence for High-Energy Marine Inundation Events on Tropical Coastlines. Springer, Singapore.
- TEZA, G., GALGARO, A., ZALTRON, N., GENEVOIS, R., 2007. Terrestrial laser scanner to detect landslide displacement fields: a new approach. *International Journal of Remote Sensing* 28 (16), 3425-3446.
- TEZA, G., PESCI, A., GENEVOIS, R., GALGARO, A., 2008. Characterization of landslide ground surface kinematics from terrestrial laser scanning and strain field computation. *Geomorphology* 97 (3-4), 424-437.
- TILLY, N., HOFFMEISTER, D., LIANG, H., CAO, Q., LIU, Y., LENZ-WIEDEMANN, V., MIAO, Y., BARETH, G., 2012. Evaluation of Terrestrial Laser Scanning for rice growth monitoring. *International Archives of the Photogrammetry, Remote Sensing and Spatial Information Sciences*, Volume XXXIX-B7, XXII ISPRS Congress (AUG-SEP, 25-01 2012), Melbourne, Australia. Copernicus Publications, Göttingen, Germany, 351-356.
- TORGE, W., 2002. Geodäsie. de Gruyter, Berlin, Germany.
- TOWNES, C.H., 2003. The first laser. In: GARWIN, L., LINCOLN, T. (Eds.), *A century of Nature: twenty-one discoveries that changed science and the world*. The University of Chicago Press, Chicago, IL, USA, 105-115.
- TSELENTIS, G.A., STAVRAKAKIS, G., SOKOS, E., GKIKA, F., SERPETSIDAKI, A., 2010. Tsunami hazard assessment in the Ionian Sea due to potential tsunamogenic sources - results from numerical simulations. *Natural Hazards and Earth System Sciences* 10 (5), 1021-1030.
- TUMBO, S.D., SALYANI, M., WHITNEY, J.D., WHEATON, T.A., MILLER, W.M., 2002. Investigations of Laser and Ultrasonic Ranging Sensors for Measurements of Citrus Canopy Volume. *Applied Engineering in Agriculture* 18 (3), 367-372.
- ÜLGEN, U.B., FRANZ, S.O., BILTEKIN, D., ÇAGATAY, M.N., ROESER, P.A., DONER, L., THEIN, J., 2012. Climatic and environmental evolution of Lake Iznik (NW Turkey) over the last ~4700 years. *Quaternary International* 274, 88-101.

References

- VAUGHN, C.R., BUFTON, J.L., KRABILL, W.B., RABINE, D., 1996. Georeferencing of airborne laser altimeter measurements. *International Journal of Remote Sensing* 17 (11), 2185-2200.
- VELLA, C., DEMORY, F., CANUT, V., DUSSOUILLEZ, P., FLEURY, T.J., 2011. First evidence of accumulation of mega boulders on the Mediterranean rocky coast of Provence (southern France). *Natural Hazards and Earth System Science* 11 (3), 905-914.
- VELODYNE LIDAR, 2013. HDL-32E. <http://www.velodynelidar.com/lidar/hdlproducts/hdl32e.aspx>, 15/09/2013.
- VENNEGEERTS, H., PAFFENHOLZ, J.-A., MARTIN, J., KUTTERER, H., 2009. Zwei Varianten zur direkten Georeferenzierung terrestrischer Laserscans. *Photogrammetrie – Fernerkundung - Geoinformation* (1), 33-42.
- VIEHBERG, F.A., ÜLGEN, U.B., DAMCI, E., FRANZ, S.O., ÖN, S.A., ROESER, P.A., ÇAĞATAY, M.N., LITT, T., MELLES, M., 2012. Seasonal hydrochemical changes and spatial sedimentological variations in Lake Iznik (NW Turkey). *Quaternary International* 274, 102-111.
- VOSSelman, G., KLEIN, R., 2010. Visualisation and structuring of point clouds. In: VOSSelman, G., MAAS, H.G. (Eds.), *Airborne and terrestrial laser scanning*. Whittles Publishing, Dunbeath, UK, 45-82.
- VOSSelman, G., MAAS, H.-G., 2010. *Airborne and terrestrial laser scanning*, 1st ed. Whittles Publishing, Dunbeath, UK.
- VÖTT, A., BRÜCKNER, H., MAY, M., LANG, F., HERD, R., BROCKMÜLLER, S., 2008. Strong tsunami impact on the Bay of Aghios Nikolaos and its environs (NW Greece) during Classical–Hellenistic times. *Quaternary International* 181 (4), 105-122.
- VÖTT, A., BRÜCKNER, H., BROCKMÜLLER, S., HANDL, M., MAY, S.M., GAKI-PAPANASTASSIOU, K., HERD, R., LANG, F., MAROUKIAN, H., NELLE, O., PAPANASTASSIOU, D., 2009. Traces of Holocene tsunamis across the Sound of Lefkada, NW Greece. *Global and Planetary Change* 66 (1-2), 112-128.
- VÖTT, A., BARETH, G., BRÜCKNER, H., CURDT, C., FOUNTOULIS, I., GRAPMAYER, R., HADLER, H., HOFFMEISTER, D., KLASSEN, N., LANG, F., MASBERG, P., MAY, S.M., NTAGERETZIS, K., SAKELLARIOU, D., WILLERSHÄUSER, T., 2010. Beachrock-type calcarenitic tsunamites along the shores of the eastern Ionian Sea (western Greece) – case studies from Akarnania the Ionian Islands and the western Peloponnese. *Zeitschrift für Geomorphologie, Supplementary Issues* 54 (3), 1-50.
- VÖTT, A., BARETH, G., BRÜCKNER, H., LANG, F., SAKELLARIOU, D., HADLER, H., NTAGERETZIS, K., WILLERSHÄUSER, T., 2011. Olympia's Harbour Site Pheia (Elis, Western Peloponnese, Greece) Destroyed by Tsunami Impact. *Die Erde* 142 (3), 259-288.
- WAGNER, B., AUFGEBAUER, A., VOGEL, H., ZANCHETTA, G., SULPIZIO, R., DAMASCHKE, M., 2012. Late Pleistocene and Holocene contourite drift in Lake Prespa (Albania/F.Y.R. of Macedonia/Greece). *Quaternary International* 274, 112-121.
- WAGNER, W., ULLRICH, A., DUCIC, V., MELZER, T., STUDNICKA, N., 2006. Gaussian decomposition and calibration of a novel small-footprint full-waveform digitising airborne laser scanner. *ISPRS Journal of Photogrammetry and Remote Sensing* 60 (2), 100-112.
- WALDHOFF, G., CURDT, C., HOFFMEISTER, D., BARETH, G., 2012. Analysis of multitemporal and multisensor remote sensing data for crop rotation mapping. *ISPRS Annals of the Photogrammetry, Remote Sensing and Spatial Information Sciences*, Volume I-7, XXII ISPRS Congress (AUG-SEP 25-01, 2012), Melbourne, Australia. Copernicus Publications, Göttingen, Germany, 177-182.
- WALKLATE, P.J., CROSS, J.V., RICHARDSON, G.M., MURRAY, R.A., BAKER, D.E., 2002. IT—Information Technology and the Human Interface: Comparison of Different Spray Volume Deposition Models Using LIDAR Measurements of Apple Orchards. *Biosystems Engineering* 82 (3), 253-267.
- WANG, X., CHENG, X., GONG, P., HUANG, H., LI, Z., LI, X., 2011. Earth science applications of ICESat/GLAS: a review. *International Journal of Remote Sensing* 32 (23), 8837-8864.
- WEHR, A., LOHR, U., 1999. Airborne laser scanning – an introduction and overview. *ISPRS Journal of Photogrammetry and Remote Sensing* 54 (2-3), 68-82.
- WEHR, A., 2009. Lidar systems and calibration. In: SHAN, J., TOTH, C.K. (Eds.), *Topographic Laser Ranging and Scanning*. Taylor & Francis Group, Boca Raton, Florida, USA, 129-172.
- WEI, G., SHALEI, S., BO, Z., SHUO, S., FAQUAN, L., XUEWU, C., 2012. Multi-wavelength canopy LiDAR for remote sensing of vegetation: Design and system performance. *ISPRS Journal of Photogrammetry and Remote Sensing* 69, 1-9.
- WEIDNER, U., FÖRSTNER, W., 1995. Towards automatic building extraction from high-resolution digital elevation models. *ISPRS Journal of Photogrammetry and Remote Sensing* 50 (4), 38-49.
- WENINGER, B., ALRAM-STERN, E., BAUER, E., CLARE, L., DANZEGLOCKE, U., JÖRIS, O., KUBATZKI, C., ROLLEFSON, G., TODOROVA, H., VAN ANDEL, T., 2006. Climate forcing due to the 8200 cal yr BP event observed at Early Neolithic sites in the eastern Mediterranean. *Quaternary Research* 66 (3), 401-420.
- WENINGER, B., 2009. Yarmoukian Rubble Slides. Evidence for Early Holocene Rapid Climate Change in Southern Jordan. *Neolithics* (1), 5-11.
- WERBROUCK, I., ANTROP, M., VAN EETVELDE, V., STAL, C., DE MAEYER, P., BATS, M., BOURGEOIS, J., COURT-PICON, M., CROMBÉ, P., DE REU, J., DE SMEDT, P., FINKE, P.A., VAN MEIRVENNE, M., VERNIERS, J., ZWERTVAEGHER, A., 2011. Digital Elevation Model generation for historical landscape analysis based on LiDAR data, a case study in Flanders (Belgium). *Expert Systems with Applications* 38 (7), 8178-8185.

References

- WESTOBY, M.J., BRASINGTON, J., GLASSER, N.F., HAMBREY, M.J., REYNOLDS, J.M., 2012. 'Structure-from-Motion' photogrammetry: A low-cost, effective tool for geoscience applications. *Geomorphology* 179, 300-314.
- WIATR, T., REICHERTER, K., PAPANIKOLAOU, I., FERNÁNDEZ-STEGER, T., MASON, J., 2013. Slip vector analysis with high resolution t-LiDAR scanning. *Tectonophysics* 608, 947-957.
- WIDLOK, T., AUFGEBAUER, A., BRADTMÖLLER, M., DIKAU, R., HOFFMANN, T., KRETSCHMER, I., PANAGIOTOPOULOS, K., PASTOORS, A., PETERS, R., SCHÄBITZ, F., SCHLUMMER, M., SOLICH, M., WAGNER, B., WENIGER, G.-C., ZIMMERMANN, A., 2012. Towards a theoretical framework for analyzing integrated socio-environmental systems. *Quaternary International* 274, 259-272.
- WILLERS, J.L., WU, J., O'HARA, C., JENKINS, J.N., 2012. A categorical, improper probability method for combining NDVI and LiDAR elevation information for potential cotton precision agricultural applications. *Computers and Electronics in Agriculture* 82, 15-22.
- WILLERSHÄUSER, T., VÖTT, A., BRÜCKNER, H., BARETH, G., NELLE, O., NADEAU, M.-J., HADLER, H., NTAGERETZIS, K., 2013. Holocene tsunami landfalls along the shores of the inner Gulf of Argostoli (Cefalonia Island, Greece). *Zeitschrift für Geomorphologie, Supplementary Issues* 57 (4), 105-138.
- WILLMES, C., KÜRNER, D., BARETH, G., 2013. Building Research Data Management Infrastructure using Open Source Software. *Transactions in GIS* (in print).
- WITTE, B., SCHMIDT, H., 2000. *Vermessungskunde und Grundlagen der Statistik für das Bauwesen*. K. Wittwer, Stuttgart, Germany.
- WITTE, T.H., WILSON, A.M., 2005. Accuracy of WAAS-enabled GPS for the determination of position and speed over ground. *Journal of Biomechanics* 38 (8), 1717-1722.
- WOODROFFE, C.D., 2002. *Coasts: Form, Process and Evolution*. Cambridge University Press, Cambridge, UK.
- WUJANZ, D., 2009. Intensity calibration method for 3D laser scanners. *New Zealand Surveyor* 299, 11-13.
- YAN, W.Y., SHAKER, A., HABIB, A., KERSTING, A.P., 2012. Improving classification accuracy of airborne LiDAR intensity data by geometric calibration and radiometric correction. *ISPRS Journal of Photogrammetry and Remote Sensing* 67, 35-44.
- YANG, B., DONG, Z., 2013. A shape-based segmentation method for mobile laser scanning point clouds. *ISPRS Journal of Photogrammetry and Remote Sensing* 81, 19-30.
- YU, K., LI, F., GNYP, M.L., MIAO, Y., BARETH, G., CHEN, X., 2013. Remotely detecting canopy nitrogen concentration and uptake of paddy rice in the Northeast China Plain. *ISPRS Journal of Photogrammetry and Remote Sensing* 78, 102-115.
- ZALAMA, E., GOMEZ-GARCIA-BERMEJO, J., LLAMAS, J., MEDINA, R., 2011. An Effective Texture Mapping Approach for 3D Models Obtained from Laser Scanner Data to Building Documentation. *Computer-Aided Civil and Infrastructure Engineering* 26 (5), 381-392.
- ZHANG, L., GRIFF, T.E., 2012. A LIDAR-based crop height measurement system for *Miscanthus giganteus*. *Computers and Electronics in Agriculture* 85, 70-76.
- ZHANG, N.Q., WANG, M.H., WANG, N., 2002. Precision agriculture - a worldwide overview. *Computers and Electronics in Agriculture* 36 (2-3), 113-132.
- ZHOU, G., YANG, J., LI, X., YANG, X., 2012. Advance of Flash Lidar development onboard UAV. *International Archives of the Photogrammetry, Remote Sensing and Spatial Information Sciences, Volume XXXIX-B3, XXII ISPRS Congress (AUG-SEP, 25-01 2012)*, Melbourne, Australia. Copernicus Publications, Göttingen, Germany, 193-198.
- ZHU, L., HYYPPÄ, J., KUKKO, A., KAARTINEN, H., CHEN, R., 2011. Photorealistic Building Reconstruction from Mobile Laser Scanning Data. *Remote Sensing* 3 (12), 1406-1426.
- ZIELHOFER, C., CLARE, L., ROLLEFSON, G., WACHTER, S., HOFFMEISTER, D., BARETH, G., ROETTIG, C., BULLMANN, H., SCHNEIDER, B., BERKE, H., WENIGER, B., 2012. The decline of the early Neolithic population center of 'Ain Ghazal and corresponding earth-surface processes, Jordan Rift Valley. *Quaternary Research* 78 (3), 427-441.
- ZIMMERMANN, A., 2012. Cultural cycles in Central Europe during the Holocene. *Quaternary International* 274, 251-258.
- ZUMBERGE, J.F., HEFLIN, M.B., JEFFERSON, D.C., WATKINS, M.M., WEBB, F.H., 1997. Precise point positioning for the efficient and robust analysis of GPS data from large networks. *Journal of Geophysical Research: Solid Earth* 102 (B3), 5005-5017.
- ZWALLY, H.J., 2002. ICESat's laser measurements of polar ice, atmosphere, ocean, and land. *Journal of Geodynamics* 34, 405-445.

Appendix

The maps show the results of the Greek sites of Cape Gerogombos A and B, Cape Schinou on Cefalonia Island, as well as Gialous Skala, Lefkada Island. Similar to the results in section 4.4.2, the first sites showed only minor changes throughout the surveys, whereas the beach site of Gialous Skala was affected by stronger changes like the site of Kaminia Beach, which is closely located. Minor changes of the first three sites are mostly due to rearrangement of pebble or vegetation development. The boulders of Cape Schinou, which are described in section 4.4.1 showed no change.

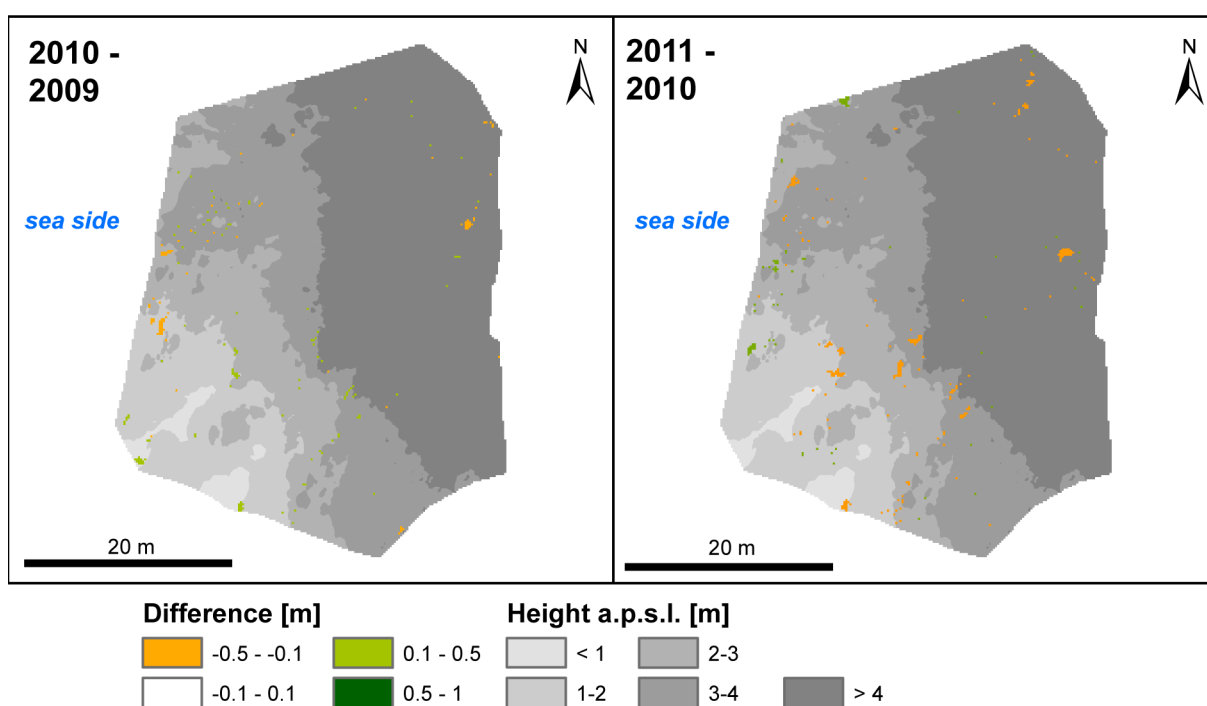


Figure A-1: Annual sediment budget for the years 2009/2010 and 2010/2011 at Cape Gerogombos A, Cefalonia Island, orange to red colours express erosion in comparison to the previous year, likewise green colors depict accumulation. Only minor changes were detected.

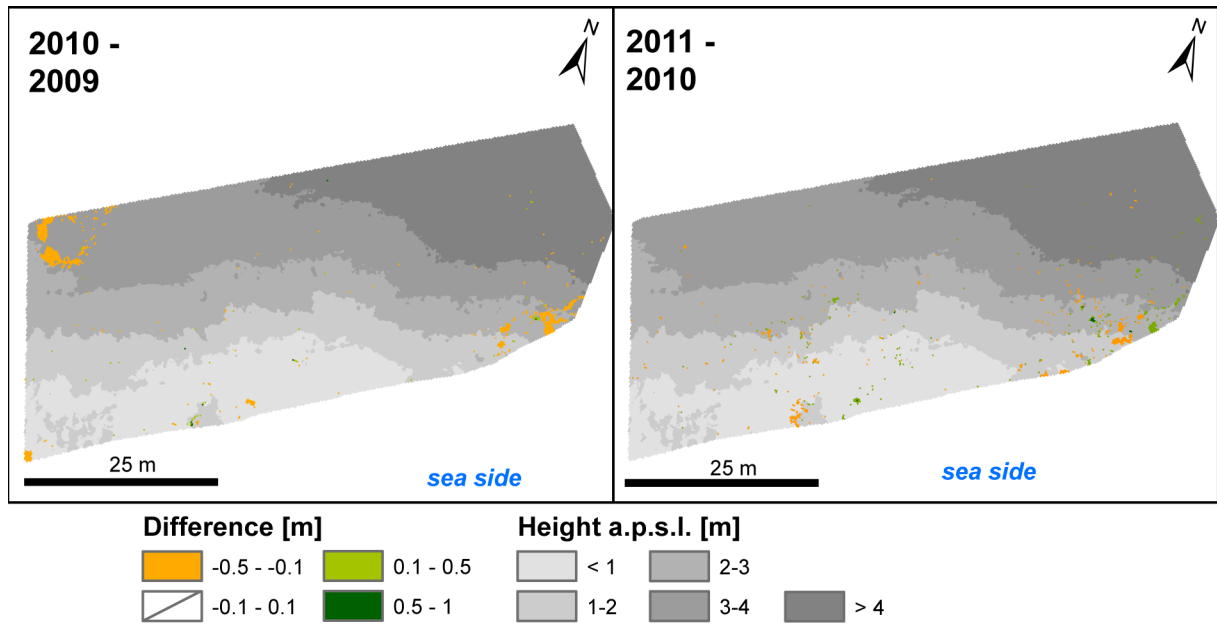


Figure A-2: Annual sediment budget for the years 2009/2010 and 2010/2011 at Cape Gerogombos B, Cefalonia Island, orange to red colours express erosion in comparison to the previous year, likewise green colors depict accumulation. Only minor changes were detected. Changes in the first comparison are a result of scan position change.

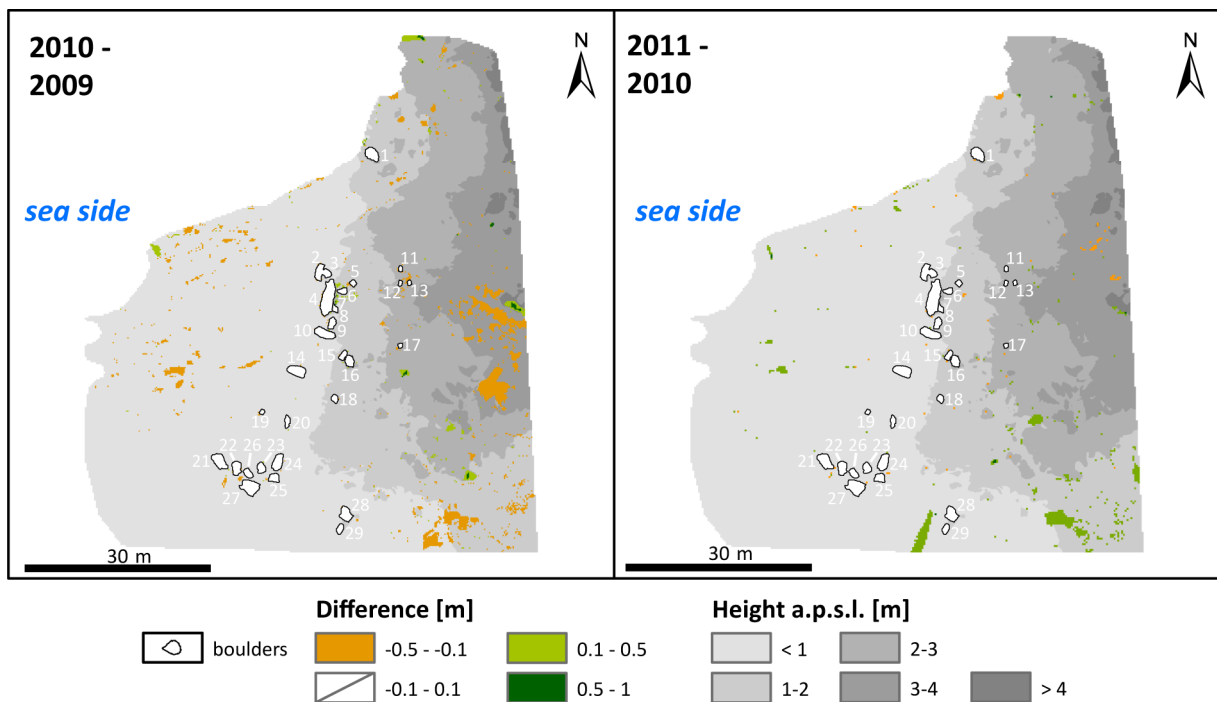


Figure A-3: Annual sediment budget for the years 2009/2010 and 2010/2011 at Cape Schinou, Cefalonia Island, orange to red colours express erosion in comparison to the previous year, likewise green colors depict accumulation. Only minor changes were detected, which correspond to vegetation change and water filling of small depressions for the comparison of 2010 to 2009.

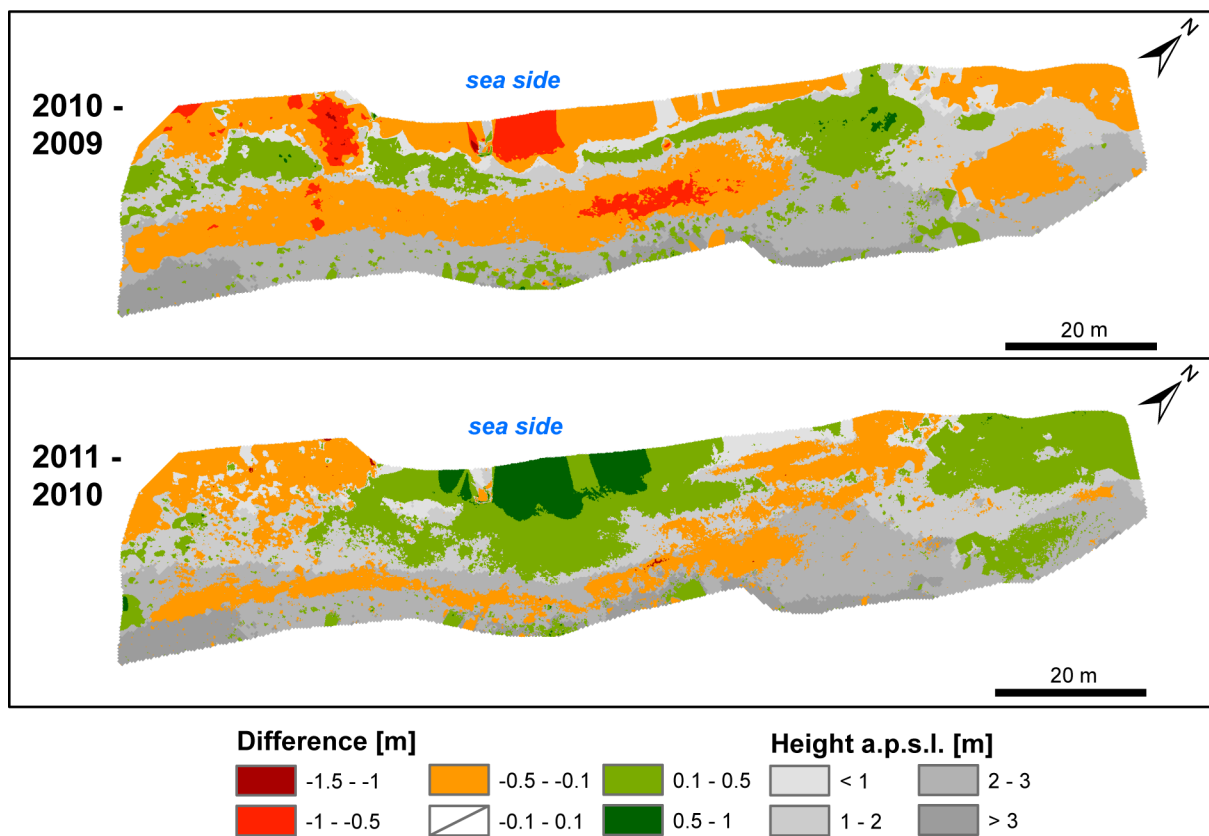


Figure A-4: Annual sediment budget for the years 2009/2010 and 2010/2011 at Gialous Skala, Lefkada Island, orange to red colours express erosion in comparison to the previous year, likewise green colors depict accumulation. The detected changes fit to the changes for the closely located site of Kaminia Beach (Figure 4-10) with slightly stronger erosion between the first years.

Erklärung

Ich versichere, dass ich die von mir vorgelegte Dissertation selbständig angefertigt, die benutzten Quellen und Hilfsmittel vollständig angegeben und die Stellen der Arbeit – einschließlich Tabellen, Karten und Abbildungen –, die anderen Werken im Wortlaut oder dem Sinn nach entnommen sind, in jedem Einzelfall als Entlehnung kenntlich gemacht habe; dass diese Dissertation noch keiner anderen Fakultät oder Universität zur Prüfung vorgelegen hat; dass sie – abgesehen von unten angegebenen Teilpublikationen – noch nicht veröffentlicht worden ist sowie, dass ich eine solche Veröffentlichung vor Abschluss des Promotionsverfahrens nicht vornehmen werde. Die Bestimmungen der Promotionsordnung sind mir bekannt. Die von mir vorgelegte Dissertation ist von Prof. Dr. Georg Bareth betreut worden.

Dirk Hoffmeister

Teilpublikationen:

HOFFMEISTER, D., BOLTEN, A., CURDT, C., WALDHOFF, G., BARETH, G., 2010. High resolution Crop Surface Models (CSM) and Crop Volume Models (CVM) on field level by terrestrial laser scanning. In: GUO, H., WANG, C. (Eds.), Proceedings of SPIE-7840, 6th International Symposium on Digital Earth: Models, Algorithms, and Virtual Reality (SEP 09-12, 2009), Beijing, China, 78400E.

HOFFMEISTER, D., TILLY, N., BENDIG, J., CURDT, C., BARETH, G., 2012. Detektion von Wachstumsvariabilität in vier Zuckerrübensorten durch multi-temporales terrestrisches Laserscanning. In: CLASEN, M., FRÖHLICH, G., BERNHARDT, H., HILDEBRAND, K., THEUVSEN, B. (Eds.), Informationstechnologie für eine nachhaltige Landwirtschaft, 32. GIL Jahrestagung (FEB-MAR 29-1, 2012), Freising, Germany. Köllen Verlag, Bonn, Germany.

HOFFMEISTER, D., NTAGERETZIS, K., AASEN, H., CURDT, C., HADLER, H., WILLERSHÄUSER, T., BARETH, G., BRÜCKNER, H., VÖTT, A., 2013a. 3D model-based estimations of volume and mass of high-energy dislocated boulders in coastal areas of Greece by terrestrial laser scanning. Zeitschrift für Geomorphologie, Supplementary Issues (in print).

HOFFMEISTER, D., TILLY, N., CURDT, C., NTAGERETZIS, K., BARETH, G., VÖTT, A., 2013b. Monitoring annual changes of the coastal sedimentary budget in western Greece by terrestrial laser scanning. Zeitschrift für Geomorphologie, Supplementary Issues 57 (4), 47-67.

HOFFMEISTER, D., WALDHOFF, G., CURDT, C., TILLY, N., BENDIG, J., BARETH, G., 2013c. Spatial variability detection of crop height in a single field by terrestrial laser scanning. In: STAFFORD, J.V. (Ed.), Precision agriculture '13, 9th European Conference on Precision Agriculture (JUL 07-11, 2013), Lleida, Spain. Wageningen Academic Publishers, Wageningen, The Netherlands, 267-274.